# Microstructure and texture evolution of high-temperature $\alpha$ phase in TiAl alloy during thermomechanical processing

Fengming Qiang

UNIVERSITÉ DE LORRAINE

NORTHWESTERN POLYTECHNICAL UNIVERSITY

# DISSERTATION

**Presented and publicly supported to obtain the doctor's degree of**

**University of Lorraine and Northwestern Polytechnical University**

**Fengming QIANG 强凤鸣**

SPECIAL FIELD: Engineering Sciences
OPTION: Materials Science

# Microstructure and texture evolution of high-temperature α phase in TiAl alloy during thermomechanical processing

**Defended on 19th October, 2021 in front of the jury:**

| | | |
|---|---|---|
| Supervisors: | Emmanuel BOUZY | Professor, LEM3, Université de Lorraine, France |
| | Hongchao KOU | Professor, Northwestern Polytechnical University, China |
| | Yudong ZHANG | Doctor HDR, LEM3, Université de Lorraine, France |
| President of the jury: | Alain HAZOTTE | Professor, LEM3, Université de Lorraine, France |
| Reviewers: | Jean-Philippe MONCHOUX | Chargé de recherche, CEMES Toulouse, France |
| | Junpin LIN | Professor, University of Science and Technology Beijing, China |
| Examinators: | Fantao KONG | Professor, Harbin Institute of Technology, China |
| | Bin TANG | Professor, Northwestern Polytechnical University, China |
| Invited member: | Weimin GAN | Doctor HDR, Helmholtz-Zentrum Hereon, Germany |

Laboratoire d'Étude des Microstructures et de Mécanique des Matériaux, LEM3
7 rue Félix Savart, 57070 Metz, France

# Contents

# Acknowledgements

The present work is accomplished at the Laboratoire d'Étude des Microstructures et de Mécanique des Matériaux (LEM3), Université de Lorraine (UL), Metz, France, and the State Key Laboratory of solidification processing, Northwestern Polytechnical University (NPU), Xi'an, China. I have the honor to work at the two laboratories and I would like to give my hearted thank to the two institutions for hosting my study and to the staff in the two laboratories for their kind help. I gratefully acknowledge the China Scholarship Council (CSC) for providing a PhD scholarship to support my study in France.

I would like to express my deepest and sincere gratitude to my supervisor, Prof. Emmanuel BOUZY, UL, in France, Prof. Hongchao KOU, NPU, in China, Dr. HDR. Yudong ZHANG, UL, in France, for their constructive suggestions, incredible patience and constant supports to my work. I profit greatly from their rigorous working style, critical thinking, strong thirst to knowledge and optimistic attitude. My heartfelt thanks are given to Prof. Jinshan LI, NPU, in China, for providing the opportunity to me to pursuit my study in French. I also sincerely gratitude to Prof. Claude ESLING for his help in my research work and daily life in France.

I would like to thank the reviewers and the jury members for taking time out of their busy schedules to achieve my dissertation defense, and special gratitude to Prof. Junpin LIN, Dr. Jean-Philippe MONCHOUX, Prof. Alain HAZOTTE, Prof. Fantao KONG, and Prof. Bin TANG for their evaluation of my dissertation and the constructive suggestions and comments.

I would like to express my gratitude to all the technicians at LEM3 who have offered their assistance to my work, especially to Mr. Olivier PERROUD for his help with the X-ray diffraction analyzes, to Mr. Lionel GERMAIN for providing the help in EBSD data reconstruction by the software Merengue 2, and to Mr. Bonoit BEAUSIR and Mr. Jean Jacques FUNDENBERGER for providing the help with data post-processing using Atex. I also greatly thank Dr. HDR. Weimin GAN, at Helmholtz-Zentrum Hereon in German, for provide the selfless help in the texture measurement using synchrotron radiation.

I am also grateful to all the staff and students in LEM3 and Northwestern Polytechnical University, and my friends who shared their experiences with me and offered help to my study, including Dr. Ke HUA, Dr. Qian WANG, Dr. Yajun ZHAO, Dr. Chunyang ZHANG, Dr. Jianchang ZHU, Dr. Meishuai LIU, Dr. Wenqing CHENG, Dr. Yanfeng YANG, Dr. Hailong SHI, Mr. Zhengtian YANG, Ms. Pengru ZHAO, Ms. Nana CHEN, Ms. Chenlou JIA, Ms. Lingling WANG, Mr. Zhihong WU and Mr. Yonghao YU.

A special gratitude and love go to my family for their endless support. I deeply appreciate my parent's incredible patience and constant support throughout my Ph.D. study. I will never truly be able to express my sincere appreciation to the both of them. Without the great help from my parents during their stay with me, I would have not been able to start my PhD work.

22/12/2021 At Xi'an

# Abstract

Increasing demands on modern turbines require ($\alpha_2+\gamma$) lamellar-structured TiAl alloys with fine colony size and properly aligned lamellae. According to the $\alpha \rightarrow \alpha_2+\gamma$ phase transformation, the lamellar structure depends directly on the high-temperature α phase. Thus, the lamellar structure optimization could be realized by the modification of high-temperature α phase through thermomechanical processing. In this work, a thorough investigation was conducted on the high-temperature α phase in two TiAl alloys in terms of the deformation behavior, dynamic recrystallization (DRX), grain growth and texture evolution.

Under uniaxial compression, the DRX of the α phase is a continuous fragmentation process (CDRX) in three characteristic stages: i) serrations of grain boundary and formation of symmetrical-tilt boundaries with <0001> disorientation axis near boundary bulging regions; ii) formation of subgrains by evolving symmetrical-tilt boundaries into asymmetrical-tilt boundaries with $<10\bar{1}x>$ disorientation axis by absorbing basal dislocations, or tilt-twist boundaries with $<11\bar{2}y>$ disorientation axis by rotational movements of the bulged parts; iii) detachment of subgrains from the parent grain with gradually increased misorientation, and mixture with the ones fragmented from other grains by grain boundary sliding. These three processes happened repeatedly from grain boundary regions toward grain interiors until the whole initial microstructure was replaced by the DRXed one.

The plastic deformation of the α phase is closely related to the crystallographic orientations of the initial α grains that play an important role in the deformation mechanism and the CDRX progress (softening). For the soft α grains, CDRX was completed quickly at a relatively small macroscopic strain by intragranular dislocation slip. The hard α grains demonstrated two ways: i) grains with <0001>//LD, in which dislocation accumulation was only assisted by the local strain accommodation with the neighboring α grains from boundary regions; ii) grains with $<11\bar{2}0>$//LD, in which dislocation accumulation was achieved by kinking through basal slip and dislocation slip in the boundary regions from incompatible local strain. These grains required large strain to accumulate sufficient dislocations for CDRX. The strain-resolved contribution of the deformation (hardening) and CDRX (softening) result in the specific flow

stress states. The texture evolution is mainly induced by dislocation slip. The orientations of the DRXed grains were largely inherited from those of the parents. With the deformation, the tilted basal fiber typed orientations developed in both the retained coarse α and the formed DRXed α grains. The hot compression produces refined α grains but not expected texture to align ($\alpha_2$+γ) lamellae.

The microstructure and texture of the α phase during hot extrusion in the (α+β) phase region exhibit different features. The extruded microstructure was very heterogenous, comprising a large population of unRXed α grains and fine primary RXed α grains with $<10\bar{1}0>$//ED and a small population of grown α grains with $<11\bar{2}0>$//ED. The two texture components are beneficial for lamella alignment. Besides, the thermally-induced α → β phase transformation interweaving with the abnormal α grain growth happened during the transition from extrusion to water-quenching, producing two types of β particles: i) intergranular β particles with the Burger OR with their neighboring α grain; ii) intragranular β particles without the OR with the hosts from the intergranular β ones after being swallowed by the abnormally grown α grains.

This work provides original information of the deformation behavior, DRX and grain growth of the high-temperature α phase in TiAl alloys, and provides new insight and guidance for microstructural optimization of ($\alpha_2$+γ) lamellar structure by the adjustment of their parent high-temperature α phase through thermomechanical processing.

***Key words:*** TiAl alloy; Thermomechanical processing; Microstructure evolution; Deformation behavior; Dynamic recrystallization (DRX); Texture.

# Résumé

La demande de performances accrues pour les turbines d'avion nécéssitent d'utiliser des alliages TiAl à structure lamellaire ($\alpha_2+\gamma$) en contrôlant la taille des colonies et l'orientation des lamelles. Comme la structure lamellaire dépend directement de la phase haute température (HT), l'optimisation de la structure lamellaire peut être réalisée en modifiant la phase HT par un traitement thermomécanique adéquat. Dans ce travail, une étude approfondie a été menée sur la phase HT α dans deux alliages TiAl en termes de comportement lors de la déformation, de la recristallisation dynamique (DRX), de la croissance des grains et d'évolution de la texture.

Sous compression uniaxiale, la DRX de la phase α se déroule selon un processus de fragmentation continue en trois étapes caractéristiques: i) déformation des joints de grain initiaux en dentures et formation de sous-joints de flexion symétrique avec axe de désorientation <0001>; ii) Evolution des joints de flexion symétriques en joints de flexion asymétrique avec axe de désorientation $<10\bar{1}x>$ ou joints de flexion-torsion avec axe de désorientation $<11\bar{2}y>$; iii) détachement des sous-grains du grain parent et mélange avec les fragments des autres grains par glissement aux joints de grains. Ce processus de fragmentation se produit d'abord dans les régions proches des joints de grain initiaux puis de proche en proche vers l'intérieur des grains.

La déformation de la phase α est étroitement liée aux orientations des grains α initiaux. Pour les grains mous, la DRX les transforme complètement pour une déformation macroscopique relativement petite. Les grains durs sont de deux types: i) grains avec <0001>//LD , pour lesquels l'accumulation de dislocations n'est assistée que par l'accommodation locale des déformations avec les grains α voisins; ii) grains avec $<11\bar{2}0>$//LD, pour lesquels l'accumulation de dislocations peut aussi être obtenue par pliage par glissement basal. Ces grains nécessitent une grande contrainte pour accumuler suffisamment de dislocations pour amorcer la DRX. Le comportement mécanique résulte des contributions respectives de la déformation et de la DRX au durcissement et à l'adoucissement. L'évolution de la texture est principalement induite par le glissement des dislocations. Les orientations des grains recristallisés sont largement héritées de celles de leurs parents. Avec la déformation, des

orientations de type fibre avec plan basal incliné se sont développées à la fois dans les gros grains retenus (grains durs) et dans les grains formés par DRX (grains mous). Cette texture ne permet pas d'aligner suffisamment les lamelles ($\alpha_2+\gamma$). Toutefois la compression à chaud produit des grains fins.

La microstructure et la texture de la phase après extrusion à chaud dans le domaine de phases ($\alpha+\beta$) présentent des caractéristiques différentes. La microstructure extrudée est très hétérogène, comprenant d'une part une population majoritaire constituée à la fois de grains non recristallisés et de petits grains recristallisés avec une texture de fibre $<10\bar{1}0>$//ED et d'autre part une population minoritaire de grains ayant subi une croissance anormale avec une texture de fibre $<11\bar{2}0>$//ED. Les deux composantes de texture sont bénéfiques pour l'alignement des lamelles. La transformation de phase $\alpha \rightarrow \beta$ induite thermiquement interfere avec la croissance anormale des grains pendant le transfert de l'extrusion à la trempe à l'eau, produisant deux types de particules $\beta$: i) particules $\beta$ intergranulaires avec relation d'orientation de type Burger avec leur grain voisin; ii) particules $\beta$ intragranulaires sans relation d'orientation avec le grain hôte qui correspondent à des particules $\beta$ intergranulaires qui ont été ensuite envahies par des grains $\alpha$ en croissance anormale.

Grâce à des analyses cristallographiques approfondies, cette étude met en évidence les mécanismes qui président à la déformation, la DRX et la croissance des grains de la phase HT $\alpha$ dans les alliages TiAl.

***Mots-clés:*** Alliage TiAl; Traitements thermomécaniques; Microstructure; Déformation; Recristallisation dynamique; Texture.

# Chapter 1 Background and bibliographic review

## 1.1 General introduction

New high-performance engine concepts for aerospace and automotive application enforce the development of materials with increased high-temperature capability. TiAl-based alloys have attracted considerable interest due to their low weight, high temperature strength, excellent burn resistance and quite good oxidation resistance, and these intermetallic alloys are regarded as strong substitute candidates for rotating blades in the high-pressure compressor (HPC) and the low-pressure turbine (LPT) of aero engines which are usually made of Nickel base superalloys. It is well known that TiAl alloys with the ($\alpha_2$+$\gamma$) lamellar structure shows outstanding characteristics for high-temperature structural applications, especially in the case where the proper alignment of the lamellae is achieved. Thus, the development of a technique to optimize the lamellar structure, i.e., colony size refinement and lamellar orientation control, has appeared as an attractive objective of research. Resulting from the decomposition of the $\alpha$ phase during cooling, the lamellar structure is constituted by lamellae of $\alpha_2$ and $\gamma$ phases, following the Blackburn orientation relationship: $\{111\}_\gamma//(0001)_\alpha$, $<1\bar{1}0>_\gamma//<11\bar{2}0>_\alpha$. All the $\alpha_2/\gamma$ lamellae in a given prior $\alpha$ grain share the same $(0001)_\alpha/(111)_\gamma$ interface. That means the characteristics of the resultant microstructure directly depend on high temperature $\alpha$ phase. Thermomechanical processing conducted above $T_{\gamma,solv}$ is the possible method to control lamellar orientation as well as refine colony size by deformation and dynamic recrystallization (DRX) of $\alpha$-phase. Thus, it is necessary to thoroughly investigate the deformation behavior, DRX, and texture evolution of $\alpha$ phase in TiAl alloys during thermomechanical processing.

This chapter is devoted to introducing some knowledge necessary for understanding this study. Firstly, a general background and the basic concepts of TiAl alloys, including the developments and applications, the phase constituents, the expected microstructure and its optimizing methods, are presented. On the basis of the corresponding literature, an idea for optimizing the lamellar microstructure of TiAl alloys by deforming the high-temperature $\alpha$ phase is proposed. Correspondingly, the dynamic recrystallization behavior, deformation mechanisms and texture development about the $\alpha/\alpha_2$ phase in TiAl alloys are displayed. Finally,

a short description of the motivation for the present thesis work is given, and the main contents are developed.

## 1.2 Basic information of TiAl alloys

### 1.2.1 Developments and applications of TiAl alloys

New structural materials have to be "stronger and lighter" to withstand the extremely high demanding conditions in the next generation of automotive and aircraft engines which are targeted to exhibit higher efficiency leading to reduced fuel consumption, significant lower emission of $CO_2$ and $NO_x$ as well as to a noticeable reduction of engine noise [1–3]. In the last two decades, TiAl-based alloys have attracted significant attention due to their attractive properties that have been considered for high-temperature applications in automotive and aerospace industries [4–8]. Their advantages are mainly seen in low density (3.9~4.2 g/cm$^3$), high specific stiffness, high specific yield strength, good high temperature creep properties and oxidation resistance. Particularly in the temperature range of 600~900 ℃, TiAl-based alloys exhibit similar or better specific strength as compared with currently used Ni-base alloys and Ti alloys [9,10], as seen in Fig. 1-1.

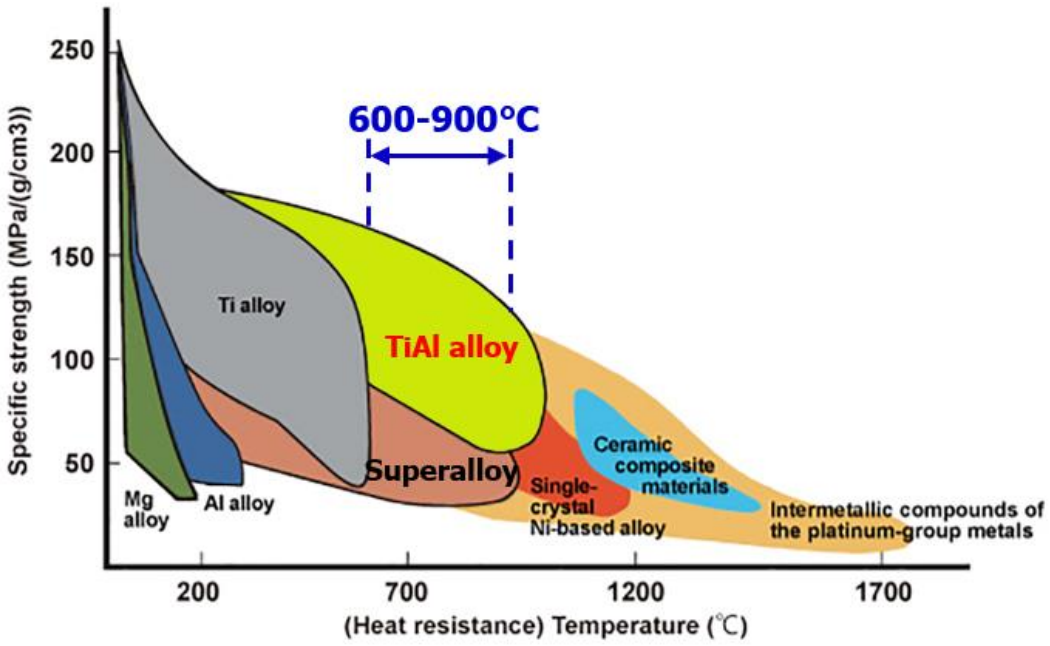


Fig. 1-1 Schematic diagram showing the specific strengths of structural materials as a function of temperature [9].

Thanks to the extensive research and development (R&D) activities during the last three decades, TiAl-based alloys have matured from ‘‘laboratory curiosities”, i.e., the 1st-generation TiAl alloy with the normal composition of Ti-48Al-1V-0.3C (all compositions in this thesis are given in at.%) [10,11], to novel structural light-weight materials which eventually found their applications [6,12,13], i.e., the 2nd-generation and the 3rd-generation TiAl alloys. The composition of the 2nd-generation TiAl alloys, the conventional engineering TiAl-based alloys, can be summarized as follows [13]:

$$\text{Ti-(45~48)Al-(1~3)X-(2~5)Y-(<1)Z}$$

where X = (Cr, Mn, V); Y = (Nb, Ta, W, Mo); Z = (Si, B, C). (The effects of selected alloying elements on mechanical properties of TiAl-based alloys are displayed in Table 1-1).

Table 1-1 Effect of selected alloying elements on mechanical properties of TiAl-based alloys [13].

| Elements | Effects |
|---|---|
| Nb | Increases oxidation and creep resistance in small amounts, also increases high temperature strength if added between 5~10% |
| Cr | Increases ductility if added in small amounts; increases oxidation resistance if added in the range of 8% |
| Mn | Increases ductility |
| Ta | Increases oxidation and creep resistance and tendency for hot cracking |
| Mo | Increases strength, and creep and oxidation resistance. |
| W | Oxidation and creep resistance |
| V | Increases ductility |
| Zr | Improves hot deformation |
| B | Grain refinement |
| C | Increases creep and oxidation resistance |
| Si | Improves oxidation resistance and creep if added between 0.5~1%, increases fluidity in casting, and reduces the tendency to hot cracking |

One of the most successful alloys in this generation is Ti-48Al-2Nb-2Cr (Ti4822). In 2006, General Electric announced the usage of investment cast blades of Ti-48Al-2Cr-2Nb alloy in the low-pressure turbine (LPT) of the GEnx™ engine [14,15]. It was the first time a TiAl-based alloy was employed for rotating parts of commercial aircraft engine. Fig. 1-2 shows one of the

many TiAl LPT blades used in the GEnx™ engine and the turbine section of the GEnx™-1B aircraft engine as used on the Boeing 787. The turbine consists of two high-pressure stages and seven low-pressure stages, including two stages (stages 6 and 7) of TiAl LPT blades. Replacement of Ni-based superalloy parts with TiAl-based alloys shows significant improvements in fuel burn, pollutant and noise emissions, and operating costs [6].

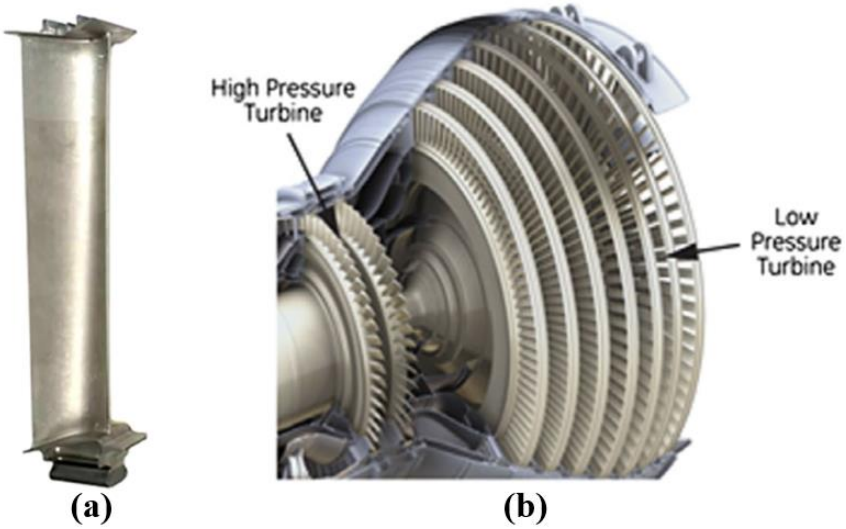


Fig. 1-2 (a) Photograph of TiAl LPT blade as used in the last stage of GEnx engine; (b) Diagrams showing the turbine section of the GEnx-1B aircraft engine as used on the Boeing 787 [6].

Despite the enormous potential for structural application that exists for TiAl-based alloys, they suffer from a major challenge in processing and machining because of the poor room temperature ductility (1~2%) [16–18]. In order to improve the hot workability and service temperature of TiAl-based alloys, the 3$^{rd}$-generation alloys are developed by introducing high content of β-stabilizing alloying elements, such as Nb and Mo. For a large number of these 3$^{rd}$-generation alloys the composition can be written as [3,6,13,19]:

$$\text{Ti-(42~46)Al-(0~10)X-(0~3)Y-(0~1)Z-(0~0.5RE)}$$

where X = (Cr, Mn, Nb, Ta); Y = (Mo, W, Hf, Zr); Z = (C, B, Si); RE refers to rare earth elements.

TiAl-based alloys with Nb contents in the range of 5~10 at.% and small additions of B and C are referred to as TNB (Ti-45Nb-(5~10)Nb-(0~0.5)(B,C)) alloys [20–23]. Further alloying and process development was undertaken to lower the content of creep-deteriorating β/$β_0$-phase within the microstructure prevailing during service, which led to the finding of the well-known

TNM alloy with a nominal composition of Ti-43.5Al-4Nb-1Mo-0.1B [7,24–28]. Pratt & Whitney have applied TNM alloy in producing LPT blades for their PW1100G geared turbofan (GTF™) engine by isothermal forging [6,7,29,30]. In September 2014, the new Airbus 320 neo equipped with two GTF™ engines completed his maiden flight.

## 1.2.2 Phase transformations and phases in TiAl alloys

### 1.2.2.1 Phase transformtions

TiAl-based alloys of interest normally with the composition of 40~48 at.% Al content, as shown in Fig. 1-3, which are solidified through the β phase region or, for a narrow range of Al content, through peritectic reactions.

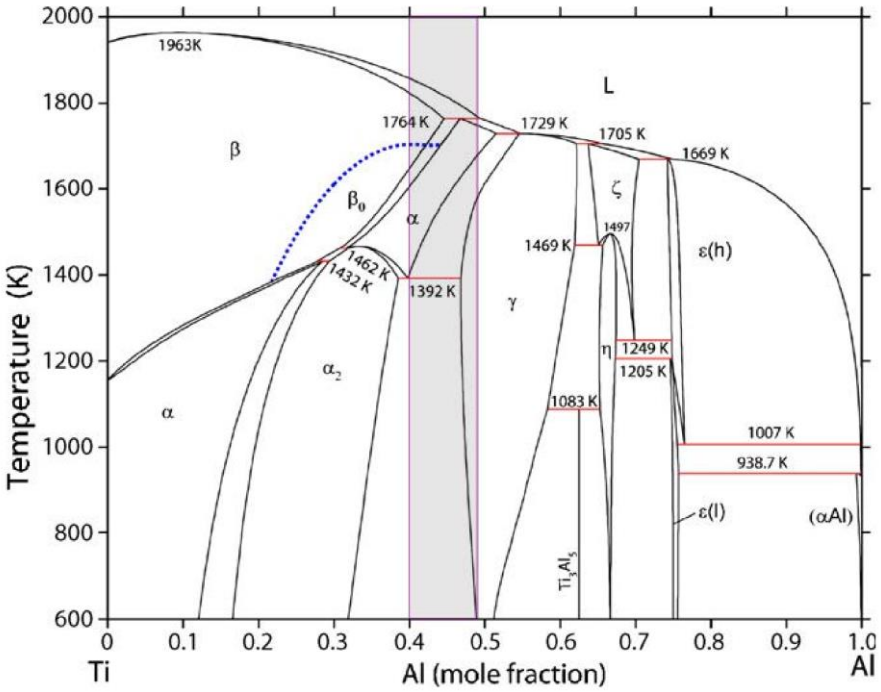


Fig. 1-3 Binary phase diagram Ti-Al [31].

In conventional TiAl-based alloys (1st- and 2nd-generation) with high Al content of 45-49 at.% solidification leads to the formation of β dendrites, followed by the peritectic formation of the α phase, L → L+β → α. Peritectically solidified alloys with high Al contents have been reported to present a characteristic structure based on coarse columnar grains which grow in the opposite direction to that of heat extraction. In general, peritectic solidification alloys results in textured cast components.

In contrast to the peritectic solidification pattern in conventional TiAl-based alloys, the solidification process of the 3rd-generation alloys is achieved as: L → L+β → β → β+α → α. As they solidify entirely through the disordered β-phase region, the 3rd-generation alloys also known as β-solidifying TiAl alloys. The β → α phase transformation follows the Burgers orientation relationship (Burgers OR) $(0001)_\alpha//(110)_\beta$, $<11\bar{2}0>_\alpha//<1\bar{1}1>_\beta$, by which α grains with up to 12 orientation variants can be formed within a single β grain, leading to an intrinsic grain refinement and a more isotropic texture which is not possible in case of a peritectic solidifying TiAl alloy. Therefore, the cast TiAl alloys following the β solidification route exhibit fine-grained homogeneous structures with weak solidification texture.

After the solidification process, the solid-state transformations occur subsequently upon cooling, which involve passing through the single α phase region or through the (β+α) phase region depending on composition. Then typical TiAl-based alloy microstructures alternating $\alpha_2/\gamma$ lamellae will be formed within the α grains following the Blackburn orientation relationship (Blackburn OR) [32]: $\{111\}_\gamma//(0001)_\alpha$, $<1\bar{1}0>_\gamma//<11\bar{2}0>_\alpha$.

#### 1.2.2.2 Phases

It can be seen from the phase diagram (Fig. 1-3) that there are three main phases of interest for Ti-Al alloys namely, $\beta/\beta_0$, $\alpha/\alpha_2$ and γ [22].

In the Ti-Al binary alloy, there exists the disordered high-temperature β phase, but it will transform into α phase in the subsequent cooling process so that there is no β phase in the resultant microstructure. However, the addition of β-stabilizing elements, such as Nb, W, etc., significantly increase the stability of β phase and prevent it from completely transforming into α phase [23,28]. The retained β phase undergoes an ordering transformation at 1175~1205 ℃, and changes into a very brittle and hard $\beta_0$-phase. The $\beta_0$-phase has a body-centered cubic (BCC) structure with the lattice parameter $a$=0.316nm [33], as displayed in Fig. 1-4 (a).

The $\alpha_2$ phase has an ordered hexagonal closed packed (HCP) structure ($D0_{19}$) with lattice parameters, $a$=0.5782 nm and $c$=0.4629 nm, as shown in Fig. 1-4 (b), which is formed between 22~39 at.% Al content and transforms from the disordered structure, high-temperature α phase, to an ordered one at ~1180 ℃. The α and $\alpha_2$ phases have similar HCP structures with different

lattice parameters. In the disordered α phase the Ti and Al atoms occupy randomly the different crystallographic sites of the HCP structure, while in the ordered $\alpha_2$ phase the Al and Ti atoms occupy specific crystallographic sites resulting in the $\alpha_2$ structure having twice the lattice parameter *a* of α while maintaining a similar *c* value. It is known that the $\alpha_2$ phase exhibit extremely poor toughness and tensile ductility at ambient temperatures while possessing good oxidation resistance and excellent elevated temperature specific strength [34].

The γ-TiAl phase contains 49~66 at.% Al content and possesses an ordered face centered tetragonal (FCT) structure with lattice parameters $a$=0.4005 nm and $c$=0.4070 nm, as shown in Fig. 1-4 (c). The tetragonality is due to different atomic radii of Ti and Al. For the stoichiometric compound, the tetragonality ratio is 1.02 [35]. The γ phase exhibits excellent oxidation resistance and has very low hydrogen absorption, but its room temperature ductility is close to none owing to the limited number of slip systems [36].

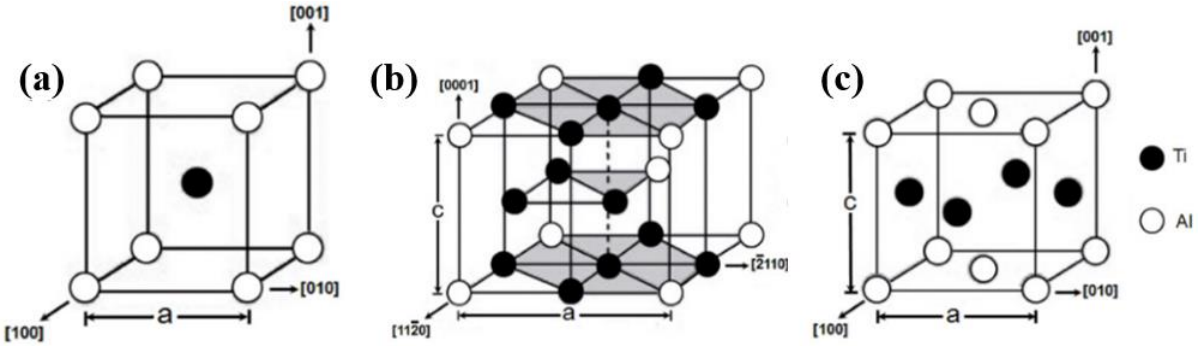


Fig. 1-4 Crystal structures of (a) $\beta_0$ phase (b) $\alpha_2$ phase and (c) γ phase in TiAl alloy [22].

## 1.2.3 Microstructural characteristics of TiAl alloys

### 1.2.3.1 Typical microstructure of TiAl alloys

Generally, four typical microstructures are usually formed in TiAl-based alloys [13,37], namely, (I) near-gamma (NG), (II) duplex, (III) nearly-lamellar (NL), and (IV) fully lamellar (FL), as displayed in Fig. 1-5.

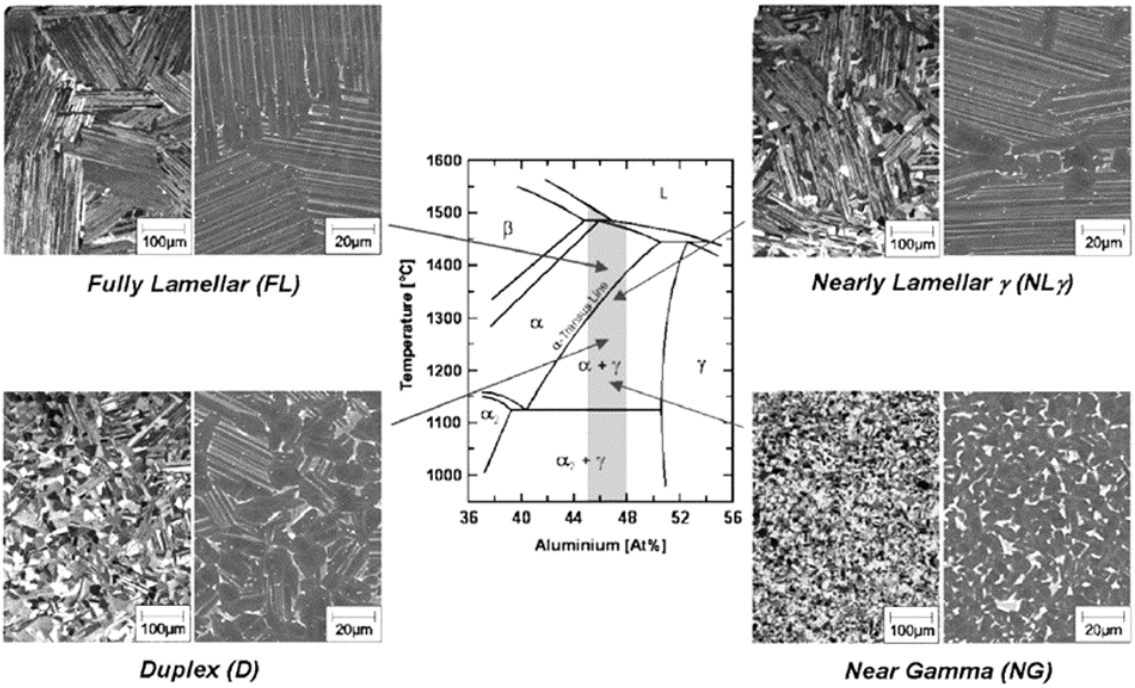


Fig. 1-5 Four kinds of typical microstructure of TiAl alloys. These microstructures were adjusted in a fine grained Ti-46.5Al-4(Cr,Nb,Ta,B) alloy by means of heat treatments [37].

(I) Near-gamma (NG) microstructure

Annealing of the material above the eutectoid temperature results in the coarsening of the existing γ grains and leads to the formation of the near-gamma microstructure. The microstructure, is made up of equiaxed γ grains with $\alpha_2$ precipitates at the grain boundaries and triple points. The average grain size for this kind of microstructure usually ranges between 30~50 μm.

(II) Duplex microstructure

The duplex microstructure is produced when fabrication temperature or heat treatment is carried out in the middle of the (α+γ) phase region where the α/γ volume ratio is close to 1. The duplex microstructure consists of fine fully lamellar colonies along with equiaxed γ grains. The mixture of these two grain morphologies forms a very fine microstructure with an average grain size around 10 μm.

(III) Nearly-lamellar (NL) microstructure

At temperatures higher or lower than where the α/γ volume ratio is close to 1, coarsening

of the predominant phase occurs. Hence, heat treatment at temperatures below the duplex microstructure temperature leads to coarsening of γ grains and the formation of the near-gamma microstructure, while heat treatment above the duplex microstructure temperature results in the coarsening of α grains and the formation of the nearly-lamellar microstructure. The nearly-lamellar microstructure is characterized by a majority of lamellar colonies with some equiaxed γ grains forming an average grain size in the range of 150~200 μm.

(IV) Fully-lamellar (FL) microstructure

The fully-lamellar microstructure forms when fabrication temperature or heat treatment is carried out at a temperature in the pure α phase region. Upon cooling to room temperature, the γ phase precipitates from the α grains ($\alpha \rightarrow \alpha/\alpha_2+\gamma$), leading to the formation of alternate lamellae of $\alpha/\alpha_2$ and γ phase with a fully lamellar morphology. The lamellar colonies are coarse and range from 200~1000 μm.

Due to the very fine grain size, the near-gamma and duplex microstructure provides adequate ductility and fatigue resistance but it exhibits low creep resistant and fracture toughness; while the microstructure with fully lamellar structure demonstrates superior fracture toughness and creep resistant but demonstrates poor ductility [10,13,37–39], as shown in Fig. 1-6. This inverse correlation between tensile properties and resistance to fracture (fracture toughness) requires a careful selection of the microstructure which makes microstructural optimization important for achieving balanced engineering properties. As the duplex microstructure does not perform well in terms of creep and fatigue resistance at high temperatures compared with that of the fully lamellar microstructure, the fully lamellar microstructures could potentially solve the problem of poor ductility at ambient temperature by refining the colony size [38,40]. It is reported that the nearly fully lamellar and/or fully lamellar microstructures could provide the much-needed combination of mechanical properties for machining using a viable production method and structural integrity during the components' lifetime [39,41–43].

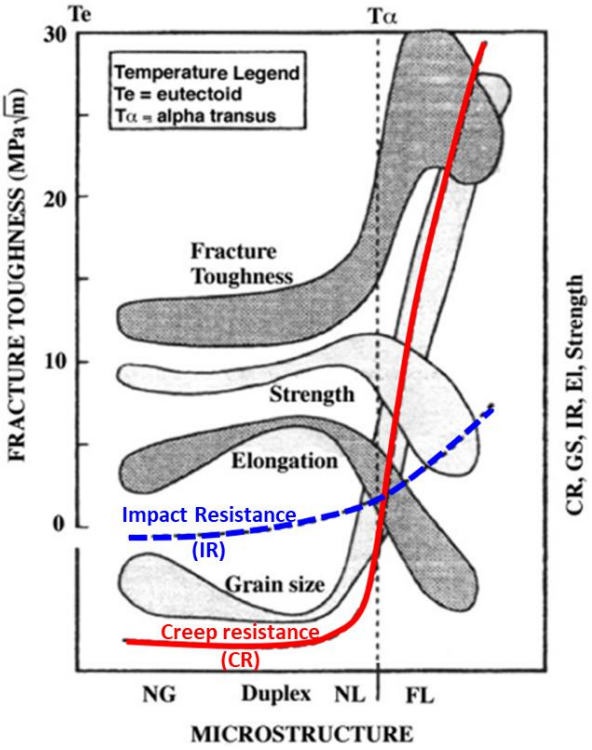


Fig. 1-6 Dependence of mechanical properties such as fracture toughness, strength, elongation, impact resistance (IR), creep resistance (CR), and grain size on the microstructure type, where NG is near-gamma, NL is nearly lamellar and FL is fully-lamellar [13].

### 1.2.3.2 Characteristics of lamellar structure and optimization methods

To achieve a good balanced mechanical property of the lamellar structure for practical applications of TiAl alloys, many studies have been carried out to optimize the lamellar structure, including (I) lamellar spacing, (II) colony size and (III) lamellar orientation, based on the detailed knowledge of the relationship between lamellar structure characteristics and mechanical properties.

(I) Lamellar spacing

The Hall–Petch relation holds between lamellar spacing and yield stress of TiAl alloy at room temperature as well as at elevated temperature [43–47], as seen in Fig. 1-7. It should be mentioned that the yield stress will reach a saturated value when the lamellar spacing drops to 100 nm [46,47]. Lamellar spacing also influences the creep and fatigue properties of the material [48,49]. The thinner the lamellae, the more lamellar interfaces per unit area, preventing the motion and multiplication of dislocations, then improving the creep resistance. Moreover,

both crack initiation and crack propagation toughness increase with decreasing lamellar spacing in a manner similar to the Hall–Petch relation since a small lamellar spacing hinders translamellar microcracking and thus linkage of the main crack with interlamellar microcracks [50]. The lamellar spacing directly depends on the cooling rate from the high-temperature α region, and air cooling is sufficient to reduce lamellar spacing [51]. Besides, the non-equilibrium phase transformation can also be used to obtain an ultrafine, nanometer-scale lamellar structure, i.e., an aging treatment is conducted on the quenched sample with supersaturated $\alpha/\alpha_2$ phase, then the ultrafine γ lamellae can precipitate from the supersaturated $\alpha/\alpha_2$ phase [52–54].

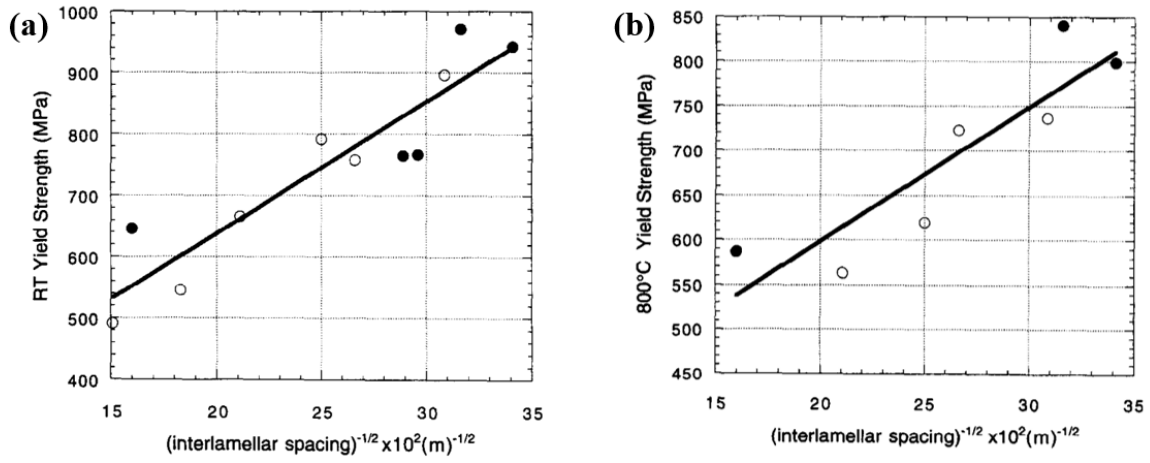


Fig. 1-7 Yield strength of IM and PM TiAl alloys against (interlamellar spacing)$^{-1/2}$. (a) At room-temperature; (b) at 800 °C. Open symbols for IM alloys and closed symbols for PM alloys [44].

(II) Colony size

The room-temperature ductility of TiAl alloys is mainly dominated by colony size, showing an increase in ductility with decreasing colony size by the Hall-Petch relationship [36,43,44], as seen in Fig. 1-8 (a). This is due to the fact that as the grain size decreases, the volume of defects such as grain boundaries increases, which in turn aids in the deformation mechanisms. It was a logical concern that lamellar structures with refined colony sizes might not have good creep resistance, because of possible sliding along colony boundaries at elevated temperatures. Actually, it has been evidenced by Hsiung et a1. [55] that the mobility of interfacial dislocations on both $\gamma/\alpha_2$ and γ/γ interfaces plays a dominant role in the creep

deformation behavior of a fully-lamellar TiAl alloy. It means that the major microstructural variable influencing the creep resistance of a lamellar-structured TiAl alloy is the lamellar spacing. Besides, the creep rates are independent of grain size as far as grain size is larger than 100 μm [48,56], as is evident in Fig. 1-8 (b). When grain size is greater than 100 μm, it is not necessary to worry about the weakening due to grain refinement. Thus, colony refinement is the preferred method to improve the overall performance of the lamellar structure [36,57]. The main ways for colony refinement can be concluded as follows:

i) Addition of element B [58–61]. The role of the B addition is mainly played in the solidification stage and served as a heterogeneous nucleation point to promote nucleation during the solidification process. It was found that B addition of 1 at.% have a strong limiting effect on β dendrite growth, resulting in much finer β dendrites contributing to grain refinement.

ii) Heat treatment [62,63]. The heat treatments for refining the colony size are expected to suppress the α → α+γ transformation, repeat α ↔ α+γ transformation by cyclic annealing around the α-transus temperature [62], or exploit the α → $\gamma_M$ massive transformation [63,64]. H. Clemens et al [63] has reported that significant grain refinement from 120 to 30~65 μm was achieved in Ti-46Al-2Cr-2Mo-0.25Si-0.3B alloy by taking advantage of solid state phase transformations, and massive phase transformation was used for microstructural refinement in the case of coarse-grained Ti-46Al-9Nb alloy.

iii) Thermomechanical processing [65–67]. Typical thermomechanical processing for the breakdown of the coarse as-cast microstructures of TiAl ingots include forging, rolling, and extrusion, during which the significant dynamic recrystallization will lead to a refinement of the microstructure. The deformed microstructure generally contains some globular γ (and β) phase, and subsequent heat treatments are needed to obtain the lamellar structure [45,68].

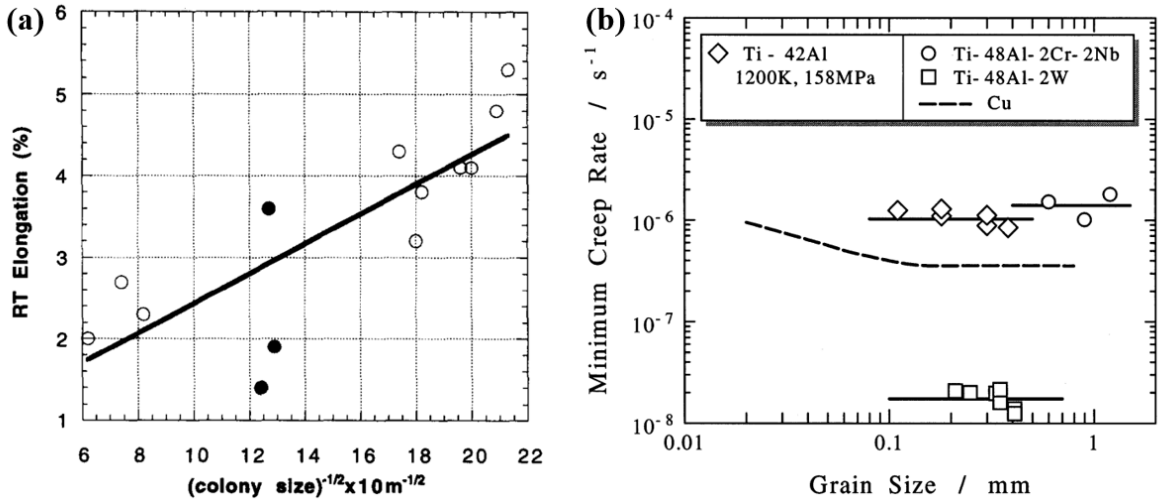


Fig. 1-8 (a) Room-temperature elongation of IM and PM TiAl alloys against (colony size)$^{-1/2}$ (Open symbols for IM alloys and closed symbols for PM alloys) [43]; (b) Grain size dependence of minimum creep rate in Ti-42Al crept at 1200 K under 158 MPa [48], together with the results of Ti-48Al-2Cr-2Nb (1123 K, 250 MPa) [56], and Ti-48Al-2W (1033 K, 276 MPa) [69].

(III) Lamellar orientation

The influence of the lamellar orientation on the performance of TiAl alloys are usually conducted using polysynthetically twinned (PST) crystals which are composed of a single grain with the lamellar structure. Researches [70–72] showed that the tensile properties of PST crystals depend strongly on $\phi$, which is the angle between the loading axis and the lamellar traces. As displayed in Fig. 1-9, PST crystals exhibit the highest strength at $\phi$=90°, however, tensile ductility at $\phi$=90° is almost zero. A good balance of strength and ductility is obtained at $\phi$=0°, where strength is not as high as that for $\phi$=90°, but tensile ductility is as large as 5~10% at room temperature. When $\phi$ is in the range of 30~60°, yield stress is much lower, and elongation is much higher than $\phi$=0° and 90°. This trend remains unchanged almost up to 1000 °C. Therefore, if one can control the orientation of the lamellar structure in each grain of a polycrystalline TiAl alloy, a good combination of strength and ductility of the fully lamellar TiAl alloy will be obtained. As the lamellar structure of TiAl-based alloys consists of lamellae of the γ and $\alpha_2$ phases with the $\{111\}_\gamma//(0001)_{\alpha_2}$, hence, to control the lamellar microstructure, the orientation of the high temperature α phase must first be controlled.

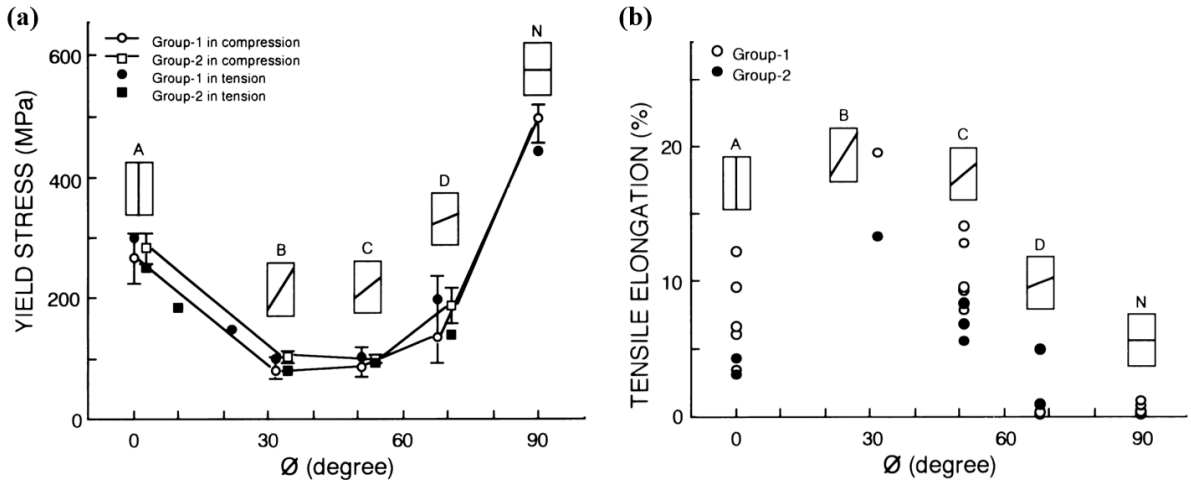


Fig. 1-9 Yield stress and elongation of PST crystals at room temperature as a function of ϕ which is the angle between the loading axis and lamellar boundaries. The γ lamellae in samples of Group-1 and Group-2 are differently oriented [70,71].

One of the most prospective methods to achieve lamellar orientation control is directional solidification (DS) process [73–75]. The main difficulty in the lamellar orientation control of TiAl alloys by DS processing is that the lamellar microstructure is not formed from the liquid but from the solid state [76]. For the α-solidifying TiAl alloys, i.e., α is the primary phase during solidification, the preferred growth direction of α dendrites is parallel to the [0001] direction, and thus simple casting operations usually result in the lamellar microstructure with the lamellar boundaries perpendicular to the growth direction, as seen in Fig. 1-10 (a). While for the β-solidifying TiAl alloys, the resulting ingot might have a microstructure consisting of columnar grains with the lamellar interface probabilities of 1/3 oriented 0° and 2/3 oriented 45° to the growth direction (Fig. 1-10 (b)) since the β phase grows along <100> and the HCP α phase is formed from the BCC β phase following the Burgers orientation relationship. Thus, there are two ways to control the lamellar boundary direction in the DS process: one is by using a seed material [73,77], and another is by controlling the solidification path [73,78]. It should be mentioned that Chen et al. [78] have successfully fabricated Ti-45Al-8Nb single crystals with controlled lamellar orientations by directional solidification without the use of complex seeding methods. During their experiments, the β → α transformation has been controlled through regulation of the nucleation driving force by controlling the withdrawal rate, since the β/α interface is $(00\bar{1})_\beta//(11\bar{2}0)_\alpha$ for 0◦-growing α phase and $(00\bar{1})_\beta//(10\bar{1}2)_\alpha$ for 45◦-growing case

showing different planar disregistries, i.e., anisotropic interfacial energies. The PST single crystals exhibit a yield strength as high as 637 MPa with 8.1% ductility and superior creep resistance at 900 ℃.

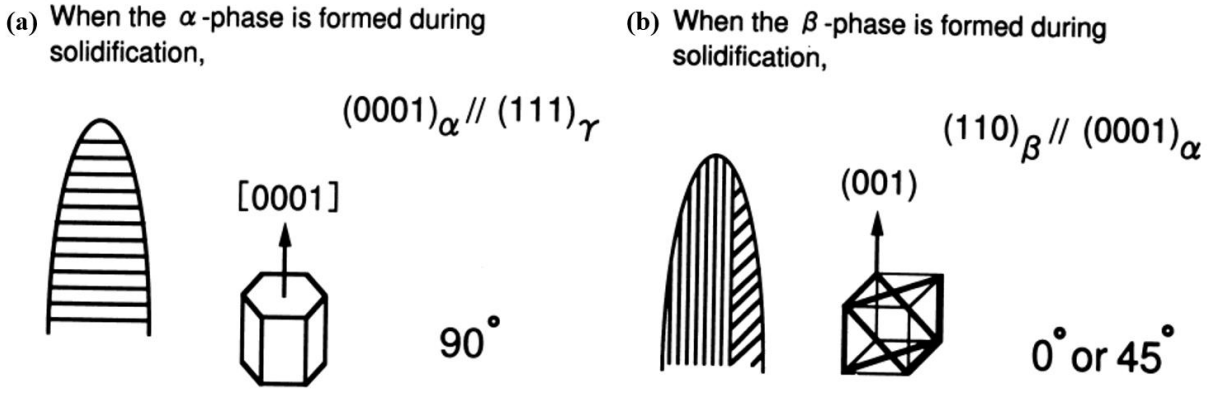


Fig. 1-10 Lamellar orientations in (a) α and (b) β dendrites [71].

Besides, it has been reported that the alignment of lamellae could be effectively controlled by high-temperature deformation in an α single phase region and related heat treatment in the (α+γ) and/or ($\alpha_2$+γ) two phase region [79–83]. Hot deformation in α phase region introduces α texture, then an additional compression process in the (α+γ) phase region to make the $(0001)_\alpha$ parallel to the compression plane, and finally the γ phase with specific orientation is formed during the subsequent cooling process.

In addition, reactive diffusion is also a method that can be used to control the lamellar orientation [84–86]. During the reactive diffusion process, the starting materials have to be textured, and the texture can be inherited to the α single phase, then an oriented lamellar structure can be obtained. For example, Fukutomi et al. [84] reported that the reactive diffusion between textured titanium foils and aluminum foils can achieve the textured α phase and control the lamellar orientation.

In summary, a fully lamellar structure with refined colony size and ultrafine lamellar spacing, especially in the case where the proper alignment of the lamellae is achieved, could produce a good combination of room temperature ductility for machining and excellent mechanical properties for structural applications at elevated temperatures. The colony size and lamellar orientation, can be manipulated by controlling the characteristics of the high

temperature α phase. At the same time, the lamellar spacing can be regulated by the rates of cooling from α phase region. It has been demonstrated that thermomechanical processing conducted above $T_{\gamma,solv}$ (the α single phase region or the (α+β) phase region) is the possible method to control both lamellar orientation and colony size by deformation and DRX of high temperature α phase, as well as the lamellar spacing by the subsequent cooling rate. Thus, fundamental researches on the deformation behavior, DRX, and texture evolution of high temperature α phase in TiAl alloys during thermomechanical processing are both of technical importance as well as of scientific interest.

## 1.3 Hot deformation behavior of α phase in TiAl alloys

Thermomechanical processing such as isothermal forging, hot rolling, and extrusion are important procedures often used to refine the as-cast coarse microstructures, improve the mechanical properties, as well as to manufacture semifinished products of TiAl alloys, especially for the β-solidifying TiAl alloys [87,88]. During the processes, the dislocation multiplication and DRX interweave each other, resulting in characteristic stress–strain behavior, microstructure and texture evolution. It should be mentioned that for different deformation temperature, the phase constituents and the existence form of the $\alpha/\alpha_2$ are different, which will influence the deformation behavior and DRX progress as well as the texture evolution of the α phase in TiAl alloys.

### 1.3.1 Microstructure evolution during thermomechanical processing

#### 1.3.1.1 Thermomechanical processing conducted below $T_{\gamma,solv}$

At present, the investigations on hot deformation of γ-TiAl alloys have mainly conducted with different thermomechanical parameters in the $(\alpha_2+\gamma)$, $(\alpha+\gamma)$ or $(\alpha+\beta_0+\gamma)$ phase regions (below $T_{\gamma,solv}$) to explore a safe hot-working window [89–94], or to improve the mechanical properties by adjusting the parameters [95–97] and post heat treatments [97–100]. The hot deformation below $T_{\gamma,solv}$ is primarily associated with the fragmentation of the lamellar structure [92,101–106], leading to an inhomogeneous microstructure consisting of fine recrystallized γ grains and $\alpha/\alpha_2$ grains, elongated $\beta_0$-phase and heavily deformed $(\alpha/\alpha_2+\gamma)$-colonies featuring

bent and buckled lamellae, such as the microstructure shown in Fig. 1-11. In order to eliminate the remnant lamellar structure, suitable thermomechanical processing conditions and post heat treatments have always been adopted to increase recrystallization and obtain more homogeneous microstructures [99,106–109]. Usually, a fine-grained duplex microstructure with random orientation can be obtained after the further deformation or post treatments. The fully lamellar structure cannot be obtained unless it is heat treated in the single α phase region. But when the heat treatment temperature is as high as in the single α phase region, the coarse remnant lamellar structure regions can result in the formation of unusually large α grains during heat treatment [97,99,108]. Thus, it can be concluded that the thermomechanical processing conditions conducted below $T_{\gamma,solv}$ cannot provide a fully lamellar structure with refined colony size, ultrafine lamellar spacing and well-aligned lamellar orientation.

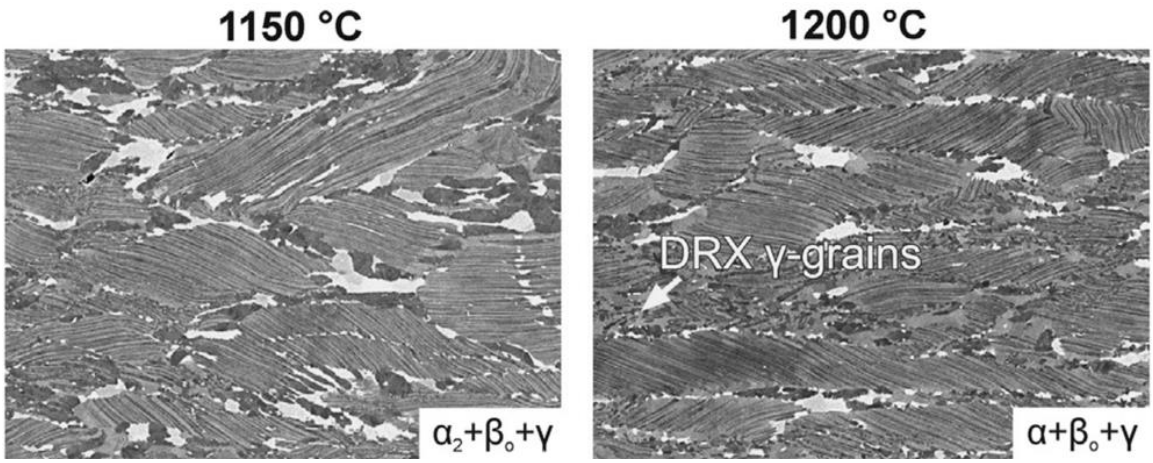


Fig. 1-11 Microstructures of the Ti-42.82Al-4.05Nb-1.01Mo-0.11B-(C+Si≤1 at %) alloy after uniaxial compression at different phase regions under a strain rate of 0.05 $s^{-1}$ to the true strain of 0.9 [90].

### 1.3.1.2 Thermomechanical processing conducted above $T_{\gamma,solv}$

Till now, only very limited researches [79,81–83,90,110] have been conducted to hot deformation above the $T_{\gamma,solv}$. It should be mentioned that influenced by the alloy composition, there may be the α single phase region or the (α+β) phase region above $T_{\gamma,solv}$. As mentioned in Section 1.2.3.2 (Page 10), the researches aiming to control the lamellar orientation by deformation are conducted in α phase region [79,81–83]. Fig. 1-12 (a) shows the micrograph of Ti-45Al-10V alloy after uniaxial compression in α single phase region. It can be seen that the α grain has fragmented into small domains of varying sizes, but the fragmentation

mechanism remains unclear. Besides, E. Schwaighofer et al. [90] gave a micrograph of Ti-42.82Al-4.05Nb-1.01Mo-0.11B-(C+Si≤1 at.%) alloy after uniaxial compression in (α+β) phase region when investigating the hot-working behavior of TNM alloy with minor additions of C and Si. The microstructure is consisted of lamellar colonies with elongated β phase. The lamellae are not inherited from the initial cast microstructures but newly formed in the recrystallized α grain during the cooling process. Compared to the microstructure obtained by thermomechanical processing below $T_{\gamma,solv}$, the fully lamellar structure with relatively good microstructural homogeneity could be obtained directly by hot deformation above $T_{\gamma,solv}$. It should be noted that deformation process must be carefully designed to avoid grain coarsening caused by too long holding time in the α phase region after deformation.

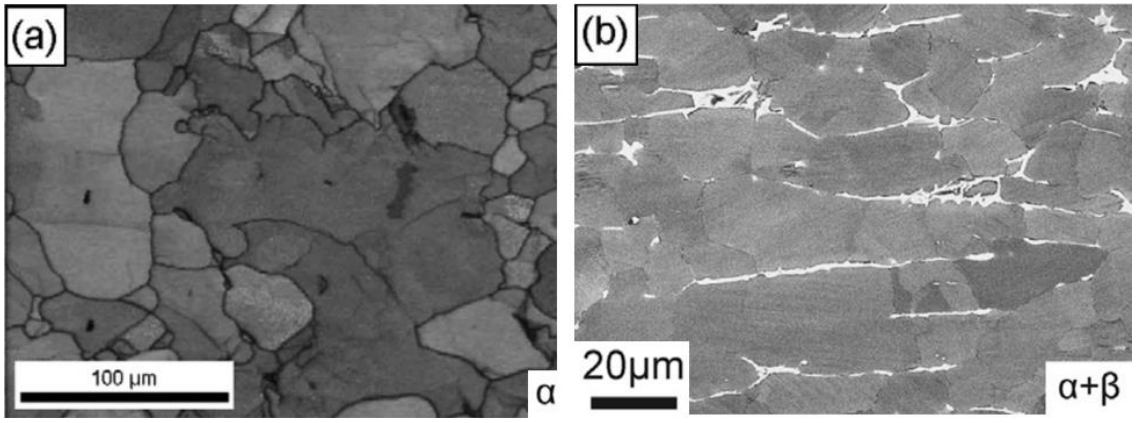


Fig. 1-12 (a) Micrograph of Ti-45Al-10V alloy after uniaxial compression at 1280°C in α single phase region under a strain rate of 0.001 $s^{-1}$ to the true strain of 1.2 [81]; (b) Micrograph of Ti-42.82Al-4.05Nb-1.01Mo-0.11B-(C+Si≤1 at.%) alloy after uniaxial compression at 1300°C in (α+β) phase region under a strain rate of 0.05 $s^{-1}$ to the true strain of 0.9 [90].

### 1.3.2 DRX behavior of α phase

When the deformation temperature is below $T_{\gamma,solv}$, the $\alpha/\alpha_2$ phase always appear as lamellae in the $(\alpha/\alpha_2+\gamma)$ lamellar colony, thus almost all the researches regard the lamellar colony as an integral whole. In the literature, the DRX behavior of the α phase has rarely been examined. Only S. Zhang et al. [93] investigated the deformation mechanism of γ laths and α laths within (α+γ) two phase region in a TNB alloy. It revealed that the disordered α phase is hardly to be recrystallized than ordered γ phase, and dynamic recovery is indeed the softening mechanism of disordered α phase, as seen in Fig. 1-13.

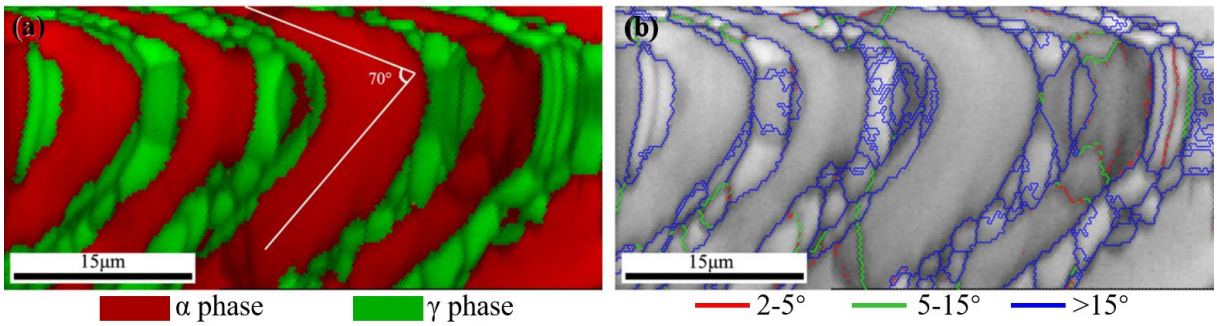


Fig. 1-13 EBSD map of Ti-44Al-8Nb-0.2W-0.2B-Y alloy deformed at 1275 °C. (a) phase + IQ map; (b) grain boundary map [93].

For the thermomechanical processing conducted in α single phase region or the (α+β) phase region above $T_{\gamma,solv}$, as mentioned above, there are only a few related researches [79,81–83,90,110] so that the recrystallization behavior of the α phase also has not been well addressed. This might be due to the fact that α grains transform into lamellar colonies on cooling after hot deformation, so that a direct observation of recrystallization in the α phase is difficult. It just has been mentioned that the change in grain size, the irregular shape of the grain boundaries as well as the work softening in the true stress–strain curve (as shown in Fig. 1-14) indicate the occurrence of DRX [79,81–83,90], but the detailed information about how the microstructure evolved and the DRX progressed is not known. Some other researches [110,111] based on in-situ high-energy X-ray diffraction (HEXRD) characterization technique also have been conducted. It has been revealed that the α phase was deformed preferentially by slip than by twinning, and the deformation was superimposed by a relatively slow dynamic recovery (DRV) and a less pronounced DRX process. There is also no microstructure evolution information obtained, so the restoration behavior needs to be further investigated.

Previously, most of the fundamental knowledge about DRX behavior were conducted on cubic materials. Discontinuous dynamic recrystallization (DDRX) during which new DRXed grains nucleate and grow at the expense of the work-hardened surroundings has been found to be dominant in FCC materials with low or medium stacking fault energy ($\gamma_{SFE}$) [112–116]. Low $\gamma_{SFE}$ will promote the formation of wider stacking faults, which makes the cross-slip or climb more difficult, materials of this type include silver, austenitic stainless steels etc. For these materials, it is difficult to form subgrain structures during deformation by DRV, instead, the

dislocation density increases to a high level and eventually some of the local differences in dislocation density become large enough to overcome the capillary term to allow the formation ofnewgrains. Finally, a new microstructure is obtained, this dynamic process is known as DDRX. During the deformation process, bulging of grain boundaries was frequently observed and regarded as a prelude for nucleation. Further analysis revealed that the bulging was operated by a mechanism closely related to the strain-induced grain boundary migration. In such a case, a significant dislocation density difference existed between the front and the behind of the bulged boundary and the migration direction was from the low density region to the high density region [117,118]. Then, a necklace of new grains formed along the boundary [113–116]. However, for BCC metals and FCC metals with high $\gamma_{SFE}$, such as Al alloys, α-iron and nickel, the dissociation of the perfect dislocation into two partials is more difficult and perfect dislocation glide, climb and cross slip takes place readily. During deformation at elevated temperatures, rapid DRV occurs readily which generally prevents the accumulation of sufficient dislocations to sustain DDRX. Well-developed subgrain structures are observed during deformation with only limited dislocations within them, Then the low angle grain boundaries are formed during deformation by DRV and evolve into high angle grain boundaries through progressive accumulation of dislocations. This process is known as continuous dynamic recrystallization (CDRX) [119,120]. Necklace microstructure could also be produced by CDRX at an intermediate stage owing to the rapid development of strain gradients near grain boundaries [120,121].

For the other HCP structured materials, such as the Mg alloys, commercially pure Ti (CP-Ti) [22], that have drawn considerable industrial attention owing to their light-weight, the related researches are much more abundant. It was found that Mg alloys usually display typical features of continuous dynamic recrystallization (CDRX) during hot deformation [122–125], i.e., low angle boundaries were introduced due to the accumulation of dislocations, and then new fine grains were developed progressively from grain boundaries to grain interiors with the gradual increase in misorientation at sub-boundaries. Due to the lack of slip systems, twinning [125–129] and kinking [123–125] served as additional mechanisms for rapidly introducing large misorientations in deformation substructures and accelerating the formation of new fine

grains. For the DRX behavior of CP-Ti, investigations [130–132] indicated that DRV was the dominant softening process for the annihilation of dislocation during high temperature deformation. The original grain boundaries become serrated with the simultaneous formation of internal subgrains. With further deformation, the microstructure was continuously recrystallized resulting in a fine DRX grain microstructure. These information about the DRX in HCP structured materials can be used as references for the investigation of the α phase in TiAl alloys.

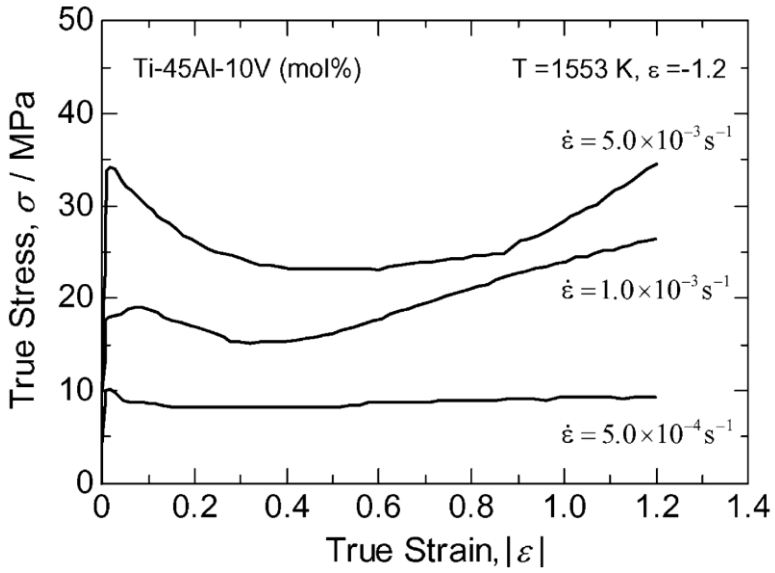


Fig. 1-14 True stress–strain curves of Ti-45Al-10V alloy compressed in the α single phase region [81].

## 1.3.3 Textures of α phase

The textures of α phase developed by plastic deformation are mainly governed by the operating deformation modes, the second phase as well as the deformation conditions, which could further evolve during recrystallization and grain growth progresses. Thus, the textures of α phase related to deformation, recrystallization and grain growth may be different.

### 1.3.3.1 Deformation modes in HCP α phase

The primary slip systems of hexagonal (HCP) metals are in $<11\bar{2}0>$-direction (<*a*> type slip) on $\{1\bar{1}00\}$ prismatic, (0001) basal and $\{10\bar{1}1\}$ pyramidal planes [133,134]. These <*a*> type slip systems cannot provide five linearly independent slip systems, and therefore additional secondary slip systems can be provided by the <*c*+*a*> type slip in $<11\bar{2}3>$-direction on $\{10\bar{1}1\}$

and {11$\bar{2}$2} pyramidal planes as well as eventually by twinning for polycrystal deformation. The slip systems in HCP materials are illustrated in Fig. 1-15.

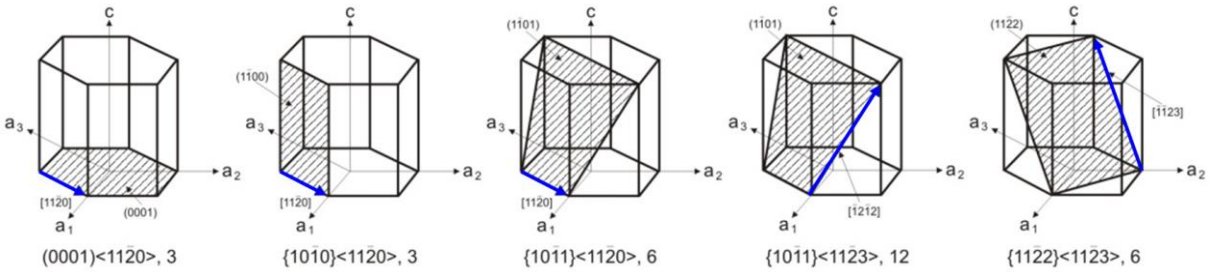


Fig. 1-15 Slip systems in HCP materials.

As is known, the α phase is the disordered structure of the $\alpha_2$-Ti3Al phase, the lattice parameter *a* of α phase can be considered as half of that in $\alpha_2$-Ti3Al phase (*a*=0.5782 nm, *c*=0.4629 nm), so the *c/a* is ~ 1.619. On the basis of the Peierls-Nabarro model, the prismatic slip is expected to replace the basal slip as the dominant deformation mode when the *c/a* ratio is below $\sqrt{3}$ [133]. Moreover, it has been proved that the prismatic slip owns the lowest critical resolved shear stress (CRSS) in the order, followed by the the basal slip and then by the pyramidal slip [134–136]. Thus, it can be concluded that the prismatic slip is the primary slip system for the high-temperature α phase in the present work. Besides, no twinning has been found in the high-temperature α phase during thermomechanical processing at these temperatures.

### 1.3.3.2 Deformation conditions related texture components of α phase

In the as-rolled condition, the texture of the α phase consists of both a basal component (characterized by the alignment of the *c*-axis of the HCP unit cell with the ND of the sheet) and a transverse component (defined by the alignment of the *c*-axis of the HCP unit cell with the TD of the sheet) [137–140], showing remarkable similarities to the textures of the HCP α phase in hot-rolled Ti and Ti-based alloys [141–144]. Fig. 1-16 shows the representative pole figures of the α phase in TNM alloy hot-rolled at different phase regions. The formation of the basal component is attributed to <*a*> and <*a*+*c*>-slip [141,143]. In contrast to the basal component, the transverse component is created during hot rolling only in the presence of a second phase, such as β or γ [139,141], and this orientation is mainly due to <*a*>-slip on primary slip systems.

As reported above, the dislocation slip on prismatic plane is most favorable in HCP α phase. Yet, prismatic planes provide only two independent slip systems. Basal planes offer two additional independent slip systems. Still, pure α phase does not meet the von-Mises criterion of five independent slip systems for homogeneous plastic deformation, thus, pyramidal glide as the third option results from of a combination of prismatic and basal components. However, since the presence of other phases could accommodate a large part of the deformation, the necessity for the activation of hard slip systems involving pyramidal glide is reduced. Grains of the α phase are deformed if orientated favorably, i.e., if the deformation can be realized with only <*a*> slip; else, they rotate with the deformation of β or γ phase to assume favorable orientations [139]. It should be mentioned that most of the researches about the hot-rolling texture of the α phase in TiAl alloys are on the results obtained by deforming the materials mainly in ($\alpha_2$+γ) or (α+$\beta_0$+γ) phase regions.

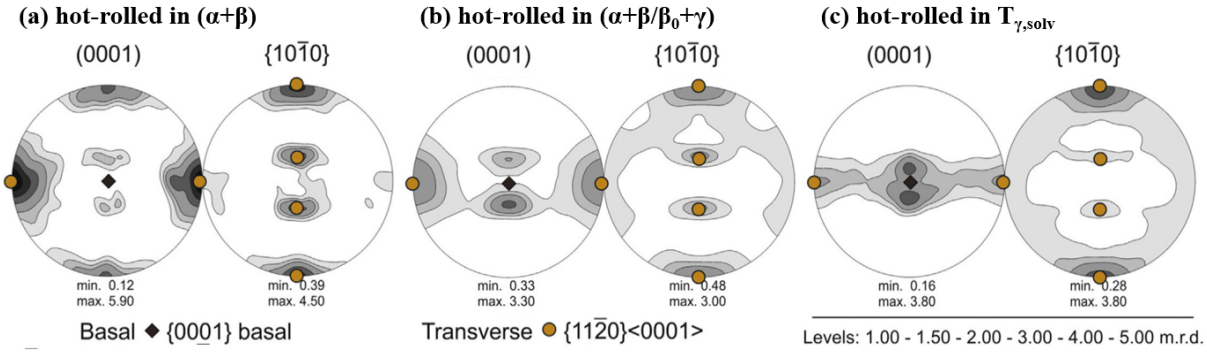


Fig. 1-16 Representative pole figures of the α phase in TNM alloy hot-rolled in different phase regions. The rolling direction (RD) is aligned vertically, and the transverse direction (TD) horizontally. Ideal texture components are indicated in the pole figures and labelled at the bottom [137].

In the case of the uniaxial compression (or near conventional forging) process in the α single phase, a tilted basal fiber texture is formed, i.e., the $(0001)_\alpha$ plane normal is tilted about 30° away from the uniaxial compression axis [79,81,145], as shown in Fig. 1-17. This kind of α texture has been reported for α-Ti and and other HCP metals with a *c/a* ratio <1.63 [143]. As investigation has shown that the positions of maximum pole (the type of texture) are almost the same, independent of the strain rate, but the densities increase with decreasing true strain rate [81]. Besides, no significant change of the α/$\alpha_2$ texture (just a slight change in the tilt angle with the compression axis) is observed in the temperature range between 800 °C and close to $T_\alpha$ in

Ti-45Al-5Nb alloy [145], as seen in Fig. 1-17. This indicates that the disorder-order transformation between the α and $\alpha_2$ structure does not influence the formation of the texture.

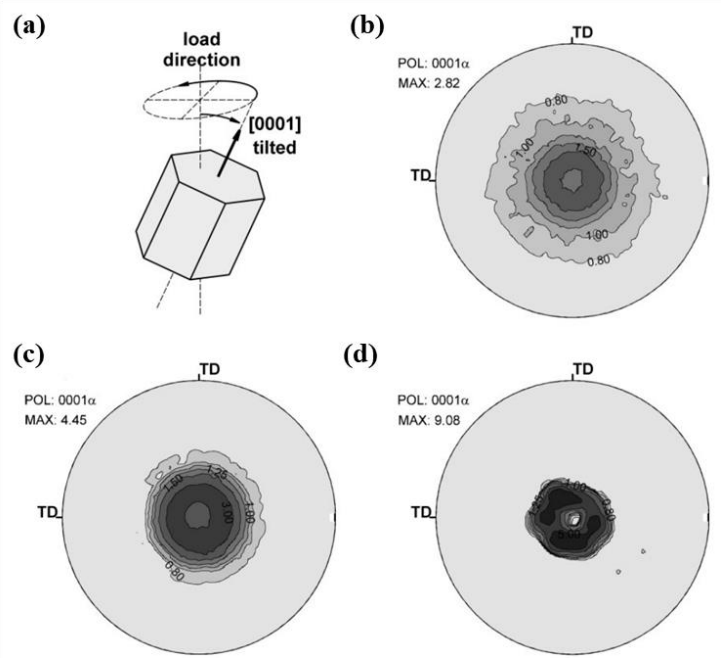


Fig. 1-17 (a) Orientation of the hexagonal unit cell in a tilted basal fiber texture (deformation conducted at temperatures between 800 and 1100°C). (b-d): Recalculated pole figures in load direction after compressive deformation at (b) 1100 °C, (c) 1270 °C and (d) close to $T_\alpha$ ($T_\alpha$=1295 °C) in Ti-45Al-5Nb alloy [145].

The research about the texture evolution in TiAl alloys during hot-extrusion is very seldom. Only R. Liu et al [99] proposed that in Ti-47Al-2Cr-2Nb-0.15B alloy a strong α phase texture $\{11\bar{2}0\}<10\bar{1}0>$ can be found after rectangular extrusion in the (α+γ) two phase region and it evolves into the $\{10\bar{1}0\}<11\bar{2}0>$ recrystallization texture via oriented growth during α solution treatment. Thus, one can concluded that the type of texture under a specific deformation method is influenced by the DRX and grain growth behavior.

### 1.3.3.3 Texture evolution of α phase during DRX and grain growth

In literature, the preferred orientation is mainly classified into the ‘deformation texture’ and ‘recrystallization (or annealing) texture’. The above-mentioned texture of the α phase in TiAl alloys mainly refers to the deformation texture. Only R. Liu et al [99] reported a change in texture components during α solution treatment. It means that the DRX and grain growth behavior may influence the texture features of the α phase. Although the texture evolution

during DRX and grain growth processes has rarely been investigated in TiAl alloys, the related researches have been conducted in other HCP metals, such as Titanium alloys [143,146–148], Magnesium alloys [149–151] and Zirconium alloys [152–155]. It can be summarized that the deformation texture characterized by a $\{0001\}<10\bar{1}0>$ component which could rotate a 30° around <0001> axis from $<10\bar{1}0>$ direction to $<11\bar{2}0>$ direction during recrystallization process or grain growth process. Whether the modification of the texture is essentially controlled by recrystallization or grain growth has triggered two theories: oriented nucleation and oriented growth. M.G. Jiang et al. [151] found that in the unDRXed region with $<10\bar{1}0>$ fiber orientation, relatively coarse DRXed and fine DRXed grains with 30°/[0001] disorientation preferentially are formed via CDRX in AZ31 magnesium alloy during extrusion, providing support for the oriented nucleation mechanism. The oriented growth has also been demonstrated in Titanium alloys [147,148] and Zirconium alloys [152–154]. It is revealed that the so-called 'recrystallisation texture' ($<11\bar{2}0>$orientation), which is significantly different from the deformation texture ($<10\bar{1}0>$ orientation), is not primary recrystallisation texture but corresponds to a further stage where the grain growth has already taken place. It is reported that these two different mechanisms are strongly linked with the local deformation structures and also with the sharpness of the deformation texture [152]. In the cases of sharper initial textures, non-oriented nucleation together with preferred growth in the clusters of recrystallized grains drives a texture change, whereas in the case of low deformed material the texture change is mostly induced by oriented nucleation. This information is useful for the investigation on textures of α phase related to deformation, recrystallization and grain growth in TiAl alloys.

### 1.3.4 Effects of β phase on DRX and texture evolution of α phase

For some β-solidifying TiAl alloys, there is no single α phase region. If the deformation was required to be executed before the formation of the lamellar structure, it is better to be conducted at the bottom of (α+β) phase region with only a small amount of β phase. Undoubtedly, the small amount of β phase would affect the deformation and recrystallization behavior of the α phase, and therefore influence the texture of the α phase. The available information about the β phase during the thermomechanical processing has just shown that the

β phase with BCC crystal structure provides enough independent slip systems at high temperature [156] and thus very ductile so that it could work like a lubricating layer to accommodate the plastic deformation of the other phases (α and γ phases) [157,158]. But the effect of the β phase on the deformation and recrystallization behavior of α phase in TiAl alloys has received little attention. Investigations on hot compression of Ti5553 alloy in the (α+β) region where the α plates dispersed in β matrix has reported that the β phase is conducive to the α globularisation process by penetrating into cusps formed at α subgrain boundaries [159]. While a competitive DRX between α grain (i.e., CDRX) and β grain (i.e., CDRX and DDRX) are found in the Ti-4Al-3V-2Mo-2Fe alloy during tensile test at 840 ℃ ($T_\beta$=890 ℃) where the alloy exhibits bimodal microstructure consisting of individual α grains and β grains. Results show that both types of recrystallized grains continuously absorb dislocations and expand towards opposite boundaries, which weakens the driving force of boundary expansion and delays the grains coarsening and in turn facilitates grain boundary sliding [158,160]. It can be speculated that the distributions and morphologies of the β phase play an important role in the deformation, DRX and grain growth of the α phase, and the β phase in TiAl alloys are totally different from that in Ti alloys in the (α+β) region. Thus, the evolution of the β phase during hot deformation and its effect on the deformation behavior, DRX, grain growth and the related texture evolution of the α phase need to be further explored.

## 1.4 Challenges in characterization

In the literature, the deformation behavior and recrystallization of the high temperature α phase has rarely been examined. This might be due to the fact that there exist some difficulties in the investigation of the deformation behavior of the α phase in the TiAl-based alloys. On one hand, it is impossible to visualize the microstructures in the required temperature range by in-situ microscopy because the α phase is a high-temperature phase. On the other hand, due to the narrow single α phase region, the microstructure produced by hot deformation may not be preserved completely to room temperature even if rapid cooling is performed [161]. It undergoes a phase transformation from α phase to the ($\alpha_2$+γ) lamellar structure during cooling [22]. The dislocation configurations produced during hot deformation are destroyed by the

formation of the γ lamellae inside the α grains. Fortunately, the α → $\alpha_2$+γ phase transformation does not destroy the α grain boundaries and the intragranular low-angle boundaries formed during hot deformation. In this thesis, the high temperature deformed α phase was reconstructed from the orientation data of the γ lamellae based on the specific Blackburn OR using the software Merengue 2 [162]. Subsequently, the intragranular misorientation axis (IGMA) analysis was applied and extended to reveal the dislocation slip and the formation of the low-angle boundaries evolved from the produced dislocations.

## 1.5 Organization of the thesis

From the perspective of the application as engine blades, TiAl alloy with well-aligned ($\alpha_2$+γ) lamellar structure is expected. It is proved that thermomechanical processing conducted above the $T_{\gamma,solv}$ (the α single phase region or the (α+β) phase region) is the possible method to control the lamellar orientation and colony size by deformation and DRX of the high-temperature α phase. Thus, it is necessary to investigate the deformation behavior, DRX, grain growth and texture evolution of single α phase and under the influence of the β phase in TiAl alloys during thermomechanical processing. At present, only very limited researches have been paid to the thermomechanical processing above the $T_{\gamma,solv}$ in TiAl alloys. Almost no microstructure evolution information of the α phase can be found, and the dynamic recrystallization behavior of the α phase have not been fully assessed and exploited. In addition, although the studies about the texture of the α phase have greatly advanced our knowledge on the texture type at different deformation temperatures under different deformation methods, investigations on the formation and evolution mechanisms of the texture are still not clearly explained in TiAl alloys. Moreover, the hot deformation behavior of the α phase with the presence of β phase has received little or no attention in TiAl alloys, and its effect on the deformation behavior, DRX, grain growth and the related texture evolution of the α phase need to be further explored. Based on such an observation, the present PhD work is dedicated to work out the deformation and DRX behavior and its related microstructure and texture evolution of α phase in TiAl alloys during thermomechanical processing.

In Chapter 2, the experimental procedures for the materials preparation and

thermomechanical processing, as well as characterization techniques and crystallographic calculation methods for the results analyses will be introduced.

In Chapter 3, special attention will be paid to the microstructure evolution and its underlying DRV and DRX mechanisms of the α phase in the $TNM^{+}$ (Ti-44.81Al-3.96Nb-0.98Mo-0.15B, at.%) alloy during uniaxial compression in the α single phase region.

In Chapter 4, a study on the correlations between microstructure evolution, deformation behavior, and texture development will be established in the $TNM^{+}$ alloy. Special effort will be made to explore the difference in deformation behavior and DRX induced fragmentation tendency between soft and hard α grains according to the crystallographic orientations, and to reveal the contributions of the deformation mechanism to the texture development of the α phase.

In Chapter 5, hot extrusion experiments will be carried out for the TNM (Ti-43.25Al-3.91Nb-0.98Mo-0.13B, at.%) alloy in the (α+β) phase region. Based on the microstructure characterization and texture measurement, the contributions of the deformation mode and the β phase to the development of the microstructure and texture of the high temperature α phase will be explored, Special attention will also be paid to the thermally-induced α → β phase transformation interweaving with the abnormal α grain growth.

The final conclusions and perspective on some future directions that would extend the current work are presented in Chapter 6.

# Chapter 2 Materials, experimental details and basic crystallographic calculations

This chapter is devoted to introduce the materials investigated in this study, sample preparation processes, and deformation methods as well as characterization techniques used in this work.

## 2.1 Materials preparation

The TiAl alloys used in the present work were fabricated by vacuum arc remelting (VAR) and cast into cylindrical ingots, then hot isostatically pressed (HIP) at 1280 ℃ for 4 h under a pressure of 140 MPa in argon atmosphere to eliminate casting porosities. The compositions of the TiAl alloys are selected based on the TNM (TiAl-Nb-Mo) alloys with a baseline of Ti-(41~45)Al-(3~5)Nb-(0.1~2)Mo-(0.1~0.2)B (all compositions are stated in at.%). One is the typical TNM alloy with the Al content of 43.25 at.%, and another is termed as TNM$^+$ processing a higher Al content (44.81 at.%). The actual chemical compositions are displayed in Table 2-1. According to the phase diagram Ti-*x*Al-4Nb-1Mo-0.1B depicted in Fig. 2-1 [163], the phase transformation pathway of the TNM alloy is L → L+β → β → α+β → α+β+γ → α+β/$\beta_0$+γ → α/$\alpha_2$+$\beta_0$+γ → $\alpha_2$+$\beta_0$+γ; whereas that of the TNM$^+$ alloy is L → L+β → β → α+β → α→ α+γ → α+β/$\beta_0$+γ → α/$\alpha_2$+$\beta_0$+γ → $\alpha_2$+$\beta_0$+γ, for which exist a narrow single α phase region and a (α+γ) phase region with no presence of β phase. Besides, it should be mentioned that for the TNM alloy the $T_{\gamma,solv}$ is about 1250 ℃, while for the TNM$^+$ alloy is about 1270 ℃.

Table 2-1 The actual chemical composition of the TNM alloys (at.%)

| Elements | Al | Nb | Mo | B | O | Ti |
|---|---|---|---|---|---|---|
| TNM$^+$ | 44.81 | 3.96 | 0.98 | 0.15 | 0.15 | Bal. |
| TNM | 43.25 | 3.91 | 0.98 | 0.13 | 0.17 | Bal. |

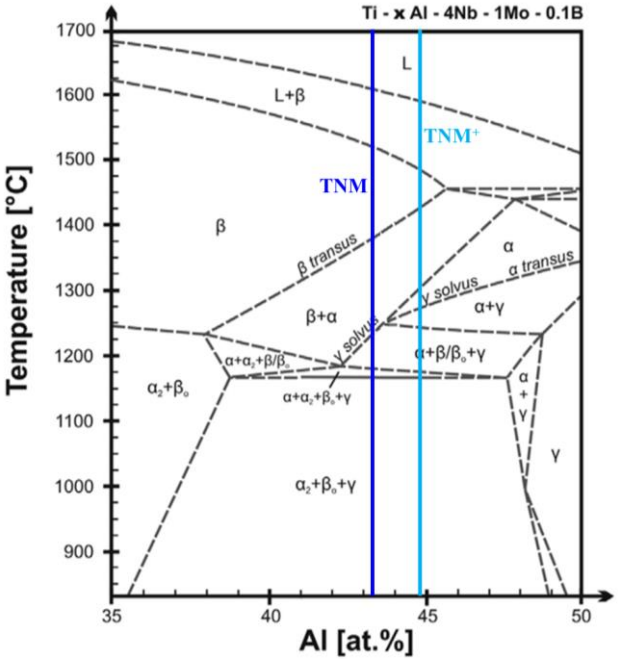


Fig. 2-1 Experimental quasi-binary phase diagram section of TNM alloying system [163]. The Al-content of the investigated alloys are indicated with the vertical lines (blue: TNM; cyan: $TNM^{+}$).

## 2.2 Thermomechanical processing

In the present work, two kinds of thermomechanical processing methods were used, one being isothermal hot compression and the other hot extrusion. The experimental details are given below.

### 2.2.1 Uniaxial compression

Cylindrical samples with dimension of Ø10 mm × 15 mm were machined from the HIPed $TNM^{+}$ ingot for uniaxial compression experiments. The uniaxial compressions were carried out in a Gleeble 3500 simulator under vacuum. Samples were heated at a rate of 20 ℃/s to 1280 ℃, and homogenized for 10 min at the deformation temperature. Then they were compressed at a strain rate of 0.01 $s^{-1}$ to respective true strains of 0.05, 0.07, 0.29, 0.60 and 1.05 and water-quenched to preserve the deformed microstructures. The strain rate was selected within the safe hot-working region based on the previous research [90]. During the compression experiments, the temperatures were controlled with the S type thermocouples spot-welded on the surface of the samples. In order to reduce the friction and ensure a uniform deformation, graphite lubricants were used between the deformation cross heads and the samples. To obtain the initial

microstructural information before the deformation, one sample was held isothermally at 1280 ℃ for 10 min in a resistance furnace and then water quenched. A schematic chart of the isothermal holding and the isothermal compression processes is shown in Fig. 2-2.

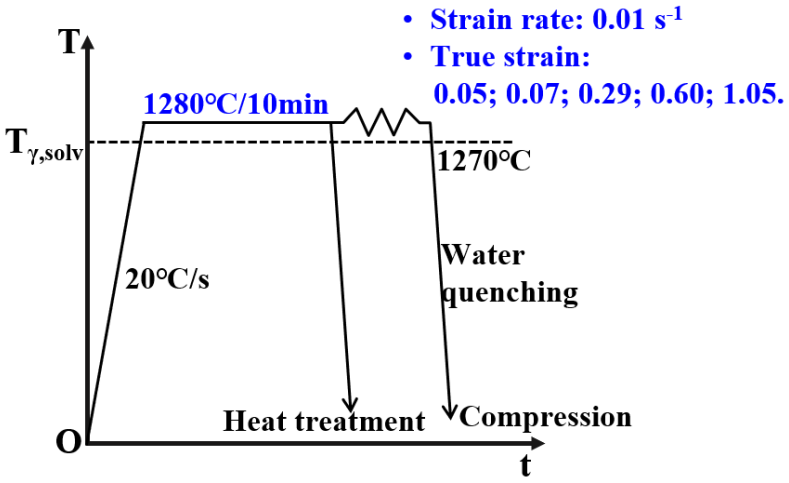


Fig. 2-2 Schematic chart of the isothermal treatment and the hot compression processes used in the present work. $T_{\gamma,solv}$ stands for the γ transus temperature.

## 2.2.2 Hot extrusion

For hot extrusion, the TNM ingots were machined into cylindrical billets with dimensions of Ø85 mm × 80 mm by electrical discharge machining, and then insulated by refractory material, Mo foil and Ni foil and capsulated in stainless-steel cans. After that, these canned billets were preheated at the selected extrusion temperature 1290 ℃ for 90 min, then extruded through a circle die with a constant ram velocity of 30 mm/s. The extrusion ratio is approximately 7.11. The schematic illustration of the extrusion process is displayed in Fig. 2-3. After extrusion, the extruded rods were immediately quenched in cold water to preserve the high-temperature microstructure for microstructure analysis and texture measurement. The whole process for extrusion was completed in about 20 s, 10 s for the deformation and 10 s for transition from end-extrusion to quenching. For reference, one sample with the dimension of Ø12 mm × 8 mm was cut from the HIPed TNM ingot and heat treated at 1290 ℃ for 20 min (Given that the dimension difference with the billet for extrusion, 20 min was selected), then water quenched to serve as the initial state for extrusion.

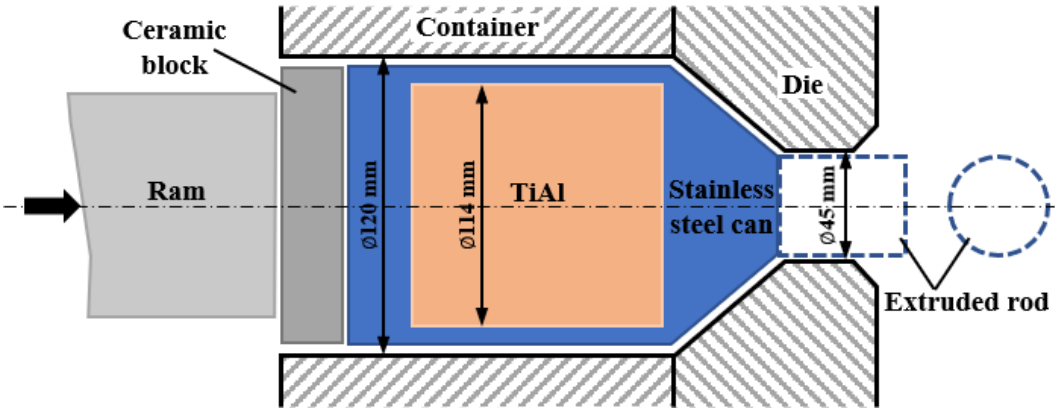


Fig. 2-3 Schematic presentation of the extrusion process.

## 2.3 Microstructural and crystallographic characterization

The microstructural features, including morphology, size, distribution, chemical composition and orientation crystallographic relationship, were examined by different characterization techniques from the macroscopic scale to the microscopic scale to ensure a statistical relevance of the results.

### 2.3.1 Characterization techniques and sample preparations

The mesoscale microstructures were characterized using a JEOL 6500F scanning electron microscope (SEM) equipped with a field emission gun. The crystallographic features of the microstructures were characterized by EBSD using an Oxford EBSD camera and the Aztec online acquisition software package (Oxford Instruments). To achieve the surface quality for EBSD measurements, the samples were first mechanically polished and then electrolytically polished with a solution of 5% perchloric acid, 35% butan-l-ol and 60% of methanol at 35 V for 10 s at temperatures lower than 5 °C. The EBSD patterns were acquired at the accelerating voltage of 20 kV under the beam-controlled mode with different step sizes.

For identifying the nano scaled microstructural and crystallographic features of the constituent phases, the examinations were performed using a FEI Talos F200X Transmission electron microscopy (TEM) operated at 300 kV. The composition analysis was performed using the energy dispersive X-ray spectroscopy (EDS) equipped in the TEM. Phase identifications and crystallographic orientations were determined by indexing the selected area electron

diffraction (SAED) patterns or the Kikuchi line patterns acquired under the convergent beam electron diffraction (CBED) mode with a homemade software Euclid's Phantasies (EP) [164] that allows automatically indexing crystal orientation with much higher spatial and angular resolutions than classical SEM/EBSD analysis technique. TEM thin films were cut from the specific location of the deformed samples and prepared firstly by mechanical thinning to a thickness of about 70 μm and then by electrolytic polishing to perforation at –25 °C in a solution of 5% perchloric acid, 35% butan-l-ol and 60% of methanol at a voltage of 30 V, using a Struers Tenupol-5 twin-jet electropolishing equipment.

### 2.3.2 Post data processing

As the deformation processes conducted in the present research are just slightly above the $T_{\gamma,solv}$, especially for the TNM$^{+}$ alloy within the very narrow single α phase region, it is hard to avoid the precipitation of the γ phase from the deformed α phase during the cooling process, even if rapid cooling was performed [161]. Thus, the microstructure of the parent α phase induced by the hot deformation at the deformation temperature could not be preserved completely to the room temperature. It undergoes a phase transformation to the lamellar structure ($\alpha_2$+γ) during cooling [22]. The dislocation structures produced during the hot deformation are destroyed by the formation of the γ lamellae inside the α grains. Fortunately, the α → $\alpha_2$+γ phase transformation does not destroy the α grain boundaries and the intragranular low-angle boundaries formed during hot deformation. Therefore, in order to analyze the microstructure characteristics of the high-temperature α phase during deformation, the transformed part of the α phase was reconstructed by the software Merengue 2 [162] from the low temperature γ phase based on the specific phase transformation orientation relationship, the Blackburn OR in the present case. The detailed principles and methods have been reported by L. Germain et al. [162] and the techniques have become mature. After reconstruction, the obtained orientation data of the α phase were analyzed with the Channel 5 (Oxford Instruments) and the ATEX [165] software package to reveal the features of grain boundaries, substructures and intragranular disorientation of the α phase.

Besides, the unavoidable phase transformation from the high-temperature α to the γ

lamellae that modified the local microstructural constituent also make it difficult to examine the dislocations in the deformed α phase by means of transmission electron microscopy (TEM). To reveal the dislocation slip and the formation of the low-angle boundaries evolved from the produced dislocations, the intragranular misorientation axis (IGMA) analysis technique [166–169] has been proved powerful, especially for hexagonal materials with limited active slip systems, and has been successfully applied to analyze the dislocation type in CP-Ti [166] and Mg alloys [167–169]. The main assumption made in the IGMA analysis approach is that under the action of dislocation slip the crystal bends around a specific crystallographic axis $\boldsymbol{T}$ (termed as ‘‘Taylor axis’’ [169–171]). $\boldsymbol{T}$ is parallel to $(\boldsymbol{b} \times \boldsymbol{n})$, in which $\boldsymbol{b}$ is the dislocation Burgers vector and $\boldsymbol{n}$ the slip plane normal. By this relation, the corresponding dislocation activities were analyzed mainly by identifying the disorientation axis of low-angle boundaries and matching the axis with the Taylor axis [169–171] listed in Table A-1 in Appendix.

The reconstruction technique and IGMA analysis method were used for analyzing the microstructure of the hot compressed TNM$^{+}$ alloy in Chapter 3.

## 2.4 Texture measurement

The texture of the α phase after hot extrusion were determined by means of high-energy X-ray diffraction (HEXRD) using an area detector. The measurements were conducted at the side-station of P07B high-energy materials science (HEMS) beam line at PETRA III (Deutsches Elektronen-Synchrotron (DESY), Hamburg, Germany). The samples were mounted on a goniometer such that the radial direction (RD) pointed upwards along the ω rotation axis, while the incoming X-ray beam impinged in transmission geometry is perpendicular to this axis. The geometrical configuration of the measurement layout is illustrated in Fig. 2-4. The samples were measured with a photon energy of 87 keV corresponding to a wavelength of 0.14235 Å, and a beam cross-section of 0.7×0.7 mm$^2$. During exposure, the samples were rotated around the ω axis from –90º to 90º at a step of 5º (37 images were recorded). The sample to detector distance was set to be 994 mm. A Perkin Elmer 1622 flat panel detector with a pixel matrix of 2048×2048 and a pixel size of 200 μm was used to record the diffraction patterns for each sample. The sample-detector distance and the instrumental broadening were calibrated using a LaB6 powder

standard. The detailed experimental parameters are summarized in Table 2-2.

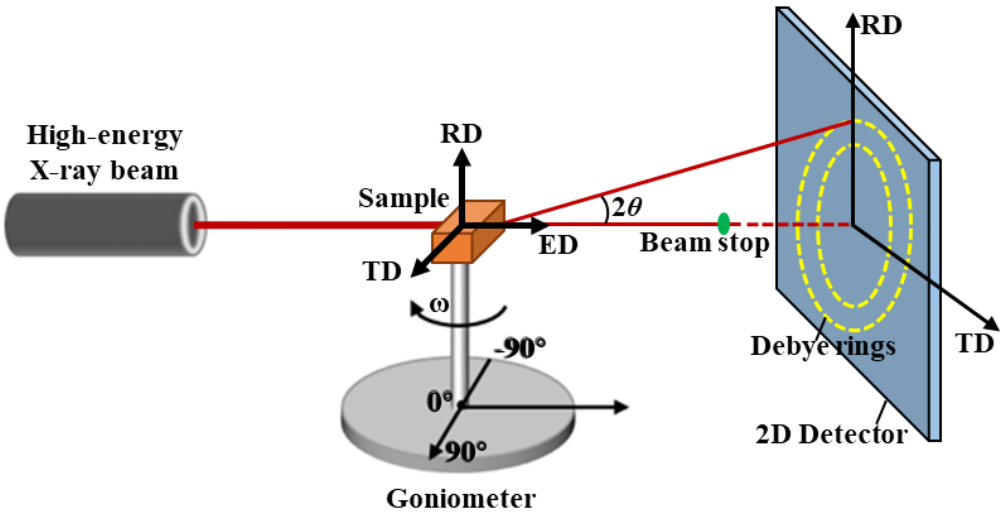


Fig. 2-4 Schema showing the synchrotron radiation diffraction for texture measurement. Here 'ED', 'RD' and 'TD' represent the extrusion direction radial direction and tangential direction of the extruded rods.

Table 2-2 Experimental parameters of texture measured by synchrotron radiation.

| Beam energy (KeV) | Wavelength (Å) | Sample to detector distance (mm) | Pixel size (mm) | Beam size (mm) | Rotation angle range (°) |
|---|---|---|---|---|---|
| 87 | 0.14235 | 994 | 0.2 | 0.7×0.7 | –90 ~ 90 |

It should be mentioned that even though at the extrusion temperature the α phase and β phase were disordered, most of them transformed into ordered $\alpha_2$ and $\beta_0$ structures during the subsequent cooling process. As the measurements were performed at the room temperature, only the textures of the ordered $\alpha_2$ and $\beta_0$ phases were measured to deduce the those of the disordered α phase and β phase. For the $\alpha_2$ phase, the $(20\bar{2}0)$, $(20\bar{2}1)$ and $(20\bar{2}2)$ diffraction rings were evaluated, and for the $\beta_0$ phase the (110) and (200) rings were evaluated. The intensity distribution along the selected Debye-Scherrer rings was transformed into pole figures using the software StressTextureCalculator (STeCa) [172]. In the calculations, corrections for the changing volume and absorption were included. For the estimation of the orientation distribution functions (ODFs), as well as for the recalculation of pole figures not accessible by direct measurement, the ATEX [165] software package was used. The textures measured by HEXRD will be presented in Chapter 4.

## 2.5 Basic crystallographic calculation

### 2.5.1 Coordinate systems and coordinate transformation

In the present PhD work, there are mainly two phases involved, β phase with cubic (BCC) structure and α phase with hexagonal (HCP) structure. For deriving the relationship between the macroscopic sample coordinate system termed as '**X-Y-Z**' and the Bravais lattice of the corresponding phases, two Cartesian coordinate systems are set for the crystallographic calculations. The first Cartesian coordinate system is set to the sample, i.e., the macroscopic sample coordinate system '**X-Y-Z**', as shown in Fig. 2-5 (a). The second Cartesian coordinate system '**i-j-k**' is related to the Bravais lattice basis of the corresponding phases (β or α phase), as also shown in Fig. 2-5 (b). The relation between the Cartesian crystal coordinate system and the Bravais lattice basis conforms to the convention described in the Channel 5 software package, as illustrated in Fig. 2-5 (b) where the ***a***, ***b***, ***c***, $\alpha$, $\beta$ and $\gamma$ are the lattice parameters.

For β phase crystal, $a=b=c$ and $\alpha=\beta=\gamma=90^{o}$, thus the coordinate transformation matrix $M_C^{\beta}$ from the Cartesian crystal coordinate system to the Bravais lattice basis of the β phase can be expressed as:

$$M_C^{\beta} = \begin{pmatrix} a & 0 & 0 \\ 0 & a & 0 \\ 0 & 0 & a \end{pmatrix} \tag{2-1}$$

For the α phase crystal, $a=b\neq c$, $\alpha=\beta=90^{o}$, and $\gamma=120^{o}$, thus the coordinate transformation matrix $M_C^{\alpha}$ from the Cartesian crystal coordinate system to the Bravais lattice basis of the α phase can be expressed as:

$$M_C^{\alpha} = \begin{pmatrix} \sqrt{3}\,a/2 & 0 & 0 \\ -a/2 & a & 0 \\ 0 & 0 & c \end{pmatrix} \tag{2-2}$$

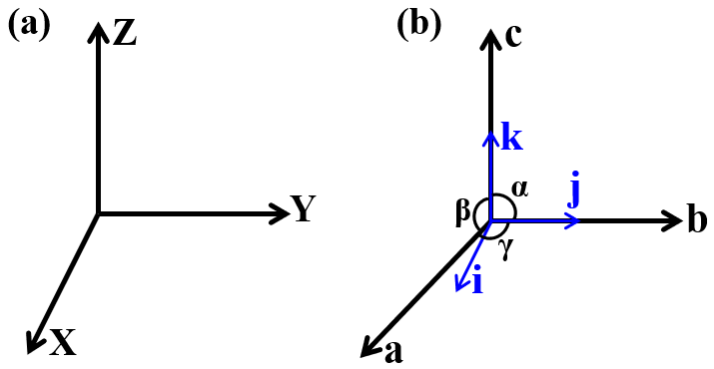


Fig. 2-5 (a) Cartesian sample coordinate system '**X-Y-Z**'; (b) Relationship between the Cartesian crystal coordinate system '**i-j-k**' and the Bravais crystal lattice '**a-b-c**'.

In order to describe the orientation of individual crystals, the concept of a triplet rotations represented in Euler angles is usually used. The most commonly used Euler angles $(\varphi_1, \Phi, \varphi_2)$ are formulated in Bunge notation [173,174], constituting a sequence of rotations as shown in Fig. 2-6. Accordingly, the Cartesian crystal coordinate system is associated with the sample coordinate system by the Euler angles. The coordinate transformation matrix $M_E$ from the macroscopic sample coordinate system to the Cartesian crystal coordinate system can be described in Eq. (2-3). The coordinate transformation matrix from the Cartesian crystal coordinate system to the macroscopic sample coordinate system is the inverse of $M_E$.

$$M_E=\begin{pmatrix} \cos\varphi_1\cos\varphi_2-\sin\varphi_1\sin\varphi_2\cos\Phi & -\cos\varphi_1\sin\varphi_2-\sin\varphi_1\cos\varphi_2\cos\Phi & \sin\varphi_1\sin\Phi \\ \sin\varphi_1\cos\varphi_2+\cos\varphi_1\sin\varphi_2\cos\Phi & -\sin\varphi_1\sin\varphi_2+\cos\varphi_1\cos\varphi_2\cos\Phi & -\cos\varphi_1\sin\Phi \\ \sin\varphi_2\sin\Phi & \cos\varphi_2\sin\Phi & -\cos\Phi \end{pmatrix} \quad (2\text{-}3)$$

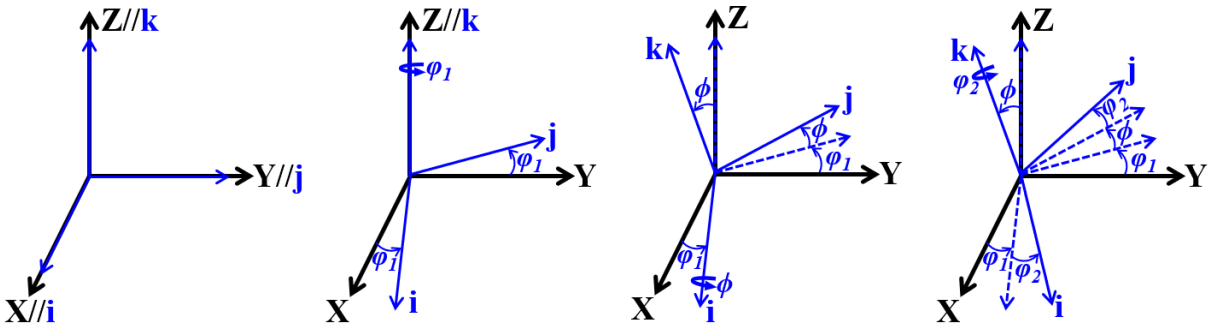


Fig. 2-6 Illustration of the three rotations in Bunge notation. '**X-Y-Z**': macroscopic sample coordinate system; '**i-j-k**': Cartesian crystal coordinate system.

## 2.5.2 Misorientation

In general, the misorientation between two crystals can be expressed in angle/axis pair — $\theta/\boldsymbol{d}$ ($\boldsymbol{d}$=($d_1$, $d_2$, $d_3$)), which describes a rotation from one symmetrically equivalent Cartesian crystal coordinate system of one crystal to one symmetrically equivalent Cartesian crystal coordinate system of the other crystal.

### 2.5.2.1 Misorientation between two crystals based on Euler angles

Normally, it can be calculated by using the Euler angles detected experimentally of the concerning crystals with respect to the macroscopic sample coordinate system. In order to determine the $\theta/\boldsymbol{d}$ ($\boldsymbol{d}$=($d_1$, $d_2$, $d_3$)), the misorientation matrix $\Delta M$ between the two crystals should be calculated first, as illustrated in Fig. 2-7.

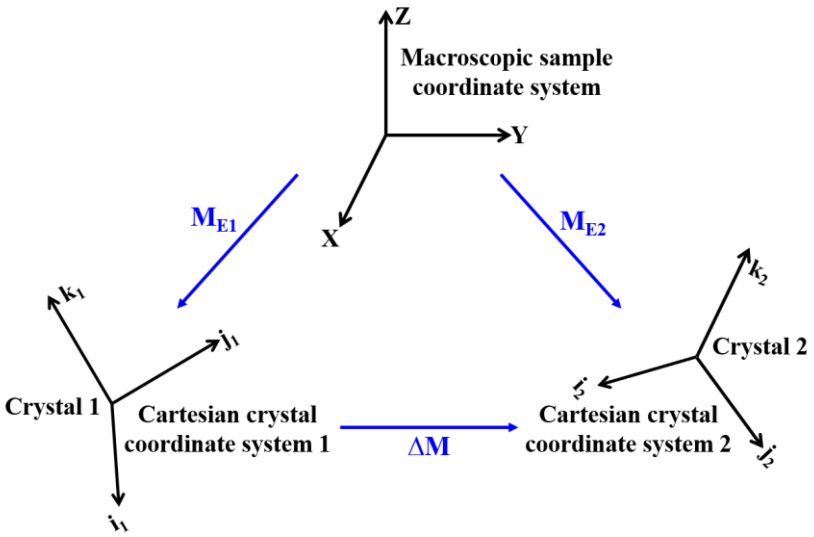


Fig. 2-7 Schematic illustrating misorientation between two crystals: '**X-Y-Z**' is the macroscopic sample coordinate system. '$\mathbf{i_1}$-$\mathbf{j_1}$-$\mathbf{k_1}$' and '$\mathbf{i_2}$-$\mathbf{j_2}$-$\mathbf{k_2}$' are the Cartesian crystal coordinate systems set to the corresponding crystals. $M_{E1}$ and $M_{E2}$ are coordinate transformation matrices from the macroscopic sample coordinate system to the Cartesian coordinate systems of the two crystals. ΔM is the misorientation matrix between the two crystals.

The calculation of the misorientation matrix $\Delta M$ between the two crystals can be described as follows:

$$\Delta M = (S_i)^{-1} \cdot (M_{E1})^{-1} \cdot M_{E2} \cdot S_j \tag{2-4}$$

where $S_i$ and $S_j$ are the rotational symmetry matrices of these two crystals, i.e., crystal 1 and crystal 2. $M_{E1}$ and $M_{E2}$ represent the coordinate transformation matrices from the macroscopic sample coordinate system to the Cartesian crystal coordinate system of these two crystals that are based on the detected Euler angles. The misorientation matrix $\Delta M$ can be described as below:

$$\Delta M=\begin{pmatrix} g_{11} & g_{12} & g_{13} \\ g_{21} & g_{22} & g_{23} \\ g_{31} & g_{32} & g_{33} \end{pmatrix} \tag{2-5}$$

Then the misorientation angle $\theta$ and its corresponding rotation axis $\boldsymbol{d}=(d_1, d_2, d_3)$ can be calculated [175] and expressed in the same Cartesian crystal coordinate system of the crystal. The calculated method is described as follows:

$$\theta= arccos\left(\frac{g_{11}+g_{22}+g_{33}-1}{2}\right), \tag{2-6}$$

The corresponding rotation axis $\boldsymbol{d}$ can be calculated according to the value of the misorientation angle $\theta$:

(1) $\theta$ =0º,

$$\boldsymbol{d} = (d_1,\ d_2,\ d_3) = (1, 0, 0); \tag{2-7}$$

(2) 0º < $\theta$ < 180º,

$$\boldsymbol{d} = (d_1,\ d_2,\ d_3) = (\frac{g_{23}-g_{32}}{2\sin\theta},\ \frac{g_{31}-g_{13}}{2\sin\theta},\ \frac{g_{12}-g_{21}}{2\sin\theta}); \tag{2-8}$$

(3) $\theta$ =180º,

$$\boldsymbol{d} = (d_1,\ d_2,\ d_3) = (\pm\sqrt{\frac{g_{11}+1}{2}},\ \pm\sqrt{\frac{g_{22}+1}{2}},\ \pm\sqrt{\frac{g_{33}+1}{2}})$$
$$with \begin{pmatrix} |d_m| = max(|d_i|, i = 1, 2, 3), \\ d_m > 0 \\ \forall\ i \neq m, d_i = sign(g_{im}) \cdot |d_i| \end{pmatrix}. \tag{2-9}$$

Due to the crystallographic symmetry of each crystal system, the misorientation matrix between the two crystals is not unique. There will be several misorientation matrices. However, all these matrices are crystallographic equivalent and thus the calculated misorientation angle $\theta$ and its corresponding rotation axis $\boldsymbol{d}$ are also crystallographic equivalent. Disorientation is introduced to describe the misorientation with the smallest possible rotation angle among all symmetrically equivalent misorientations between two crystals. It is also denoted by the angle/axis pair $\theta_{min}/<d_1\ d_2\ d_3>$, where $\theta_{min}$ is the disorientation angle, which is the minimum of misorientation angle, and the corresponding rotation axis $<d_1\ d_2\ d_3>$.

#### 2.5.2.2 Misorientation matrix from rotations angle and axis

If the misorientation was expressed by a rotation axis $\boldsymbol{d}=(d_1, d_2, d_3)$ and the associated rotation angle $\theta$, the misorientation matrix can be calculated as follows [176]:

$$M=\begin{bmatrix} (1-{d_1}^2)\cos\theta+{d_1}^2 & d_1d_2(1-\cos\theta)-d_3\sin\theta & d_1d_3(1-\cos\theta)+d_2\sin\theta \\ d_1d_2(1-\cos\theta)+d_3\sin\theta & (1-{d_2}^2)\cos\theta+{d_2}^2 & d_2d_3(1-\cos\theta)-d_1\sin\theta \\ d_1d_3(1-\cos\theta)-d_2\sin\theta & d_2d_3(1-\cos\theta)+d_1\sin\theta & (1-{d_3}^2)\cos\theta+{d_3}^2 \end{bmatrix} \quad (2\text{-}10)$$

The application instance of the Eq. (2-10) will be given in Chapter 3 and Appendix. It is used to extend the IGMA analysis approach.

### 2.5.3 Stereographic projection and traces determination

The stereographic projection is a particular mapping that projects a sphere onto a plane, which is used commonly in crystallography to plot the pole figures, i.e., project a vector (or a plane normal) to the equatorial plane, as illustrated in Fig. 2-8.

To calculate the projection of a crystalline direction [$u\ v\ w$], this direction should be expressed in the coordinate system of the projection (the macroscopic sample coordinate frame '**X-Y-Z**' in Fig. 2-8 (a)) as $\boldsymbol{V_s}$ with the following equation:

$$V_S = M_E \cdot S_k \cdot M_c \cdot \begin{pmatrix} u \\ v \\ w \end{pmatrix} \quad (2\text{-}11)$$

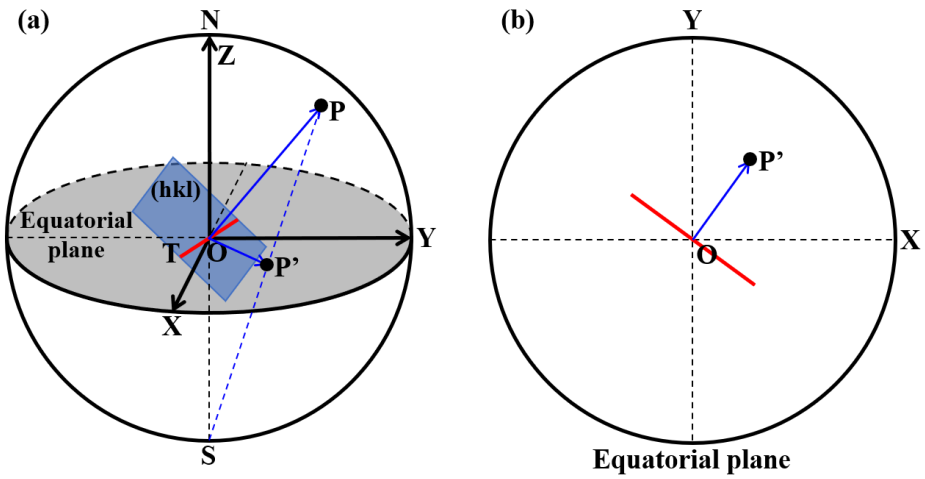


Fig. 2-8 Illustration of stereographic projection on the equatorial plane *XOY* of vec*tor* ***OP***. Point *P'* is the projection pole of vector ***OP*** on the equatorial plane and points *N*, *S* are the north and south pole of the projection sphere.

Here, $M_E$ is the coordinate transformation matrix from the macroscopic sample coordinate system to the Cartesian crystal coordinate system, $S_k$ is the rotational symmetry matrices of the crystal system, $M_C$ is the coordinate transformation matrix from the Cartesian crystal coordinate system to the Bravais lattice basis and [*u v w*] is the Miller indices of the crystalline direction.

As presented in Fig. 2-8 (a), vector ***OP*** represents the vector $\boldsymbol{V_S}$ ($\boldsymbol{OP//V_S}$). *P* is the intersection of vector ***OP*** with the sphere. Suppose the radius of the projection sphere *R=1,* the coordinates of vector $\boldsymbol{V_S}$ in the macroscopic sample coordinate system are (*X, Y, Z*), thus

$$\mathrm{R}=(X^2+Y^2+Z^2)^{1/2}=1 \tag{2-12}$$

Let the line connecting point *P* and the South Pole *S* be line *PS*. Line *PS* intersect the equatorial plane at point *P'*. *P'* is the stereographic projection of pole *P*. On the equatorial plane, *P'* is positioned with the coordinate (*x, y*), where

$$\frac{x}{X}=\frac{y}{Y}=\frac{R}{R+Z}=\frac{1}{Z+1} \tag{2-13}$$

It can be deduced that the abscissa and ordinate values of the stereographic projection *P'* of the crystalline direction [*u v w*] are:

$$x=\frac{X}{Z+1}$$
$$y=\frac{Y}{Y+1} \tag{2-14}$$

To plot the projection of a crystalline plane (*h k l*), the normal vector ***n*** should be calculated first with the following equation:

$$\boldsymbol{n} = G^* \times \begin{pmatrix} h \\ k \\ l \end{pmatrix} \tag{2-15}$$

where $G^*$ is the reciprocal metric tensor [177] of the corresponding crystal system:

$$G^* = \begin{pmatrix} a^* \cdot a^* & a^* \cdot b^* & a^* \cdot c^* \\ b^* \cdot a^* & b^* \cdot b^* & b^* \cdot c^* \\ c^* \cdot a^* & c^* \cdot b^* & c^* \cdot c^* \end{pmatrix} \tag{2-16}$$

Here, $a^*$, $b^*$, $c^*$ are the three basis vectors of the reciprocal space of the crystal. Then, repeat the procedures using Eqs. (2-11) ~ (2-14), and the stereographic projection of a given crystalline plane (*h k l*) can be obtained.

In this case, vector ***OP*** is the vector normal to the crystalline plane (*h k l*). The red line *OT* in Fig. 2-8 (a) is the trace of the crystalline plane (*h k l*) in the equatorial plane which is also the observed plane during EBSD characterization or the sample surface. As line *OT* is on the the equatorial plane, one can known that the line *OT* is perpendicular to line *OS*. Similarly, it can be noticed that the line *OT* is perpendicular to line *OP*, which leads to the conclusion that line *OT* is perpendicular to *OP'* that lies in plane defined by lines *OS* and *OP*. Thus, one can determine the trace of a crystalline plane that is perpendicular to the line connecting the original point and the projection point of the crystalline plane, as clarified in Fig. 2-8 (b).

### 2.5.4 Schmid factor

In order to trigger a plastic deformation through slip, a shear stress is needed to act to a slip system, i.e., in the slip plane and along the slip direction. Under an external loading

condition, the stress that is defined as resolved shear stress (RSS) $\tau$ is the shear component of an applied stress resolved on a slip system. The applied force $F$ along the long axis of a cylindrical single crystal sample with cross-sectional area $A$ is shown in Fig. 2-9. It can be easily deduced that the RSS $\tau$ on the slip plane in the slip direction is:

$$\tau = \frac{F \cdot \cos\lambda}{A/\cos\varphi} = \frac{F}{A}(\cos\lambda\cos\varphi) = \sigma m \tag{2-17}$$

where $\sigma$ is the magnitude of the applied stress, $\varphi$ is the angle between the normal of the slip plane and the direction of the applied force, and $\lambda$ is the angle between the slip direction and the direction of the applied force.

Eq. (2-17) is called Schmid's law. The geometrical factor $\cos\lambda\cos\varphi$ is reffered to as Schmid factor $m$:

$$m=\cos(\varphi)\cos(\lambda) \tag{2-18}$$

The Schmid factor describes the relationship between external stresses and the shear stresses resolved to a slip system. The maximum possible absolute value of Schmid factor is 0.5. The absolute value of Schmid factor is closer to 0.5, indicating that a larger shear stress is resolved to the slip system and the corresponding slip is more likely to be activated.

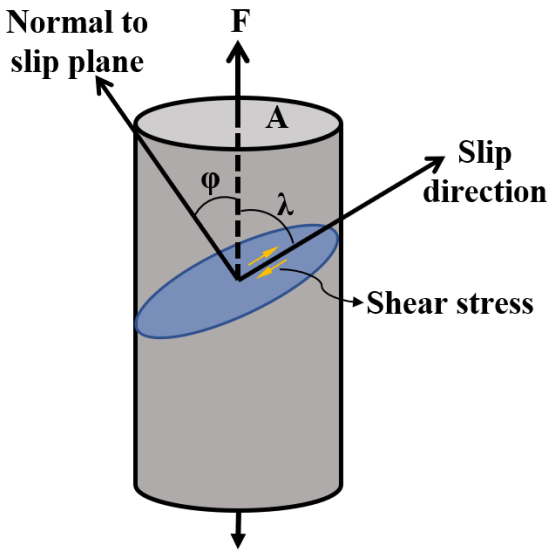


Fig. 2-9 Resolved shear stress on the slip plane in the slip direction in a single crystal.

# Chapter 3 Dynamic recrystallization behavior and its related microstructure evolution of single high temperature α phase

## 3.1 Introduction

The control of microstructure as well as of grain refinement by dynamic recrystallization (DRX) during thermomechanical processing has been developed extensively and has been recognized as being both of technical importance as well as of scientific interest. As the characteristics of the expected microstructure, ($\alpha_2$+$\gamma$) lamellar structure, in TiAl alloys directly depend on the high-temperature α phase. Thus, the microstructure responses of the high temperature α phase during thermomechanical processing has been a key point for optimizing the ($\alpha_2$+$\gamma$) lamellar structure. Heretofore, only few researches referring to the deformation behavior of the high temperature α phase in TiAl alloys conclude that the α phase was deformed preferentially by slip rather than by twinning, superimposed by a relatively slow dynamic recovery (DRV) and a less important DRX process. The DRV and DRX behavior of the α phase in TiAl alloys have not been well addressed and no microstructural evolution information was obtained. In this chapter, special attention will be paid to the microstructure evolution of the α phase during uniaxial compression and its underlying DRV and DRX mechanisms. This work will provide original information of continuous DRX (CDRX) of hexagonal materials.

## 3.2 Experimental process

In this chapter, a simple deformation mode, uniaxial compression, was applied to the $TNM^+$ at 1280 ℃ where is the single α phase region (referring Fig. 2-1 [163]). The detailed information on uniaxial compression is given in Section 2.2.1 (Page 30). The hot compressed microstructures were analyzed based on the electron backscatter diffraction (EBSD) measurement data. The high-temperature α phase was reconstructed using the home-made software, Merengue 2 (as detailed in [162]), based on the measured EBSD data and the Blackburn OR. Furthermore, the IGMA method was used and extended to reveal the dislocation slip and the formation mechanisms in formation of the low-angle boundaries.

## 3.3 Microstructure of the initial α phase free of deformation

Fig. 3-1 ($a_1$) shows the reconstructed as-thermally-treated α phase (1280 ℃/10 min/water quenching) that was the initial microstructure for the hot compression. For reference, the original EBSD band quality indexed micrograph demonstrating the γ lamellae formed during cooling within the α grains is displayed in Fig. 3-1 ($a_2$). It can be seen from Fig. 3-1 ($a_1$) that the α grains are in equiaxed shape with an average grain size of 220±84.0 μm. The disorientation angle distribution of the α phase in Fig. 3-1 (b) is in good agreement with the well-known Mackenzie distribution [178] for materials with random crystal orientations, indicating that the initial α grains do not possess any preferred crystallographic orientations or texture.

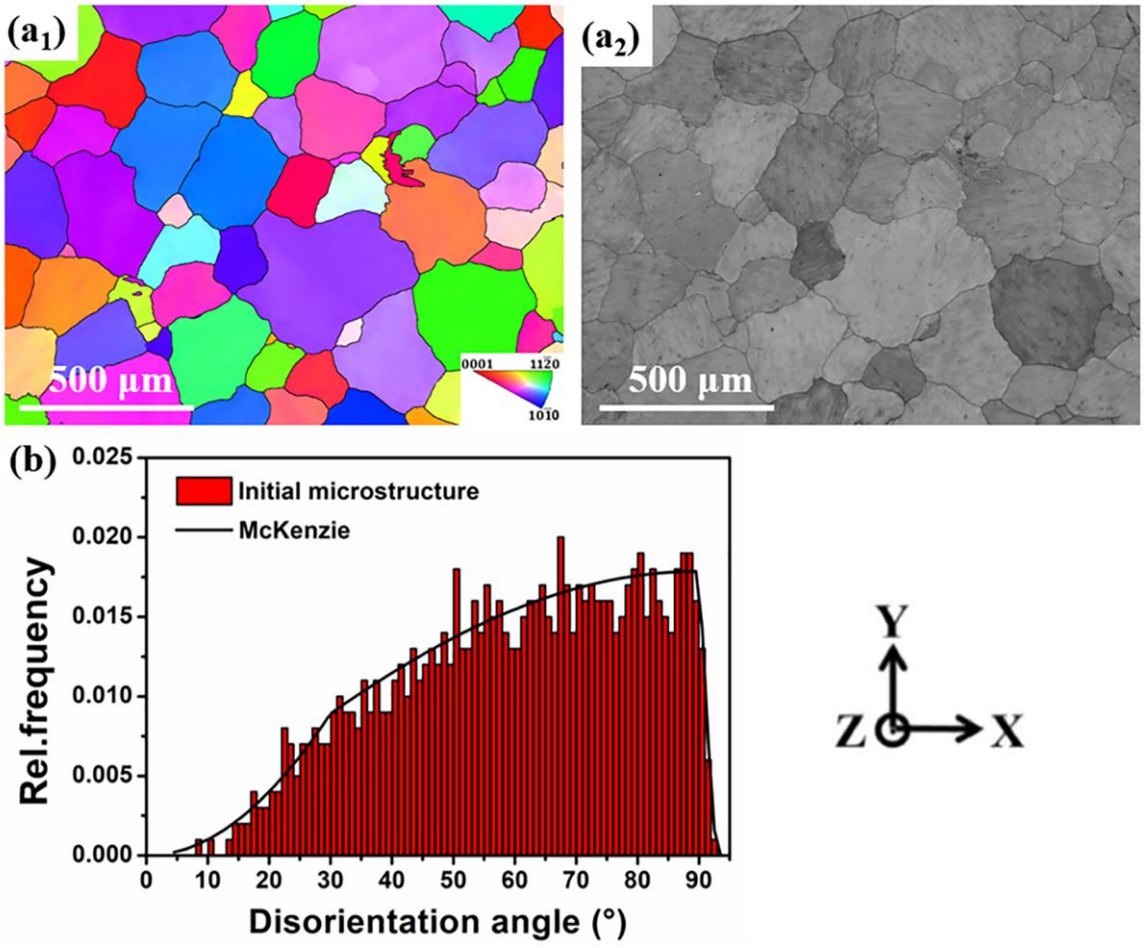


Fig. 3-1 Initial microstructure. ($a_1$) EBSD Y axis inverse pole figure (IPF) micrograph of the reconstructed high-temperature α phase; ($a_2$) EBSD band quality indexed micrograph before reconstruction; (b) disorientation angle distribution of α phase.

## 3.4 Microstructure evolution related to dynamic recovery (DRV)

### 3.4.1 Grain boundary bulging

Fig. 3-2 shows the EBSD Y axis (//LD) IPF micrographs of the sample deformed to the true strain of 0.05 (reconstructed micrograph in Fig. 3-2 ($a_1$) and original band quality indexed one in Fig. 3-2 ($a_2$)) (The original non-reconstructed micrographs used in the figures hereafter will not be provided). It is seen from Fig. 3-2 ($a_1$) that although the α grains are still in equiaxed shape, remarkable changes happened to their boundaries. Serrations or bulges appeared along some α grain boundaries, as shown by the two examples outlined with black rectangle in Fig. 3-2 ($a_1$). One can infer that some parts of the grain sheared in one direction and extruded into the neighboring grain, and the other parts were subjected to an "extruding in" from the neighboring grain on the other side. Further local disorientation analysis represented by the Kernel average misorientation (KAM) micrograph displayed in Fig. 3-2 (b) demonstrates that numerous low-angle disorientations appear along the bulged boundary regions, suggesting that a large number of dislocations were accumulated in front of the bulges. Interestingly, in some locations, the densities of local disorientations inside the bulges are higher than those in front of the bulges, as indicated with the arrows (1 to 4) in Fig. 3-2 (b). This is opposite to the well-known strain-induced grain boundary migration, where grain boundaries migrate into high dislocation density regions, leaving the region behind with a lower dislocation density [117]. So, in the present work, the boundary bulging should be from a different origin.

To find out the origin behind the boundary bulges, the orientation variation feature near the bulged boundaries is further analyzed. A representative example is shown in Fig. 3-3 (a). The evolution of the disorientation with respect to the starting point along line $L_1$ in Grain 1 (G1) from the grain interior (starting point) to the bulged parts is also displayed in the figure. It is seen that the accumulated disorientation angle along $L_1$ exhibits plateaus and jumps (1~3º). The disorientation angles and axes at A, B and C with respect to the orientation of the point before each jump are 1.8º/<000$\bar{1}$>, 1.2º/<$\bar{2}$ 1 1 $\overline{12}$>, and 2.4º/<2 $\bar{1}$ $\bar{1}$ $\overline{12}$>, respectively. The maximum disorientation reaches 5.4º/<000$\bar{1}$> when approaching the boundary. Interestingly, the rotation axes are always close to <000$\bar{1}$>. It is known that among the possible slip modes

in the disordered hexagonal α phase [133,134], only the prismatic <*a*> provides a lattice rotation with the Taylor axis in the <000$\bar{1}$> direction [166–168,171] (see Table A-1 in Appendix). This suggests that the deformation was mainly realized by the prismatic <*a*> slip. With this information, the relation between the bulge direction and the possible active slip system (slip plane and direction) are further examined. Then, the pole figures of the prismatic slip plane and the slip direction of G1 are plotted and display in Fig. 3-3 (b). Among the three prismatic slip variants, the one possessing the highest Schmid Factor, –0.47, for compression is highlighted with the blue circles. This variant was in the favorable orientation to be activated during the deformation. The slip plane trace of this slip variant is also plotted with the black solid line in the $\{1\bar{1}00\}$ pole figure. It is found that the orientation of this trace is in reasonable coincidence with the bulging direction (Line $L_1$ in Fig. 3-3 (a)). This suggests that the bulging of the boundary is related to the dislocation movement on this prismatic slip system.

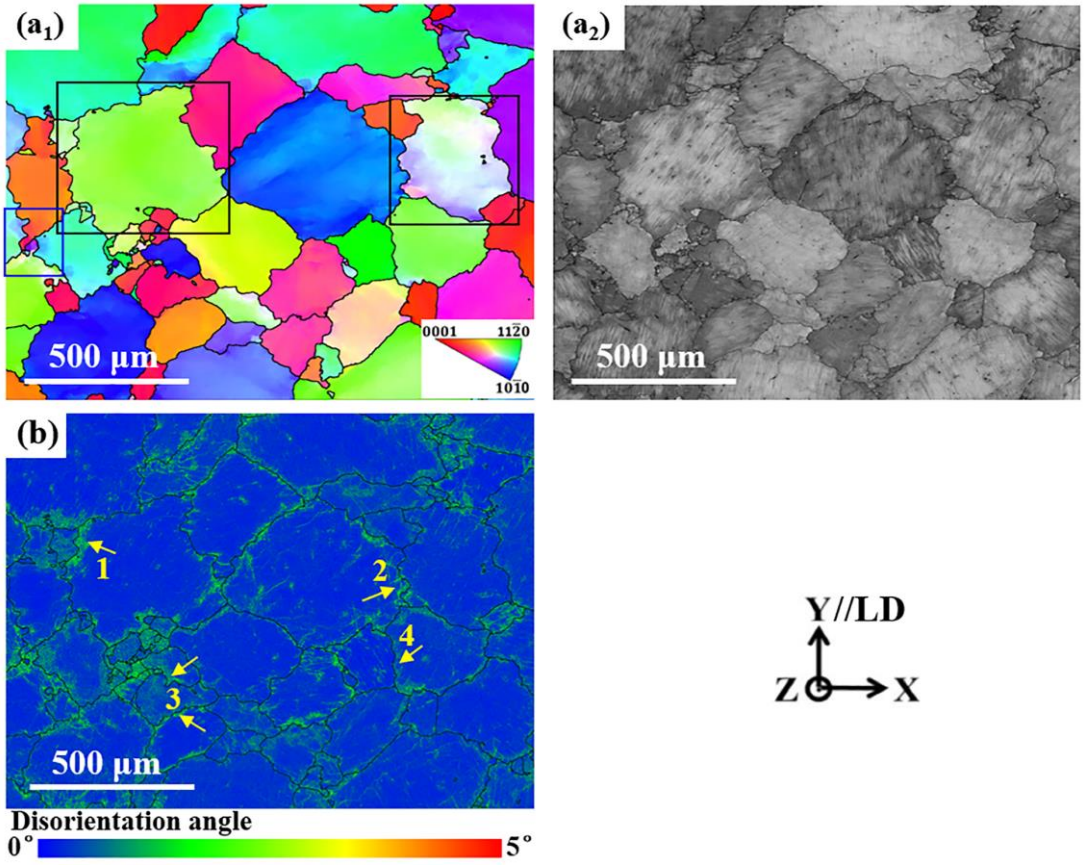


Fig. 3-2 Deformed high-temperature α microstructure at true strain of 0.05. ($a_1$) EBSD Y axis IPF micrograph of α phase; ($a_2$) original EBSD micrograph with band quality indexed contrast. The black lines stand for grain boundaries and the red lines for the bulged boundaries. (b) Kernel average misorientation (KAM) micrograph of ($a_1$).

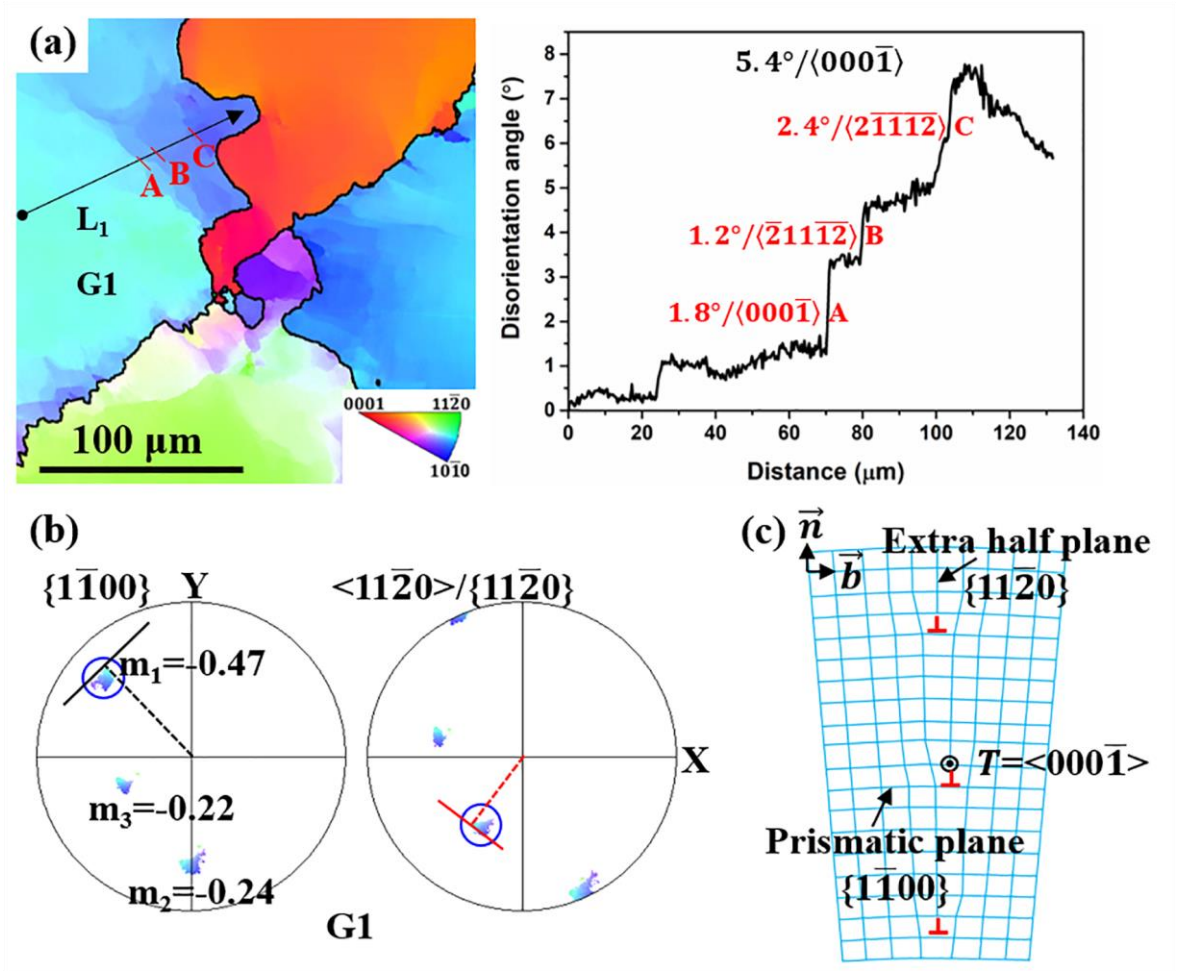


Fig. 3-3 (a) EBSD Y axis IPF micrograph of a representative example of boundary bulge regions and the correlated disorientations (in angle and axis) along L1 in grain G1. (b) Prismatic slip plane and direction ({1$\bar{1}$00} and <11$\bar{2}$0>) pole figures of G1. (c) Illustration of low-angle boundary formed by edge prismatic <*a*> dislocations characterized by a rotation around <000$\bar{1}$> and a boundary plane of {11$\bar{2}$0}.

Another microstructural phenomenon near the bulge regions is the formation of the segments of low-angle boundaries as shown by the abrupt change of the colors (marked with the lines at A, B and C) along L1 in Fig. 3-3 (a), where abrupt disorientation changes are present. This suggests that dislocation rearrangement happened accompanying the deformation. Further trace orientation analysis showed that those low-angle boundaries (lines at A, B and C) in Fig. 3-3 (a) are oriented very close to the trace of the {11$\bar{2}$0} plane (the red line in the <11$\bar{2}$0>/{11$\bar{2}$0} pole figure in Fig. 3-3 (b)). This plane is just perpendicular to the active slip plane, *i.e.*, the {1$\bar{1}$00} plane. Such boundaries, in fact, align with the extra half planes of the prismatic <*a*> dislocations, as illustrated in Fig. 3-3 (c). Geometrically, a prismatic <*a*> edge

dislocation is built by an extra half-plane of $\{11\bar{2}0\}$ that intersects the $\{1\bar{1}00\}$ prismatic slip plane on a line of $<000\bar{1}>$ that is the dislocation line, as indicated in Fig. 3-3 (c). For a low-angle boundary made up of the same type of edge prismatic <*a*> dislocations aligned normal to the prismatic slip plane, as the case in Fig. 3-3 (c), the rotation axis between the two parts separated by the boundary is coincident with the $<000\bar{1}>$ direction and the boundary plane is marked by the extra half-planes of the dislocations, *i.e.*, the $\{11\bar{2}0\}$ plane. The situation in Fig. 3-3 (a) is typical and appears frequently in many other positions in the sample.

As the small deformation was performed at high temperature, 1280 ℃ ($0.85T_m$), the atomic bonding is weakened and the vacancy concentration is increased. Thus, the disordered boundary regions could be further extended, i.e., the grain boundaries should be broadened, as illustrated in Fig. 3-4 (a). When the favorably oriented prismatic slip was activated in the α grains, dislocations of prismatic <*a*> were generated and moved through the grain interiors and arrived at grain boundary regions (Fig. 3-4 (b)). The broadened boundaries functioned as dislocation sinks with enhanced free volume. When one dislocation moved out of the grain and annihilated in the boundary, an atomic step of ***a*** is formed extruding to the boundary region. When large amount of the same typed dislocations on several bundles of parallel slip planes moved into the boundary region, the boundary becomes microscopically bulged (Fig. 3-4 (c)). Such a grain boundary bulging mechanism was also evidenced in a hot deformed AZ31 alloy [179]. With the deformation, more dislocations were multiplicated and started to accumulate in front of the grain boundaries, thus, under thermal agitation dislocation climb happened, initiating dislocation rearrangement process and then forming the low-angle boundaries in front of the bulged parts (Fig. 3-4 (d)). The fact that most of the low-angle boundaries at the present stage (true strain of 0.05) are characterized by a rotation around the $<000\bar{1}>$ axis and the boundary plane coincides with the $\{11\bar{2}0\}$ plane demonstrates that only one prismatic <*a*> slip was mainly activated and the low-angle boundary is composed of the same type of edge dislocations, as illustrated in Fig. 3-4 (d). Such boundaries belong to the symmetrical-tilt boundary.

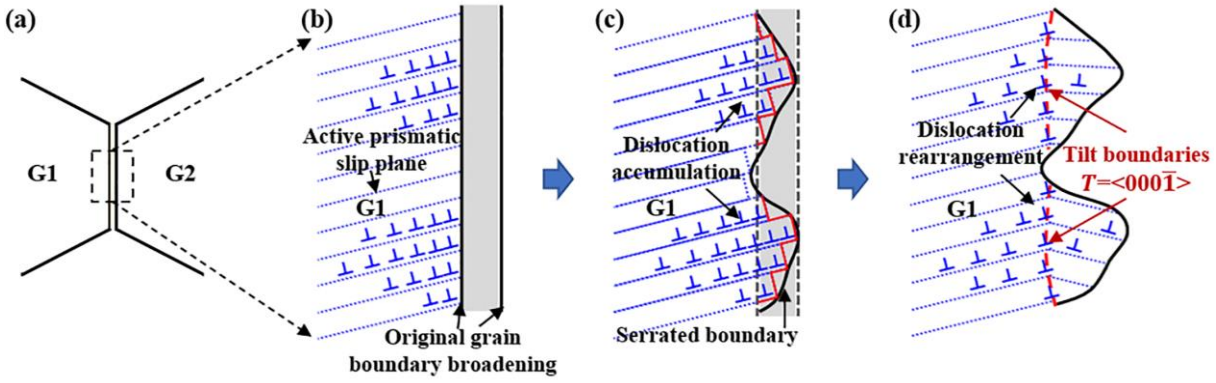


Fig. 3-4 Schema illustrating the formation of boundary bulging by dislocation slip and the formation of symmetric-tilt low-angle boundary by dynamic recovery (DRV). (a) Grain boundary broadening; (b) activation of dislocation slip and dislocation pile-ups in front of broadened boundary; (c) annihilation of dislocations at grain boundary and formation of boundary bulge; (d) rearrangement of dislocations to form symmetrical-tilt low-angle boundary.

### 3.4.2 Formation of subgrain

When the true strain was increased to 0.07, almost all the grain boundaries were bulged. Low-angle boundaries (3~15º) frequently appeared near triple junctions or grain boundary bulges, as marked with the white lines in Fig. 3-5 (a). These low-angle boundaries tended to form a closed region with the bulged boundaries, suggesting that subgrains were forming along the bulged grain boundary regions. Detailed orientation analysis of the low-angle boundaries in terms of disorientation angle and the rotation axis in large sample areas (3 EBSD micrographs each covering an area of 1.6×1.2 $mm^2$) revealed that the disorientation axes of 92.6% (in number) of low-angle boundaries fall into the following three categories, as also marked in Fig. 3-5 (a).

(i) <0001> (39.4%), marked in white in the figure;

(ii) <10$\bar{1}x$> ($|x|\geq 0$) (32%), marked in black in the figure;

(iii) <11$\bar{2}y$> ($|y|\geq 0$) (21.2%), marked in yellow in the figure.

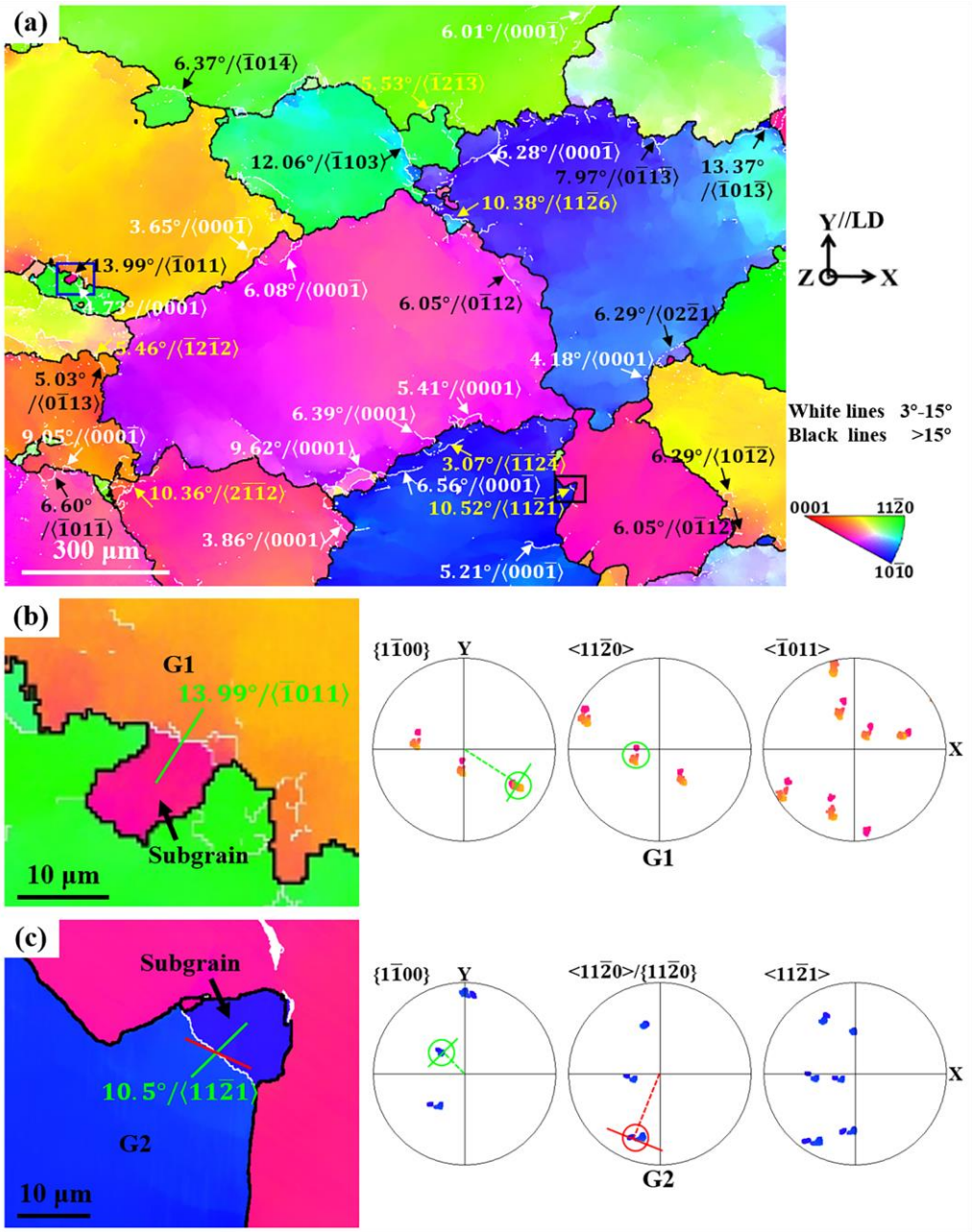


Fig. 3-5 Microstructural and crystallographic features of α grains in sample deformed to true strain of 0.07. (a) EBSD Y axis IPF micrograph of high-temperature α phase; (b) EBSD Y axis IPF micrograph of the area outlined with blue rectangle in (a), and pole figures of prismatic slip plane and direction ({1$\bar{1}$00} and <11$\bar{2}$0>) and the disorientation axis <$\bar{1}$011> in G1; (c) EBSD Y axis IPF micrograph of the area outlined with black rectangle in (a), and pole figures of prismatic slip plane and direction ({1$\bar{1}$00} and <11$\bar{2}$0>) and the disorientation axis <11$\bar{2}$1> in G2.

The disorientation axis <0001> are the Taylor axis corresponding to the symmetrical-tilt boundaries formed by the arrangement of the prismatic <*a*> dislocations. These boundaries are mainly the ones that are not yet totally connected with the original grain boundary to form the subgrains, suggesting that in these regions the DRV is in progress. However, for the low angle

boundaries with the disorientation axes of <10$\bar{1}x$> or <11$\bar{2}y$>, they are usually connected with the bulging boundaries and the enclosed regions possess a larger deviated orientation from that of the parent grain, becoming the subgrains separated from the parent grains. To analyze the formation process of the new kinds of boundaries, two representative examples were selected and are displayed in Fig. 3-5 (b) and (c). In the first case (Fig. 3-5 (b)), the disorientation between the subgrain and the original grain is 13.99º/<$\bar{1}$011>, and in the second case (Fig. 3-5 (c)), the disorientation is 10.5º/<11$\bar{2}$1>. Analysis revealed that in either case the grain bulging direction (marked with the green lines) is largely consistent with the trace of one prismatic slip plane, as highlighted with the green lines in the {1$\bar{1}$00} pole figures in Fig. 3-5 (b) and (c). This indicates that the formation of the low-angle boundaries proceeded by two steps. The first was the formation of a tilt boundary with a disorientation of $\theta_1/T_1$ ($T_1$=<0001>) from single prismatic slip and dislocation rearrangement. The second was another rotation $\theta_2$ around $T_2$ of the bulged part.

The second rotation could be realized by the absorption of the dislocations of another slip system to the yet formed tilt boundaries $\theta_1/T_1$. Thus, using the $\theta_1/T_1$ rotation ($\theta_1$=1~10º; $T_1$=<0001>) as the first rotation and the $\theta_2/T_2$ ($\theta_2$=1~10º; $T_2$= corresponds to Taylor axis of one of the other slip systems in Table A-1 in Appendix) as the second rotation, to resolve the second one by calculating the total disorientation and then comparing it with the measured disorientation. The second rotation should be the one providing the minimum deviation of the calculated total disorientation from the measured disorientation. The corresponding Taylor axis $T_2$ reveals the newly activated slip system that contributed to the further evolution of the sub-grain boundaries. The detailed formulation to resolve the second rotation is given in Appendix.

The calculation results show that for the $T$=<10$\bar{1}x$> boundaries, the second rotation axis $T_2$ is <10$\bar{1}$0>, corresponding either to a basal <$a$> slip or a pyramidal II <$c$+$a$> slip (Table A-1). More examples with disorientation axis of <10$\bar{1}x$> are displayed in Table A-3 in Appendix. The occurrence of the basal slip is more probable because the CRSSs of prismatic, basal and pyramidal slip are ordered increasingly from the prismatic to the pyramidal slip [134–136]. The basal slip has lower CRSS than the pyramidal slip, thus, under specific local stress, the basal slip could easily be activated. Further analysis show that the Schmid factors of the activated

basal slip are not always very high. Even in some grains, all the absolute values of the Schmid factors of the basal slip are smaller than 0.3, indicating that the activation was mainly driven by local incompatible deformation between the neighboring grains in the boundary regions. These results confirmed that the appearance of the $<10\bar{1}x>$ low-angle boundaries was indeed realized by two steps. The first is the formation of the symmetrical tilt low-angle boundaries with disorientation axis of <0001> by the rearrangement of the prismatic <*a*> dislocations, and the evolution of the symmetrical tilt boundaries to the asymmetrical low-angle boundaries by absorption of the basal <*a*> dislocations, as illustrated in Fig. 3-6 (a).

However, for the $T=<11\bar{2}y>$ boundaries, the Taylor axis of all the possible slip systems in hexagonal structures have been tried, but no reasonable match between the calculated total rotation and the measured disorientation could be found. This means that the second rotation was not realized by dislocation activity but by a different mechanism. Interestingly, it was found that although the disorientation axis of the boundaries was no longer <0001>, the trace of the low-angle boundary (in white) is very close to the trace of the $\{11\bar{2}0\}$ plane, as indicated with the red line in the IPF micrograph and in the $<11\bar{2}0>/\{11\bar{2}0\}$ pole figure in Fig. 3-5 (c). This means that the boundary plane still remained the $\{11\bar{2}0\}$ plane. As analyzed above (Fig. 3-3 (c)), this plane corresponded to the extra half-plane of the edge prismatic <*a*> dislocations formed during the first step, inferring that during the second step the evolution of the boundary could only be realized by a rotation around the axis normal to the low-angle boundary formed in the first step, *i.e.,* $<11\bar{2}0>$ axis. Thus, using $T_2=<11\bar{2}0>$ as the second rotation axis to calculate the total rotation, good matches appeared between the calculated dislocations and the measured ones, confirming that the second rotation was indeed realized by a rotation around the axis normal to the boundary. More examples with disorientation axis of $<11\bar{2}y>$ are displayed in Table A-4 in Appendix. This result evidenced that at the present stage of deformation grain boundary sliding happened through which the tilt symmetrical low-angle boundaries further evolved into the tilt-twist boundaries, as illustrated in Fig. 3-6 (b). As the sliding is rotational, one can denote such boundary sliding by rotational boundary sliding. By these two ways, the orientations of bulged parts continuously deviated from those of original grains, initiating the formation of the subgrains.

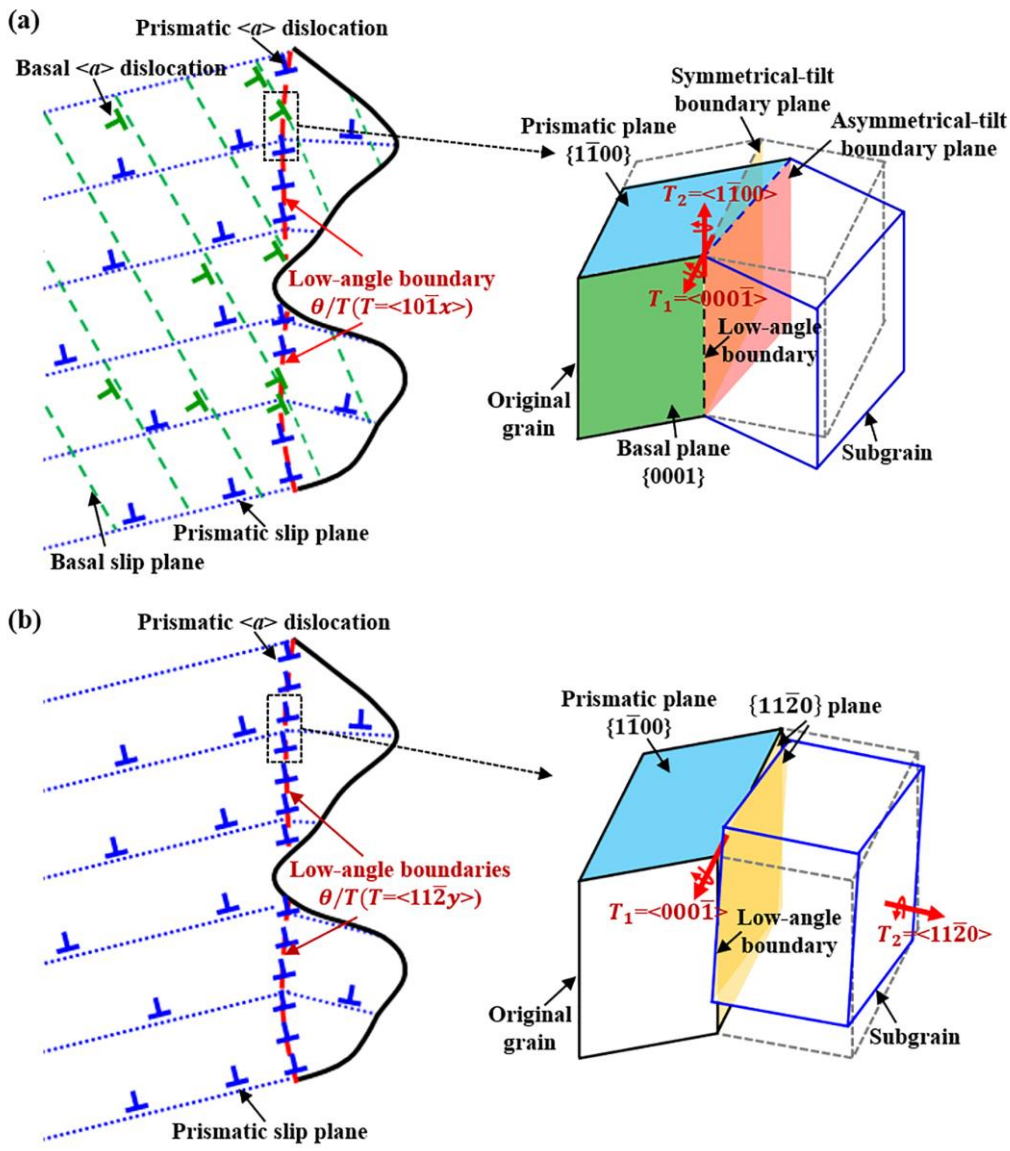


Fig. 3-6 Schema illustrating the evolution of low-angle boundaries with further deformation. (a) Asymmetrical-tilt boundaries with disorientation of $\theta/T$ ($T$=<10$\bar{1}x$>) formed by the first rotation $\theta_1/T_1$ ($T_1$=<000$\bar{1}$>) and the second rotation $\theta_2/T_2$ ($T_2$=<1$\bar{1}$00>); (b) Tilt-twist boundary with the disorientation of $\theta/T$ ($T$=<11$\bar{2}y$>) formed by the first rotation $\theta_1/T_1$ ($T_1$=<000$\bar{1}$>) and the second rotation $\theta_2/T_2$ ($T_2$=<11$\bar{2}$0>).

## 3.5 Microstructure evolution associated with continuous dynamic recrystallization (CDRX)

### 3.5.1 Necklace structure

Fig. 3-7 is the microstructure of the sample deformed to the true strain of 0.29. It can be clearly seen that the microstructure exhibits bimodal grain structure, composed of the newly

formed small grains and the remnants of the initial coarse grains (Fig. 3-7 (a)). The newly formed small grains with an average size of about 26±11.4 μm are distributed along the initial grain boundaries, forming a necklace structure. When the strain increased from 0.07 to 0.29, the grain size of the retained coarse grains decreased, from an average size of 580±216.3 μm to an average size of 490±284.5 μm, and the area fraction of the small grains increased from 4.5% to 35.6%. The KAM micrograph displayed in Fig. 3-7 (b) shows that the newly formed small grains indicated by the yellow arrows possess much less amount of local disorientation, thus, these small grains possess the feature of recrystallized grains. This suggests that the recrystallization process was realized by a continuous detachment of the subgrains from the grain boundary regions, and such a process occurred repeatedly toward grain interiors, demonstrating a CDRX feature. From the color features of the small grains along the coarse grain boundary regions in Fig. 3-7 (a), one can see that the small grains detached from the two neighboring coarse grains were further mixed during the deformation process.

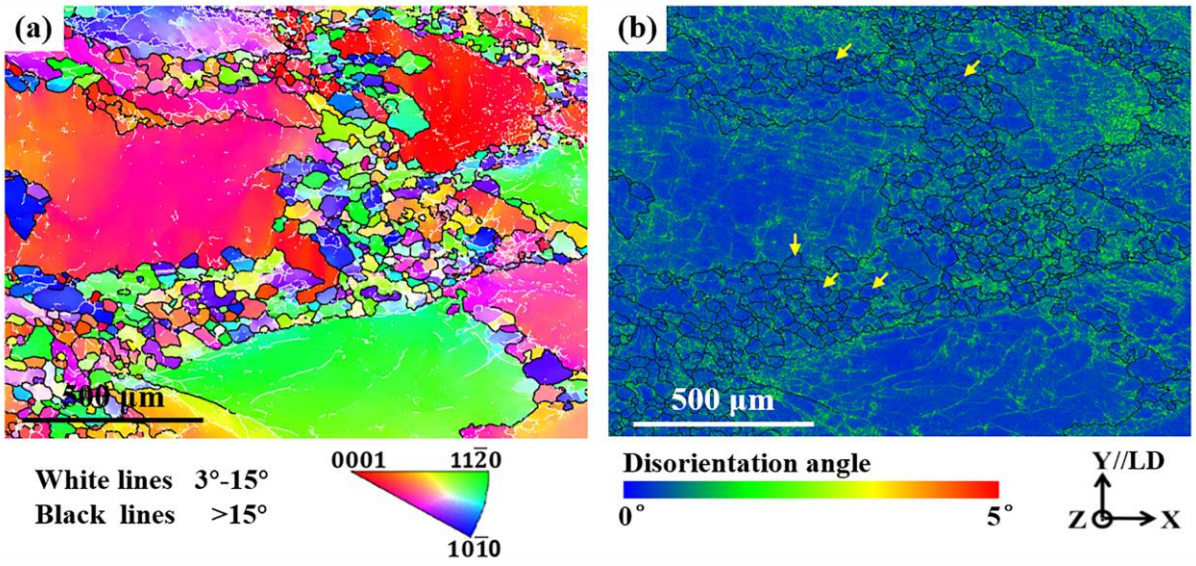


Fig. 3-7 Micrographs of the α phase in the sample deformed to the true strain of 0.29. (a) EBSD Y axis IPF micrograph; (b) KAM micrograph.

To reveal the mechanism of the mixing process of the recrystallized grains, the crystallographic orientation features of two examples of necklace areas, the one with a few small grains representing the beginning of detachment and the other with some more small grains representing the penetrating of the small grains into neighboring small grain regions

displayed in Fig. 3-8, were further analyzed. It is seen from Fig. 3-8 (a) that the two coarse grains with distinct orientations (represented by the {0001} and $\{1\bar{1}00\}$ pole figures) were separated by a layer of small sized domains delimitated either by high-angle boundaries (black lines) or low-angle boundaries (white lines) or the mix of the two. This suggests that for these two coarse grains the formation of the "necklace" just started. Although the small domains were separated from the neighboring coarse grains by boundaries with disorientation angles higher than 15º, their orientations are characteristically either close to G1 or to G2. For example, in the EBSD IPF micrograph in Fig. 3-8 (a), the orientations of domains D1 and D2 (enclosed in the blue and black squares in the pole figures) are close to that of G2 and those of domains D3 and D4 (enclosed in the red and green circles in the pole figures) are close to that of G1. Clearly these orientation domains were detached from the two coarse grains (G1 and G2) and mixed in the necklace layer. For the case shown in Fig. 3-8 (b), the thick "necklace" layer was formed around the coarse red grain. The {0001} and $\{1\bar{1}00\}$ pole figures in Fig. 3-8 (b) are from the small red domains and the coarse red grain in the EBSD Y axis IPF micrograph. One can see that the small red domains possess close crystallographic orientations to that of the coarse red grain. However, the small red domains were already separated by layers of small domains detached from the other neighboring coarse grains. This suggests that grain boundary sliding between the detached small domains happened, resulting in the mixing of these small grains.

In this case the boundary sliding is both translational and rotational. The former allows the detached grains to spatially separate from their parent grain but does not affect their orientation. The latter is opposite. It does not make spatial separation but deviates their orientations from those of the parent. The evidence of the spatial separation of the new grains from the parent grain and their orientation deviation from the parent orientation infers the existence of the two types of boundary sliding. The occurrence of grain boundary sliding is quite reasonable under the present deformation conditions. Firstly, the deformation temperature (1280 °C) was very high ($0.8T_m$), thus grain boundary strength was very low. Secondly, the deformation strain rate was relatively low (0.01 $s^{-1}$) that offered a sufficient time window for the slow process of sliding to occur, Thirdly, the sizes of the detached domains were relatively small that provided a high amount of boundary area. All these factors favored the occurrence of grain boundary sliding.

This mechanism should also be an important deformation mechanism for the small grains to contribute to the external deformation and allow the spatial separation of the detached grains from their parent grains.

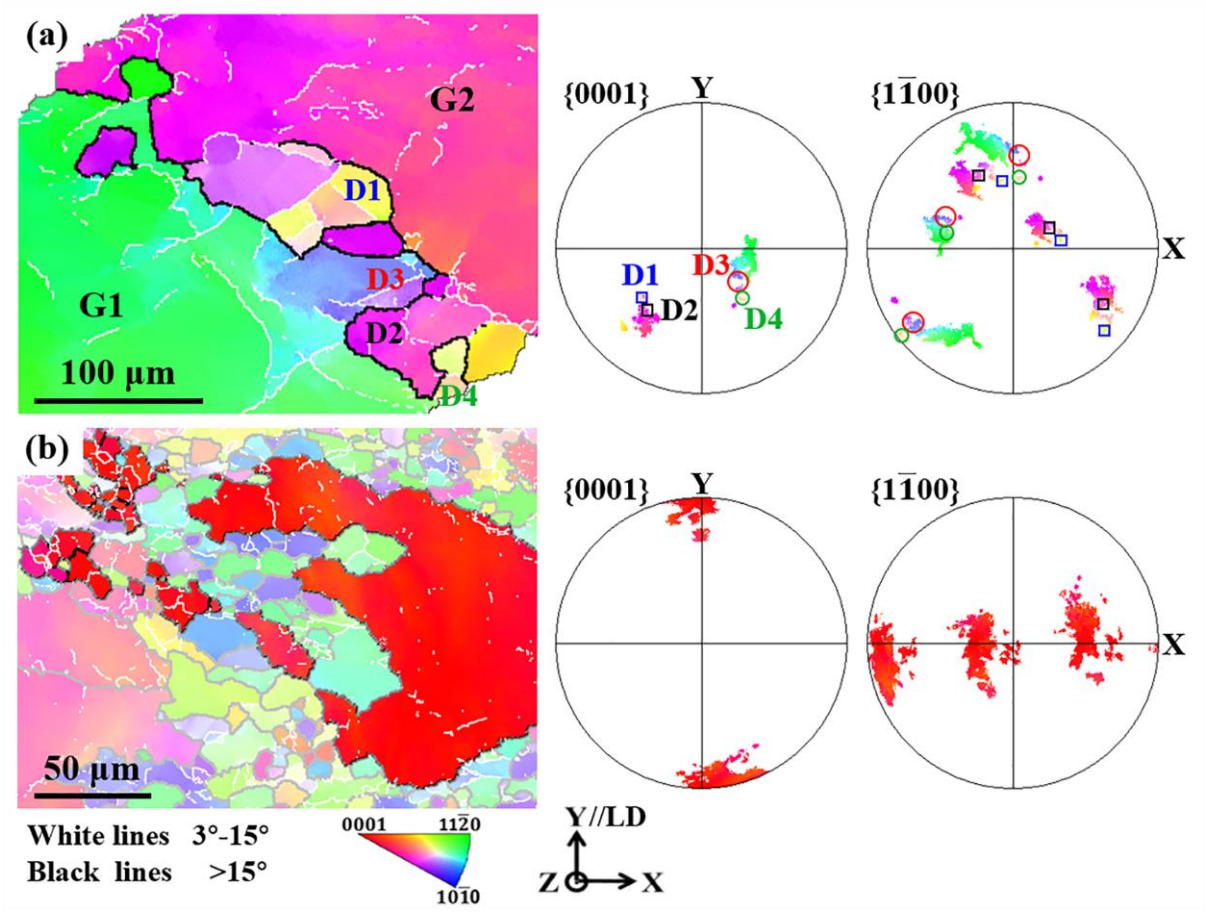


Fig. 3-8 EBSD Y axis IPF micrographs and the corresponding {0001} and {1$\bar{1}$00} pole figures of the grains in two necklace regions. (a) Necklace region with less small grains representing the beginning of grain detachment; (b) Necklace region with more small grains representing the mixing of small grains. The poles in the pole figures in (b) are from the coarse red grain and the small red domains.

### 3.5.2 Equiaxed grains

Fig. 3-9 displays the EBSD micrograph of the sample deformed to the true strain of 1.05. It can be seen that the microstructure is mainly composed of nearly equiaxed small grains, indicating the completion of the recrystallization process. The average grain size is about 45±23.9 μm. However, it is worth mentioning that in some relatively large grains there exist segments of high-angle boundaries connected with segments of low-angle boundaries, as marked with the black arrows in Fig. 3-9. This suggests that the grain fragmentation process

was still in progress. The low-angle boundaries would further evolve into high-angle boundaries and eventually divided the coarse grains into differently oriented small grains.

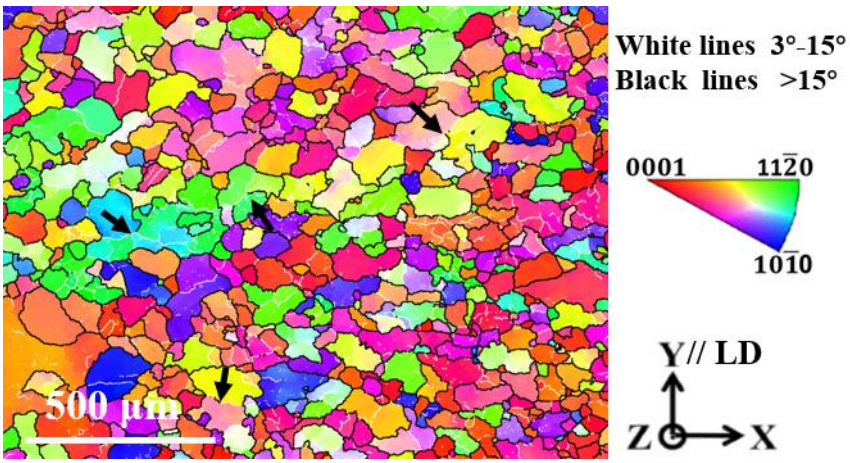


Fig. 3-9 EBSD Y axis IPF micrograph of the sample deformed to the true strain of 1.05.

Although the nucleation of the recrystallized grains in the present work also started from subgrains as the recrystallized nuclei, it is quite different from the commonly reported nucleation modes related to subgrains, *i.e.*, nucleation by sub-boundaries migration and nucleation by subgrain coalescence [180]. There was neither subgrain boundary migration nor subgrain coalescence, but subgrain detachment from the parent grains by the increasing disorientation and grain boundary sliding. In consequence, the nuclei formed in this way were very large with sizes of several tens of micrometers and the recrystallization did not obviously undergo the grain growth stage. The recrystallization progressed (with the deformation) rather by continuous repetition of the formation of the subgrains and the detachment of the subgrains from grain boundary bulges, which developed from grain boundary region toward grain interior until all the initial coarse grains were fragmented. Such a feature should be related to the lack of slip systems of hexagonal crystals and also the slow deformation condition of the present work. During the deformation, only one or two slips systems were activated. On one hand, the produced dislocations could smoothly move to grain boundary regions without much hindrance, and on the other hand, no dislocation entanglement could occur in the grain interiors to form intragranular subgrains. As the subgrains is formed preferentially at the boundary regions, grain boundary sliding is much easier than in grain interiors. Thus, subgrain detachment (especially translational sliding) prevailed over sub-boundaries migration and subgrain coalescence.

## 3.6 Summary

In this chapter, the mechanisms of DRV and CDRX of high-temperature α phase under a uniaxial isothermal compression at 1280 ℃ were thoroughly investigated by means of microstructural and crystallographic analysis with an extended IGMA analysis method. The recrystallization process can be categorized into three characteristic stages, *i.e.*, grain boundary bulging with the formation of symmetrical-tilt boundaries near boundary bulging regions, subgrain formation at bulged boundary regions by evolving symmetrical-tilt boundaries into asymmetrical-tilt or tilt-twist boundaries and the formation of recrystallized grain by subgrain detachment from the parent grain.

During the first stage, the favorable prismatic slip systems were activated. Edge prismatic <*a*> dislocations were generated and piled up near grain boundaries. Under the unidirectional compression, grain boundaries that were not normal to the compression axis were broadened due to the tension in the direction perpendicular to the compression axis. Dislocations were annihilated in the broadened boundary and formed steps bulging into the neighboring grains, resulting in bulging boundaries. Due to thermal agitation, accumulated dislocations also rearranged by dislocation climb accompanying the boundary bulging. Symmetrical-tilt boundaries characterized by a disorientation axis of <0001> were formed.

When the deformation progressed to the second stage, the formed symmetrical-tilt boundaries further evolved in two different ways. The one was by absorbing basal <*a*> dislocations formed due to incompatible deformation between neighboring grains in the bulged boundary regions, which transformed the symmetrical-tilt boundaries into asymmetrical-tilt boundaries characterized by a rotation around $<10\bar{1}x>$. The other was by a rotational movement of the bulged parts around the normal axis of the symmetrical-tilt boundary (rotational sliding), which transformed the symmetrical-tilt boundary into a tilt-twist boundary characterized by a rotation around $<11\bar{2}y>$. This resulted in the formation of the subgrains from the bulged grain boundary regions.

When the deformation progressed to the third stage, the formed subgrains are detached from the parent grains and mixed with the ones detached from the neighboring grains by

boundary sliding. Such a nucleation process from subgrain formation is also different from the classical subgrain growth by boundary migration or subgrain growth by coalescence. The three processes repeatedly happened from grain boundary regions toward grain interiors until the whole initial microstructure was replaced by the recrystallized grains.

The results of the present work provided original information of the CDRX of hexagonal structured materials. The extended IGMA analysis method developed in the present study is applicable to the related investigations on deformation behavior of high-temperature phases when dislocations could not be preserved to room temperature.

# Chapter 4 Correlations between microstructure evolution, deformation behavior, and texture development of high temperature α phase

## 4.1 Introduction

During hot deformation, two opposite effects interweave together, i.e., hardening from crystallographic orientation related defect multiplication, and softening from defect rearrangement or annihilation via recovery and recrystallization, resulting in specific microstructure and texture evolution as well as characteristic stress–strain behavior. Due to the limited numbers of slip systems in HCP structured materials with low crystal symmetry, considerable anisotropy will be produced during the plastic deformation of the high temperature α phase. This means that the dislocation emission and motion are varied with the crystallographic orientations of the grains. Thus, the dislocation activities were affected that have a significant effect on the DRX of the high-temperature α phase during the thermomechanical processing, and consequently on the microstructure and texture evolution as well as the deformation responses. So far, the effects of crystallographic orientation on the DRX and deformation behavior of the high temperature α phase remain unclear. Thus, the related crystallographic orientation evolution during the thermomechanical processing also needs further exploration. Based on the DRX mechanism of the high temperature α phase revealed in Chapter 3, this chapter will focus on the correlation between the microstructure evolution and the hot compression stress–strain behavior. Special attention will be paid to the differences of DRX induced fragmentation tendency between the soft and the hard grains according to the crystallographic orientations, and then efforts will be made to reveal the contributions of the deformation mechanism to the texture development of the α phase.

## 4.2 Experimental process

In this chapter, the used alloy is $TNM^{+}$ and the alloy was uniaxially compressed. The detailed information on uniaxial compression is given in Section 2.2.1 (Page 30). The

microstructural and crystallographic features were characterized using SEM-EBSD, then the high-temperature α phase was reconstructed by the home-made software, Merengue 2 [162]. The hot compressed microstructures and crystallographic orientations were analyzed based on the reconstructed EBSD data by the Channel 5 (Oxford Instruments) and the ATEX [165] software package.

## 4.3 Initial microstructure

Fig. 4-1 shows the high-temperature α phase in the initial microstructure, i.e., isothermally held at 1280 ℃ for 10 min and then quenched in water. Fig. 4-1 (a) and (b) display the original EBSD band quality indexed contrast micrograph and grain size distribution. It can be seen that the initial microstructure mainly consisted of equiaxed α grains (Fig. 4-1 (a)) with an average grain size of 220±84.0 μm (Fig. 4-1 (b)). The large standard deviation indicates that the grain size distribution has a wide spread, as also shown by the grain size histogram. Some straight traces can be observed inside the α grains that were from the precipitation of γ lamellae during the cooling process. In order to better analyze and understand the high-temperature α phase, the orientation data of the γ lamellae have been reconstructed to their parent α phase by Merengue 2. The EBSD Y axis inverse pole figure (IPF) of the high-temperature α phase based on the reconstructed EBSD data is shown in Fig. 4-1 (c). Here the α grains present various colors, suggesting that their crystallographic orientations are random. To further characterize the texture of the high temperature α phase in the initial state, the {0002}, $\{10\bar{1}0\}$ and $\{11\bar{2}0\}$ poles figures (PFs) of the high-temperature α phase obtained from 4 EBSD maps each with an area of 1.6×1.2 $mm^2$ are displayed in Fig. 4-1 (d). It can be seen from the PFs that the initial α grains are indeed randomly oriented. Here the discrete poles are related to the coarse α grains.

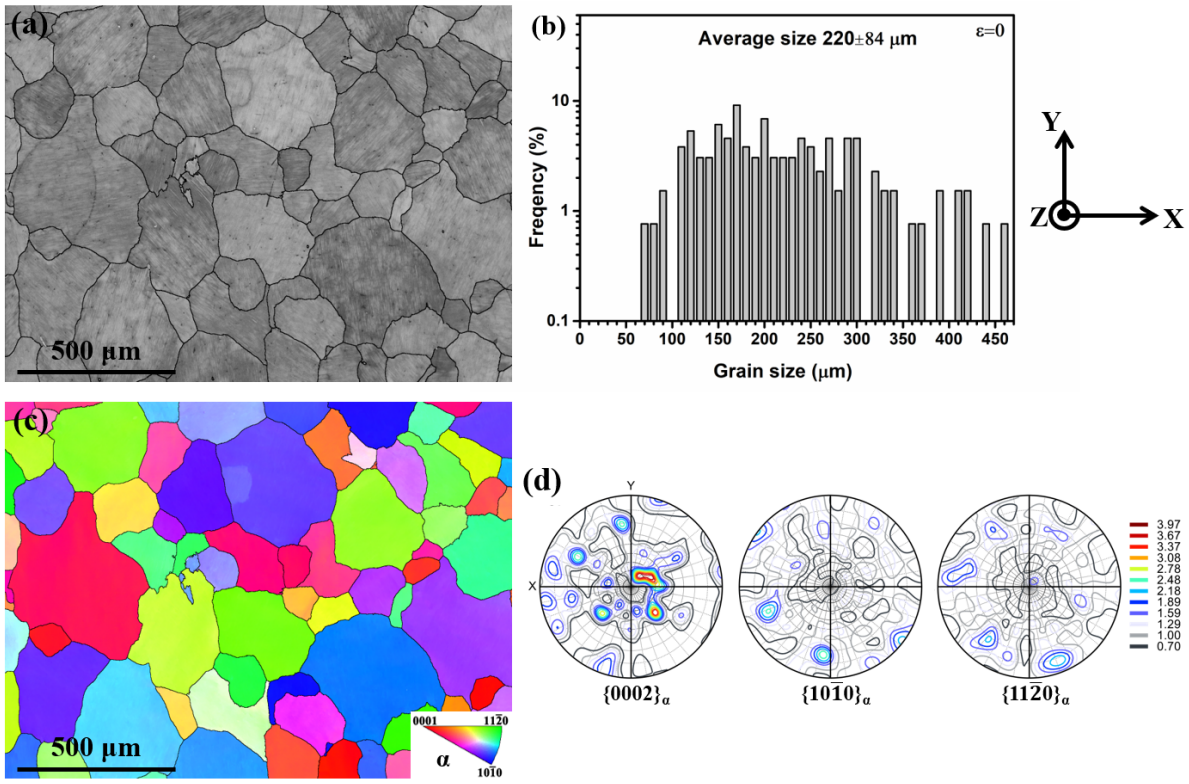


Fig. 4-1 Micrographs of the sample in initial state (1280 ºC /10 min/WQ) without deformation. (a) Band quality indexed contrast micrograph; (b) α grain size distribution; (c) EBSD Y axis inverse pole figure (IPF) micrograph of the high-temperature α phase based on the reconstructed EBSD data; (d) {0002}, {10$\bar{1}$0} and {11$\bar{2}$0} poles figures (PFs) of the high-temperature α phase based on 4 EBSD maps each with an area of 1.6×1.2 mm$^2$.

## 4.4 Strain-stress during uniaxial compression

Fig. 4-2 shows the true stress – true strain curves of the TNM$^+$ alloy compressed to different true strains. The curve compressed to a true strain of 1.05 displays an elastic stage and a plastic stage. During the plastic stage, a work hardening and a stress peak occur at a relatively high true strain [90,94], and then the flow stress decreases gradually to a steady state with the increase of the strain. This means that the plastic deformation of this alloy at 1280 ℃ exhibits a typical flow stress feature composed of three stages: work hardening stage (I), work softening stage (II) and steady stage (III). To figure out the detailed microstructure evolution during the different deformation stages, the samples were compressed to different true strains. As seen in Fig. 4-2, the samples with the true strain of 0.05 and 0.07 correspond to the work hardening stage, the samples with the true strain of 0.29 and 0.60 correspond to the softening stage, and the sample with the true strain of 1.05 corresponds to the steady stage. It should be mentioned

that the peak stresses are varied with different samples with a maximum deviation about 20 MPa. That is because the initial microstructures have so coarse grain sizes that the crystallographic orientation have a significant influence on the deformation behavior [181,182].

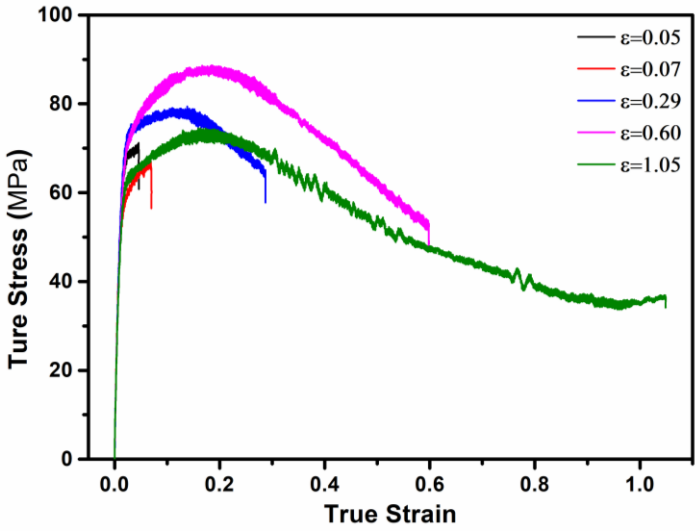


Fig. 4-2 True stress – true strain curves of the TNM$^{+}$ alloy compressed at 1280 °C under a strain rate of 0.01 s$^{-1}$ to different true strains of 0.05, 0.07, 0.29, 0.60 and 1.05.

## 4.5 Correlations between microstructure evolution and deformation behavior

### 4.5.1 Work hardening stage (I)

The microstructures of the samples with the true strain of 0.05 and 0.07 during work hardening stage are displayed in Fig. 4-3 (a) and (b), respectively. The micrographs are presented with EBSD band quality indexed contrast, in which the Y axis is parallel to the axial axis of the cylindrical samples and also the load direction (LD). Compared with the initial microstructure in Fig. 4-1 (a), the morphologies and the sizes of the α grains have changed greatly with the increase of the true strain. Firstly, one can notice that the grain boundaries change from the rather smooth ones in the initial microstructure (Fig. 4-1 (a)) to extensively serrated or bulged ones (Fig. 4-3 (a)). This phenomenon is related to the prismatic dislocation slip and has been analyzed in detail in Section 3.4.1 (Page 47). When the true strain increases to 0.07, low-angle boundaries appear frequently near grain boundaries, as highlighted with the

thin white lines in Fig. 4-3 (b). Meanwhile, some small α subgrains begin to be fragmented from the original α grains along the grain boundary serrations by the DRV and CDRX mechanism. The newly-formed small α grains have an average grain size of 12±6 μm, taking up about 4.5% of the whole area observed. Besides, it can be seen that obvious grain growth occurs resulting from the high deformation temperature. Statistical results show that the average grain size increases from initially 220±84 μm (Fig. 4-1 (b)) to 326±160 μm when the sample is deformed to ε=0.05 (Fig. 4-3 (c)), and further to 580±216 μm when the strain goes up to ε=0.07 (Fig. 4-3 (d)). One can find interestingly that the standard deviations of the average grain size were nearly doubled at ε=0.05 (160 μm) compared wtih the initial (84 μm) and almost tripled at ε=0.07 (216 μm). This indicates that the grain size is widely distributed. On one hand, some α grains are growing, but some are shrinking and being swallowed by the grown ones. On the other hand, some fine DRXed grains (~ 4.5%) are being developed near grain boundaries.

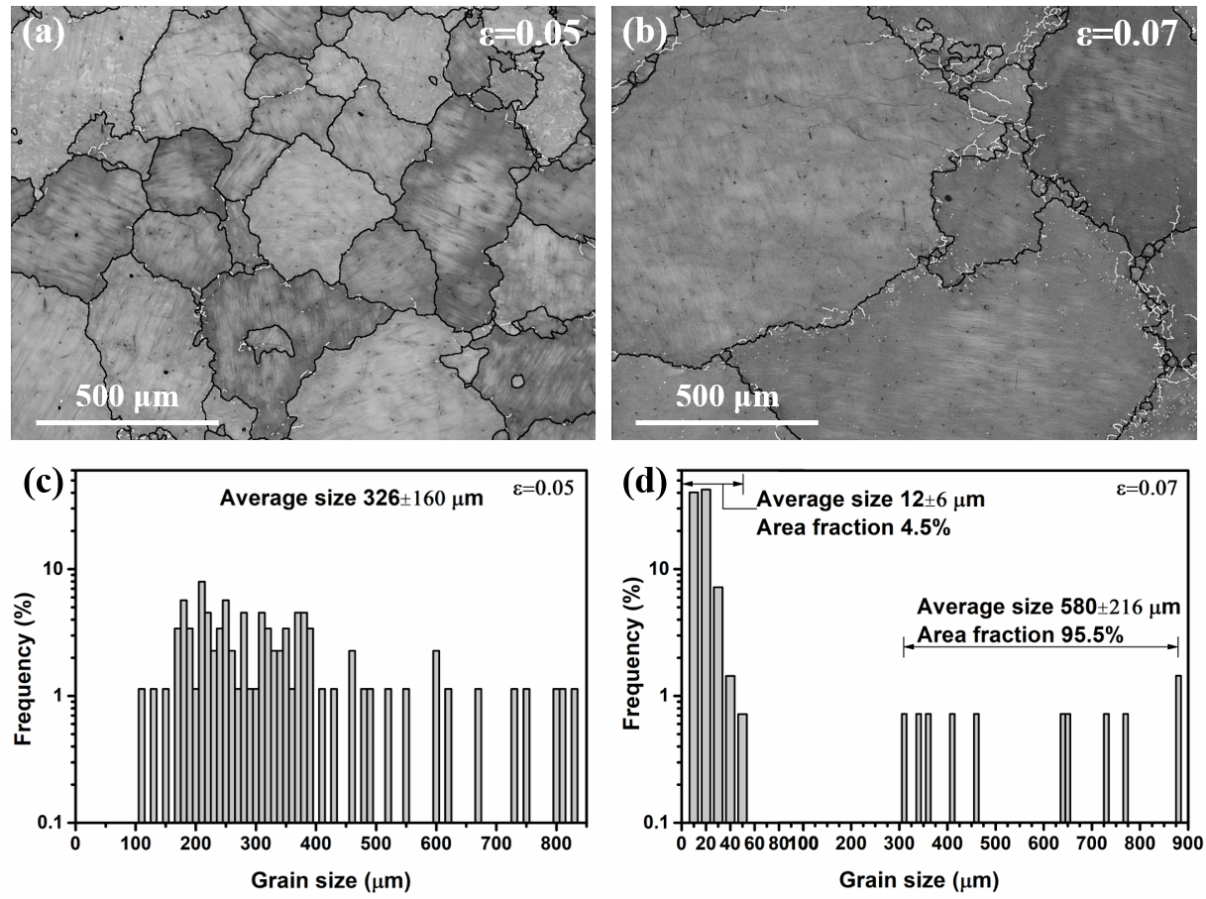


Fig. 4-3 (a) and (b) EBSD band quality indexed contrast micrographs; (c) and (d) Grain size distribution of the samples after uniaxial compression at 1280 °C under a strain rate of 0.01 $s^{-1}$ to the true strains of 0.05 ((a) and (c)) and 0.07 ((b) and (d)), respectively.

Fig. 4-4 shows the EBSD Y axis IPF micrograph of the sample deformed to the true strain of 0.07. As pointed by the white arrow in G1, the disorientation usually begins to generate at grain boundaries. Given that the atomic arrangements are more disordered near grain boundaries at such a high deformation temperature, the grain boundaries were serving as dislocation sources. To realize macroscopic deformation, the dislocations generated at grain boundaries need to move through the grain interiors and arrive at another grain boundary to produce microscopical grain boundary bulgings and finally the macroscopical deformation. It should be mentioned that the obvious grain growth, on one hand, reduces dislocation sources, as the total boundary area decreases by grain growth. Accordingly, to provide the increasing macroscopic strain, larger stress is needed to activate more dislocations. On the other hand, the coarse grain size increases the transgranular trajectories of dislocation glide. Thus, the dislocations may encounter more obstacles or react with the other dislocations to increase the slip resistance. As is known, dislocation activation, multiplication and movement are the main factors contributing to the work hardening. Thus, grain growth contributes to the work hardening to the deformation. However, with the accumulation of dislocations at grain boundary regions, the strong thermal agitation at high temperatures leads to dislocation polygonalization to form low-angle boundaries by dislocation rearrangement (i.e., DRV), and subsequently to form subgrains and even fine DRXed α grains from the original α grains (i.e., CDRX). This process (DRV followed by CDRX) contributes to the softening of the material. The two processes counter balance each other and give rise to an overall microscopic stress–strain behavior of the deformation depending on which process is in prevalence. In the present case of small strain ($\varepsilon$=0.07), the area fraction of the recrystallized part is only about 4.5%, indicating that the softening caused by DRV and CDRX during this stage is relatively weak, and the work hardening induced by dislocation slip is dominant. Besides, due to the limited numbers of slip systems in HCP structure, the dislocation accumulation in the high-temperature α phase is a sluggish process, and consequently the DRV and CDRX of α grains is relatively slow. Thus, the stress peak occurred at a relatively high true strain (~ $\varepsilon$=0.17) compared to that ($\varepsilon$<0.05) when the alloy was hot compressed at ($\alpha_2$+$\gamma$) or ($\alpha_2$+$\beta_0$+$\gamma$) phase regions [90,94], despite the current compressions were conducted at a much higher temperature.

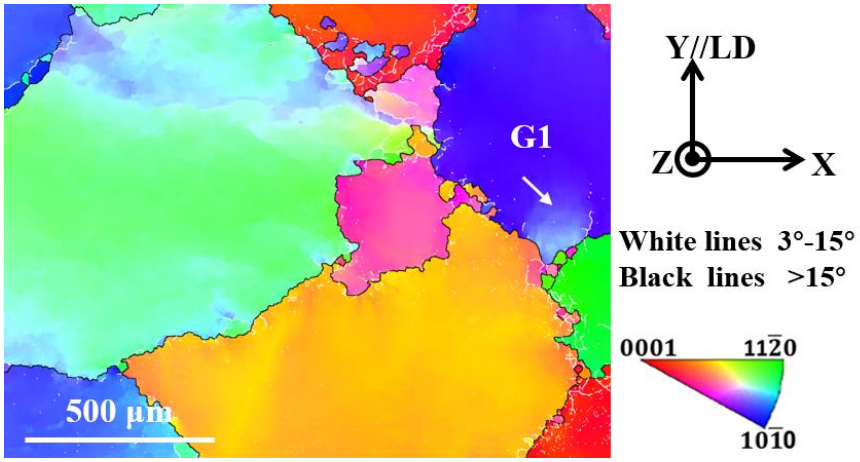


Fig. 4-4 EBSD Y axis (//LD) IPF micrograph of the sample deformed to the true strain of 0.07.

## 4.5.2 Work softening stage (II)

### 4.5.2.1 Microstructure related deformation behavior

From the true stress – strain curves in Fig. 4-2, the deformation of the high temperature α phase experienced a work softening stage spanning a wide range of true train after the work hardening stage. To reveal the deformation mechanism of the high temperature α phase at this stage, the microstructures of the samples deformed to different true strains of 0.29 and 0.60 corresponding to different softening states are displayed in Fig. 4-5 (a) and (b), respectively. It can be seen that the microstructures exhibit bimodal structure consisting of small α grains and some exceptionally coarse α grains. The small ones are the newly-formed grains fragmented from the initial coarse α grains, whereas the coarse ones are those retained from the initial α grains. As the strain increases from 0.29 to 0.60, the area fraction of the newly-formed small α grains increases from 35.6% to 63.3% (Fig. 4-5 (c) and (d)). Accordingly, the area fraction of the retained coarse α grains is decreased, and the average size also decreases from 490±284 μm at ε=0.29 to 289±106 μm at ε=0.60. The increased amount of the small α grains indicates that the CDRX induced grain fragmentation has largely happened and the process was still in progress. It is known that during deformation process, DRX is a softening process. Thus, the progressive lowering of the stress with strain in the softening stage in Fig. 4-2 is the counter-balanced result of softening by CDRX and the hardening by dislocation activities of the retained coarse grains. With the increase of the true strain, the work softening is enhanced with the

increasing fraction of the newly-formed small α grains, and the work hardening is weakened with the decrease of the grain size of the retained coarse α grains, resulting in a continuous decrease in flow stress. The softening caused by the CDRX of the newly-formed small α grains became overwhelming to the hardening induced by the dislocation slip in the retained coarse α grains. Besides, it should be mentioned that the average grain size of the retained coarse α grains has a relatively large standard deviation, which suggests that the CDRX did not occur uniformly throughout the microstructure but varied from grain to grain. Such a behavior will be analyzed in detail in the next section.

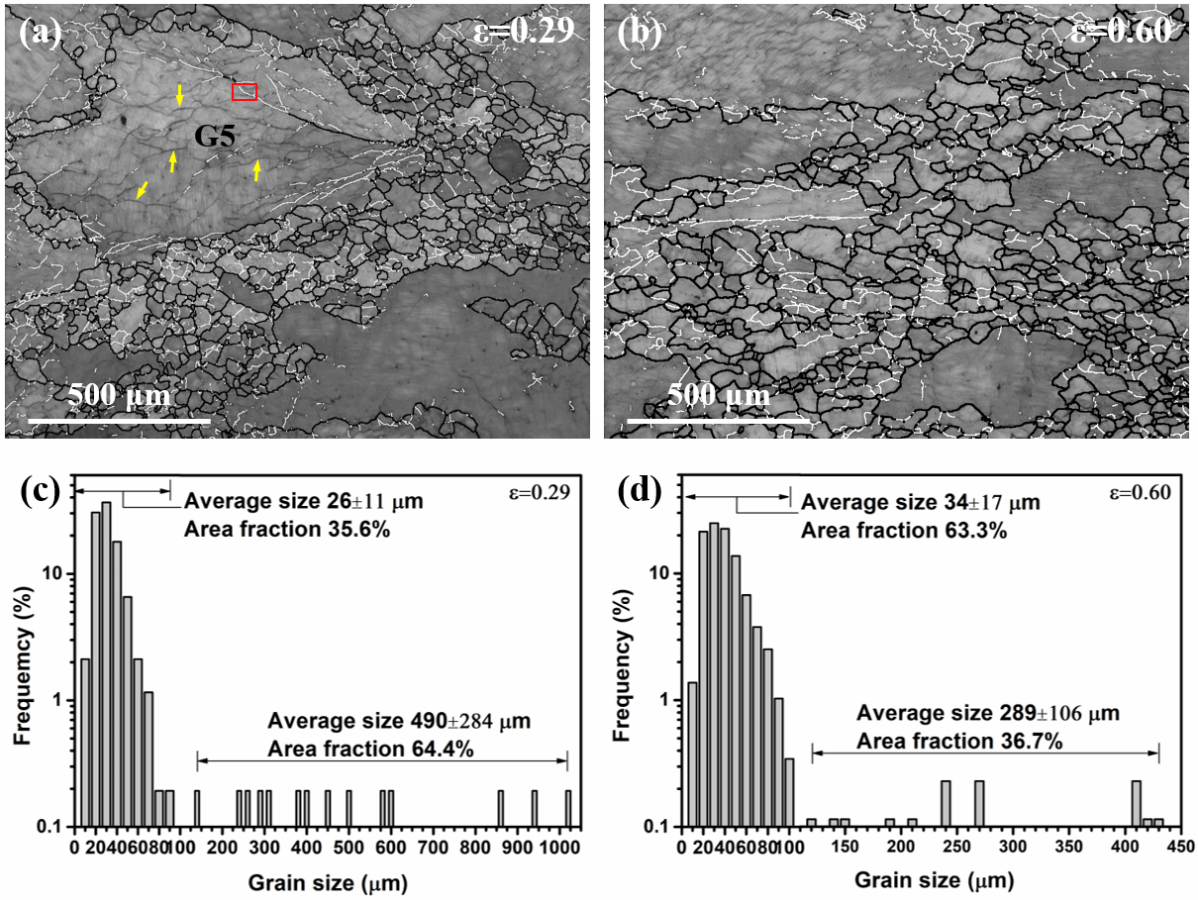


Fig. 4-5 (a) and (b) EBSD band quality indexed contrast micrographs; (c) and (d) Grain size distribution of the samples after uniaxial compression at 1280 °C under a strain rate of 0.01 $s^{-1}$ to the true strains of 0.29 ((a) and (c)) and 0.60 ((b) and (d)), respectively.

### 4.5.2.2 Crystallographic orientation dependent grain fragmentation

To investigate the difference in CDRX through grain fragmentation of different α grains, the crystallographic orientation and the orientation features of the prismatic slip systems of the

retained coarse α grains were characterized. Fig. 4-6 (a) shows the EBSD Y axis IPF micrograph of the sample deformed to the true strain of 0.29, in which the retained coarse α grains are highlighted and marked as G1~G5. The corresponding PFs and SFs of the prismatic slip systems are presented in Fig. 4-6 (b). The SFs are calculated based on the Euler angles obtained at the pixel of each grain center. It should be pointed out that at this stage the deformation behavior of crystals can be affected by local stress, but for these retained coarse grains the macroscopic stress is still the main factor and their deformation behavior can be evaluated by the Schmid law. As seen in Fig. 4-6 (b), grains G1~G4 show so low SFs ($|m|<0.3$) that the prismatic slip systems were not massively active, thus these α grains are retained due to the limited or rare dislocation accumulation for CDRX. Especially, for grain G1 (in red) with the crystallographic orientation of the <0001> direction nearly parallel to LD, all the three $\{1\bar{1}00\}$ plane are parallel to the LD and the SFs of the prismatic systems are close to 0. It belongs to the hardest grains. However, unexpectedly, grain G5 (in green) possesses two independent prismatic slip systems with relatively high SFs, but it is also retained with relatively coarse grain size. The same situation can be found in the sample with the true strain of 0.60 where the retained coarse α grains and the corresponding PFs are highlighted in Fig. 4-7. It can be noticed that, in addition to the hardest α grains in red color, the green α grains are also hard (Fig. 4-7 (a)). The PFs in Fig. 4-6 (b) and Fig. 4-7 (b) reveal that the retained green α grains like G5 exhibit the special crystallographic orientation with $<11\bar{2}0>$//LD (one of the $\{1\bar{1}00\}$ planes nearly parallel to LD). These results show that the crystallographic orientations of the α grains are responsible for the difference in grain fragmentation tendency. The orientations of the retained coarse α grains that exhibited a relatively slow fragmentation tendency can be categorized into two types:

(i) Grains with <0001>//LD (all the three $\{1\bar{1}00\}$ planes are parallel to the LD), colored in red in the IPF micrographs;

(ii) Grains with $<11\bar{2}0>$//LD (one of the $\{1\bar{1}00\}$ planes nearly parallel to LD), colored in green in the IPF micrographs.

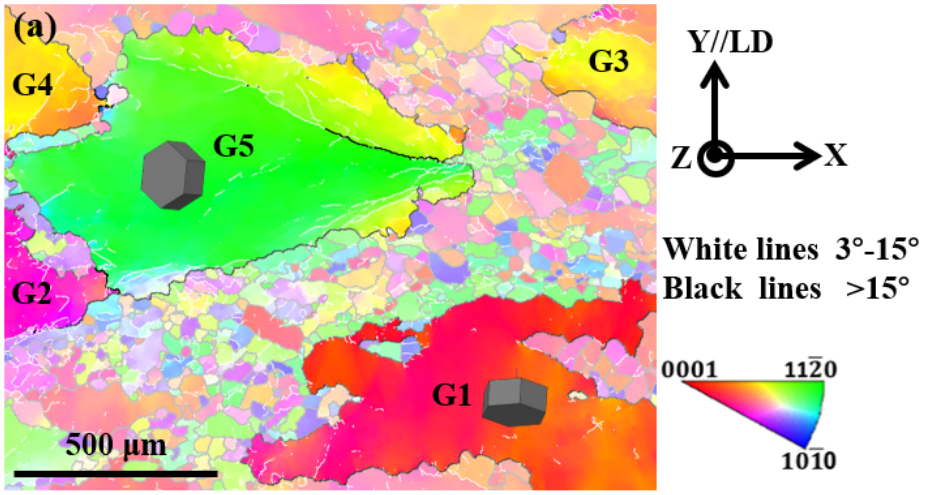


| (b) Euler angle | SF | PFs |
|---|---|---|
| G1 (173.9, 111.4, 7.1) | $m_1$=-0.0684<br>$m_2$=-0.0163<br>$m_3$=-0.0521 | |
| G2 (148.5, 64.2, 24.5) | $m_1$=-0.1783<br>$m_2$=-0.1774<br>$m_3$=-0.0008 | |
| G3 (48.9, 94.7, 30.7) | $m_1$=-0.2674<br>$m_2$=-0.0475<br>$m_3$=-0.2200 | |
| G4 (137.9, 73.4, 8.5) | $m_1$=-0.1950<br>$m_2$=-0.0340<br>$m_3$=-0.2291 | |
| G5 (78.5, 137.2, 24.2) | $m_1$=-0.4462<br>$m_2$=-0.0460<br>$m_3$=-0.4002 | |

Fig. 4-6 (a) EBSD Y axis IPF micrograph of the deformed sample with the true strain of 0.29. (b) PFs of the retained coarse α grain G1-G5 in (a), and the corresponding Schmid Factors of the prismatic slips calculated from the Euler angles of the pixel at grain center.

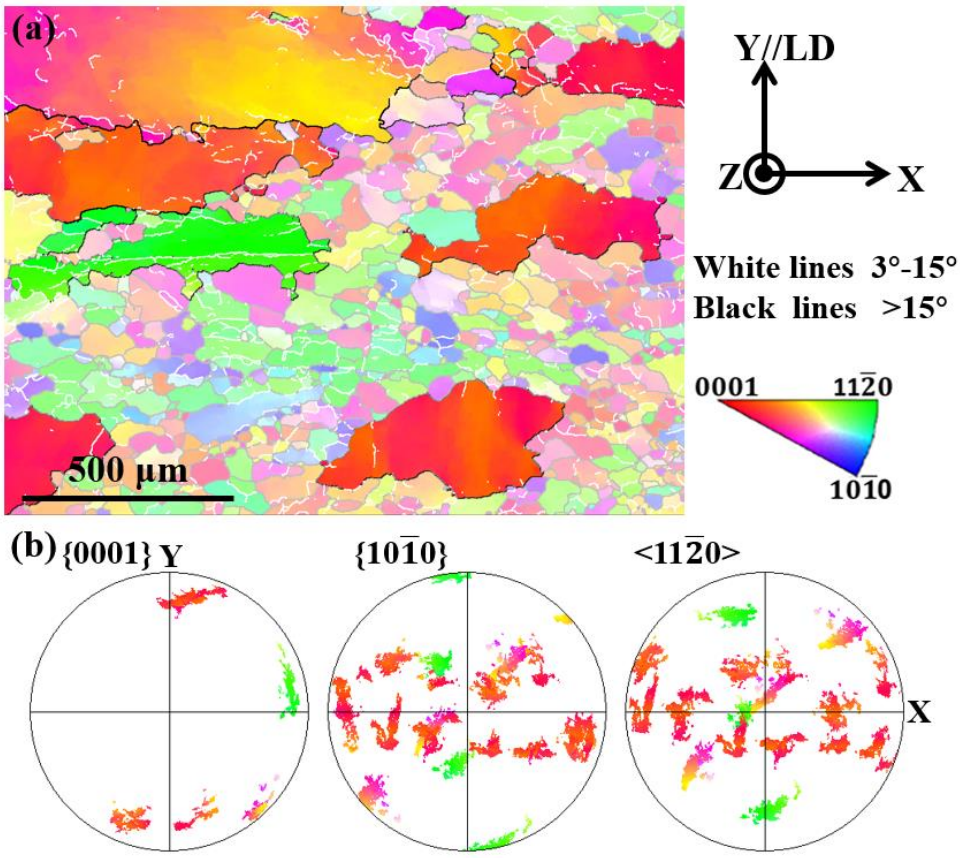


Fig. 4-7 (a) EBSD Y axis IPF micrograph of the deformed sample with the true strain of 0.60 with the highlighted coarse α grains; (b) PFs of the retained coarse α grains in (a).

(i) Grains with <0001>//LD.

It is easy to understand why CDRX proceed very slowly for the α grains with <0001>//LD. In terms of the macro external stress, the Schmid factors of all the prismatic slip variants are equal to 0. Even the Schmid factors of the basal slips are also equal to 0. Only the pyramidal slip has relatively high Schmid factors but it possesses the highest critical resolved shear stress (CRSS). Thus, it is very difficult for dislocations to generate in this kind of α grains by macro external stress. Due to the potential lack of the available slip systems, incompatible deformation with the neighbor grains may give rise to the local stress concentration near grain boundaries. As the direction of these local stresses are different from that of the macro external stress, some dislocation slip systems can be activated. In addition, because of strain accommodation between the neighboring α grains, grain rotation could happen for these hard α grains, as shown by the PFs of G1 in Fig. 4-6 and the PFs of the red grains in Fig. 4-7 (b). It can be noticed that the <0001> direction of the retained coarse α grains are deviating from the LD with the increase of

the true strain. The crystallographic orientation change by grain rotation can assist dislocation activation and multiplication. It should be pointed out that the local stress induced by the neighboring α grains are much lower than the macro external stress, thus the α grains with <0001>//LD process relatively low dislocation density. As the Kernel average misorientation (KAM) micrograph displayed in Table 4-1, under the same true strain, the grain with <0001>//LD processes the lowest disorientation, and the disorientations are just distributed near the grain boundaries. Besides, this grain also has the smallest average disorientation angle (4.49°), and the maximum disorientation angle can only reach 12.55°. Thus, there is not any segments of high-angle boundary that can be detected in grain G1. Due to the lack of enough dislocations, this kind of α grains are the last ones to complete the CDRX. As seen in Fig. 4-7 (a), the retained coarse α grains are mainly this kind of grains when deformed to ε=0.60. This means that at such a large true strain, dislocation accumulation, i.e., work hardening, is still in progress in this kind of α grains.

(ii) Grains with <11$\bar{2}$0>//LD.

As for the α grains with <11$\bar{2}$0>//LD the Schmid factor of one prismatic slip system is equal to 0, while the Schmid factors of the other two are equal with relatively high absolute values. As illustrated in Fig. 4-8 (a), the two prismatic slip variants and the corresponding Schmid factors are:

$$S_1\text{: } (\bar{1}100)[\bar{1}\bar{1}20] \; or \; (1\bar{1}00)[11\bar{2}0], \;\; m = -0.43;$$

$$S_2\text{: } (01\bar{1}0)[2\bar{1}\bar{1}0] \; or \; (0\bar{1}10)[\bar{2}110], \;\; m = -0.43.$$

It is generally accepted that the activity of slip system $S$ rotates the crystalline lattice around the axis $T_S||(b \times n)_S$ (the Taylor axis), in which $b$ denotes the Burgers vector, and $n$ is the slip plane normal vector [171]. By using this rotation-axis equation, it is therefore deduced that these two slip systems tend to rotate the crystalline lattice in opposite directions, i.e., $T_1 = [000\bar{1}]$ and $T_2 = [0001]$. Due to such a characteristic feature, the deformation induced by these two slip systems was cancelled out, and the macroscopic deformation cannot be achieved just by these prismatic slip systems.

Table 4-1 Comparison of DRX progress for the α grains with different original crystallographic orientations in the deformed sample with the true strain of 0.29 based on KAM micrographs and the statistics of disorientation angle distribution.

| Original grains | IPF<br>White lines 3°-15°<br>Black lines >15°<br>0001 11$\bar{2}$0 1$\bar{0}$10 | KAM<br>0° 5° | Disorientation angle distribution |
|---|---|---|---|
| (i)<br><0001>//LD | 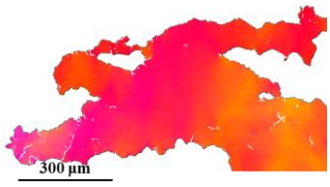 | 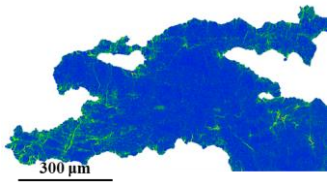 | 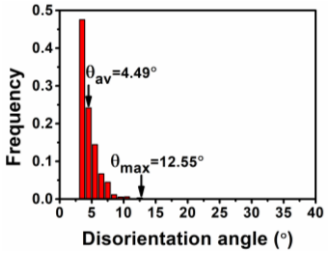 |
| (ii)<br>⟨11$\bar{2}$0⟩//LD | 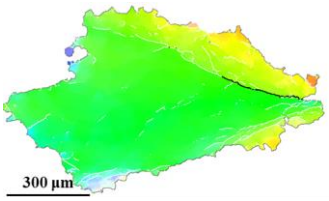 | 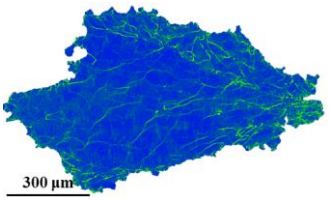 | 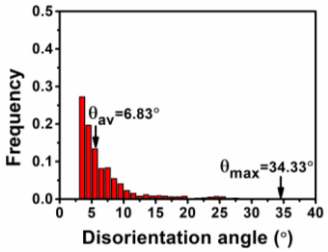 |
| (iii)<br>Soft grain | 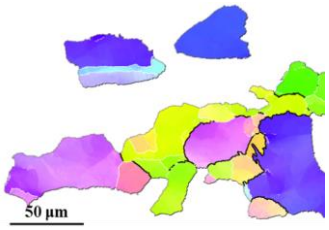 | 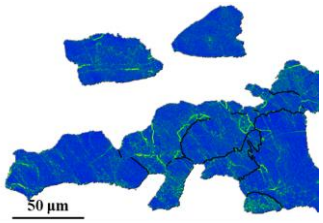 | 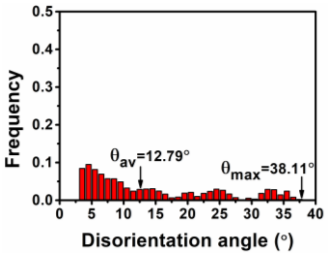 |

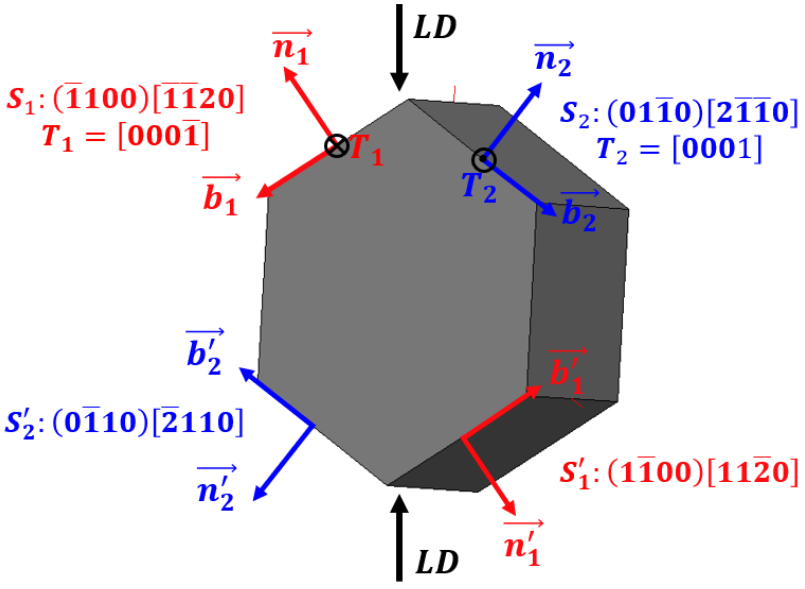


Fig. 4-8 The active prismatic slip systems in the α grain with ⟨11$\bar{2}$0⟩//LD.

From the EBSD band quality indexed contrast micrograph in Fig. 4-5 (a), it can be seen that some obvious intragranular traces indicated by the yellow arrows appear in this kind of α grain interior, as the case in grain G5 (with $<11\bar{2}0>_{\alpha}$//LD). To characterize this feature in detail, a local area (marked with the red rectangle) containing the intragranular traces in Fig. 4-5 (a) is further represented with the magnified BSE micrograph in Fig. 4-9 (a). It can be seen that the intragranular traces noted by the yellow arrows actually correspond to the intragranular boundaries. Besides, the straight line-shaped dark contrast (highlighted by the dashed black lines) can be clearly seen. These straight lines correspond to the traces of the interfaces of the γ lamellae with the parent α phase that were formed during the cooling process after the deformation. Under the Blackburn OR ($\{111\}_{\gamma}//(0001)_{\alpha}$, $<1\bar{1}0>_{\gamma}//<11\bar{2}0>_{\alpha}$) of the α to γ transformation, the α/γ interface is always in perfect coincidence with the basal plane $(0001)_{\alpha}$ of the α phase. Thus, the orientation variation of the α/γ interfaces allows to identify the lattice rotation of the α grain during the deformation. From Fig. 4-9 (a), one can see the abrupt kinks of the $(0001)_{\alpha}$ planes at the intragranular boundaries, as indicated by the yellow arrows. The formation of these intragranular boundaries (low-angle boundaries) should be the result of dislocation polygonalization from the deformation. The kinks of the $\{0001\}_{\alpha}$ planes indicates that the deformation represented by the kink of the $\{0001\}_{\alpha}$ planes was not caused by the prismatic slip, as the lattice rotation induced by the prismatic slip is around the axis of $<0001>_{\alpha}$ that is perpendicular to the $\{0001\}_{\alpha}$ planes and will not change the orientation of the $\{0001\}_{\alpha}$ planes. This result indirectly verifies our above hypothesis that in the α grains with $<11\bar{2}0>$//LD although they possess two favourably oriented prismatic systems, the deformation that contribute to the macroscopic strain is by a different mechanism.

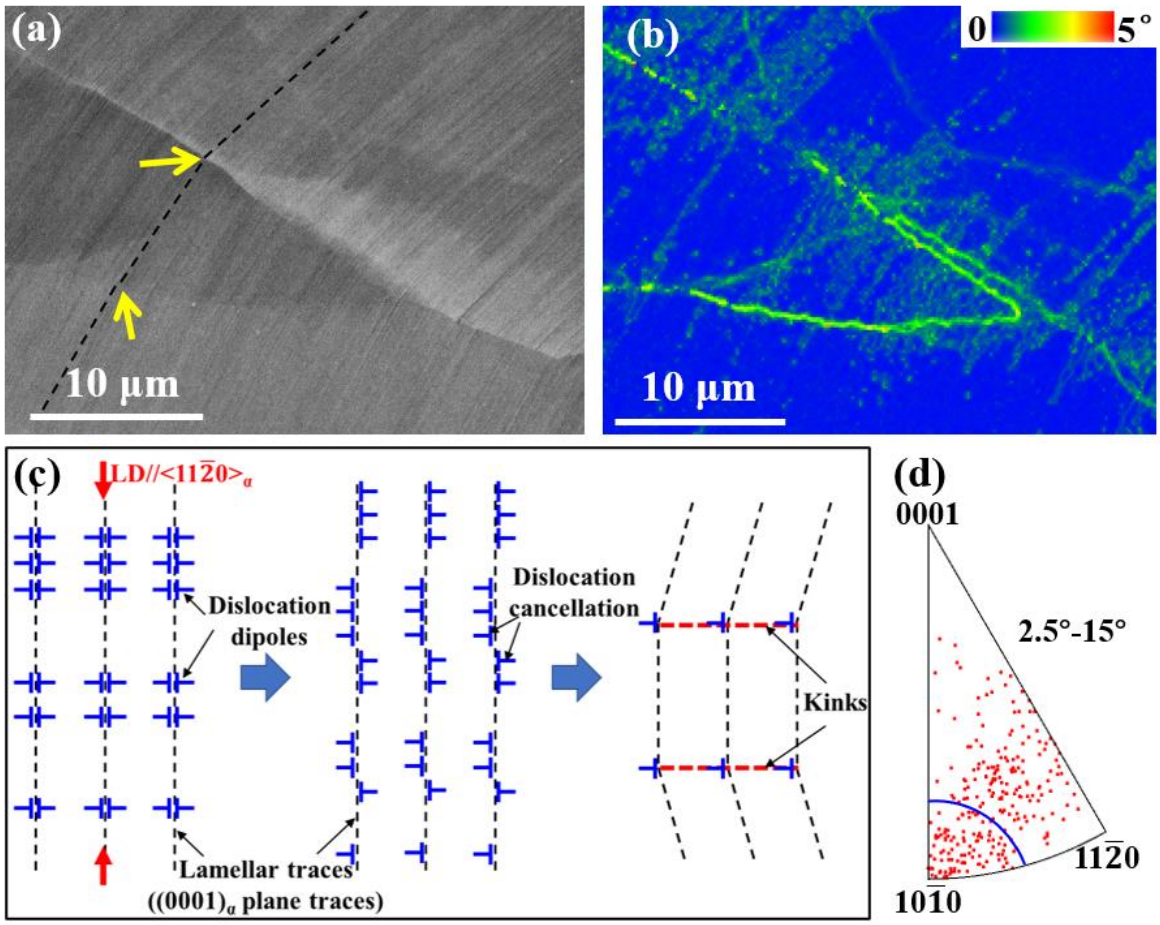


Fig. 4-9 (a) SEM-BSE micrograph of the magnified local areas outlined with red rectangle in G5 orientated with nearly <11$\bar{2}$0>$_\alpha$//LD in Fig. 4-5 (a); (b) Kernel Average Misorientation (KAM) micrograph; (c) Schematic diagram illustrating the formation of kinks; (d) Disorientation axis projection.

To reveal this different deformation mechanism, the internal disorientation distribution was further analyzed and displayed with the KAM micrograph in Fig. 4-9 (b). Indeed, the disorientations are mainly located at the intragranular boundaries. Such abrupt orientation change at the intragranular boundaries suggests that the deformation of the <11$\bar{2}$0>//LD grains may be realized by kinking, as frequently observed in the deformed hexagonal-structured materials [124,125,133,136,169,183–187]. Deformation kinking in metallic materials was first recognized by Orowan [184] in cadmium. It demonstrated that if a crystal with its slip plane parallel or nearly parallel to the compression axis, it could collapse by forming peculiar kinks with sharp ridges. Such morphological ridges correspond to the sudden orientation change of the crystal that separates the kinked part from the unkinked part. The ridges are in fact the kink

boundaries. In the present situation, the obvious intragranular boundaries resemble the kink boundaries, marking the abrupt orientation change of the deformed crystal. This suggests that the deformation in the α grains with <11$\bar{2}$0>//LD is by kinking. It is commonly accepted that the deformation kink boundaries are walls of edge dislocations aligned perpendicular to the slip plane. However, for the kink initiation mechanism there are several different models [183,188,189], among which the model [169,183] stating that the initial plastic flow in kink formation begins with the generation of dislocation pairs having opposite signs is more pertinent to the kinking of single phased metallic materials. For the α grains with <11$\bar{2}$0>//LD, their {0001} basal slip systems (the second easy slip systems) are parallel to the LD, thus the basal slip system is in the ideal orientation for kinking. The dislocation dipoles on the {0001} planes with Burgers vector in <11$\bar{2}$0>//LD direction, as illustrated in Fig. 4-9 (c), could be developed by lattice misfits. During the dislocation movement, the cancellation of the positive dislocations from one part of the crystal with the negative ones from the neighboring part could happen. As the positive ones and the negative ones do not possess equal quantities, some dislocations are retained (the middle figure in Fig. 4-9 (c)). The retained dislocations in different layers of the slip planes tend to arrange into planar arrays to accommodate the local flexure, leading to the formation of kinks (the figure on the right in Fig. 4-9 (c)). The disorientation axis projection of this area is displayed in Fig. 4-9 (d). It can be noticed that most of the disorientation axes are located near the <10$\bar{1}$0> axis which is the Talyor axis of basal slip, indicating that the kinking deformation is formed by the basal slip dislocation accumulation. Due to such dislocation activity, the basal planes $\{0001\}_{\alpha}$ are kinked. This is well revealed by the bending of the α/γ interface traces in Fig. 4-9 (a). The other disorientation axes may be developed by the coalescence of the kink boundary with the other induced incidental boundaries, as demonstrated by Hagihara et al [190]. Compained with the KAM micrograph of the whole grain G5 in Table 4-1, it can be seen clearly that although these kink boundaries are densely distributed in the grain interior, most of the disorientation angles are below 3°, especially in the center of the grain, as seen from the IPF micrograph in Table 4-1. That is because the dislocation type is single at the kink boundaries, and there are not many interactions with other type of dislocations. Only at the grain boundaries can the dislocation accumulation be assisted by the

strain accommodation with the neighboring α grains. The low-angle boundaries have been developed with relatively large disorientation angles, as seen in the IPF and KAM micrographs in Table 4-1. The average disorientation angle in this grain is 6.83°, indicating that these disorientations need to absorb large amount of dislocations to realize the subdivision of this kind of α grains. This explains why such grains are retained when the other oriented grains were largely fragmented, i.e., well in the progress of CDRX. Thus, this kind of grains can be categorized as hard grains for the deformation. Due to the existence of dislocation creation and slip, such oriented grain still demonstrated hardening contribution to the global deformation even at the global softening stage of the compression.

(iii) Soft grains.

The preferentially DRXed α grains were from the fragmentation of the initial soft α grains. As these initial grains possess favorably oriented prismatic slip systems, dislocations were easily created and accumulated, which provided sufficient amount of dislocations for rearrangement and polygonalization for the development of the subgrains. Fig. 4-10 shows the EBSD micrographs of a local area with the DRXed small α grains in the sample deformed to the true strain of 0.29. According to the lamellar traces outlined with the dotted red lines in Fig. 4-10 (a), it can be speculated that the highlighted grains are fragmented from the same original α grain by progressive subgrain rotation that is further supported by the corresponding IPF (Fig. 4-10 (b)) and the PF of the selected area (Fig. 4-10 (c)). Compared with the hard α grains, the soft α grains possess the largest average disorientation angle (12.79º), and the maximum disorientation angle can reach 38.11°, as shown in Table 4-1. Accordingly, many segments of the high-angle boundaries connected with the segments of low-angle boundaries can be seen frequently from the IPF micrograph in this area. The disorientation usually located at the low-angle boundaries (KAM micrograph), indicating that these domains are at the late stage of the CDRX before the low-angle boundaries further evolve into high-angle boundaries. Besides, it should be noted that the small blue domains D1 and D2 in Fig. 4-10 (b) are separated from the other domains by a layer of small domains fragmented from other coarse α grains. This indicates that the CRDX was followed by grain boundary sliding which served as an important deformation mechanism for the small grains to contribute to the external deformation and to

allow the mixing of the small domains. Both the CDRX and grain boundary sliding are responsible for the softening.

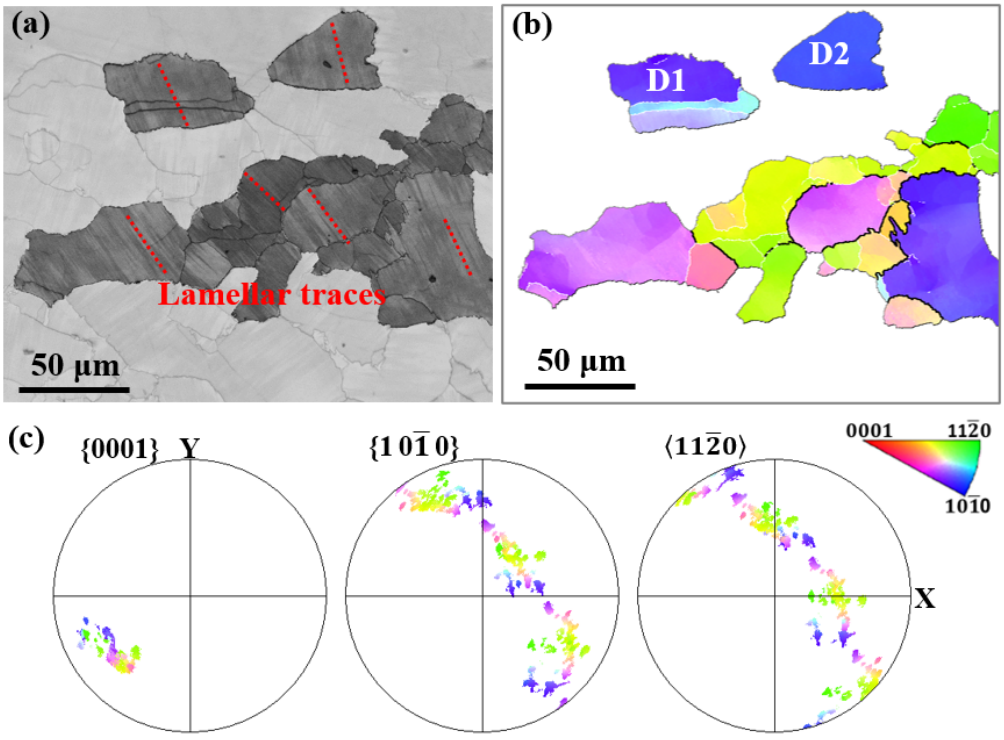


Fig. 4-10 EBSD micrographs of a local area with small α grains in the sample deformed to the true strain of 0.29. (a) EBSD band quality indexed contrast micrograph; (b) EBSD Y axis IPF of the α grains highlighted in (a); (c) the corresponding PF of the α grains in (b). The red dotted lines highlight the γ lamellar phase interfaces.

The above analyses show that the deformation mechanisms of differently oriented α grains are different, and thus the macroscopic stress–strain behavior is the mixture of their different contributions (hardening or softening). The soft grains experienced a short deformation stage and quickly entered the CDRX process. On the contrary, the hard α grains experienced a relatively long period of deformation, either by dislocation slip or by kinking. In these grains, the dislocation activation was much difficult, and the accumulation of dislocation is much slow, thus the CDRX is largely postponed. The CDRX of the initial soft α grains acts as the main softening mechanism, and the dislocation slip and kinking of the hard α grains contributed to the work hardening. The former counter-balanced the latter. With the deformation, the amount of CDRX increased very progressively due to the resistance of the hard grains. With the increase of the true strain, the hard α grains began to fragment. For the hard grains with <0001>//LD,

the local strain accommodation with neighboring α grains assisted the fragmentation in grain boundary regions. For the hard α grains with <11$\bar{2}$0>//LD, in addition to the effect of strain accommodation with the neighboring α grains, kinks were developed in grain interiors to help the subdivision of these α grains. For the already DRXed small α grains, grain boundary sliding is the main deformation mechanism. Thus, the overall effect came from the grain boundary sliding of the DRXed small α grains, the DRV and DRX of some retained hard α grains, and the intragranular deformation of the several retained hardest α grains. The respective contributions of softening or hardening of all these processes are weak and slow, resulting in a slow drop in the flow stress.

### 4.5.3 Steady stage (III)

When the true strain is increased to 1.05, the stress–strain curve is close to a steady stage. Small α grains are developed homogeneously and almost fill up the whole microstructure (Fig. 4-11 (a)). The grain size shows a normal distribution with an average size of about 45 ± 24 μm, as seen in Fig. 4-11 (b). This indicates that most of the α grains have nearly completed the CDRX. Fig. 4-11 (c) displays the EBSD Y axis IPF micrograph in which the low-angle boundaries are decorated with the white lines. It can be found that the hard α grains have not completely fragmented into small ones, such as G1 (orientated nearly with <0001>//LD) and G2 (orientated nearly with <11$\bar{2}$0>//LD) outlined with the blue lines. There still exist segments of high-angle boundaries connected with segments of low-angle boundaries. This suggests that these grains are at the late stage of the CDRX before the low-angle boundaries further evolve into high-angle boundaries. Although the CDRX has not been finished completely, the remaining portion is very small and the deformation is maintained at a constant stress level. For the already DRXed small α grains, as mentioned above, grain boundary sliding is the major deformation mechanism. In addition to this, intragranular dislocation slip started to be active, as inferred by the color variation the IPF micrograph of most α grains and their elongated morphology along the direction perpendicular to the LD, for example G3 and G4. This suggests that dislocation slip worked as another deformation mechanism in addition to grain boundary sliding. Here, the hardening induced by the intragranular dislocation slip and the softening

caused by CDRX and grain boundary sliding reach to a balance, and accordingly the flow stress stays in a steady state.

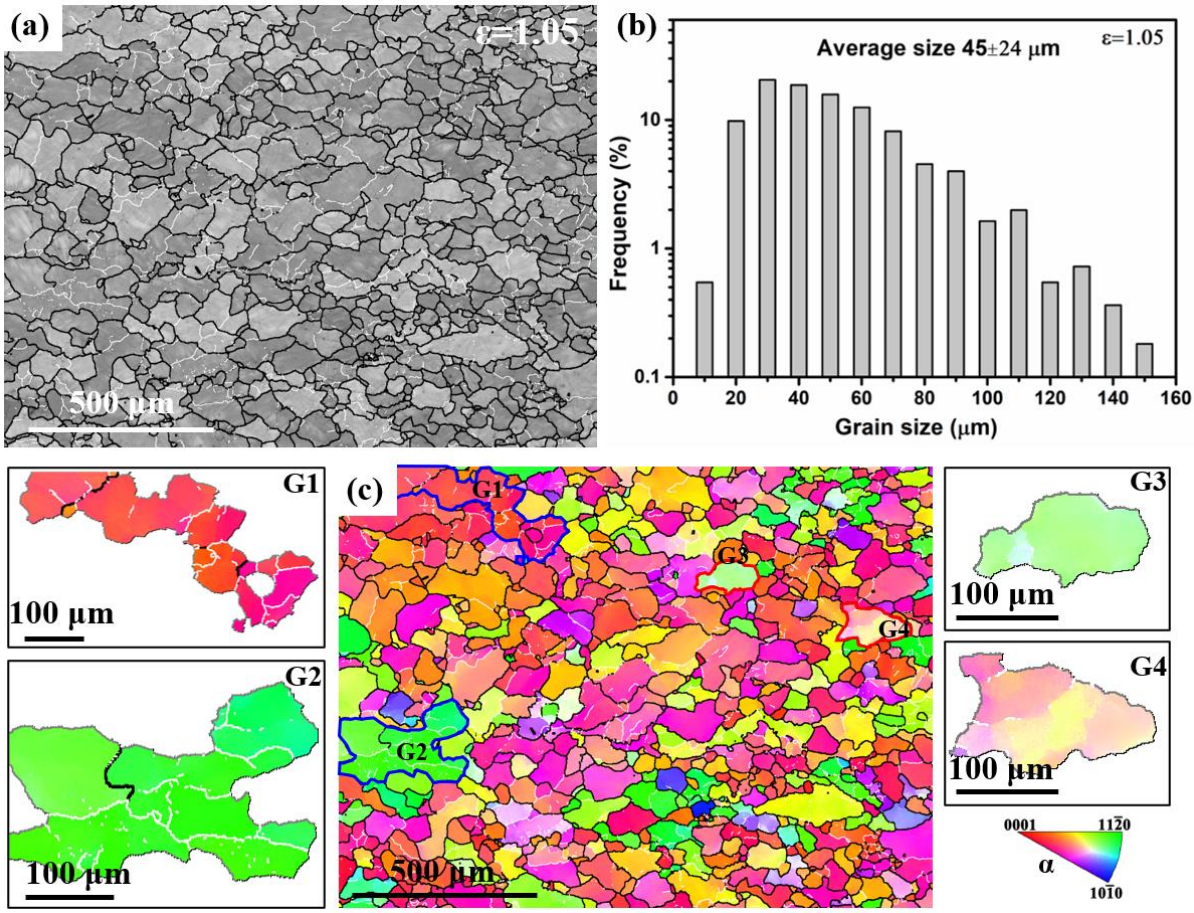


Fig. 4-11 Microstructure features of the deformed sample with the true strain of 1.05. (a) EBSD band quality indexed contrast micrograph; (b) Grain size distribution; (c) EBSD Y axis IPF micrograph with the enlarged IPF micrographs of G1-G4; (d) {0001}, {10$\bar{1}$0} and {11$\bar{2}$0} PFs calculated from two EBSD maps each with an area of 1.6 × 1.2 mm$^2$.

## 4.6 Contribution of different deformation modes to texture evolution

Fig. 4-12 present the {0002}, {10$\bar{1}$0} and {11$\bar{2}$0} PFs of the high temperature α phase in the samples with different true strains (here LD//Y). From these figures one can find the crystallographic orientation evolution during the compression process. Fig. 4-12 (a) and (b) show the pole figures of the high temperature α phase at the work hardening stage (ε=0.05 and 0.07). It can be seen that the PFs of the α phase consist of several isolated poles distributed randomly, indicating that at the work hardening stage the crystallographic orientations of the α grains still stay random. Compared with the corresponding PFs of the initial state (Fig. 4-1 (d)),

although the number of the high intensity poles are decreased, the maximum intensities is obviously increased with the increase of the true strain (Fig. 4-12 (a) and (b)). This phenomenon is related to the grain growth happening during this stage. The large observation areas are only occupied by a small number of grown α grains. Thus, the intensity distribution is mainly influenced by these large grains.

At the work softening stage (ε=0.29 and 0.60), the microstructures exhibit bimodal structure consisting of the DRXed small α grains and the retained coarse α grains, thus their grain orientations are discussed separately. Fig. 4-12 ($c_1$) and ($c_2$) show the PFs of the respective DRXed α grains and the retained coarse α grains in the sample with a true strain of 0.29. It can be seen that the DRXed α grains exhibit a random texture (Fig. 4-12 ($c_1$)), and it should be emphasized that almost all strong poles in the {0002} PF (Fig. 4-12 ($c_1$)) of the DRXed α grains are in close coincidence with the poles in the {0002} PF (Fig. 4-12 ($c_2$)) of the retained coarse α grains, as outlined by the corresponding red rectangles in Fig. 4-12 ($c_1$) and ($c_2$). That is because here the fraction of the DRXed α grains is not very high (~ 34.6 %). The DRXed α grains are just fragmented from the grain boundary regions of the original soft α grains by CDRX. Thus, the crystallographic orientations of the DRXed α grains are not far from those of the initial α grains that have not been fragmented completely. For the retained coarse α grains (Fig. 4-12 ($c_2$)), the crystallographic orientations consist of several individual poles. The weak poles are usually related to the α grains that are still in the progress of fragmentation, whereas the strong poles outlined by the red circles are from the two kinds of hard α grains, i.e., grains with nearly <0001>//LD and grains with <11$\bar{2}$0>//LD. When the true strain is increased to 0.60, the area fraction of the small DRXed α grains is increased to 63.3%, and the retained coarse α grains is only 36.7%. For the retained coarse α grains, intragranular dislocation slip is the main deformation mechanism. Thus, these grains are gradually deviated from the hard orientations, and a weak texture has been developed (Fig. 4-12 ($d_2$)), i.e., the basal plane normal was tilted about 20~35° away from the LD (the Y axis), as indicated by the black dotted curves in Fig. 4-12 ($d_1$) and ($d_2$). This tilted basal fiber texture component has been reported for α-Ti and other HCP metals with a c/a<1.63 after compressive deformation [145,191]. The tilted angle could vary with the alloy and the deformation conditions. As at the present deformation stage only a

limited number of the coarse α grains are retained, the texture does not assume a fiber form but is rather composed of several individual poles distributed along the fiber line (Fig. 4-12 ($d_2$)). This result infers that before fragmentation the retained coarse α grains should have undergone a typical orientation evolution to the basal fiber orientations induced by dislocation slip. This can be further confirmed by the texture features of the DRXed small α grains. As seen in Fig. 4-12 ($d_1$), although there are more individual high intensity poles, most of them are located nearly the tilted basal fiber line (the black dotted curves), such as those outlined by the red and blue rectangles, especially the ones in the red rectangles. These poles outlined in red can be found in the {0002} PF of the retained coarse α grains, as outlined by the corresponding red rectangles in Fig. 4-12 ($d_2$), indicating that these α grains are just fragmented from the retained coarse α grains. This texture feature of the DRXed α grains further indicate that the orientations of the DRXed α grains are largely inherited from those of their parents, especially when the fragmentation is just finished. Apart from this part, there are still some other individual poles for the DRXed α grains that are located far from the tilted basal fiber (the black dotted curves), for example the one outlined with the blue circle. Further microstructure correlation analysis shown in Fig. 4-13 demonstrated that such orientations are related to the DRXed small clusters with <11$\bar{2}$0>//LD (in green). Thus, such orientations are originated from the initial hard α grains with <11$\bar{2}$0>//LD and deformed by kinking.

Fig. 4-12 (e) shows the texture of the α phase in the sample compressed to the true strain of 1.05 corresponding to the steady stage and also the fully recrystallized state. It can be found that a partial tilted basal fiber component, i.e., the basal plane normal was tilted about 30~50º away from the LD, has been developed. This indicates most of the α grains are oriented with their basal plane normal tilted about 30-50º away from the LD. At this state, the recrystallized α grains include two parts, i.e., a minor amount of just DRXed α grains and a majority amount of previously DRXed α grains. As mentioned above, the just DRXed α grains inherited the deformation texture feature of the retained coarse α grains. Similarly, the previously formed DRXed α grains underwent plastic deformation during the subsequent deformation, which can be assessed from the microstructural features (the elongation along the direction perpendicular to the compression axis and the appearance of the low-angle boundaries) of the sample in Fig.

4-12 ($c_1$). Thus, the partial fiber corresponds to the deformation texture component under compression. It should be noted that the fiber is not complete and does not reflect the sample symmetry. The first may be due to the effect of the initial coarse grain microstructure and insufficient orientations to occupy the whole orientation space. The second may be related to the sampling position of the samples for characterization.

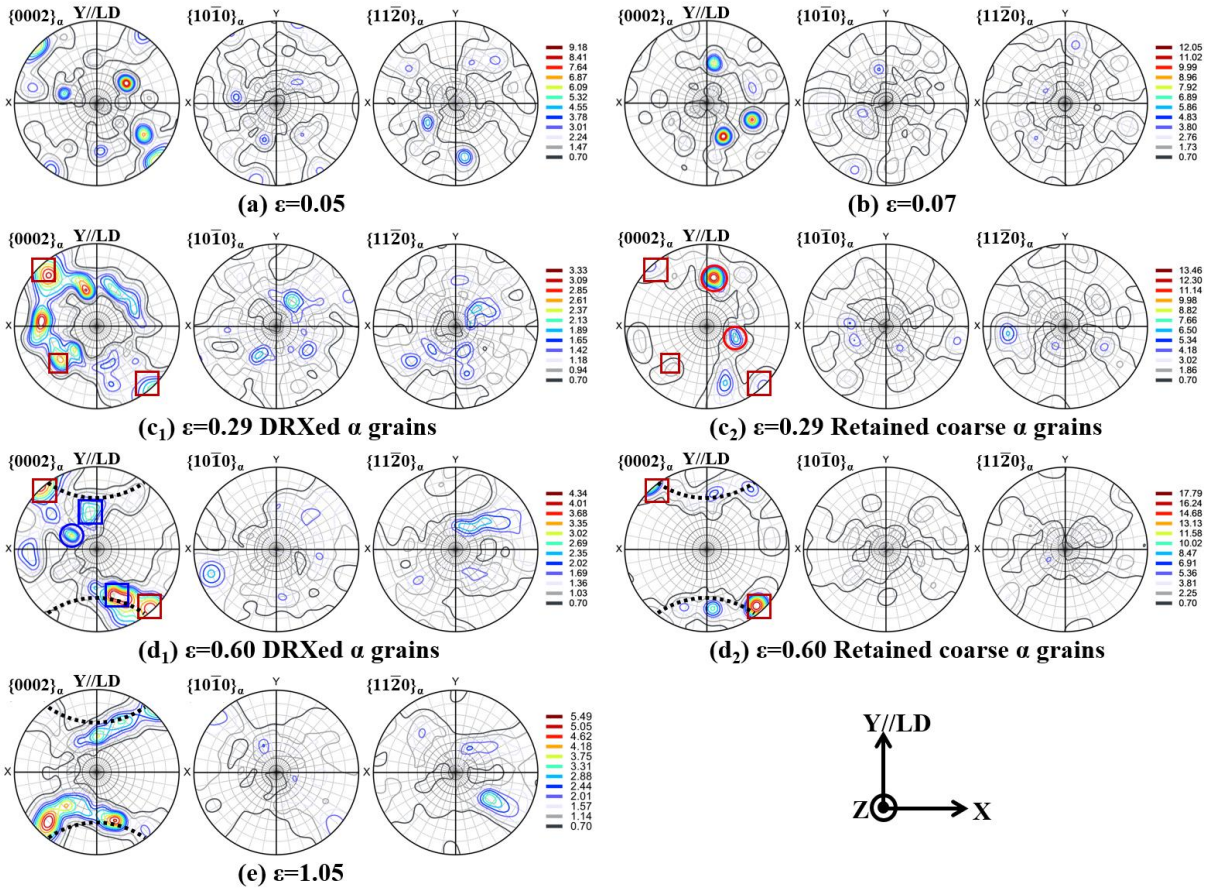


Fig. 4-12 {0002}, {10$\bar{1}$0} and {11$\bar{2}$0} PFs of the high temperature α phase in the samples with the different true strains. (a) 0.05; (b) 0.07; ($c_1$, $c_2$) 0.29; ($d_1$, $d_2$) 0.60; (e) 1.05. ($c_1$) and ($d_1$) are the PFs of the DRXed small α grains in the sample with the true strain of 0.29 and 0.60 respectively; ($c_2$) and ($d_2$) are the PFs of the retained coarse α grains in the sample with the true strain of 0.29 and 0.60 respectively. Given that the coarse grain size at the work hardening stage, the PFs in (a) and (b) are calculated from four EBSD maps each with an area of 1.6 × 1.2 $mm^2$. As for the α phase at the softening stage and steady stage, the PFs in ($c_1$; $c_2$), ($d_1$; $d_2$) and (e) are calculated from two EBSD maps each with an area of 1.6 × 1.2 $mm^2$. The black dashed lines in ($d_1$), ($d_2$) and (e) represent the texture component in other HCP metals with a $c/a$<1.63 under compression deformation.

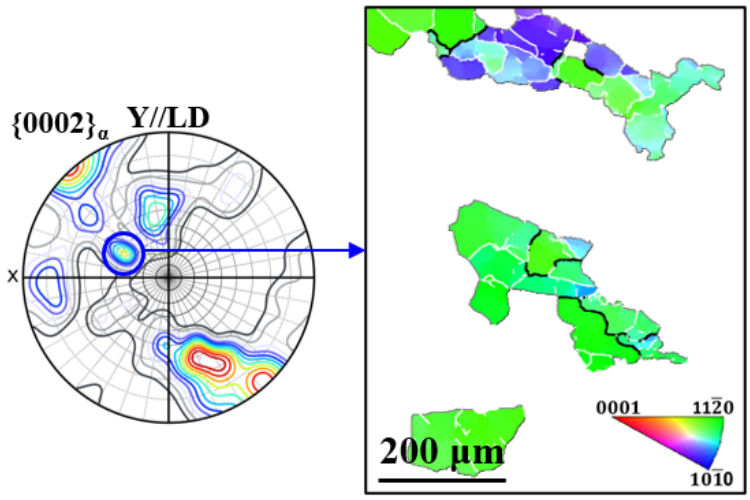


Fig. 4-13 EBSD Y axis(//LD) IPF micrograph showing the α grains corresponding to the pole outlined with blue circle in the {0002} PF of the DRXed small α grains (Fig. 4-12 ($d_1$)) in the sample with the true strain of 0.60.

The above analysis shows that due to the different deformation mechanisms induced by the anisotropy of the HCP structured α phase, it requires a relatively large true strain to accomplish the CDRX and to develop a texture through uniaxial compression in single α phase region, and then the α phase exhibits a refined grain size and a weak tilted basal fiber. Accordingly, a fully-lamellar structure can be obtained by adopting suitable cooling method after the compression deformation. Due to the specific Blackburn OR during the $\alpha \rightarrow \alpha_2+\gamma$ and the heredity in microstructure, the characteristics of the fully-lamellar structure will directly depend on the features of the α grains. As the grain size of the α grains has been refined by CDRX during the deformation, the fully-lamellar structure should possess a fine colony size. But in terms of lamellar orientation, as the α grains display a weak titled basal fiber with their $\{0001\}_\alpha$ plane normal tilted about 30~50º away from the LD, the α/γ interfaces of a part of lamellar colonies should tilt 40~60º away from the LD in the three dimensional space. In that way, the lamellar orientation of the fully-lamellar structure is relatively random. Consequently, the effect of a uniaxial compression in the single α phase region is mainly on the refinement of the colony sizes of a fully-lamellar structure when the alloy is deformed sufficiently (ε=1.05 in the present case), but through compression it is hard to control the lamellar orientation in a well-aligned manner. To achieve lamellar orientation alignment, other deformation methods should be explored.

## 4.7 Summary

In this chapter, the deformation processes of high-temperature α phase in the $TNM^{+}$ alloy under a uniaxial isothermal compression at 1280 ºC were thoroughly investigated by correlating the stress–strain behavior with the microstructure and crystallographic orientation evolution.

The plastic deformation of this alloy exhibits typical flow stress curve composed of three stages: work hardening stage (I), softening stage (II) and steady stage (III). In the work hardening stage (I), accompanying grain boundary bulging and the formation of subgrains, obvious grain growth occurred. The grain boundary bulging is related to the prismatic dislocation slip, and the coarse grain size increases the transgranular trajectories of dislocations glide. Both of them contribute to the increase of the flow stress. In the softening stage (II), the microstructure exhibits bimodal structure consisting of newly-formed small α grains and retained coarse α grains, which is attributed to the difference in deformation mechanism and CDRX progress of differently oriented α grains. It was found that there are two types of hard α grains: (i) those with <0001>//LD under which none of the prismatic and basal slip systems can be activated, thus dislocation accumulation in this α grains only can be assisted by the local strain accommodation with neighboring α grains; (ii) those with $<11\bar{2}0>$//LD, for which the two active prismatic slip systems rotate the grain in opposite directions, cancelling out the contribution to the macroscopic deformation. Dislocation accumulation in this kind of α grains is achieved by the development of kinks through basal slip and the effect of local strain accommodation with neighboring α grains. Both of these two kinds of hard α grains require relatively large true strain for dislocation accumulation and grain fragmentation. Whereas, for the soft α grains, CDRX can be completed quickly at a relatively small true strain by intragranular dislocation slip, then grain boundary sliding happened with the increase of the strain. The softening caused by the CDRX of the soft α grains became overwhelming to the hardening induced by the dislocation slip in the hard α grains, resulting in the decrease in flow stress. In the steady stage (III), small α grains (~ 45 μm) are developed homogeneously and almost fill up the whole microstructure. The α grains have nearly completed the CDRX and the grain boundary sliding is one of the mechanisms of plasticity. In many DRXed α grains,

intragranular dislocation slip can be activated and works as one kind of deformation mechanism in addition to grain boundary sliding. The hardening induced by the intragranular dislocation slip and the softening caused by CDRX and grain boundary sliding reach to a balance, and accordingly the flow stress stays in a steady state.

The deformation and CDRX behavior also affect the texture development. The crystallographic orientations of the preferentially DRXed α grains are not far from that of the original α grains and exhibit a random feature, while the retained coarse α grains mainly show the hard crystallographic orientations with <0001>//LD or <11$\bar{2}$0>//LD. With the increase of the true strain, the retained coarse α grains underwent a typical orientation evolution to the tilted basal fiber texture induced by dislocation slip. Thus, the crystallographic orientations of the just DRXed α grains are largely inherited from their parent coarse α grains. Similarly, the previously formed DRXed α grains also experienced plastic deformation by intragranular dislocation slip during the subsequent deformation process. As a result, a weak tilted basal fiber texture has been developed during the uniaxial isothermal compression, i.e., the basal plane normal was tilted about 30~50º away from the uniaxial compression axis.

The present work provides new information about the correlations between microstructure evolution, deformation behavior, and texture development of high temperature α phase in TiAl alloys under uniaxial isothermal compression, and verifies the possibility of both controlling lamellar orientation by the formation of deformation texture and grain size refinement by dynamic recrystallization (DRX) of α phase under thermomechanical processing, i.e., hot compression conducted in the α single phase region can produce refined α grains to refine the ($\alpha_2$+γ) colony size but cannot obtain an expected texture to align ($\alpha_2$+γ) lamellae.

# Chapter 5 Microstructure and texture evolution of high-temperature α phase under severe extrusion in (α+β) phase region

## 5.1 Introduction

Given that there is no α single phase region in most of the β-solidifying TiAl alloys, if deformation is supposed to be conducted above the $T_{\gamma,solv}$ the alloy is mainly composed of the high temperature α phase and limited amount of grain boundary β phase. The deformation behavior of the high-temperature α phase should be more complicated and heterogeneous as the α phase will undergo a complex process interweaving with deformation, dynamic recrystallization, grain growth, and this process will be affected by the grain boundary β phase. The hot deformation of the β-solidifying TiAl alloys in the (α+β) two phase region has seldom been addressed. Based on the investigations of the Chapter 3 and Chapter 4, it can be concluded that the completion of the dynamic recrystallization and the formation of the deformation texture of the high-temperature α phase need a much severe deformation. Here hot extrusion will be selected to provide severe deformation, and as another deformation mode to develop the texture of the high-temperature α phase. It should be mentioned that due to the narrow processing window for TiAl alloys the hot extrusion process is generally performed at high speeds in order to reduce temperature losses and avoid cracking, during which the adiabatic heating is inevitable, and as a result the thermally-induced phase transformation probably happens during the hot-extrusion process. In this chapter, a thorough investigation on microstructure and texture evolution of the high temperature α phase in the TNM alloy during the practical extrusion processing at the (α+β) phase region will be conducted. The effort is going towards investigating the contribution of the deformation mode and the β phase on the development of the microstructure and texture of the high temperature α phase. Special attentions will also be paid to the thermally-induced α → β phase transformation interweaving with the abnormal α grain growth.

## 5.2 Experimental process

In this chapter, the used material is the TNM alloy. The hot extrusion experiment was carried out for the TNM alloy at 1290 ℃ with the extrusion ratio of 7.11. The detailed information on the preparation of TNM ingots and the hot extrusion experiment are given in Section 2.2.2 (Page 31). The samples for microstructure examination were cut from the center of the extruded rod, as illustrated in Fig. 5-1. The microstructural and crystallographic features were investigated by SEM-EBSD and TEM. The bulk texture was measured by X-ray synchrotron diffraction. The detailed information is given in Section 2.4 (Page 34).

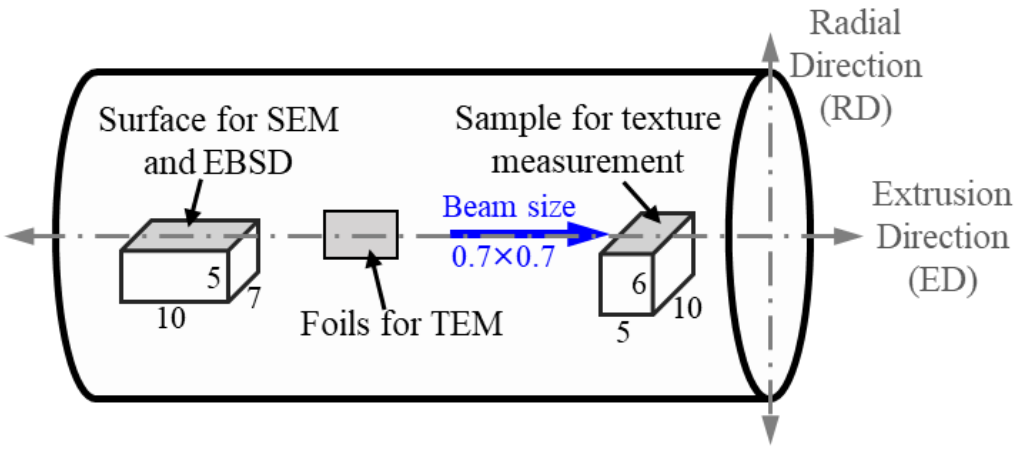


Fig. 5-1 Positions of the samples for microstructural observation and texture measurement in the extruded rod. The extrusion direction (ED) and radial direction (RD) constitute the coordinate system of samples for texture measurement and EBSD observation. Dimensions indicated in the figure are in mm.

## 5.3 Initial microstructure and texture

Fig. 5-2 shows the BSE micrograph of the initial microstructure before extrusion, i.e., isothermally held at 1290 ℃ for 20 min and then water quenched. It is seen that the microstructure consists of α grains (dark grey) with a small amount of residual β phase (~ 6 vol.%) (light grey). The α grains exhibit the typical lath-like morphology [192] with an average grain size around 62 μm. The β phase is in small blocks mainly distributed along the α grain boundaries.

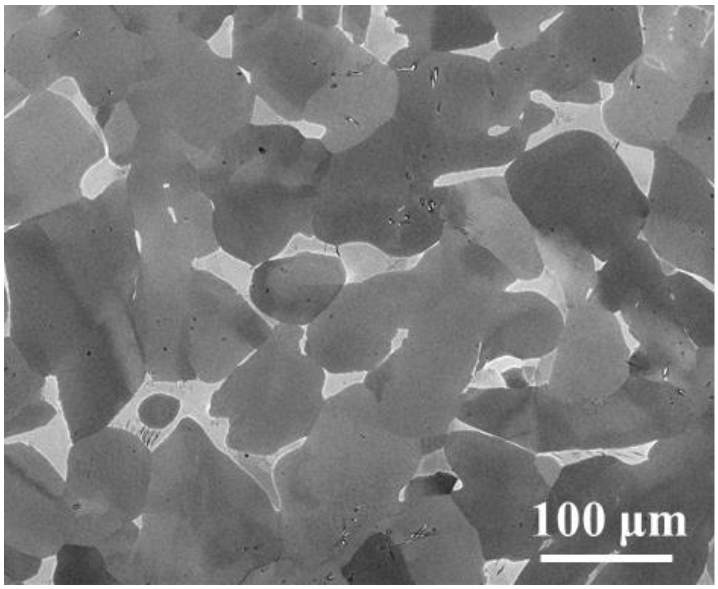


Fig. 5-2 SEM Backscattered electron (BSE) micrograph of initial microstructure (1290 ºC/20 min/WQ).

The EBSD inverse pole figure (IPF) micrographs of the β phase and α phase are given in Fig. 5-3 (a) and (b), respectively. The orientation examination shows that most of the β blocks obey the Burgers orientation relationship (OR) with their neighboring α grains, i.e., $(0001)_\alpha//(110)_\beta$, $<11\bar{2}0>_\alpha//<1\bar{1}1>_\beta$. This indicates that the α grains are formed by the β → α phase transformation, and the β blocks are retained from the transformation. Fig. 5-3 (c) and (d) show the EBSD pole figures (PFs) of the β and the α phase. To achieve a global representation of the texture, three EBSD maps each with an area of 1.28 × 0.94 $mm^2$ were used. It is seen that the PFs of the β phase (Fig. 5-3 (c)) are characterized by some individual poles, which are related to the coarse prior β grains at high temperature. One example of an initial coarse β grain is delineated by the red line (within which the crystallographic orientations of the β domains are the same) in Fig. 5-3 (a). The PFs of the α phase in Fig. 5-3 (d) represent the similar features, i.e., composed of individual orientations but with further orientation diversification. The isolated maxima outlined with the red cycles in the $(0001)_\alpha$ PF (Fig. 5-3 (d)) show excellent coincidence with those in the $(110)_\beta$ PF (Fig. 5-3 (c)), which resulted from the Burgers OR existing between the neighboring β and α phases. It should be noted that 12 α orientation variants can be obtained from one parent β grain according to the Burgers OR. This is the reason why the orientations of the α grains in the initial microstructure are further diversified.

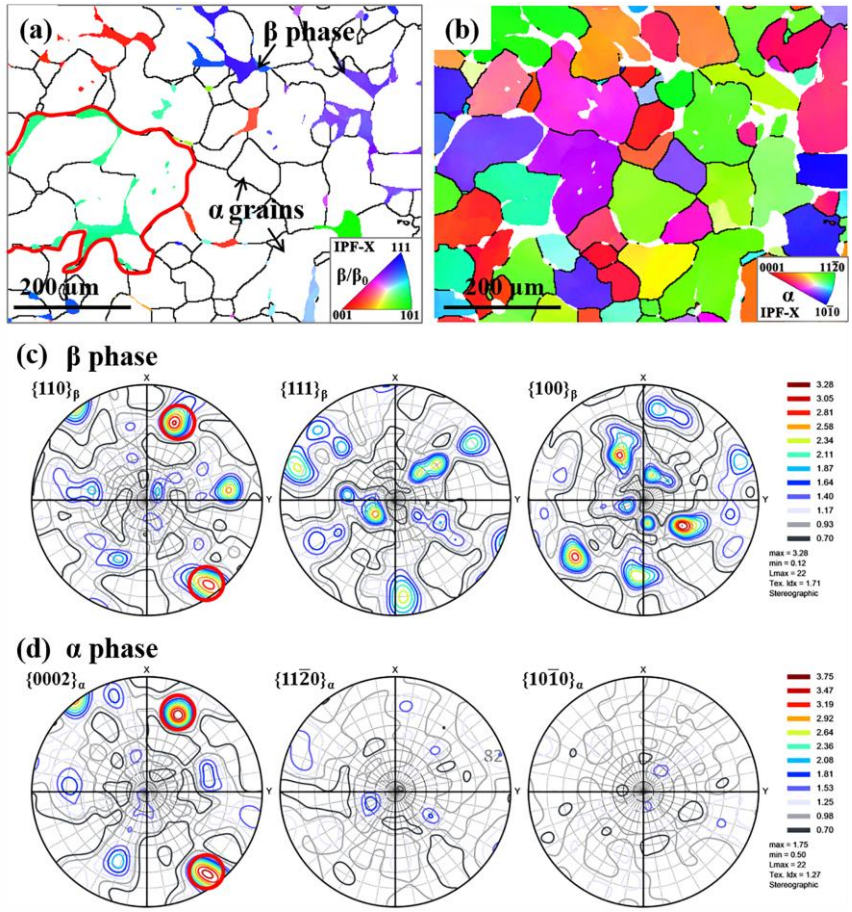


Fig. 5-3 EBSD micrographs of the initial microstructure and corresponding pole figures. (a, b) X axis inverse pole figure (IPF) micrographs of (a) β phase (in which α grains are in white and outlined with high angle grain boundaries in black) and of (b) high-temperature α phase (in which β blocks are in white); (c, d) Pole figures (PFs) of (c) β phase and (d) α phase, where the coincident $\{110\}_\beta$ and $\{0001\}_\alpha$ are outlined in red circles.

## 5.4 Microstructure and texture in extruded sample

### 5.4.1 Microstructural morphology

Fig. 5-4 (a) shows the SEM-BSE micrograph of the extruded sample. It can be seen that the deformed microstructure is still composed of α phase that is in a majority amount and β phase that is in a minor amount (~ 6.4 vol.%), however, the morphologies of the two phases change greatly. The original grain boundary (GB) β phase is elongated along the ED and presents as long-strips, framing the α grains in between. To clearly visualize the morphology of the α grains, the corresponding EBSD micrograph in which α phase is represented with band quality indexed contrast is displayed in Fig. 5-4 (b). One can find that the α grains evolve into

the so-called bimodal microstructure, some coarsened and others refined. As shown by the α grain size distribution presented in Fig. 5-4 (c), the grain size has a very wide distribution ranging from 5 μm to 160 μm. The shapes of the coarse grains become irregular with certain significantly elongated in ED, as indicated with the yellow arrows in Fig. 5-4 (b). The refined grains always tend to agglomerate in clusters and become bands of gains distributed along the ED. It should be mentioned that although the grain size is not uniform, the average grain size of the α phase has largely decreased after extrusion, i.e., from 62 μm in the initial microstructure to 16 μm in the current state. This indicates that recrystallization happened for the α phase but with varied progresses. As for the β phase, other than the β strips, some tiny white particles which are supposed to be the β phase according to the similar contrast to that of the β strips, appear in some α grains, especially in the grown ones, as pointed out by the black arrows in Fig. 5-4 (a). Due to their small sizes, the particles are rarely detected by the EBSD measurement and thus are not present in the EBSD micrograph (Fig. 5-4 (b)). The tiny white particles will be further identified by high resolution EBSD and TEM, and its formation mechanism will be analyzed and discussed in Section 5.6 (Page 103).

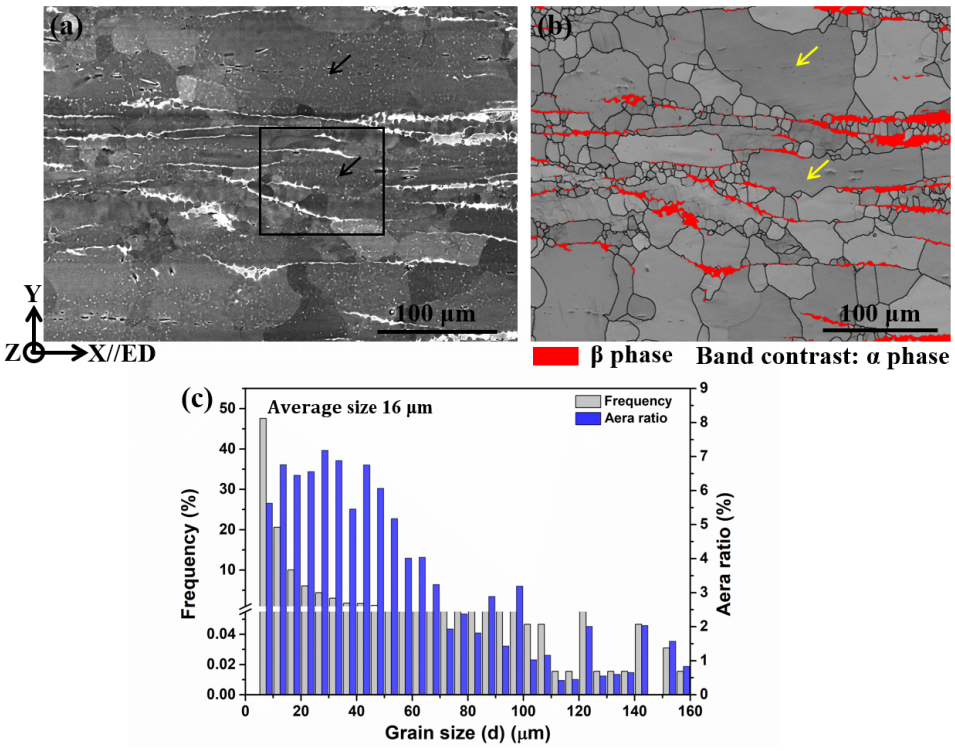


Fig. 5-4 (a) SEM-BSE micrograph and (b) the corresponding EBSD micrograph (in which α phase is represented with band quality indexed contrast and β in red) of the extruded sample with the extrusion ratio of 7.11. (c) α grain size distribution according to number frequency and area ratio.

### 5.4.2 Texture features

The macro-texture of the α phase after extrusion has been measured by synchrotron diffraction and illustrated by the $\{0002\}_\alpha$, $\{11\bar{2}0\}_\alpha$, and $\{10\bar{1}0\}_\alpha$ pole figures in Fig. 5-5 (a). It can be seen that after extrusion the initial texture changes to the basal fiber texture {0001}//ED containing a principal texture component of $<10\bar{1}0>$//ED and a weak texture component of $<11\bar{2}0>$//ED. It has been revealed in other hexagonal metals and alloys that the $<10\bar{1}0>$//ED texture component is associated with the deformed microstructure and also with the primary recrystallized microstructure because there are not big texture changes during primary recrystallization [143,155,193–196], consequently the deformed microstructure cannot be separated from the primary recrystallized microstructure on the simple criterion of texture. The $<11\bar{2}0>$//ED texture component results from the secondary recrystallization, i.e., the abnormal growth of the recrystallized (RXed) grains [148]. This means that the deformed/RXed α grains will be the main microstructure constituent in the extruded sample. The texture of the β phase is illustrated by $\{100\}_\beta$, $\{110\}_\beta$ and $\{111\}_\beta$ pole figures in Fig. 5-5 (b). It can be seen that the <110>//ED fiber is developed in the extruded sample. In addition, it should be mentioned that the Burgers OR between the α phase and the β phase detected in the initial microstructure has been destroyed, which is seen clearly through the loss of the coincidences of the $\{0002\}_\alpha$ poles in Fig. 5-5 (a) with respect to the $\{110\}_\beta$ poles in Fig. 5-5 (b).

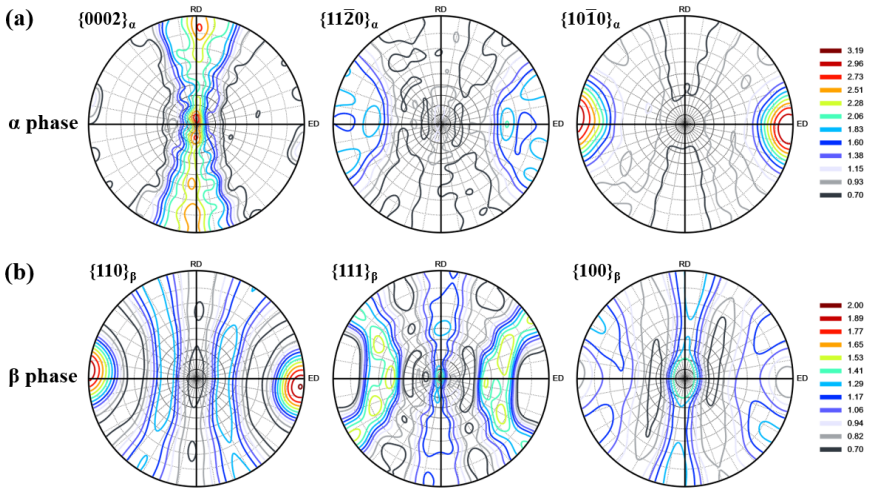


Fig. 5-5 Representative pole figures of (a) the α phase and (b) the β phase in the extruded sample with the extrusion ratio of E7.11. All pole figures were recalculated from the results obtained by X-ray synchrotron diffraction.

The above analysis shows that after the severe extrusion in (α+β) phase region, the α grains in the extruded microstructure exhibit a wide grain size distribution and a basal fiber texture. Although the grain size of α grains is not uniform (with a range of 5~160 μm), the average grain size is refined by the recrystallization process. Meanwhile, the developed basal fiber texture is beneficial for lamella alignment during the $\alpha \rightarrow \alpha_2+\gamma$ transformation. Thus, it can be deduced that hot extrusion conducted above the $T_{\gamma,solv}$ could be a suitable method to modify the high-temperature α phase and then optimize the ($\alpha_2+\gamma$) lamellar structure. To obtain a homogenous microstructure, it is necessary to investigate the recrystallization process of the α phase and its related microstructure evolution during the current extrusion process.

## 5.5 Recrystallization progress of α phase and microstructure heterogeneity

### 5.5.1 Correlation between microstructure heterogeneity and texture components

Fig. 5-6 (a) shows the EBSD IPF (ED-axis) micrographs, where the α grains with $<11\bar{2}0>$//ED are colored in green and those with $<10\bar{1}0>$//ED in blue. Consistent with the macro-texture measured by synchrotron diffraction (Fig. 5-5), most of the α grains in the extruded sample are oriented with $<10\bar{1}0>$//ED, i.e., in blue according to the color legend (Fig. 5-6 (a)). As expected, remarkable differences in intragranular substructures of the two texture components are emerged, i.e., frequent appearances of intragranular low-angle boundaries in the $<10\bar{1}0>$-oriented α grains but none in the $<11\bar{2}0>$-oriented α grains, indicating that the progress of recrystallization for the two components are different. It should be noted that there existed a transfer time from end-extrusion to quenching which is equivalent to a short-term annealing. Thus, the observed microstructure actually should have experienced a hot deformation process plus a short-term annealing process. Both the dynamic recrystallization (DRX) and static recrystallization (SRX) happened.

To further reveal the differences in recrystallization progress in the texture components, the unRXed α grains colored in yellow are separated from the RXed α grains colored in blue

on the criterion of grain average misorientation (GAM [197]. For a grain *i* with the number of pixels *J(i)*, $\mathrm{GAM}(i) = \left[\frac{1}{J(i)}\right] \sum_j \mathrm{KAM}(j)$. KAM is the Kernel average misorientation given for a pixel *j*, $\mathrm{KAM}(j) = \left[\frac{1}{K}\right] \sum_k \omega_{jk}$, where *K* is the number of pixels around the pixel number *j* (8 in our case) and $\omega_{jk}$ the misorientation angle between pixel couples (*j, k*)), as shown in Fig. 5-6 (b). If the GAM angle in a grain exceeds the defined minimum angle ($\theta_c$=0.8º) to define a subgrain, the grain is classified as being unRXed. Then, the unRXed α grains are extracted and shown with the IPF micrograph and their orientations are displayed in PFs in Fig. 5-6 (c). It can be seen that all the unRXed α grains are blue in the IPF map, and they possess a pure <10$\bar{1}$0>//ED fiber texture, which is consistent with the results found in other hexagonal materials under extrusion deformation [193–196,198]. However, the IPF micrograph and the corresponding PFs of the RXed α grains in Fig. 5-6 (d) suggest that both the <10$\bar{1}$0>-oriented α grains and the <11$\bar{2}$0>-oriented α grains co-exist. Here, the RXed α grains exhibit severe grain size heterogeneity. According to the IPF in Fig. 5-6 (d), one can also notice that the preferred growth happened to some specific RXed α grains. In order to investigate the correlation between grain growth and crystallographic orientation of the α grains, the IPF sections and the corresponding PFs are computed from the smallest (the equivalent diameter less than 15 μm) and from the largest (the equivalent diameter larger than 80 μm) RXed α grains and displayed in Fig. 5-6 (e) and (f). It can be clearly seen that the smallest grains are mainly the blue grains (Fig. 5-6 (e)) orientated with <10$\bar{1}$0>//ED. These grains belong to the primary RXed grains showing similar orientation with the retained unRXed grains (Fig. 5-6 (c)). Thus, one can assume that the <10$\bar{1}$0>-oriented α grains are mainly at the deformation and primary recrystallization stage. It should be mentioned that there also exist some fine RXed grains orientated with <11$\bar{2}$0>//ED, seeing the green grains in Fig. 5-6 (e), but the amount of the <11$\bar{2}$0>-oriented α grains is very low and their intensity in the PF is very weak. For the largest grains, clearly, most of them are in green (Fig. 5-6 (f)), i.e., orientated with <11$\bar{2}$0>//ED, as confirmed by the {11$\bar{2}$0} PF. This confirms that the <11$\bar{2}$0>-oriented α grains have been fully recrystallized and already entered the stage of grain growth.

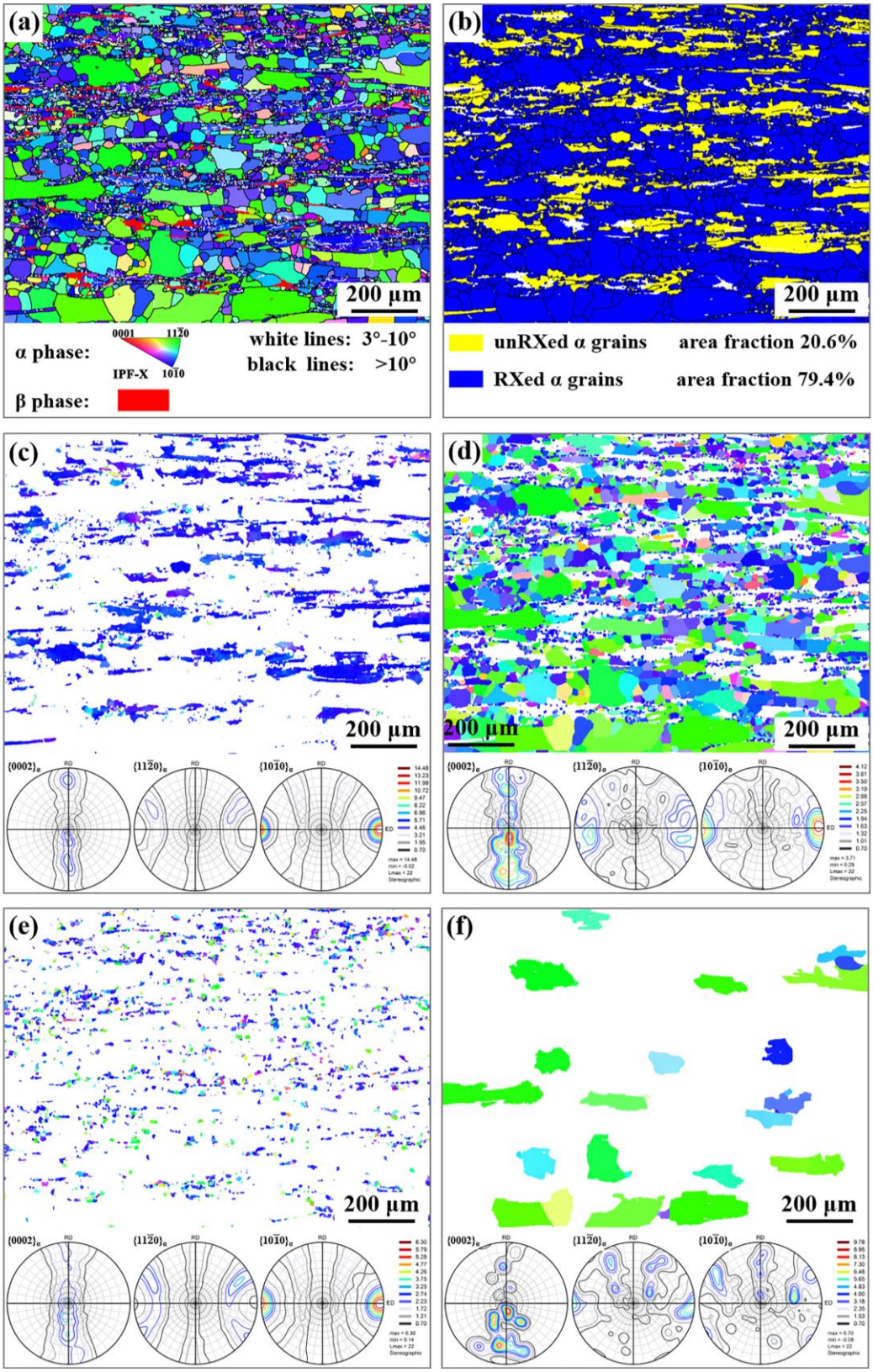


Fig. 5-6 EBSD micrographs of the extruded samples with the extrusion ratio of E7.11. (a) X//ED axis IPF micrograph; (b) Micrograph separating the RXed α grains (blue) from the unRXed α grains (yellow) according to the average grain misorientation. (c-f) IPF and corresponding PF micrographs of (c) the unRXed α grains, (d) the RXed α grains, (e) the sections selecting the smallest DRXed α grains less than 15 μm, and (f) the largest DRXed α grains more than 80 μm.

It is evident above that the unRXed α grains and the primary RXed fine α grains are strongly textured with <10$\bar{1}$0>//ED (Fig. 5-6 (c)). This non-oriented nucleation has been reported in many previous researches [147,148,152–154], i.e., the main texture feature of the deformed state evolved only slightly during the primary recrystallisation. Whereas, some fine RXed grains orientated with <11$\bar{2}$0>//ED can also be observed in Fig. 5-6 (e), thus, the formation of the <11$\bar{2}$0>-oriented fine α grains created some discussion. In my opinion, the deformation texture may be a <10$\bar{1}$0>-<11$\bar{2}$0> double fiber texture containing both the <10$\bar{1}$0>//ED component and the <11$\bar{2}$0>//ED component depending on the types of the activated dislocations. As evidenced by the unRXed α grain in Fig. 5-7 (a), the IPF micrograph of the unRXed α grain consists of blue- (<10$\bar{1}$0>//ED) and green- (<11$\bar{2}$0>//ED) colored domains. The line profile of point-to-origin along the black arrow AB (Fig. 5-7 (b)) reveals that the disorientation angle increases gradually and a continuous change of orientation induced by plastic deformation occurs. Moreover, many low-angle boundaries can be detected between the different domains, as indicated by the red arrows in Fig. 5-7 (a). The formation of these low-angle boundaries is resulted from dislocations accumulation and rearrangement, i.e., DRV, giving rise to the abrupt change in disorientation (Fig. 5-7 (b)). As the deformation intensifies, these low-angle boundaries could trap more mobile dislocations and transform themselves into high-angle boundaries, eventually turning subgrains into new RXed grains by CDRX mechanism. Hence, the RXed grains with the <11$\bar{2}$0>//ED will separate themselves from the RXed grains with <10$\bar{1}$0>//ED via DRV and CDRX mechanism, leading to the coexistence of the fine green RXed α grains and fine blue RXed α grains in Fig. 5-6 (e). However, it should be mentioned that in the current situation the unRXed α grains are always strongly textured with <10$\bar{1}$0>//ED, and such unRXed α grains with <11$\bar{2}$0>//ED cannot be found frequently. That may be related with the dislocation mobility, and it is probably higher in the <11$\bar{2}$0>-oriented α grains than that in <10$\bar{1}$0>-oriented α grains. Thus, the DRX of the <11$\bar{2}$0>//ED α grains could be progressed faster than that of the <10$\bar{1}$0>//ED α grains after such a severe deformation. Accordingly, these preferentially DRXed α grains with <11$\bar{2}$0>//ED have an advantage in abnormal grain growth due to low dislocation density and the highly misorientation with the unRXed α grains with <10$\bar{1}$0>//ED. Accordingly, in the current

extruded microstructure the <11$\bar{2}$0>-oriented α grains in unRXed state cannot be found frequently, but some fine RXed α grains and majority of abnormal grown α grains orientated with <11$\bar{2}$0>//ED can be observed. In contrary, the same microstructure feature shown in Fig. 5-7 (a) has been presented in AZ31 magnesium alloy [151], and it is thought that the <11$\bar{2}$0>-oriented α domains are not induced by plastic deformation but result from the deformed α domains with <10$\bar{1}$0>//ED rotating a 30° around <0001> axis via CDRX, i.e., the oriented nucleation mechanism. Based on the current results, it is hard to determine which explanation is the real mechanism. To reveal the underlying mechanism, further examinations on dislocation activity during the deformation is needed in the future work.

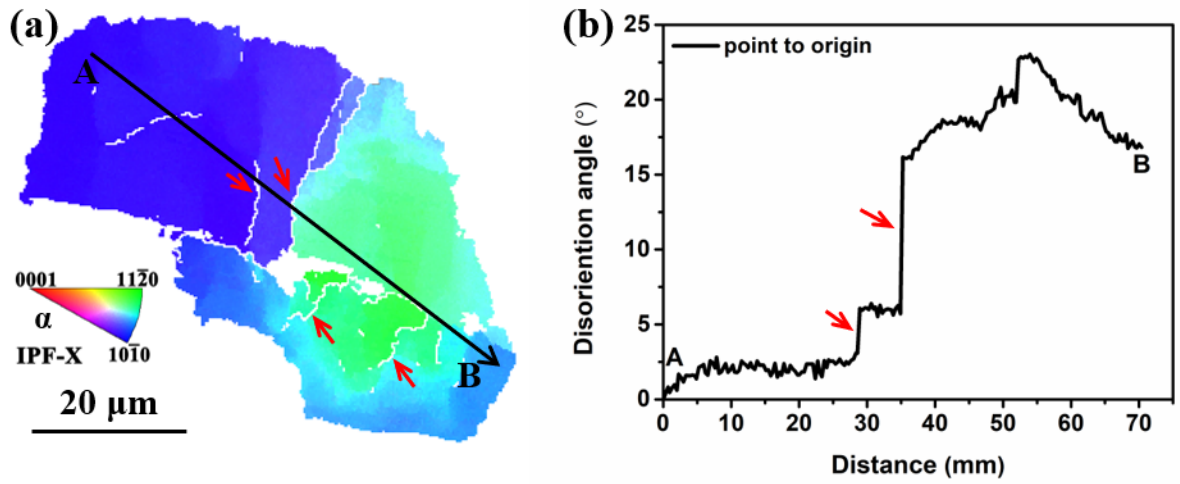


Fig. 5-7 The unRxed α grain showing lattice rotation. (a) X(//ED) axis IPF micrograph; (b) line profile of disorientation angle along the arrow L1 in (a).

In the current extrusion process, a severe deformation (extrusion ratio is 7.11) was realized within a very short time (10s). The severe deformation, on one hand, provided high driving force for DRV and DRX, and on the other hand, imposed challenges to the restoration processes as the short distance atomic diffusion for crystal restoration was constantly counteracted by the high-speed dislocation proliferation. According to the resultant microstructure, there are 20.6 vol.% (Fig. 5-6 (b)) of the α grains still at the unRXed state. That is the rate of dislocation multiplication is higher than that of dislocation arrangement, and no enough time for the formation of subgrains or for the low-angle boundaries to evolve into high-angle boundaries in the originally deformed α grains even if they have experienced a short annealing. As for the α grains have finished the DRX, the grain growth occurred during the short annealing time. It is

well known that grain growth is achieved by the migration of grain boundaries. The driving force for grain boundaries migration is mainly the disorientation between the neighbor grains, i.e., interface energy. The larger the disorientation angle is, the higher the probability to migrate is. In the current extruded state, the majority of the grains are in the deformed state and oriented with $<10\bar{1}0>$//ED. For the primary RXed grains, they possess the similar orientations to the deformed ones. Their boundaries with the deformed grains possess low driving force for migration. However, for the small amount of $<11\bar{2}0>$-oriented RXed α grains, they possess relatively high disorientation with their neighbor grains. So, this kind of grain boundary has fast migration rate and it will move quickly until reaching a grain with which the growing grain forms a low energy grain boundary. Consequently, an explosive growth will occur to the $<11\bar{2}0>$-oriented α grains, as evidenced by the coarse green grains shown in Fig. 5-6 (f).

### 5.5.2 Effect of the β phase on the microstructure heterogeneity of α phase

Except the microstructure inhomogeneity reflected by the differently oriented α grains, one can notice that even in the same texture component the microstructure features of the α grains also vary from one to another. To analyze the differences in recrystallization progress of the α grains belonging to the same texture component, their crystalline perfection was further analyzed with the intragranular Kernel average misorientation (KAM) and displayed in Fig. 5-8. Combined with the EBSD IPF micrograph (Fig. 5-8 (a)) and the intragranular KAM features (Fig. 5-8 (b)), the blue α grains with $<10\bar{1}0>$//ED can be classified into three types: (I) those with equiaxed shape and free of any internal disorientation features (T1 grains in Fig. 5-8 (a)); (II) those with equiaxed shape but divided into domains with high crystalline perfection by the low-angle boundaries (T2 grains); (III) those with elongated shape along the ED and also divided into domains by low-angle boundaries within which there exist discrete disorientations (<3º) (T3 grains). The existence of the three types of blue grains evidences the different stages of the restoration process of the deformed microstructure. The type I grains indicate the completion of recrystallization, the type II indicate the late stage of the recrystallization before the low-angle boundaries further evolve into high angle boundaries and the type III suggest recovery stage. Similarly, although most of the green α grains with $<11\bar{2}0>$//ED are free of the

intragranular disorientation, the grain sizes and morphologies are varied. For example, the G1 grain in Fig. 5-8 (a) is grown abnormally along the extrusion direction, while the G2 is grown into coarse equiaxed morphology. Besides, it can be noticed that some <11$\bar{2}$0>-oriented α grains have just finished the recrystallization and exhibit very fine grain size, like the grain G3.

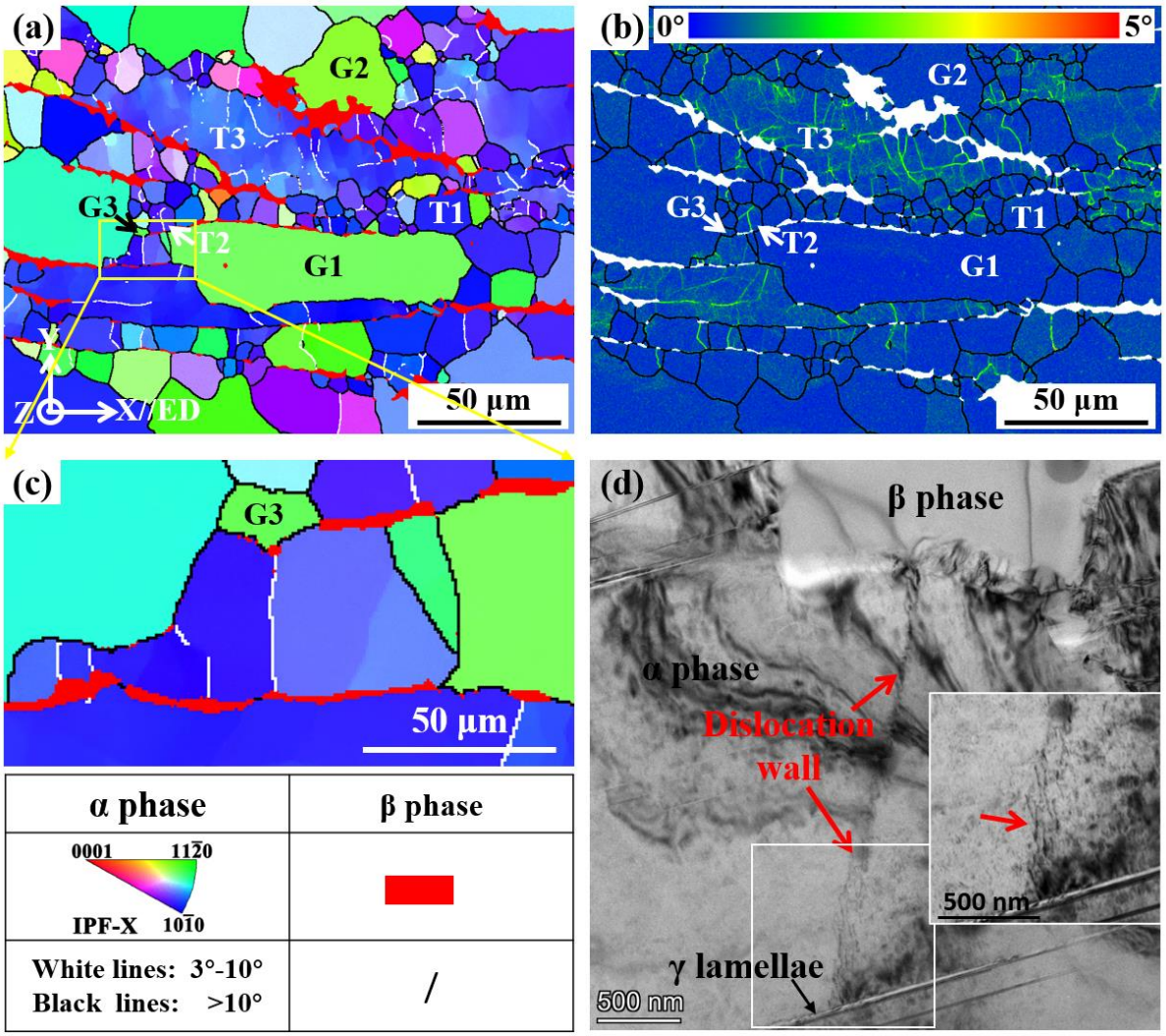


Fig. 5-8 EBSD and TEM micrographs showing the intragranular substructure features of the E7.11 sample. (a) EBSD X(//ED)-axis IPF; (b) Kernel average misorientation (KAM) micrographs; (c) The high magnified EBSD micrograph of the area outlined with yellow retangle in (a); (d) TEM bright micrograph showing the dislocation wall in an α grain connecting with the GB β phase.

Interestingly, the <10$\bar{1}$0>-oriented blue α grains with intragranular disorientations or having very fine grain sizes are located preferentially near the β strips, as seen in Fig. 5-8 (a). It is worth pointing out that most of the low-angle boundaries inside the blue α grains are connected with the grain boundary (GB) β phase (Fig. 5-8 (a)). This kind of features can be

observed clearly from the high magnified micrograph displayed in Fig. 5-8 (c). Based on the TEM bright micrograph shown in Fig. 5-8 (d), it can be seen that the low-angle grain boundaries in the $<10\bar{1}0>$-oriented α grain interiors are actually composed of dislocation walls. It means that the dislocations in the α grain are connected with the GB β phase. Moreover, the GB β strips also influence the grain size of the RXed α grains, i.e., if the spacing of two neighboring β strips is wider, the α grains in between possess relatively larger sizes, and vice versa. This implies that the deformation and the microstructural evolution of the β phase should be also responsible for the microstructural heterogeneity of the α phase, especially when it was highly deformed into long strips.

It is well known that the mechanical responses of the two phases are essentially different due to their difference in crystal structures – HCP for α and BCC for β phase. Deformation should progress in a compatible way between the β blocks and their neighboring α grains, resulting in different deformation and restoration (recovery and recrystallization) behavior and kinetics of the β-adjacent α grains from the non β-adjacent α grains. As the β phase possessing more slip systems could be deformed more easily, which resulted in incompatible deformation with the neighboring α grains that have limited numbers of slip systems. Thus, stress concentration might be created by the local incompatible deformation, leading to more dislocations produced in the neighboring α grains. At the same time, the β blocks homogeneously distributed in the initial microstructure (Fig. 5-3 (a)) were deformed into long strips along the ED after extrusion (Fig. 5-4 (a)) that separated the microstructure into bands. That means that the contacting area between the β strips and the neighboring α grains was significantly increased. The β strips pinned the dislocation walls and the low-angle boundaries that intersect the α/β interfaces in the deformed adjacent α grains, as seen in Fig. 5-8 (c) and (d). This effect prohibited such low-angle boundaries from evolving into high-angle boundaries that is the major mechanism for CDRX of the present alloy [199].

Besides, the morphology and distribution of the β strips caused by the severe deformation would also affect the static recovery (SRV), SRX and grain growth of the neighboring α grains during the short-term annealing process. On one hand, the β strips still play an important role in pinning the dislocation walls and constraining the transition from low-angle boundaries to

high-angle boundaries in the α grains. On the other hand, the β strips are obstacles for the recrystallized α grains to grow up, i.e., the β phase distributed along the ED constrains the grain growth of the RXed α grains in the direction perpendicular the ED, and therefore the α grains only can grow along the ED, as the α grain G1 presented in Fig. 5-8 (a). Due to the different spacing between the β strips, the limits for grain growth are different, resulting in the grain sizes and morphology heterogeneity of the grown α grains.

## 5.6 Thermally-induced phase transformation and abnormal grain growth

As mentioned in Section 5.4.1 (Page 92), except the large sized β strips, some tiny white particles which are supposed to be β phase according to the contrast can be observed in certain areas (Fig. 5-4 (a)). Fig. 5-9 shows the magnified SEM-BSE image of the area outlined by the black rectangle in Fig. 5-4 (a), in which the white particles are noted by yellow arrows. To further identify the white particles, the high-angle annular dark-field mapping of the scanning transmission electron microscopy (STEM-HAADF) and the selected area electron diffraction (SAED) pattern were used and the micrographs are displayed in Fig. 5-10 (a) and (b), respectively. One can clearly see from the Fig. 5-10 (a) that there do exist some white particles with the sizes in sub-micrometer range (0.5-1 μm) in the α grain. The corresponding chemical composition analysis suggests that the deficiency of Al and the enrichment of Mo occur at these white particles. The enrichment of the β-phase stabilizing element Mo indicates that these white particles are most likely β phase [200]. Besides, the SAED pattern (Fig. 5-10) of the particle indicated with the yellow circle in Fig. 5-10 (a) suggests that the particle possesses a BCC structure. Thus, it can be further confirmed that the white particles in the BSE images (Fig. 5-9) are β phase where high atomic number (Z) elements exist. Close observation revealed that the locations of the tiny β particles demonstrate two different features: (i) along boundaries of some small α grains (intergranular β), as outlined with the yellow rectangle in Fig. 5-9; (ii) in grain interiors of large α grains (intragranular β), as outlined with the orange rectangle in Fig. 5-9. The crystallographic orientation features of the tiny β particles will be analyzed in detail in the following part.

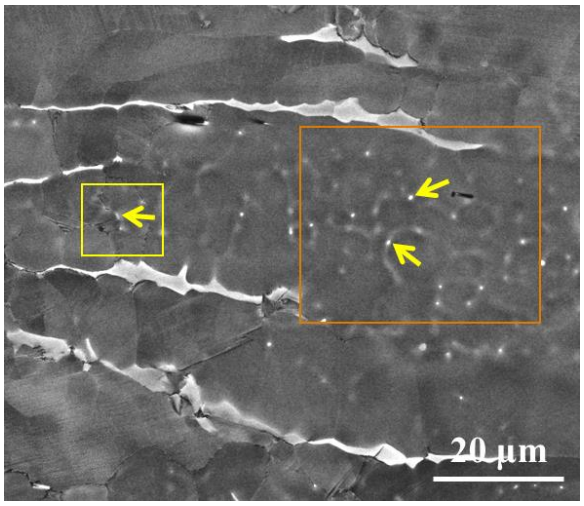


Fig. 5-9 Magnified SEM-BSE image of the area outlined by black rectangle in Fig. 5-4 (a).

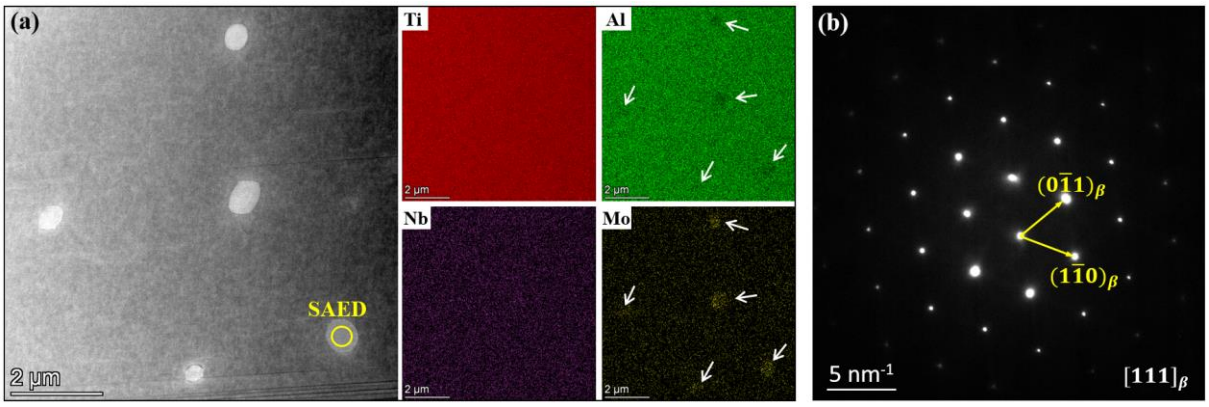


Fig. 5-10 (a) High-angle annular dark-field (STEM-HAADF) Z-contrast image for the area containing white particles and the elemental mapping of Ti, Al, Nb and Mo measured by the energy dispersive X-ray spectroscopy (EDS); (b) the selected area electron diffraction (SAED) pattern of the particle noted with yellow circle in (a).

The tiny intergranular β particles are further represented with the magnified EBSD X-IPF micrograph in Fig. 5-11 (a) (corresponding to the outlined area with the yellow rectangle in Fig. 5-9 (b)). Orientation analysis shows that different from the β strips, these tiny intergranular β particles obey the Burgers OR with at least one of their neighboring α grains. For example, the OR plane ($\{110\}_\beta$-$\{0001\}_\alpha$) and OR direction ($\langle 1\bar{1}1\rangle_\beta$-$\langle 11\bar{2}0\rangle_\alpha$) pole figures of the $\beta_1$ particle and its neighboring α grains ($\alpha_1$-$\alpha_3$) are presented in Fig. 5-11 (b). As highlighted by the green rectangles, the $\beta_1$ particle obeys the Burgers OR with all of their neighboring α grains. In the current case, the $\beta_2$ particle possesses similar crystallization orientation with the $\beta_1$ particle, and it also obeys the Burgers OR with all of their neighboring α grains, but $\beta_3$ particle only has the Burgers OR with $\alpha_3$ grain, as listed in Fig. 5-11 (a). Same result can be obtained by TEM

characterization, as clarified in Fig. 5-12. Fig. 5-12 (a) shows the TEM bright field image with an intergranular β particle distributed between the α grains G1 and G2. The corresponding SAED pattern of the area outlined with the white circle is shown in Fig. 5-12 (b). It can be known that the intergranular β particle follows the Burgers OR with the α grains G1. This confirms that the α → β phase transformation happened at the α grain boundaries during or after the deformation. As the β particles do not demonstrate any deformation morphology (elongated along the ED (Fig. 5-11 (a))), without dislocations inside (Fig. 5-12 (a)) and possess perfect Burgers OR with the adjacent α grains (Fig. 5-11 and Fig. 5-12), they could only form after the deformation (i.e., during the transition time from end-extrusion to quenching).

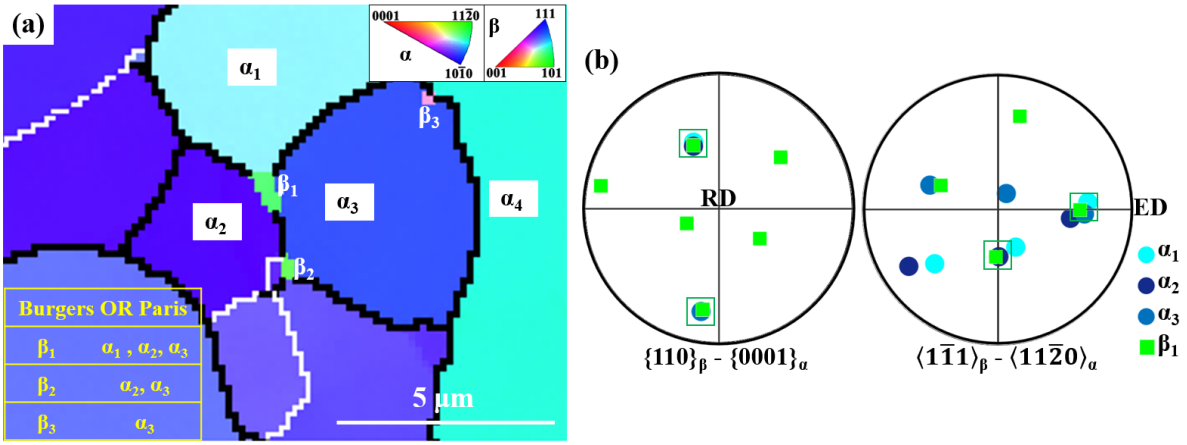


Fig. 5-11 (a) EBSD X-axis IPF micrograph showing the tiny intergranular β particles with their surrounding α grains (corresponding to the area outlined with yellow rectangle in Fig. 5-9 (b)); (b) $\{110\}_\beta$-$\{0001\}_\alpha$ and $\langle 1\bar{1}1\rangle_\beta$-$\langle 11\bar{2}0\rangle_\alpha$ pole figures of the $\beta_1$ particles and its neighboring α grains ($\alpha_1$-$\alpha_3$) in (a). Here the step size is 0.15 μm.

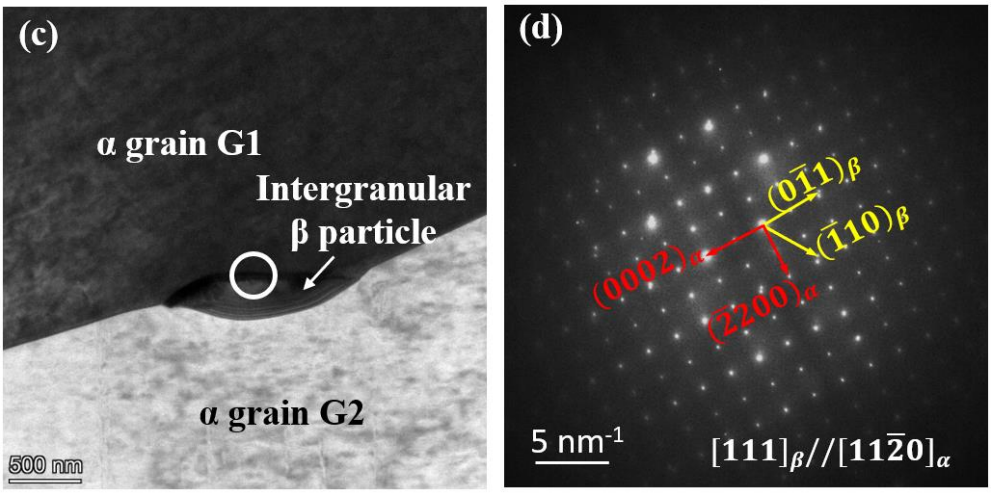


Fig. 5-12 (a) TEM bright field image showing the intergranular β particle; (b) SAED pattern of α/β interface outlined with white circle in (a). The zone axis is $[111]_\beta//[11\bar{2}0]_\alpha$.

Similarly, for the intragranular β particles dispersed in the α grains, an EBSD X-IPF micrograph of the area corresponding to the orange rectangle in Fig. 5-9 (b) is displayed in Fig. 5-13 (a). Like the Burgers OR plane ($\{110\}_\beta$-$\{0001\}_\alpha$) and OR direction ($\langle 1\bar{1}1\rangle_\beta$-$\langle 11\bar{2}0\rangle_\alpha$) pole figures of the β particles and the α matrix displayed in Fig. 5-13 (b), in this case there are in total nine β particles of which seven β particles do not obey the Burgers OR and only two ($\beta_2$ and $\beta_3$), highlighted by the black circles in Fig. 5-13 (b) do. Unexpectedly, most of the β particles do not obey the Burgers OR with the α matrix. In order to verify this result, an area with two β particles β1 and β2 dispersing in the α matrix is further characterized by TEM bright field imaging and the micrograph is displayed in Fig. 5-14 (a). The corresponding Kikuchi patterns of the α matrix and particles β1 and β2 are acquired in the convergent beam electron diffraction (CBED) mode and indexed with a homemade software Euclid's Phantasies (EP) [164], which allows automatically indexing crystal orientation with much better spatial and angular resolution than classical SEM/EBSD analysis technique. According to the Euler angles, the Burgers OR plane ($\{110\}_\beta$-$\{0001\}_\alpha$) and OR direction ($\langle 1\bar{1}1\rangle_\beta$-$\langle 11\bar{2}0\rangle_\alpha$) pole figures of the α matrix and the two β particles are displayed in Fig. 5-14 (b). It can be concluded that the β particles indeed have no Burgers OR with the matrix α phase. This suggests that the intragranular β particles may not directly precipitate from the α matrix.

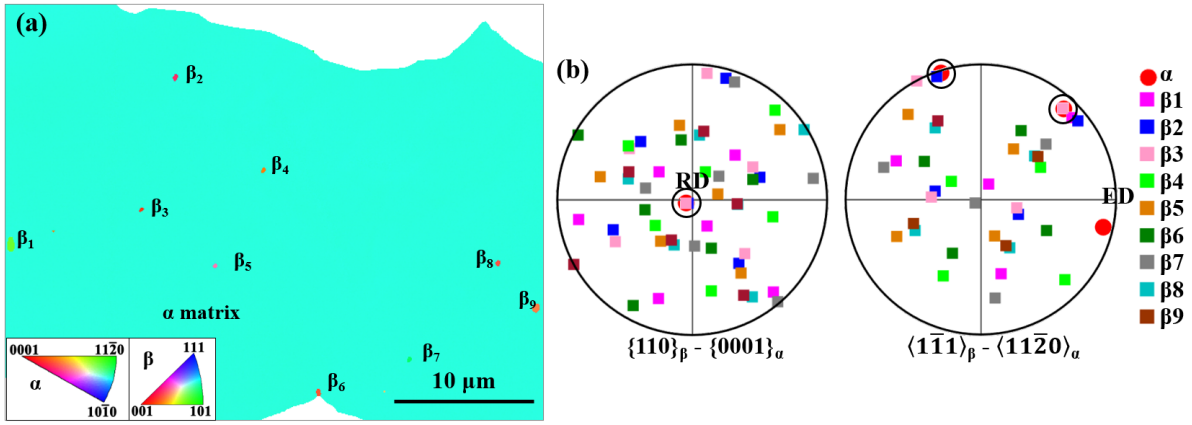


Fig. 5-13 (a) EBSD X-axis IPF micrograph showing the tiny intragranular β particles in α matrix (corresponding to the area outlined with orange rectangle in Fig. 5-9 (b)); (b) $\{110\}_\beta$-$\{0001\}_\alpha$ and $\langle 1\bar{1}1\rangle_\beta$-$\langle 11\bar{2}0\rangle_\alpha$ pole figures of the β particles and α grains in (a). Here the step size is 0.07 μm.

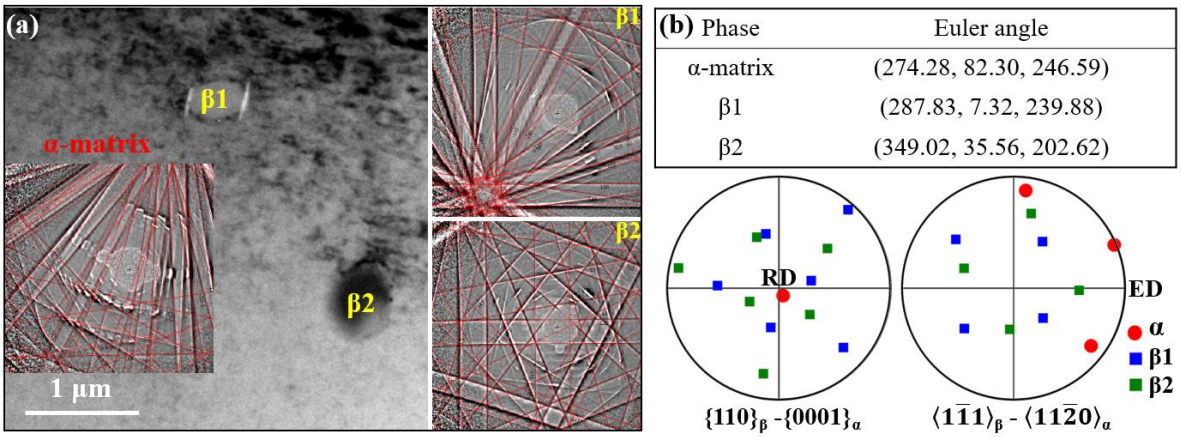


Fig. 5-14 (a) TEM bright field image showing the intragranular particles β1 and β2 dispersing in the α matrix and the respective Kikuchi bands from convergent beam electron diffraction (CBED) patterns by a homemade software Euclid's Phantasies (EP) [164]; (b) $\{110\}_{\beta}$-$\{0001\}_{\alpha}$ and $\langle 1\bar{1}1\rangle_{\beta}$-$\langle 11\bar{2}0\rangle_{\alpha}$ pole figures of the β particles and α matrix in (a).

To find out the reasons for the appearance of the β particles without Burgers OR in the α matrix, the intragranular disorientation features of the α grains have been further analyzed. Fig. 5-15 show the EBSD X-axis IPF micrograph (Fig. 5-15 (a)) and the KAM micrograph (Fig. 5-15 (b)) of the α grains from the area in Fig. 5-9. According to the KAM values and the grain sizes, the α grains can be classified into three types. (I) Those are unRXed α grains with substructures and intragranular disorientations, such as G1 and G2. (II) Those are just completely recrystallized α grains with equiaxed shape, relatively small in size and free of any internal disorientations, such as G3 and G4. (III) Those have experienced the abnormal grain growth and possess very large sizes but without any internal disorientations, such as G5, and G6. Combined with the BSE image in Fig. 5-9 where the tiny β particles can be observed clearly, one can notice that the intragranular β particles appear rather in the type III α grains, i.e., the grown α grains, than in the type I or II α grains, i.e., the non-recrystallized or primarily recrystallized α grains. The intergranular β particles are rather located along the boundaries of the type II α grains which are just at the growth front of the grown α grain. Interestingly, the sizes of the white halos connecting the intragranular β particles in the type I α grains are in good coincidence with those of the type II α grains. This phenomenon indicates that the intragranular β particles may be the residuals of the intergranular β particles initially around the type II α grains when these grains were eaten by the abnormally grown α grains.

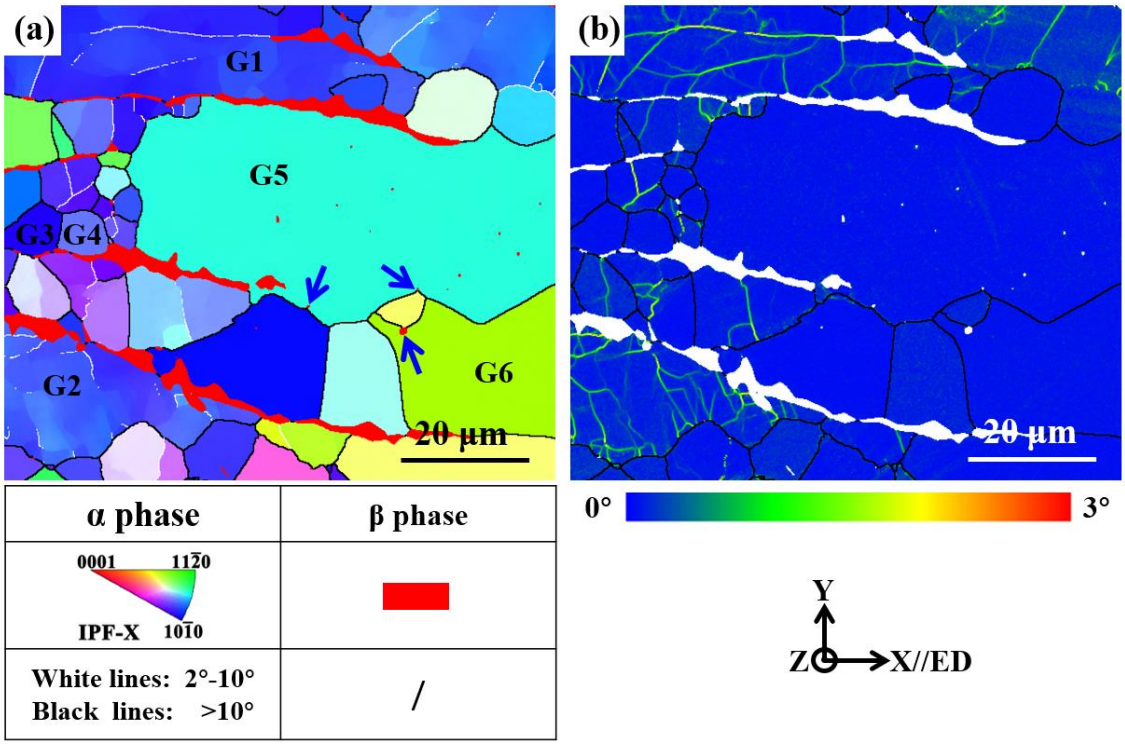


Fig. 5-15 EBSD micrographs of the whole area in Fig. 5-9. (a) X-axis IPF micrograph; (b) KAM micrograph of α phase.

It is known that during the deformation process heat could be generated in the deformed material due to the internal friction. The deformation heating will become adiabatic when the deformation strain rate is high, such as the case of extrusion [201]. Thus, in the present extrusion that has very high extrusion rate and high extrusion ratio, the adiabatic heating could increase the temperature of the deformed material, and induce the α → β phase transformation, as predicted by the thermodynamic calculations for the TNM alloy which show that above a temperature around 1275°C the fraction of β phase strongly increases with temperature [26]. This transformation occurs preferentially at α grain boundaries. Besides, it should be noted that in the present extrusion process there existed a short transition time from the end-extrusion to water quenching. This transition time had the same duration as that of the extrusion, thus, during this time and affected by the temperature rise, two processes occurred in an interweaving way. The one is the above mentioned α → β phase transformation around the just recrystallized α grains, forming the intergranular β precipitates. The other is the abnormal grain growth of certain α grains, as discussed in Section 5.5.1 (Page 95). When the abnormal grain growth of certain α grains happened, they swallowed the neighboring small α grains together with the

intergranular β precipitates, as indicated by the blue arrows in Fig. 5-15 (a). The swallowed α grains merged into the grown α grain and their crystallographic orientations were replaced by that of the grown one. However, the β precipitates were not erased by the grown α grain, thus, these β precipitates appeared as intragranular β particles for the grown α grains. Under such a circumstance, the β particles did not possess any specific orientation relationship with their new host α grains. After the increase of temperature due to adiabatic heating, the subsequent drop of temperature during the transition period between the end-extrusion and water quenching tends to thermodynamically destabilize the β particles. It induces shrinkage and dissolution and results in small sized particles connected by the white halos that is the enrichment regions of the β-stabilizers. As in the SEM-BSE micrograph (Fig. 5-9), the contrast in a well recrystallized monocrystalline α matrix is from its chemical composition variation.

## 5.7 Summary

In this Chapter, the microstructure and texture evolutions in the TNM alloy after the hot extrusion at the (α+β) phase region with the extrusion ratio of 7.11 were thoroughly investigated by SEM, EBSD and TEM.

After the fast, severe extrusion deformation, the microstructure become very heterogenous. The α phase exhibits a bimodal structure with a wide grain size distribution (5~160 μm) but with a refined average size (~ 16 μm). Synchrotron diffraction and EBSD results show that the α phase in the extruded microstructure present a basal fiber with two different components, i.e., a strong $<10\bar{1}0>$//ED fiber component and a weak $<11\bar{2}0>$//ED fiber component. This features of the high-temperature α phase are beneficial to developing an expected ($\alpha_2$+γ) lamellar structure. The original grain boundary β phase has been elongated along the extrusion direction and presents as long-strips, framing the α grains between the β strips. The β phase after extrusion shows a <110>//ED fiber. The Burgers OR between the α phase and the β phase detected in the initial microstructure has been destroyed.

Due to the deformation conditions and the influence of grain boundary β phase, the recrystallization progresses of the α grains are varied, leading to a mixture of unRXed grains and fine primary RXed grains with the texture component of $<10\bar{1}0>$//ED, as well as coarse

abnormally grown grains with the texture component of $<11\bar{2}0>$//ED. The severe deformation, on one hand, provided high driving force for DRV and DRX, and on the other hand, imposed challenges to the restoration processes as the short distance atomic diffusion for crystal restoration was constantly counteracted by the high-speed dislocation proliferation. The effects of these two factors were further perturbed by the presence of the β phase. The one was that stress concentration created by the local incompatible deformations, leads to more dislocations produced in the neighboring α grains. The other effect was that the β strips pinned the dislocation walls and inhibited the low-angle boundaries to evolve into high-angle boundaries. Thus, for the favorable α grains, the recrystallization can proceed completely, while for the unfavorable α grains, the recrystallization cannot. As the majority of the α grains are oriented with $<10\bar{1}0>$//ED, the $<11\bar{2}0>$-oriented α grains possess relatively high disorientation with their neighboring grains, which promotes the abnormal grain growth during the transition period from the end-extrusion to the water quenching and leads to the development of the $<11\bar{2}0>$//ED fiber component.

In addition to the elongated β strips evolved from the original grain boundary β blocks, the β phase also appeared in the extruded microstructure as tiny particles along the boundaries of the small sized recrystallized α grains (intergranular β) and in the interiors of certain abnormally grown α grains (intragranular β). Crystallographic orientation analysis revealed that the intergranular β particles possess the Burgers orientation relationship with at least one of their neighboring α grains, whereas the intragranular β particles did not follow any specific orientation relationship with their host α matrix. These β particles were not evolved from the original grain boundary β blocks, but resulted from the α → β phase transformation induced by the adiabatic heating due to the high-speed deformation. The precipitation process happened during the transition period from the end-extrusion to the water quenching of the extruded sample and interwove with the abnormal α grain growth process. The appearance of the intragranular β particles was stemmed from the intergranular β precipitates after their surrounding α grains were swallowed by the abnormally grown α grains.

The present work provides new information about the complex process with interweaving of deformation, dynamic and static recrystallization, grain growth, and thermally-induced phase

transformation in TiAl alloys during extrusion in the (α+β) phase region and the following cooling process, and verifies the possibility that hot extrusion conducted above the $T_{\gamma,solv}$ could be a suitable method to control the lamellar orientation and colony size of the ($\alpha_2$+γ) lamellar structure by texturing and recrystallizing the high-temperature α phase.

# Chapter 6 Conclusions and perspectives

## 6.1 Conclusions

This thesis aims to provide theoretical guidance for controlling the resultant ($\alpha_2+\gamma$) lamellar structure in TiAl alloys by controlling their parent high-temperature α phase, using thermomechanical processing. Thus, the microstructure and texture evolution as well as the related deformation behavior, dynamic recrystallization (DRX) and grain growth of the high-temperature α phase have been investigated during thermomechanical processing in the single α phase region of the Ti-44.81Al-3.96Nb-0.98Mo-0.15B ($TNM^+$) alloy and in the (α+β) phase region of Ti-43.25Al-3.91Nb-0.98Mo-0.13B (TNM) alloy. From the experimental data and theoretical investigations, the following important conclusions can be drawn:

**(I) Dynamic recrystallization mechanism of the single high-temperature α phase**

The DRX of the high-temperature α phase is a continuous grain fragmentation process, which can be categorized into three characteristic stages: i) grain boundary bulging and the formation of symmetrical-tilt boundaries characterized by <0001> disorientation axis near boundary bulging regions, resulted from the generation, accumulation and rearrangement of the edge prismatic <*a*> dislocations near grain boundaries; ii) subgrain formation at bulged boundary regions by evolving symmetrical-tilt boundaries into asymmetrical-tilt boundaries characterized with $<10\bar{1}x>$ disorientation axis by absorbing basal <*a*> dislocations, or into tilt-twist boundaries characterized with $<11\bar{2}y>$ disorientation axis by a rotational sliding of the bulged parts around the boundary plane normal; iii) detachment of the subgrains from the parent grain with gradually increased misorientation, and mixture with the ones fragmented from other parent grain by grain boundary sliding. The three processes repeatedly happened from grain boundary regions toward grain interiors until the whole initial microstructure was replaced by the recrystallized grains.

**(II) Deformation behavior and texture development of high-temperature α phase under compression deformation**

The plastic deformation of the high-temperature α phase exhibits typical flow stress-strain curve composed of three stages: work hardening stage, work softening stage and steady stage. At the work hardening stage, accompanying grain boundary bulging and the formation of subgrains, obvious grain growth occurred. The grain boundary bulging was related to the prismatic dislocation slip, and the coarse grain size increased the transgranular trajectories of dislocations glide. Both of them contributed to the increase of the flow stress. During the softening stage, the microstructure exhibited bimodal structure consisting of DRXed small α grains and retained coarse α grains, attributed to the differences in deformation mechanism and CDRX progress of differently oriented α grains. For the soft α grains, CDRX was completed quickly by intragranular dislocation slip, then grain boundary sliding happened. The hard α grains was categorized into two types: (i) grains with <0001>//LD, in which dislocation accumulation was only assisted by the local strain accommodation with the neighboring α grains from boundary regions; (ii) grains with $<11\bar{2}0>$//LD, in which dislocation accumulation was achieved by the development of kinks through basal slip and dislocation slip in the boundary regions from incompatible local strain. These hard α grains required relatively large strain to accumulate sufficient dislocations for CDRX, leading to a long period of softening stage. At the steady stage, the CDRX of the α grains largely completed. It was found that in many DRXed α grains intragranular dislocation slip was active and worked as a kind of deformation mechanism in addition to grain boundary sliding.

The specific deformation mechanism and CDRX behavior affected the texture development. The crystallographic orientations of the preferentially DRXed α grains were not far from those of the original α grains and exhibited a random feature, while the retained coarse α grains mainly exhibited the hard crystallographic orientations with <0001>//LD or $<11\bar{2}0>$//LD. With the increase of the true strain, the retained coarse α grains underwent a typical orientation evolution to the tilted basal fiber texture induced by dislocation slip. Thus, the crystallographic orientations of the just DRXed α grains were largely inherited from their parent coarse α grains. Similarly, the previously formed DRXed α grains also experienced plastic deformation by intragranular dislocation slip during the subsequent deformation process.

As a result, a weak tilted basal partial fiber texture developed during the uniaxial isothermal compression, i.e., the basal plane normal was tilted about 30~50º away from the uniaxial compression axis.

**(III) Heterogeneous recrystallization and abnormal grain growth of high-temperature α phase under extrusion deformation**

After the fast, severe extrusion deformation, the microstructure become heterogenous. The α phase exhibited a bimodal structure with a wide grain size distribution. The original grain boundary β phase was elongated along the extrusion direction and presented as long-strips, framing the α grains between the β strips. Synchrotron diffraction and EBSD results showed that the α phase in the extruded microstructure presents a strong $<10\bar{1}0>$//ED fiber component and a weak $<11\bar{2}0>$//ED fiber component, and the β phase shows a <110> fiber. The Burgers OR between α phase and β phase detected in the initial microstructure has been destroyed.

Due to the deformation condition and the influence of grain boundary β phase, the recrystallization progresses of the α grains varied, leading to a mixture of unRXed α grains and fine primary RXed α grains with the texture component of $<10\bar{1}0>$//ED and grown α grains with the texture component of $<11\bar{2}0>$//ED. The severe deformation, on one hand, provided high driving force for DRX, and on the other hand, imposed challenges to the restoration processes that were constantly counteracted by the high-speed dislocation proliferation. The effects of these two factors were further dis-equilibrated by the presence of the β phase. One effect was that stress concentration created by the local incompatible deformation, leading to more dislocations produced in the neighboring α grains, and the other was that the β strips pinned the dislocation walls and inhibited the low-angle boundaries to evolve into high-angle boundaries. Thus, for some α grains, the recrystallization can be completely, whereas for the other α grains, it cannot. As the majority of the α grains are oriented with $<10\bar{1}0>$//ED, the $<11\bar{2}0>$-oriented α grains possessed relatively high disorientation with their neighbor grains, which favored the abnormal grain growth during the transition period from the end-extrusion to the water quenching and led to the development of the $<11\bar{2}0>$//ED fiber component.

**(IV) Thermally-induced α → β phase transformation interweaving with abnormal α grain growth**

In the extruded microstructure, except the elongated β strips evolved from the original grain boundary β blocks, some β phase appeared as tiny particles along small sized recrystallized α grain boundaries (intergranular β) and in the interiors of certain abnormally grown α grains (intragranular β). Crystallographic orientation analysis suggests that the intergranular β particles possessed the Burgers orientation relationship with at least one of their neighboring α grains, whereas the intragranular β particles did not follow any specific orientation relationship with their host α matrix. The intergranular β particles were resulted from the α → β phase transformation induced by the adiabatic heating from the high-speed deformation. The precipitation process happened during the transition period from the end-extrusion to the water quenching of the extruded sample and interwove with the abnormal α grain growth process, leading to the appearance of the intragranular β particles stemmed from the intergranular β precipitates after their surrounding α grains were swallowed by the abnormally grown α grains.

**(V) Guidance for optimizing ($\alpha_2$+γ) lamellar structure by modifying high-temperature α phase through thermomechanical processing**

After compressed in α single phase region to a large strain (1280 ℃, ε=1.05), the sizes of the α grains have been greatly reduced by DRX (from 220 to 45 μm), and a weak tilted basal partial fiber texture (the basal plane normal tilted about 30~50º away from the compression axis) has been developed. It suggested that through uniaxial compression in α single phase region can produce refined α grains to refine the ($\alpha_2$+γ) colony size but cannot obtain an expected texture to align ($\alpha_2$+γ) lamellae.

After the severe extrusion deformation in (α+β) phase region, the α phase exhibits an ideal basal fiber texture, which is beneficial for lamella alignment. However, the size of α grains is not uniform (with a range of 5~160 μm) due to the difference in DRX progress and grain growth. Thus, hot extrusion conducted above $T_{\gamma,solv}$ could be a suitable method to modify the high-

temperature α phase and then optimize the ($\alpha_2$+γ) lamellar structure only if the proper extrusion parameters are explored.

## 6.2 Perspectives

The current research conducted a thoroughly study on the deformation behavior, DRX and grain growth of the high-temperature α phase in TiAl alloys during thermomechanical processing. Comprehensive information concerning these fundamental issues could provide new perspectives on further investigations of TiAl alloys system and can be summarized as follows:

(I) It is known that the CDRX of the high-temperature α phase has not proceeded completely under uniaxial compression to a true strain of 1.05 with the strain rate of 0.01 $s^{-1}$. Maybe adjusting the thermomechanical parameters could help to accomplish the CDRX. Indeed, a complete systematic study on CDRX by varying deformation temperatures and strain rates is still missing. Thus, it is necessary to investigate their effects on the CDRX behavior and provide quantitative data on flow stress, crystal size and orientation evolution.

(II) Since the microstructure and texture evolution of the high-temperature α phase are closely related to the extrusion conditions, investigations on the influence of extrusion temperatures and extrusion ratios could help to find suitable parameters for obtaining a homogenous microstructure and provide more information about the mechanism of texture evolution. Besides, crystal plasticity analysis is deserved to explore the correlation between dislocation activity and texture development.

(III) The α phase with fine grain size and strong texture has been obtained by the hot extrusion, but there still exist some retained β phase, especially the elongated β strips. The retained β phase will undergo an ordering transformation and change into a very brittle and hard $\beta_0$ phase during cooling. Therefore, it is necessary to explore a method to eliminate or reduce the retained β/$\beta_0$ phase while maintaining the small grain size and strong texture. The properties of the resultant microstructure also need to be evaluated.

# Appendix: Extended Intragranular Misorientation Axis (IGMA) Analysis

In this appendix, an extension of the Intragranular Misorientation Axis (IGMA) analysis to complex cases is presented where different slip modes or even slip and grain boundary sliding are both activated in a grain. The IGMA analysis allows to determine the dominant slip system inside a grain by matching the theoretical rotation axis (Taylor axis) for a given slip system to those of the geometrically necessary dislocation (GND) forming the low-angle boundaries in a deformed grain. This analysis method works well for hexagonal materials of which only a few slip systems are available and often one is dominant. The theoretical Taylor axes have been calculated for different slip modes in hexagonal materials (Table A-1). Below, the analysis method is extended, in addition to the primary slip mode, to identify a secondary slip mode or a rotational grain boundary sliding.

It is assumed that the disorientation ($\theta/T$: $\theta$ rotation angle and $T$ rotation axis) associated to a low-angle boundary constituted of dislocations, can be decomposed into several single or basic disorientations each characterized by a specific rotation axis. The basic disorientations are either from symmetrical-tilt boundaries made of dislocations with the same Burgers vector and the rotation axis is the so-called Taylor axis, as listed in Table A-1, or from rotational boundary sliding around the axis normal to the boundary, as listed in Table A-2. For clarity and simplicity, suppose that $\theta/T$ is composed of two single rotations, $\theta_1/T_1$ and $\theta_2/T_2$ (Fig. A-1 (a)). Thus the following relation in matrix notation of the rotations holds:

$$G = S_i \cdot G_1 \cdot S_j \cdot G_2 \tag{A-1}$$

where $G$, $G_1$ and $G_2$ are the rotational matrices representing the misorientation of $\theta/T$, $\theta_1/T_1$ and $\theta_2/T_2$, as illustrated with the flow chart in Fig. A-1 (b), and $S_i$ and $S_j$ the i$^{th}$ and j$^{th}$ rotational symmetry matrices of the crystal structure. The rotational matrix of $G$ can be calculated using the rotation angle $\theta$ and the unit rotation axis $T(d_1, d_2, d_3)$ as follows:

$$G = \begin{bmatrix} (1-{d_1}^2)\cos\theta + {d_1}^2 & d_1d_2(1-\cos\theta) - d_3\sin\theta & d_1d_3(1-\cos\theta) + d_2\sin\theta \\ d_1d_2(1-\cos\theta) + d_3\sin\theta & (1-{d_2}^2)\cos\theta + {d_2}^2 & d_2d_3(1-\cos\theta) - d_1\sin\theta \\ d_1d_3(1-\cos\theta) - d_2\sin\theta & d_2d_3(1-\cos\theta) + d_1\sin\theta & (1-{d_3}^2)\cos\theta + {d_3}^2 \end{bmatrix} \quad \text{(A-2)}$$

By knowing any of two rotations, the remaining rotation can be resolved. This formulation can be readily extended to a rotation composed of multiple single rotations.

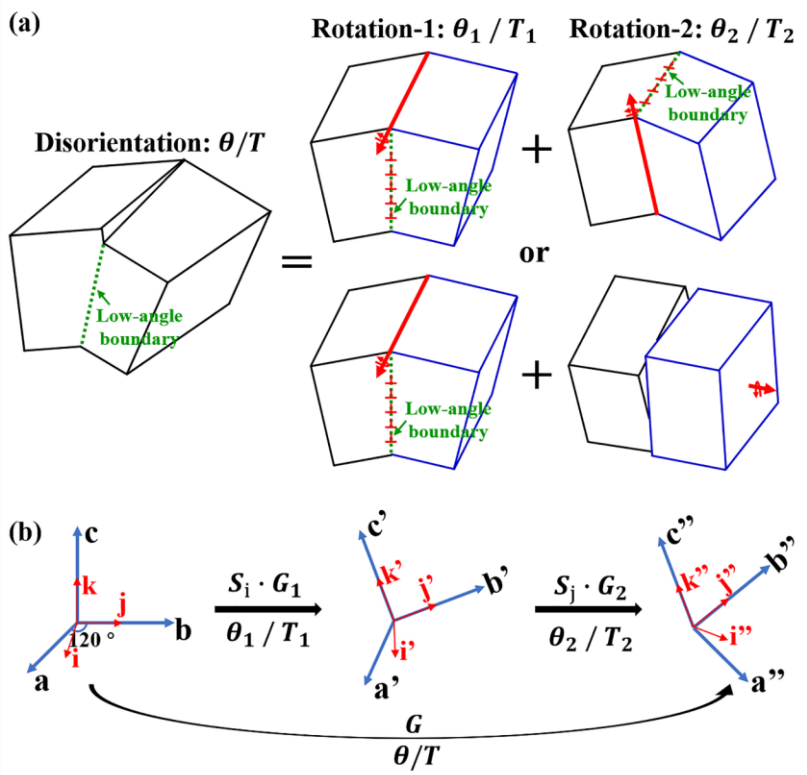


Fig. A-1 (a) Schema illustrating the decomposition of the low-angle boundary into two symmetrical tilt boundaries made of dislocation with two different Burgers vectors or into one symmetrical-tilt boundary and a rotational sliding around the axis normal to the extra-half plane of the dislocation of symmetrical-tilt boundary; (b) schema showing the corresponding crystallographic rotations.

Now the two characteristic rotations found in the present work can be used to illustrate the analysis procedure. The first case corresponds to the low-angle boundaries featured by a rotation around $\langle 10\bar{1}x\rangle$ and the second to the low-angle boundaries featured by a rotation around $\langle 11\bar{2}y\rangle$. In the two cases, the first rotation is $\theta_1/T_1$ ($T_1 = \langle 0001\rangle$) and assume that $\theta_1$= 1 to 10°. Supposing that the second rotation $T_2$ corresponds to a Taylor axis of another slip system (as listed in Table A-1) or to the axis normal to the extra half-plane of the corresponding boundary dislocations (as listed in Table A-2), and $\theta_2$= 1 to 10°. The total rotation $G$ ($\theta/T$) can be calculated. Then the calculated $G$ is further compared with the

measured $G^{ex}$ $(\theta/T)^{ex}$, the $\theta_2/T_2$ provides the smallest deviation ($\Delta\theta$) from the experimental $G^{ex}$ $(\theta/T)^{ex}$ is assessed as the second rotation.

Table A-1 Possible slip modes in disordered α-$Ti_3Al$ (c/a=1.60) and the corresponding Taylor axes.

| **Slip mode** | **Slip type** | **Taylor axis** |
|---|---|---|
| $\{1\bar{1}00\}\langle11\bar{2}0\rangle$ | Prismatic $\langle a\rangle$ | $\langle000\bar{1}\rangle$ |
| $\{0001\}\langle11\bar{2}0\rangle$ | Basal $\langle a\rangle$ | $\langle1\bar{1}00\rangle$ |
| $\{10\bar{1}1\}\langle1\bar{2}10\rangle$ | Pyramidal $\langle a\rangle$ | $\langle\bar{1}012\rangle$ |
| $\{10\bar{1}1\}\langle11\bar{2}\bar{3}\rangle$ | Pyramidal-I $\langle c+a\rangle$ | $\langle27\ 44\ \overline{17}\ 10\rangle$ |
| $\{11\bar{2}2\}\langle11\bar{2}\bar{3}\rangle$ | Pyramidal-II $\langle c+a\rangle$ | $\langle1\bar{1}00\rangle$ |

Table A-2 Slip modes in disordered α-$Ti_3Al$ (c/a=1.60) and the axis normal to the extra-half plane of dislocation.

| **Slip mode** | **Extra half plane / Symmetrical-tilt boundary plane** | **Rotation axis of grain boundary sliding** |
|---|---|---|
| $\{1\bar{1}00\}\langle11\bar{2}0\rangle$ | $\{11\bar{2}0\}$ | $\langle11\bar{2}0\rangle$ |
| $\{0001\}\langle11\bar{2}0\rangle$ | $\{11\bar{2}0\}$ | $\langle11\bar{2}0\rangle$ |
| $\{10\bar{1}1\}\langle1\bar{2}10\rangle$ | $\{1\bar{2}10\}$ | $\langle1\bar{2}10\rangle$ |
| $\{10\bar{1}1\}\langle11\bar{2}\bar{3}\rangle$ | $\{5\ 5\ \overline{10}\ \overline{26}\}$ | $\langle11\bar{2}\bar{3}\rangle$ |
| $\{11\bar{2}2\}\langle11\bar{2}\bar{3}\rangle$ | $\{5\ 5\ \overline{10}\ \overline{26}\}$ | $\langle11\bar{2}\bar{3}\rangle$ |

For the first case, the low-angle boundaries with disorientation axes of $\langle10\bar{1}x\rangle$, $T_2 = \langle10\bar{1}0\rangle$ provides the smallest deviation ($\Delta\theta$) of the calculated $G$ $(\theta/T)$ from the experimental $G^{ex}$ $(\theta/T)^{ex}$. The results of several examples are displayed in Table A-3. For the second case, the low-angle boundaries with disorientation axis of $\langle11\bar{2}y\rangle$, $T_2 = \langle11\bar{2}0\rangle$ offers the smallest $\Delta\theta$. The results of several examples are displayed in Table A-4.

A total rotation $\theta/T$ that is produced by the combination of the two rotations $\theta_1/T_1$ ($\theta_1 = 1-10°$; $T_1 = \langle0001\rangle$) and $\theta_2/T_2$ ($\theta_2 = 1-10°$; $T_2 = \langle10\bar{1}0\rangle$ *or* $\langle11\bar{2}0\rangle$) is further simulated. The results are shown with the variation of $\theta$ as a function of $\theta_1$ and $\theta_2$ and with the stereographic projection of $T$ as a function of the $\theta_1/\theta_2$ ratio in Fig. A-2. When $T_2 = \langle10\bar{1}0\rangle$, it is seen that the two rotation angles $\theta_1$ and $\theta_2$ have a symmetrical contribution with respect to $\theta_1/\theta_2 = 1$ to the total disorientation angle. For the rotation axis,

whatever the two rotations $\theta_1/\langle 0001\rangle$ and $\theta_2/\langle 10\bar{1}0\rangle$, the total rotation axis always falls near the $\langle 10\bar{1}x\rangle$ line (the thick black line in Fig.A-2 (a)) that runs from $\langle 0001\rangle$ to $\langle 10\bar{1}0\rangle$. Similar to the case of $\langle 10\bar{1}x\rangle$, when $T_2 = \langle 11\bar{2}0\rangle$ the combination of the two rotation angles also has a symmetrical contribution with respect to $\theta_1/\theta_2 = 1$ to the final disorientation angle, as shown in Fig. Fig. A-2 (b). For the rotation axis, whatever the two rotations $\theta_1/\langle 0001\rangle$ and $\theta_2/\langle 11\bar{2}0\rangle$, the final rotation axis always falls near the $\langle 11\bar{2}y\rangle$ line (the thick black line in Fig. A-2 (b)) that runs from $\langle 0001\rangle$ to $\langle 11\bar{2}0\rangle$.

The above results demonstrate that the extended IGMA approach is capable of revealing the mechanisms driving the evolution of the low-angle boundaries, when direct dislocation examination is not possible for the materials.

Table A-3 Calculation results for low-angle boundaries with disorientation axis around $\langle 10\bar{1}x\rangle$.

| **Experimental result** $G^{ex}\,(\theta/T)^{ex}$ | $T_1$ | $T_2$ | $\theta_1$ | $\theta_2$ | **Calculated result** $G\,(\theta/T)$ | $\Delta\theta$ |
|---|---|---|---|---|---|---|
| $6.37°/\langle\bar{1}01\bar{4}\rangle$ | | | 5.6° | 3.0° | $6.3524°/\langle\overline{0.4579}\ \overline{0.0266}\ 0.4845\ \overline{1.9040}\rangle$ | 0.1502 |
| $12.06°/\langle\bar{1}103\rangle$ | | | 9.8° | 7° | $12.0383°/\langle\overline{0.5505}\ 0.6079\ \overline{0.0574}\ 1.7564\rangle$ | 0.6018 |
| $7.97°/\langle 0\bar{1}1\bar{3}\rangle$ | | | 6.5° | 4.7° | $8.0197°/\langle 0.0383\ \overline{0.6037}\ 0.5654\ \overline{1.7499}\rangle$ | 0.2703 |
| $13.37°/\langle\bar{1}01\bar{3}\rangle$ | | | 10.8° | 7.8° | $13.3154°/\langle\overline{0.5514}\ \overline{0.0637}\ 0.6150\ \overline{1.7495}\rangle$ | 0.7373 |
| $6.05°/\langle 0\bar{1}12\rangle$ | $\langle 0001\rangle$ | $\langle 10\bar{1}0\rangle$ | 4.1° | 4.4° | $6.0135°/\langle\overline{0.0302}\ \overline{0.7152}\ 0.7454\ 1.4722\rangle$ | 0.1637 |
| $6.29°/\langle 02\bar{2}1\rangle$ | | | 1.4° | 6.1° | $6.2584°/\langle 0.0137\ 0.9663\ \overline{0.9801}\ 0.4828\rangle$ | 0.0818 |
| $5.03°/\langle 0\bar{1}13\rangle$ | | | 4.1° | 2.9° | $5.0216°/\langle\overline{0.0238}\ \overline{0.5645}\ 0.5883\ 1.7634\rangle$ | 0.1141 |
| $6.60°/\langle\bar{1}01\bar{1}\rangle$ | | | 2.8° | 6.0° | $6.6206°/\langle\overline{0.8920}\ \overline{0.0255}\ 0.9175\ \overline{0.9128}\rangle$ | 0.1494 |
| $6.29°/\langle 10\bar{1}\bar{2}\rangle$ | | | 4.3° | 4.6° | $6.2960°/\langle 0.7134\ 0.0316\ \overline{0.7450}\ \overline{1.4746}\rangle$ | 0.1760 |
| $13.99°/\langle\bar{1}011\rangle$ | | | 5.8° | 12.7° | $13.9568°/\langle\overline{0.9344}\ 0.0531\ 0.8813\ 0.8941\rangle$ | 0.6480 |

Table A-4 Calculation results for low-angle boundaries with disorientation axis around $\langle 11\bar{2}y\rangle$.

| **Experimental result** $G^{ex}\,(\theta/T)^{ex}$ | $T_1$ | $T_2$ | $\theta_1$ | $\theta_2$ | **Calculated result** $G\,(\theta/T)$ | $\Delta\theta$ |
|---|---|---|---|---|---|---|
| $5.53°/\langle\bar{1}2\bar{1}\bar{3}\rangle$ | $\langle 0001\rangle$ | $\langle 11\bar{2}0\rangle$ | 3.5° | 4.3° | $5.5438°/\langle\overline{0.4707}\ 0.8940\ \overline{0.4234}\ \overline{1.3632}\rangle$ | 0.1391 |
| $10.38°/\langle 11\bar{2}6\rangle$ | | | 8.8° | 5.5° | $10.3745°/\langle 0.3457\ 0.2644\ \overline{0.6101}\ 1.8310\rangle$ | 0.4220 |
| $5.46°/\langle\bar{1}2\bar{1}2\rangle$ | | | 2.6° | 4.8° | $5.4586°/\langle\overline{0.4869}\ 1.0137\ \overline{0.5268}\ 1.0284\rangle$ | 0.1137 |
| $3.07°/\langle\bar{1}\bar{1}24\rangle$ | | | 2.2° | 2.1° | $3.0413°/\langle\overline{0.3848}\ \overline{0.4113}\ 0.7960\ \overline{1.5625}\rangle$ | 0.0573 |
| $10.36°/\langle 2\bar{1}\bar{1}2\rangle$ | | | 4.9° | 9.1° | $10.3329°/\langle 1.0148\ \overline{0.5450}\ \overline{0.4698}\ 1.0223\rangle$ | 0.3914 |
| $10.52°/\langle 11\bar{2}1\rangle$ | | | 3.1° | 10.1° | $10.5639°/\langle 0.5252\ 0.5769\ \overline{1.1021}\ 0.6323\rangle$ | 0.4717 |

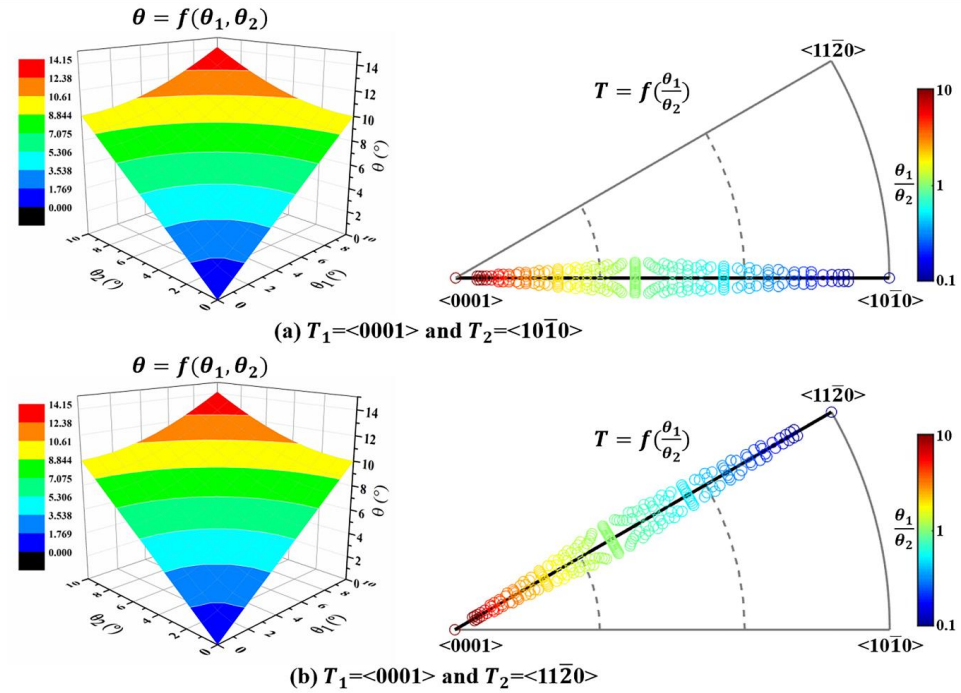


Fig. A-2 Calculated disorientation of low-angle boundary, in terms of $\theta/T$ on function of the first rotation $\theta_1/T_1$ ($T_1 = \langle 0001\rangle$) and the second rotation $\theta_2/T_2$. (a) $T_2 = \langle 10\bar{1}0\rangle$; (b) $T_2 = \langle 11\bar{2}0\rangle$.

# Résumé étendu en français

## Evolution de la microstructure et de la texture de la phase α à haute température d'alliages TiAl lors de traitements thermomécaniques

La demande de performances accrues pour les turbines d'avion nécéssite d'utiliser des alliages TiAl à structure lamellaire ($\alpha_2+\gamma$) en contrôlant la taille des colonies et l'orientation des lamelles. Selon la relation d'orientation spécifique de Blackburn (Blackburn OR: $\{111\}_\gamma//(0001)_\alpha$, $<1\bar{1}0>_\gamma//<11\bar{2}0>_\alpha$) lors de la transformation de phase $\alpha \rightarrow \alpha_2+\gamma$, l'orientation de la structure lamellaire dépend directement de la phase α à haute température. Ainsi, l'optimisation de la structure lamellaire pourrait être réalisée en modifiant la phase α à haute température par un traitement thermomécanique mené au-dessus de la $T_{\gamma,solv}$ (le domaine monophasé α ou le domaine biphasé (α+β)). Actuellement, seules des recherches très limitées ont été consacrées aux traitement thermomécaniques au-dessus du $T_{\gamma,solv}$ dans les alliages TiAl. On dispose de très peu d'informations sur l'évolution de la microstructure de la phase α. En particulier, les possibilités qu'offre la recristallisation dynamique (DRX) de la phase α n'ont pas été pleinement évaluées et encore moins exploitées. Par ailleurs, les investigations sur les mécanismes de formation et d'évolution de la texture de la phase α ne sont toujours pas clairement expliquées. De plus, le comportement en déformation à chaud de la phase α avec la présence de phase β n'a reçu que peu ou pas d'attention, en particulier l'influence de la phase β sur la déformation plastique, la DRX, la croissance des grains et l'évolution de la texture associée de la phase α n'a pas été étudiée. Aussi, ce travail est dédié à l'étude de la déformation et de la DRX de la phase α à haute température, au suivi de l'évolution de sa microstructure et de sa texture selon que le traitement thermomécanique est effectué dans le domaine monophasé α ou dans le domaine biphasé (α+β) de manière à contrôler la taille et l'orientation de la structure lamellaire ($\alpha_2+\gamma$) qui en résultent à basse température.

Les matériaux utilisés dans cette thèse sont des alliages TiAl de nuance TNM. L'un est l'alliage Ti-44.81Al-3.96Nb-0.98Mo-0.15B ($TNM^+$) présentant un domaine monophasé α à haute température, l'autre est l'alliage Ti-43.25Al-3.91Nb-0.98Mo-0.13B (TNM) présentant un domaine biphasé phase (α+β) à haute température. Deux modes de déformation, la compression

uniaxiale et l'extrusion, ont été mis en oeuvre respectivement sur les alliages TNM$^{+}$ et TNM au-dessus de la $T_{\gamma,solv}$. Il convient de mentionner qu'il existe certaines difficultés dans la caractérisation de la microstructure de la phase déformée à haute température. D'une part, il est impossible de visualiser les microstructures dans la plage de température de déformation requise par microscopie in-situ car la phase α existe à très haute temperature (> 1250 °C). D'autre part, la transformation de phase α → $\alpha_2$+γ se produit lors du refroidissement, ainsi les configurations de dislocation dans les grains α produites lors de la déformation sont détruites par la précipitation des lamelles γ. Heureusement, la transformation de phase α → $\alpha_2$+γ ne détruit pas les joints de grains et les sous-joints intragranulaires de faible désorientation formés lors de la déformation à chaud. Afin d'analyser les caractéristiques de la microstructure de la phase α déformée à haute température, la partie transformée de la phase α a été reconstruite à l'aide du logiciel Merengue 2 (Germain et al., 2012, Acta Mater.) à partir des données d'orientation EBSD des lamelles ($\alpha_2$+γ) en se basant sur l'OR spécifique de Blackburn. Avec les données EBSD reconstruites, l'angle et l'axe de désorientation entre différentes zones dans les grains α déformés peuvent être examinés. Ensuite l'analyse IGMA (Chun et al., 2010, Metall Mater Trans A) permet de déterminer le système de glissement dominant à l'intérieur d'un grain déformé en faisant correspondre l'axe de rotation théorique (axe de Taylor) pour un système de glissement donné à ceux qui sont associés aux sous-joints faiblement désorientés (formés de dislocations géométriquement nécessaire (GND)) que l'on trouve dans le grain déformé. Les axes de Taylor pour différents modes de glissement dans la phase à haute température ont été calculés et affichés dans le Tableau 1. Cette méthode IGMA originale ne s'applique qu'à un système de glissement unique. Dans cette étude, la méthode d'analyse IGMA est étendue (Qiang et al., 2021, Intermetallics) : en plus du mode de glissement primaire, il est possible d'identifier un mode de glissement secondaire ou un glissement rotationnel le long des joints de grains.

Tableau 1 Modes de glissement possibles dans la phase α et axes de Taylor correspondants.

| **Slip mode** | **Slip type** | **Taylor axis** |
|---|---|---|
| $\{1\bar{1}00\}\langle 11\bar{2}0\rangle$ | Prismatic $\langle a\rangle$ | $\langle 000\bar{1}\rangle$ |
| $\{0001\}\langle 11\bar{2}0\rangle$ | Basal $\langle a\rangle$ | $\langle 1\bar{1}00\rangle$ |
| $\{10\bar{1}1\}\langle 1\bar{2}10\rangle$ | Pyramidal $\langle a\rangle$ | $\langle \bar{1}012\rangle$ |
| $\{10\bar{1}1\}\langle 11\bar{2}\bar{3}\rangle$ | Pyramidal-I $\langle c+a\rangle$ | $\langle 27\ 44\ \overline{17}\ 10\rangle$ |
| $\{11\bar{2}2\}\langle 11\bar{2}\bar{3}\rangle$ | Pyramidal-II $\langle c+a\rangle$ | $\langle 1\bar{1}00\rangle$ |

A l'aide de la technique de reconstruction et la méthode d'analyse IGMA étendue, les mécanismes de DRV et DRX de la phase α à haute température dans l'alliage Ti-44.81Al-3.96Nb-0.98Mo-0.15B (at. %) sous compression à chaud dans le domaine monophasé α ont été minutieusement étudiés. Cela a permis de montrer que la formation des grains recristallisés est un processus continu de fragmentation des grains, c'est-à-dire CDRX, composé de trois étapes caractéristiques, comme le montre la Fig. 1. La première étape correspond à l'apparition d'une dentelure des joints de grains induite par la contrainte et à la formation dans ces régions dentelées de sous-joints de flexion symétriques d'axe de désorientation <0001> induits par le glissement prismatique <a>. La seconde étape correspond à la transformation de ces sous-joints de flexion symétriques en sous-joints de flexion asymétriques caractérisés par un axe de désorientation $<10\bar{1}x>$ du fait d'un glissement local basal <a>, ou à des sous-joints de flexion + torsion caractérisés par un axe de désorientation $<11\bar{2}y>$ du fait d'une rotation au niveau du joint de grain. La troisième étape correspond au détachement des sous-grains et au mélange de ces sous-grains par glissement aux joints de grains. Les trois étapes se déroulent de manière continue et répétée des régions proches des anciens joints de grains de la phase α vers l'intérieur de ces grains jusqu'à l'achèvement de la recristallisation.

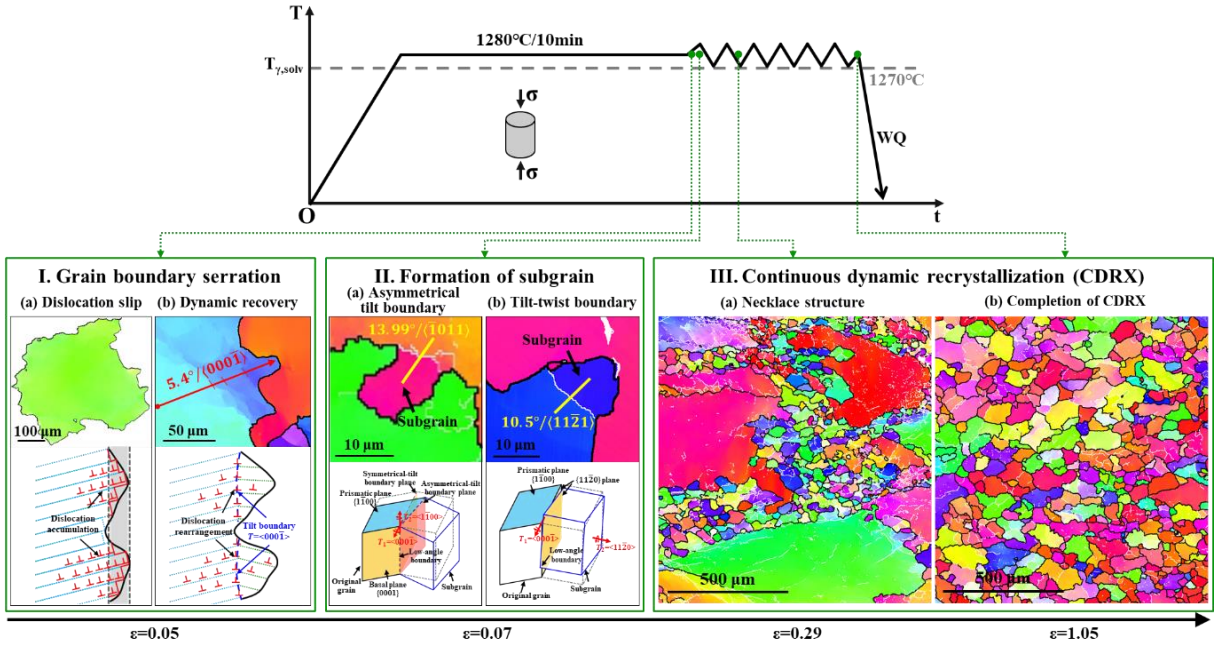


Fig. 1 Les mécanismes de CDRX de la phase α à haute température dans l'alliage $TNM^{+}$ sous compression à chaud à 1280 °C dans le domaine monophasé α.

La courbe contrainte – déformation de l'alliage TNM$^{+}$ pendant la compression uniaxiale est représentée sur la Fig. 2 (a). Elle présente une longue période d'adoucissement qui est liée au fait que les mécanismes de déformation et de CDRX varient selon l'orientation des grains α. Outre les grains mous, il existe deux types de grains durs: (i) ceux avec <0001>//LD (G1 sur la Fig. 2 (b)) pour lesquels aucun des systèmes de glissement prismatique et basal ne peut être activé, ainsi l'accumulation de dislocations dans ces grains α ne provient que de l'accommodation locale des déformations avec les grains voisins (Fig. 2 (c)); ceux avec <11$\bar{2}$0>//LD (G2 dans la Fig. 2 (b)), pour lesquels les deux systèmes de glissement prismatique actifs font tourner le grain dans des directions opposées, annulant ainsi la contribution à la déformation macroscopique. L'accumulation de dislocations dans ce type de grains est obtenue par le développement de bandes en genoux par glissement basal et par l'effet de l'accommodation des contraintes locales avec les grains α voisins (Fig. 2 (d)). Ces deux types de grains α durs nécessitent une déformation vraie relativement importante pour que se produisent une accumulation des dislocations et la CDRX subséquente. La déformation et la CDRX affectent aussi le développement de la texture. Les orientations cristallographiques des grains préférentiellement fragmentés sont largement héritées des grains parents. Avec la déformation supplémentaire, les grains DRXed précédemment formés et les grains durs ont tous deux subi une déformation plastique supplémentaire par glissement de dislocations intragranulaires. La phase α développe alors une faible texture de fibre basale inclinée pendant la compression isotherme uniaxiale, c'est-à-dire que la normale au plan basal est inclinée d'environ 30 à 50º par rapport à l'axe de compression uniaxiale, comme le montre la Fig. 3. Cette première partie de l'étude suggère que la compression uniaxiale menée dans le domaine monophasé α peut produire un affinement des grains α qui a pour effet de diminuer la taille des colonies lamelleires mais ne peut pas produire la texture attendue qui permettrait d'aligner les lamelles ($\alpha_2$+γ).

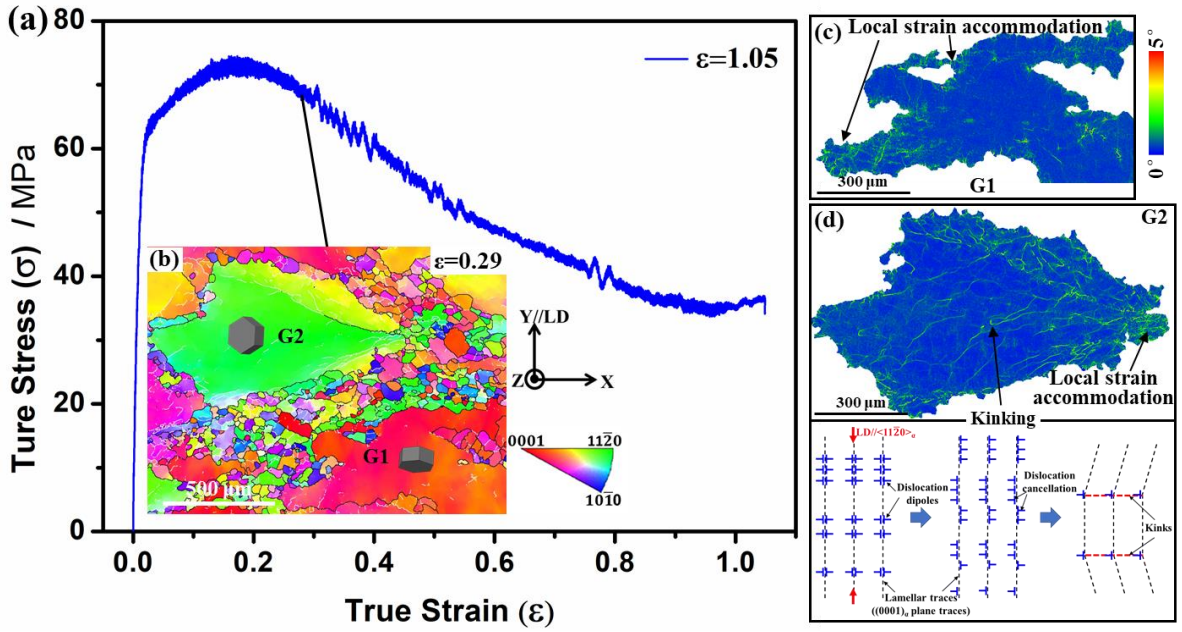


Fig. 2 (a) Courbe de contrainte –déformation de l'alliage TNM+ comprimé à 1280 °C sous une vitesse de déformation de 0.01 $s^{-1}$ jusqu'à une déformation vraie de 1.05; (b) Micrographie IPF de l'axe Y EBSD de l'échantillon déformé avec la contrainte vraie de 0.29; (c, d) Micrographies de désorientation moyenne du noyau (KAM) des grains G1 et G2 en (b); (e) Diagramme schématique illustrant la formation de bandes en genoux.

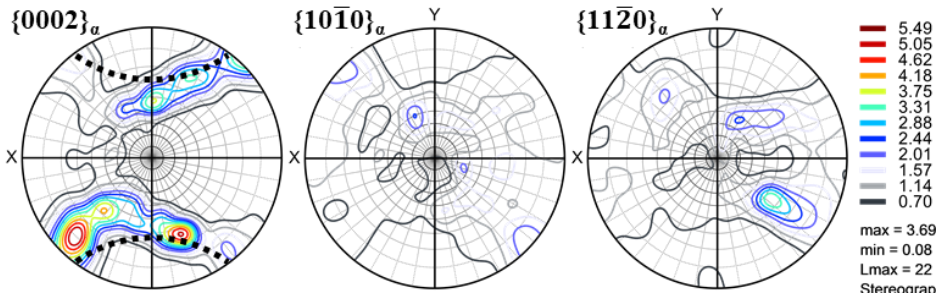


Fig. 3 Figures de pôles {0002}, {10$\bar{1}$0} et {11$\bar{2}$0} de la phase α à haute température dans l'alliage $TNM^{+}$ comprimé à 1280 °C sous une vitesse de déformation de 0,01 $s^{-1}$ à la déformation vraie de 1.05.

Pour obtenir une texture de fibre basale idéale, un autre mode de déformation, l'extrusion à chaud, a été mis en œuvre sur l'alliage Ti-43.25Al-3.91Nb-0.98Mo-0.13B (TNM) dans le domaine biphasé (α+β) avec un rapport d'extrusion de 7.11. La macro-texture après extrusion est mesurée par diffraction RX synchrotron. On peut voir que la phase α présente une texture de fibre basale {0001}//ED, comme le montre la Fig. 4 (a). Elle contient une composante de texture principale <10$\bar{1}$0>//ED correspondant aux grains non RXed et aux grains fins RXed primaires, et une composante de texture minoritaire <11$\bar{2}$0>//ED correspondant à de gros grains RXed ayant subi une croissance anormale (Fig. 4 (b)). L'hétérogénéité microstructurale est

attribuée au procédé de déformation par extrusion rapide et sévère. La déformation sévère, d'une part, a fourni une force motrice élevée pour les DRV et DRX, et d'autre part, a imposé des limitations aux processus de restauration, car la diffusion atomique à courte distance pour la restauration des cristaux est constamment contrecarrée par la prolifération des dislocations. Les effets de ces deux facteurs sont de plus perturbés par la présence de la phase β. Elle consiste en ce que la concentration de contraintes créée par les déformations locales incompatibles le long des grains β, conduit à davantage de dislocations produites dans les grains α voisins. Ainsi, la progression de la recristallisation et la croissance des grains variant selon les grains α, ce qui conduit à une microstructure bimodale avec deux composantes de texture de fibre.

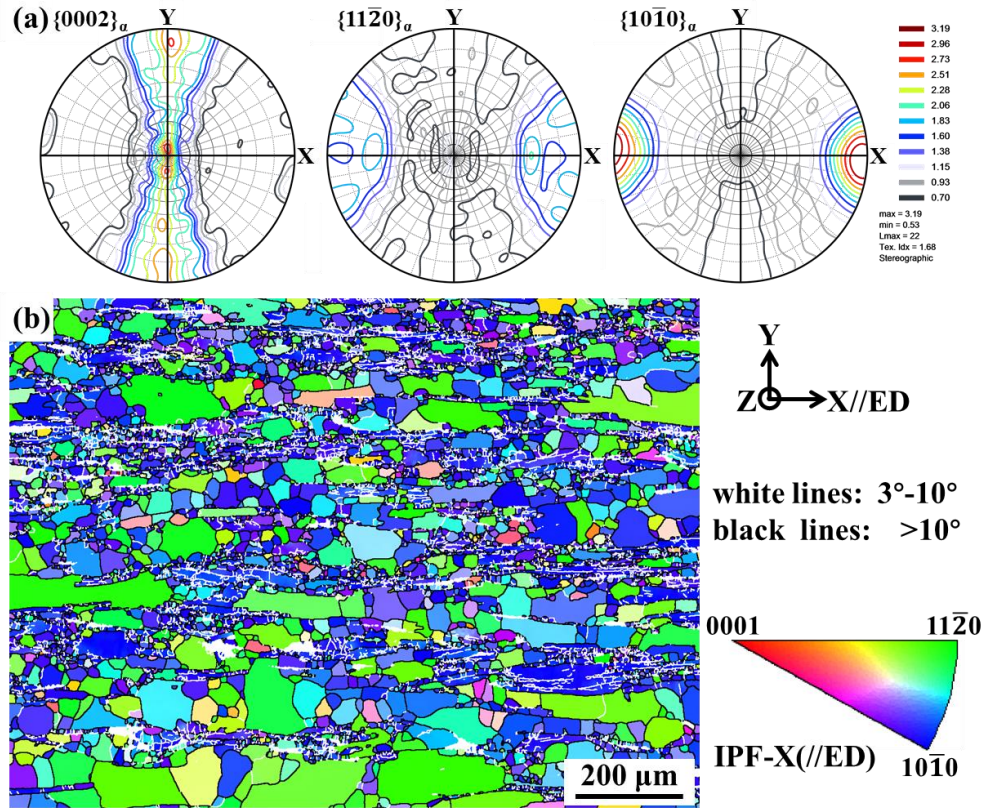


Fig. 4 (b) Figures de pôles représentatives et (b) Micrographie IPF EBSD X (//ED) de la phase dans l'alliage TNM extrudé avec le rapport d'extrusion 7.11. Les figures de pôles sont recalculées à partir des résultats obtenus par diffraction synchrotron des rayons X.

L'hétérogénéité de la microstructure se manifeste non seulement dans les sous-structures et la taille des grains des grains α, mais aussi dans l'état de précipitation, comme le montre la Fig. 5 (a) et (b). En raison du chauffage adiabatique produit pendant le processus d'extrusion rapide, une transformation de phase α → β se superpose à la croissance anormale des grains α,

conduisant à l'apparition de particules β intergranulaires et intragranulaires. Les particules β intergranulaires obéissant à la relation d'orientation de Burgers avec au moins un des grains voisins (Fig. 5 (c) et (d)). Les particules β intragranulaires ne montrant aucune relation d'orientation spécifique avec le grain hôte (Fig. 5 (e) et (f)). Ces résultats de la seconde partie de notre étude montrent que l'extrusion à chaud menée au-dessus de $T_{\gamma,solv}$ pourrait être une méthode appropriée pour d'une part affiner la phase α et d'autre part obtenir une texture qui permettrait d'orienter la structure lamellaire ($\alpha_2+\gamma$). Toutefois, il reste à optimiser les paramètres d'extrusion.

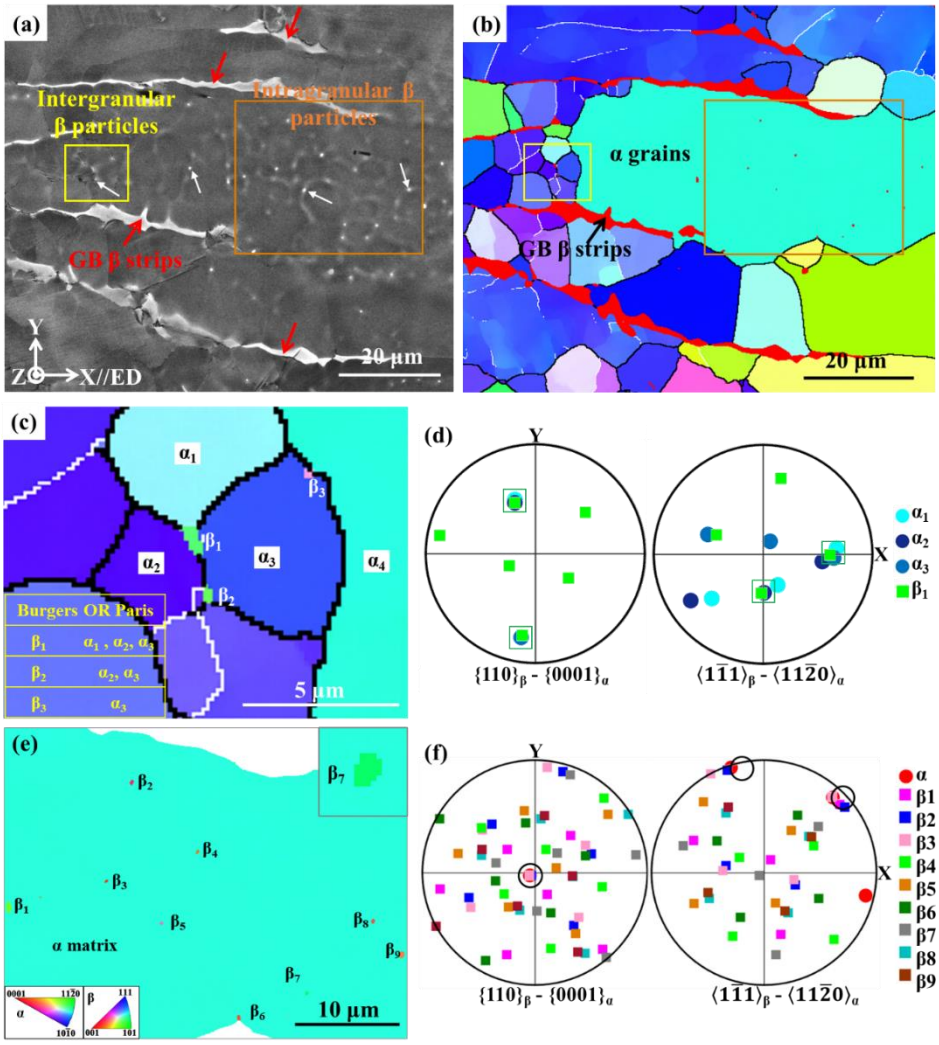


Fig. 5 (a) Micrographie SEM-BSE et (b) la micrographie IPF EBSD X (//ED) correspondante de l'alliage TNM extrudé avec le rapport d'extrusion de E7.11. (c) Micrographie IPF sur l'axe X de l'EBSD et figures polaires (d) montrant les minuscules particules intergranulaires avec leurs grains environnants (correspondant à la zone délimitée par un rectangle jaune en (a)). (e) Micrographie IPF EBSD sur l'axe X et figures polaires (f) montrant les minuscules particules intragranulaires dans la matrice α (correspondant à la zone délimitée par un rectangle orange en (a)).

# References

[1] J.C. Williams, E.A. Starke, Progress in structural materials for aerospace systems, Acta Materialia. 51 (2003) 5775–5799.

[2] J.J. Bertin, R.M. Cummings, Fifty years of hypersonics: Where we've been, where we're going, Progress in Aerospace Sciences. 39 (2003) 511–536.

[3] F. Appel, H. Clemens, F.D. Fischer, Modeling concepts for intermetallic titanium aluminides, Progress in Materials Science. 81 (2016) 55–124.

[4] P.A. Bartolotta, D.L. Krause, Titanium aluminide applications in the high speed civil transport, Gamma Titanium Aluminides. (1999) 3–10.

[5] E.A. Loria, Gamma titanium aluminides as prospective structural materials, Intermetallics. 8 (2000) 1339–1345.

[6] B.P. Bewlay, S. Nag, A. Suzuki, M.J. Weimer, TiAl alloys in commercial aircraft engines, Materials at High Temperatures. 33 (2016) 549–559.

[7] H. Clemens, S. Mayer, Intermetallic titanium aluminides in aerospace applications – processing, microstructure and properties, Materials at High Temperatures. 33 (2016) 560–570.

[8] Y.W. Kim, S.L. Kim, Advances in Gammalloy Materials–Processes–Application Technology: Successes, Dilemmas, and Future, JOM. 70 (2018) 553–560.

[9] D.. Dimiduk, Gamma titanium aluminide alloys—an assessment within the competition of aerospace structural materials, Materials Science and Engineering: A. 263 (1999) 281–288.

[10] Y.W. Kim, Ordered intermetallic alloys, part III: Gamma titanium aluminides, JOM. 46 (1994) 30–39.

[11] M.J. Blackburn, M.P. Smith, Titanium Alloys of the TiAl Type, 1981.

[12] J. Chrapoński, W. Szkliniarz, A. Kościelna, B. Serek, Microstructure and chemical

composition of phases in Ti-48Al-2Cr-2Nb intermetallic alloy, Materials Chemistry and Physics. 81 (2003) 438–442.

[13] K. Kothari, R. Radhakrishnan, N.M. Wereley, Advances in gamma titanium aluminides and their manufacturing techniques, Progress in Aerospace Sciences. 55 (2012) 1–16.

[14] GE Aviation—The GEnx Commercial Aircraft Engine, (2006). https://www.geaviation.com/commercial/engines/genx-engine.

[15] G. Norris, Power House, Flight International. (2006).

[16] T. Tetsui, K. Shindo, S. Kaji, S. Kobayashi, M. Takeyama, Fabrication of TiAl components by means of hot forging and machining, Intermetallics. 13 (2005) 971–978.

[17] X. Wu, Review of alloy and process development of TiAl alloys, Intermetallics. 14 (2006) 1114–1122.

[18] S.D. Castellanos, A.J. Cavaleiro, A.M.P. de Jesus, R. Neto, J.L. Alves, Machinability of titanium aluminides: A review, Proceedings of the Institution of Mechanical Engineers, Part L: Journal of Materials: Design and Applications. 233 (2019) 426–451.

[19] P. V. Cobbinah, W.R. Matizamhuka, Solid-State Processing Route, Mechanical Behaviour, and Oxidation Resistance of TiAl Alloys, Advances in Materials Science and Engineering. 2019 (2019).

[20] W.E. Voice, M. Henderson, E.F.J. Shelton, X. Wu, Gamma titanium aluminide, TNB, Intermetallics. 13 (2005) 959–964.

[21] F. Appel, M. Oehring, R. Wagner, Novel design concepts for gamma-base titanium aluminide alloys, Intermetallics. 8 (2000) 1283–1312.

[22] F. Appel, J.D.H. Paul, M. Oehring, Gamma Titanium Aluminide Alloys: Science and Technology, 2011.

[23] C. Kenel, C. Leinenbach, Influence of Nb and Mo on microstructure formation of rapidly solidified ternary Ti-Al-(Nb, Mo) alloys, Intermetallics. 69 (2016) 82–89.

[24] H. Clemens, H.F. Chladil, W. Wallgram, G.A. Zickler, R. Gerling, K.D. Liss, S. Kremmer, V. Güther, W. Smarsly, In and ex situ investigations of the β-phase in a Nb and Mo containing γ-TiAl based alloy, Intermetallics. 16 (2008) 827–833.

[25] W. Wallgram, T. Schmölzer, L. Cha, G. Das, V. Güther, H. Clemens, Technology and mechanical properties of advanced γ-TiAl based alloys, International Journal of Materials Research. 100 (2009) 1021–1030.

[26] H. Clemens, W. Wallgram, S. Kremmer, V. Güther, A. Otto, A. Bartels, Design of novel β-solidifying TiAl alloys with adjustable β/B2-phase fraction and excellent hot-workability, Advanced Engineering Materials. 10 (2008) 707–713.

[27] R.M. Imayev, V.M. Imayev, M. Oehring, F. Appel, Alloy design concepts for refined gamma titanium aluminide based alloys, Intermetallics. 15 (2007) 451–460.

[28] J.P. Lin, L.L. Zhao, G.Y. Li, L.Q. Zhang, X.P. Song, F. Ye, G.L. Chen, Effect of Nb on oxidation behavior of high Nb containing TiAl alloys, Intermetallics. 19 (2011) 131–136.

[29] Pratt and Whitney PW1100G Geared Turbofan Engine, (2013). https://theflyingengineer.com/flightdeck/pw1100g-gtf/.

[30] P. Janschek, Wrought TiAl blades, Materials Today: Proceedings. 2 (2015) S92–S97.

[31] V.T. Witusiewicz, A.A. Bondar, U. Hecht, S. Rex, T.Y. Velikanova, The Al-B-Nb-Ti system. III. Thermodynamic re-evaluation of the constituent binary system Al-Ti, Journal of Alloys and Compounds. 465 (2008) 64–77.

[32] D.W. James, D.M. Moon, The Science, Technology and Application of Titanium, 1970.

[33] T. Novoselova, S. Malinov, W. Sha, A. Zhecheva, High-temperature synchrotron X-ray diffraction study of phases in a gamma TiAl alloy, Materials Science and Engineering A. 371 (2004) 103–112.

[34] S. Djanarthany, J.C. Viala, J. Bouix, An overview of monolithic titanium aluminides

based on Ti3Al and TiAl, Materials Chemistry and Physics. 72 (2001) 301–319.

[35] F.H. Froes, C. Suryanarayana, D. Eliezer, Synthesis, properties and applications of titanium aluminides, Journal of Materials Science. 27 (1992) 5113–5140.

[36] M. Yamaguchi, H. Inui, K. Ito, High-temperature structural intermetallics, Acta Materialia. 48 (2000) 307–322.

[37] H. Clemens, S. Mayer, Design, processing, microstructure, properties, and applications of advanced intermetallic TiAl alloys, Advanced Engineering Materials. 15 (2013) 191–215.

[38] Y.W. Kim, Strength and ductility in TiAl alloys, Intermetallics. 6 (1998) 623–628.

[39] M. Burtscher, T. Klein, S. Mayer, H. Clemens, F.D. Fischer, The creep behavior of a fully lamellar γ-TiAl based alloy, Intermetallics. 114 (2019) 106611.

[40] S. Gao, Y. Liang, T. Ye, S. Xu, J. He, J. Lin, In-situ control of microstructure and mechanical properties during hot rolling of high-Nb TiAl alloy, Materialia. 1 (2018) 229–235.

[41] F. Appel, U. Brossmann, U. Christoph, S. Eggert, P. Janschek, U. Lorenz, J. Müllauer, M. Oehring, J.D.H. Paul, Recent progress in the development of gamma titanium aluminide alloys, Advanced Engineering Materials. 2 (2000) 699–720.

[42] Y. Kim, Microstructural evolution and mechanical properties of a forged gamma titanium aluminide alloy, Acta Metallurgica et Materialia. 40 (1992) 1121–1134.

[43] G. Cao, L. Fu, J. Lin, Y. Zhang, C. Chen, The relationships of microstructure and properties of a fully lamellar TiAl alloy, Intermetallics. 8 (2000) 647–653.

[44] C.T. Liu, P.J. Maziasz, Microstructural control and mechanical properties of dual-phase TiAl alloys, Intermetallics. 6 (1998) 653–661.

[45] D.X. Wei, Y. Koizumi, M. Nagasako, A. Chiba, Refinement of lamellar structures in Ti-Al alloy, Acta Materialia. 125 (2017) 81–97.

[46] K. Maruyama, N. Yamada, H. Sato, Effects of lamellar spacing on mechanical properties of fully lamellar Ti - 39.4mol%Al alloy, Materials Science and Engineering A. 319–321 (2001) 360–363.

[47] K. Maruyama, G. Suzuki, H.Y. Kim, M. Suzuki, H. Sato, Saturation of yield stress and embrittlement in fine lamellar TiAl alloy, Materials Science and Engineering A. 329–331 (2002) 190–195.

[48] K. Maruyama, R. Yamamoto, H. Nakakuki, N. Fujitsuna, Effects of lamellar spacing, volume fraction and grain size on creep strength of fully lamellar TiAl alloys, Materials Science and Engineering A. 239–240 (1997) 419–428.

[49] C.E. Wen, K. Yasue, J.G. Lin, Y.G. Zhang, C.Q. Chen, The effect of lamellar spacing on the creep behavior of a fully lamellar TiAl alloy, Intermetallics. 8 (2000) 525–529.

[50] Y. Mine, K. Takashima, P. Bowen, Effect of lamellar spacing on fatigue crack growth behaviour of a TiAl-based aluminide with lamellar microstructure, Materials Science and Engineering A. 532 (2012) 13–20.

[51] T. Tetsui, K. Shindo, S. Kobayashi, M. Takeyama, Strengthening a high-strength TiAl alloy by hot-forging, Intermetallics. 11 (2003) 299–306.

[52] Y.Q. Sun, Nanometer-scale, fully lamellar microstructure in an aged TiAl-based alloy, Metallurgical and Materials Transactions A. 29 (1998) 2679–2685.

[53] L. Cha, C. Scheu, H. Clemens, H.F. Chladil, G. Dehm, R. Gerling, A. Bartels, Nanometer-scaled lamellar microstructures in Ti-45Al-7.5Nb-(0; 0.5)C alloys and their influence on hardness, Intermetallics. 16 (2008) 868–875.

[54] F. Qiang, H. Kou, B. Tang, L. Song, J. Li, Effect of cooling rate on microstructure evolution of Ti-45Al-8.5Nb-0.2W-0.2B-0.02Y alloy during multi-step heat treatment, Materials Characterization. 145 (2018) 210–217.

[55] L.M. Hsiung, A.J. Schwartz, T.G. Nieh, In situ observation of deformation-induced interface migration in a fully-lamellar TiAl alloy, Scripta Materialia. 36 (1997) 1017–

1022.

[56] D.I. Kimm, J. Wolfenstine, Effect of grain size on the creep behavior of fully transformed γ-TiAl, Scripta Metallurgica et Materialia. 30 (1994) 615–619.

[57] Y.-W. Kim, D.M. Dimiduk, Progress in the understanding of gamma titanium aluminides, JOM. 43 (1991) 40–47.

[58] J.D. Bryant, L. Christodou, J.R. Maisano, Effect of TiB2 additions on the colony size of near gamma titanium aluminides, Scripta Metallurgica et Materialia. 24 (1990) 33–38.

[59] D. Gosslar, R. Günther, U. Hecht, C. Hartig, R. Bormann, Grain refinement of TiAl-based alloys: The role of TiB2 crystallography and growth, Acta Materialia. 58 (2010) 6744–6751.

[60] D. Hu, C. Yang, A. Huang, M. Dixon, U. Hecht, Solidification and grain refinement in Ti45Al2Mn2Nb1B, Intermetallics. 22 (2012) 68–76.

[61] M. Oehring, A. Stark, J.D.H. Paul, T. Lippmann, F. Pyczak, Microstructural refinement of boron-containing β-solidifying γ-titanium aluminide alloys through heat treatments in the β phase field, Intermetallics. 32 (2013) 12–20.

[62] J. Yang, J.N. Wang, Y. Wang, Q. Xia, Refining grain size of a TiAl alloy by cyclic heat treatment through discontinuous coarsening, Intermetallics. 11 (2003) 971–974.

[63] H. Clemens, A. Bartels, S. Bystrzanowski, H. Chladil, H. Leitner, G. Dehm, R. Gerling, F.P. Schimansky, Grain refinement in γ-TiAl-based alloys by solid state phase transformations, Intermetallics. 14 (2006) 1380–1385.

[64] H.I. Aaronson, V.K. Vasudevan, General discussion session of the symposium on “the mechanisms of the massive transformation,” Metallurgical and Materials Transactions A: Physical Metallurgy and Materials Science. 33 (2002) 2445–2470.

[65] S.M.L. Sastry, R.N. Mahapatra, D.F. Hasson, Microstructural refinement of Ti-44Al-11Nb by severe plastic deformation, Scripta Materialia. 42 (2000) 731–736.

[66] X.J. Xu, J.P. Lin, Y.L. Wang, J.F. Gao, Z. Lin, G.L. Chen, Effect of forging on microstructure and tensile properties of Ti-45Al-(8-9)Nb-(W,B,Y) alloy, Journal of Alloys and Compounds. 414 (2006) 175–180.

[67] P. Tian, G. Yang, Z. Ge, Y. Wang, L. Cheng, Y. Liu, H. Kou, Microstructural Refinement of a Ti-40Al-8Nb-0.5B Alloy by Hot Deformation Within (α+β) Phase Field and Subsequent Tempering, Advanced Engineering Materials. 21 (2019) 1–8.

[68] S.Z. Zhang, Z.W. Song, C.J. Zhang, J.C. Han, Y.B. Zhao, J.P. Lin, F. Yang, Fine grained fully lamellar structure acquisition and microstructure characteristics of Ti-44Al-4Nb-4V-0.3Mo-Y alloy, Materials Characterization. 144 (2018) 141–147.

[69] J. Triantafillou, J. Beddoes, L. Zhao, W. Wallace, Creep properties of near γ-TiAl+W with a lamellar microstructure, Scripta Metallurgica et Materiala. 31 (1994) 1387–1392.

[70] M.H. Oh, H. Inui, A. Nakamura, M. Yamaguchi, Recovery and recrystallization of cold-rolled polysynthetically twinned (PST) crystals of TiAl, Acta Metallurgica Et Materialia. 40 (1992) 167–176.

[71] M. Yamaguchi, D.R. Johnson, H.N. Lee, H. Inui, Directional solidification of TiAl-base alloys, Intermetallics. 8 (2000) 511–517.

[72] K. Kishida, H. Inui, M. Yamaguchi, Deformation of PST crystals of a TiAl/Ti3Al two-phase alloy at 1000°C, Intermetallics. 7 (1999) 1131–1139.

[73] D.R. Johnson, H. Inui, S. Muto, Y. Omiya, T. Yamanaka, Microstructural development during directional solidification of α-seeded TiAl alloys, Acta Materialia. 54 (2006) 1077–1085.

[74] X.F. Ding, J.P. Lin, L.Q. Zhang, Y.Q. Su, H.L. Wang, G.L. Chen, Lamellar orientation control in a Ti-46Al-5Nb alloy by directional solidification, Scripta Materialia. 65 (2011) 61–64.

[75] M.C. Kim, M.H. Oh, J.H. Lee, H. Inui, M. Yamaguchi, D.M. Wee, Composition and

growth rate effects in directionally solidified TiAl alloys, Materials Science and Engineering A. 239–240 (1997) 570–576.

[76] M. Yamaguchi, H. Inui, S. Yokoshima, K. Kishida, D.R. Johnson, Recent progress in our understanding of deformation and fracture of two-phase and single-phase TiA1 alloys, Materials Science and Engineering A. 213 (1996) 25–31.

[77] W. Luo, J. Shen, Z. Min, H. Fu, Lamellar orientation control of TiAl alloys under high temperature gradient with a Ti-43Al-3Si seed, Journal of Crystal Growth. 310 (2008) 5441–5446.

[78] G. Chen, Y. Peng, G. Zheng, Z. Qi, M. Wang, H. Yu, C. Dong, C.T. Liu, Polysynthetic twinned TiAl single crystals for higherature applications, Nature Materials. 15 (2016) 876–881.

[79] H. Fukutomi, A. Nomoto, T. Ota, Control of lamellar arrangement in TiAl alloys by high-temperature deformation in α single phase and subsequent annealing in two phase region, Materials Transactions, JIM. 36 (1995) 610–614.

[80] T. Suzuki, Y. Tomota, T. Tsujimoto, T. Furuyama, K. Shibue, Control of lamellar orientation in TiAl base alloy using a combination of heavy extrusion and reactive sintering, Philosophical Magazine Letters. 75 (1997) 337–342.

[81] M. Hasegawa, H. Fukutomi, Lamellar orientation control in TiAl base alloys by a two-step compression process at high temperature, Materials Science and Engineering A. 508 (2009) 106–113.

[82] M. Hasegawa, K. Sakurai, L. Stratil, I. Dlouhy, H. Fukutomi, Fracture toughness of a lamellar orientation-controlled TiAl-based alloy processed by either one-step or two-step compression at high temperature, Materials Science and Engineering A. 721 (2018) 303–310.

[83] K.S. Park, D.S. Bae, G.H. Lee, S.K. Lee, Orientation control of a lamellar microstructure in a Ti-Al intermetallic compound by high-temperature compression in an alpha single-phase and/or in a two-phase region and the alpha re-heat treatment,

Metals and Materials International. 11 (2005) 481–486.

[84] H. Fukutomi, M. Ueno, M. Nakamura, T. Suzuki, S. Kikuchi, Production of TiAl sheet with oriented lamellar microstructure by diffusional reaction of aluminum and textured titanium foils, Materials Transactions, JIM. 40 (1999) 654–658.

[85] T. Suzuki, H. Fukutomi, Y. Tomota, T. Tsujimoto, Formation of oriented lamellar colonies in a TiAlMn alloy produced by a reactive sintering, Materials Transactions, JIM. 40 (1999) 1032–1037.

[86] K.S. Park, D.S. Bae, H.J. Kim, C.Y. Kang, S.K. Lee, Deformation behavior of TiAl intermetallic compounds and orientation control by reactive diffusion and high-temperature uniaxial compression deformation, Metals and Materials International. 12 (2006) 447–451.

[87] C.T. Liu, J.H. Schneibel, P.J. Maziasz, J.L. Wright, D.S. Easton, Tensile properties and fracture toughness of TiAl alloys with controlled microstructures, Intermetallics. 4 (1996) 429–440.

[88] F. Kong, Y. Chen, D. Zhang, S. Zhang, High temperature deformation behavior of Ti-46Al-2Cr-4Nb-0.2Y alloy, Materials Science and Engineering A. (2012).

[89] W.J. Zhang, U. Lorenz, F. Appel, Recovery, recrystallization and phase transformations during thermomechanical processing and treatment of TiAl-based alloys, Acta Materialia. 48 (2000) 2803–2813.

[90] E. Schwaighofer, H. Clemens, J. Lindemann, A. Stark, S. Mayer, Hot-working behavior of an advanced intermetallic multi-phase γ-TiAl based alloy, Materials Science and Engineering A. 614 (2014) 297–310.

[91] G. Wang, L. Xu, Y. Tian, Z. Zheng, Y. Cui, R. Yang, Flow behavior and microstructure evolution of a P/M TiAl alloy during high temperature deformation, Materials Science and Engineering A. 528 (2011) 6754–6763.

[92] J. Li, Y. Liu, Y. Wang, B. Liu, Y. He, Dynamic recrystallization behavior of an as-cast

TiAl alloy during hot compression, Materials Characterization. 97 (2014) 169–177.

[93] S.Z. Zhang, C.J. Zhang, Z.X. Du, Z.P. Hou, P. Lin, F.T. Kong, Y.Y. Chen, Deformation behavior of high Nb containing TiAl based alloy in α+γ two phase field region, Materials and Design. 90 (2016) 225–229.

[94] S. Zeng, A. Zhao, H. Jiang, Y. Ren, Flow behavior and processing maps of Ti-44.5Al-3.8Nb-1.0Mo-0.3Si-0.1B alloy, Journal of Alloys and Compounds. 698 (2017) 786–793.

[95] L.M. Hsiung, T.G. Nieh, D.R. Clemens, Effect of extrusion temperature on the microstructure of a powder metallurgy TiAl-based alloy, Scripta Materialia. 36 (1997) 233–238.

[96] W.C. Xu, D.B. Shan, H. Zhang, X.A. Li, Y.Z. Zhang, S. Nutt, Effects of extrusion deformation on microstructure, mechanical properties and hot workability of B containing TiAl alloy, Materials Science and Engineering A. 571 (2013) 199–206.

[97] C.T. Liu, J.L. Wright, S.C. Deevi, Microstructures and properties of a hot-extruded TiAl containing no Cr, Materials Science and Engineering A. 329–331 (2002) 416–423.

[98] Y. Luo, W. Zeng, Z. Xi, X. Mao, Y. Yang, J. Wu, H. Su, Microstructure, mechanical properties and oxidation behavior of a hot-extruded TiAl containing Ta, Rare Metal Materials and Engineering. 44 (2015) 282–287.

[99] R. Liu, D. Liu, J. Tan, Y. Cui, R. Yang, F. Liu, P.A. Withey, Textures of rectangular extrusions and their effects on the mechanical properties of thermo-mechanically treated, lamellar microstructure, Ti-47Al-2Cr-2Nb-0.15B, Intermetallics. 52 (2014) 110–123.

[100] W. Xu, X. Jin, K. Huang, Y. Zong, S. Wu, X. Zhong, F. Kong, D. Shan, S. Nutt, Improvement of microstructure, mechanical properties and hot workability of a TiAl-Nb-Mo alloy through hot extrusion, Materials Science and Engineering A. 705 (2017) 200–209.

[101] S. Tian, H. Jiang, W. Guo, G. Zhang, S. Zeng, Hot deformation and dynamic recrystallization behavior of TiAl-based alloy, Intermetallics. 112 (2019) 106521.

[102] V. Singh, C. Mondal, A. Kumar, P.P. Bhattacharjee, P. Ghosal, High temperature compressive flow behavior and associated microstructural development in a β-stabilized high Nb-containing γ-TiAl based alloy, Journal of Alloys and Compounds. 788 (2019) 573–585.

[103] H.T. Jiang, S.W. Zeng, S.W. Tian, B. Wu, A.M. Zhao, Z.H. Xia, Microstructural Evolution and Dynamic Recrystallization Behavior of β–γ TiAl-based Alloy during Hot Compression, Advanced Engineering Materials. 19 (2017) 1–8.

[104] H. Jiang, S. Zeng, A. Zhao, X. Ding, P. Dong, Hot deformation behavior of β phase containing γ-TiAl alloy, Materials Science and Engineering A. 661 (2016) 160–167.

[105] R.M. Imayev, V.M. Imayev, M. Oehring, F. Appel, Microstructural Evolution during Hot Working of Ti Aluminide Alloys : Influence of Phase Constitution and Initial Casting Texture, Metallurgical and Materials Transactions A. 36 (2005) 859–867.

[106] W.J. Zhang, U. Lorenz, F. Appel, Recovery, recrystallization and phase transformations during thermomechanical processing and treatment of TiAl-based alloys, Acta Materialia. 48 (2000) 2803–2813.

[107] H. Zhou, F. Kong, X. Wang, Y. Chen, High strength in high Nb containing TiAl alloy sheet with fine duplex microstructure produced by hot pack rolling, Journal of Alloys and Compounds. 695 (2017) 3495–3502.

[108] Y. Su, F. Kong, Y. Chen, N. Gao, D. Zhang, Microstructure and mechanical properties of large size Ti-43Al-9V-0.2Y alloy pancake produced by pack-forging, Intermetallics. 34 (2013) 29–34.

[109] H.Z. Niu, R.L. Tong, X.J. Chen, T.B. Zhang, D.L. Zhang, Rapid decomposition of lamellar microstructure and enhanced hot workability of an as-cast triphase Ti–45Al–6Nb–1Mo alloy via one-step alpha-extrusion & annealing, Materials Science and Engineering A. 801 (2021) 140438.

[110] T. Schmoelzer, K.D. Liss, C. Kirchlechner, S. Mayer, A. Stark, M. Peel, H. Clemens, An in-situ high-energy X-ray diffraction study on the hot-deformation behavior of a β-phase containing TiAl alloy, Intermetallics. 39 (2013) 25–33.

[111] K.D. Liss, T. Schmoelzer, K. Yan, M. Reid, M. Peel, R. Dippenaar, H. Clemens, In situ study of dynamic recrystallization and hot deformation behavior of a multiphase titanium aluminide alloy, Journal of Applied Physics. 106 (2009) 113526.

[112] A.M. Wusatowska-Sarnek, H. Miura, T. Sakai, Nucleation and microtexture development under dynamic recrystallization of copper, Materials Science and Engineering A. (2002).

[113] A. Belyakov, H. Miura, T. Sakai, Dynamic recrystallization under warm deformation of a 304 type austenitic stainless steel, Materials Science and Engineering A. 255 (1998) 139–147.

[114] E. Brünger, X. Wang, G. Gottstein, Nucleation mechanisms of dynamic recrystallization in austenitic steel alloy 800H, Scripta Materialia. 38 (1998) 1843–1849.

[115] A. Dehghan-Manshadi, M.R. Barnett, P.D. Hodgson, Recrystallization in AISI 304 austenitic stainless steel during and after hot deformation, Materials Science and Engineering A. 485 (2008) 664–672.

[116] D. Ponge, G. Gottstein, Necklace formation during dynamic recrystallization: Mechanisms and impact on flow behavior, Acta Materialia. 46 (1998) 69–80.

[117] J. Humphreys, G.S. Rohrer, A. Rollett, Recrystallization and Related Annealing Phenomena (3rd edition), 2017.

[118] W. Roberts, B. Ahlblom, A nucleation criterion for dynamic recrystallization during hot working, Acta Metallurgica. 26 (1978) 801–813.

[119] S. Gourdet, F. Montheillet, A model of continuous dynamic recrystallization, Acta Materialia. 51 (2003) 2685–2699.

[120] T. Sakai, H. Miura, A. Goloborodko, O. Sitdikov, Continuous dynamic recrystallization during the transient severe deformation of aluminum alloy 7475, Acta Materialia. (2009).

[121] F. Musin, A. Belyakov, R. Kaibyshev, Y. Motohashi, G. Itoh, K. Tsuzaki, Microstructure evolution in a cast 1421AI alloy during hot equal-channel angular extrusion, Reviews on Advanced Materials Science. 25 (2010) 107–112.

[122] X. Yang, Y. Okabe, H. Miura, T. Sakai, Effect of prior strain on continuous recrystallization in AZ31 magnesium alloy after hot deformation, Materials Science and Engineering A. 535 (2012) 209–215.

[123] Y. Yang, X. Yang, Z. Xiao, D. Zhang, J. Wang, T. Sakai, Annealing behavior of a cast Mg-Gd-Y-Zr alloy with necklace fine grains developed under hot deformation, Materials Science and Engineering A. 688 (2017) 280–288.

[124] X. Yang, H. Miura, T. Sakai, Dynamic nucleation of new grains in magnesium alloy during hot deformation, Materials Science Forum. 419–422 (2003) 515–520.

[125] H. Miura, M. Ito, X. Yang, J.J. Jonas, Mechanisms of grain refinement in Mg-6Al-1Zn alloy during hot deformation, Materials Science and Engineering A. 538 (2012) 63–68.

[126] O. Sitdikov, R. Kaibyshev, Dynamic recrystallization in pure magnesium, Materials Transactions. 42 (2001) 1928–1937.

[127] M.R. Barnett, Z. Keshavarz, A.G. Beer, D. Atwell, Influence of grain size on the compressive deformation of wrought Mg-3Al-1Zn, Acta Materialia. 52 (2004) 5093–5103.

[128] A. Galiyev, R. Kaibyshev, G. Gottstein, Correlation of plastic deformation and dynamic recrystallization in magnesium alloy ZK60, Acta Materialia. 49 (2001) 1199–1207.

[129] H. Miura, X. Yang, T. Sakai, H. Nogawa, S. Miura, Y. Watanabe, J.J. Jonas, High temperature deformation and extended plasticity in Mg single crystals, Philosophical

Magazine. 85 (2005) 3553–3565.

[130] Q. Chao, H. Beladi, I. Sabirov, P.D. Hodgson, Deformation behaviour of a commercial pure titanium alloy during hot compression testing, Materials Science Forum. 773–774 (2014) 281–286.

[131] Z. Zeng, Y. Zhang, S. Jonsson, Deformation behaviour of commercially pure titanium during simple hot compression, Materials and Design. 30 (2009) 3105–3111.

[132] C. Yan, A. Feng, S. Qu, J.L. Sun, J. Shen, Hot deformation and grain refinement mechanisms of commercially pure titanium processed via three-directional cryo-compression, Materials Science and Engineering A. 731 (2018) 266–277.

[133] P.G. Partridge, The crystallography and deformation modes of hexagonal close-packed metals, Metallurgical Reviews. 12 (1967) 169–194.

[134] T.B. Britton, F.P.E. Dunne, A.J. Wilkinson, On the mechanistic basis of deformation at the microscale in hexagonal close-packed metals, Proceedings of the Royal Society A: Mathematical, Physical and Engineering Sciences. 471 (2015).

[135] Y. Umakoshi, T. Nakano, T. Takenaka, K. Sumimoto, T. Yamane, Orientation and temperature dependence of yield stress and slip geometry of Ti3Al and Ti3Al-V single crystals, Acta Metallurgica Et Materialia. 41 (1993) 1149–1154.

[136] T.R. Bieler, S.L. Semiatin, The origins of heterogeneous deformation during primary hot working of Ti-6Al-4V, International Journal of Plasticity. 18 (2002) 1165–1189.

[137] P. Erdely, P. Staron, E. Maawad, N. Schell, J. Klose, S. Mayer, H. Clemens, Effect of hot rolling and primary annealing on the microstructure and texture of a β-stabilised γ-TiAl based alloy, Acta Materialia. 126 (2017) 145–153.

[138] P. Erdely, P. Staron, E. Maawad, N. Schell, J. Klose, H. Clemens, S. Mayer, Design and control of microstructure and texture by thermomechanical processing of a multi-phase TiAl alloy, Materials and Design. 131 (2017) 286–296.

[139] W. Schillinger, A. Bartels, R. Gerling, F.P. Schimansky, H. Clemens, Texture

evolution of the γ- And the α/α 2-phase during hot rolling of γ-TiAl based alloys, Intermetallics. 14 (2006) 336–347.

[140] A. Stark, A. Bartels, R. Gerling, F.-P.F.P. Schimansky, H. Clemens, Microstructure and Texture Formation during Hot Rolling of Niobium-Rich γ TiAl Alloys with Different Carbon Contents, Advanced Engineering Materials. 8 (2006) 1101–1108.

[141] D. Dunst, H. Mecking, Analysis of experimental and theoretical rolling textures of two-phase titanium alloys, Zeitschrift Fuer Metallkunde/Materials Research and Advanced Techniques. 87 (1996) 498–507.

[142] S. Suwas, R.K. Ray, A.K. Singh, S. Bhargava, Evolution of hot rolling textures in a two-phase (α2+β) Ti3Al base alloy, Acta Materialia. 47 (1999) 4585–4598.

[143] A.K. Singh, R.A. Schwarzer, Texture and anisotropy of mechanical properties in titanium and its alloys, Zeitschrift Fuer Metallkunde/Materials Research and Advanced Techniques. 91 (2000) 702–716.

[144] S.K. Sahoo, R.K. Sabat, S. Sahni, S. Suwas, Texture and microstructure evolution of commercially pure titanium during hot rolling: Role of strain-paths, Materials and Design. 91 (2016) 58–71.

[145] A. Stark, A. Bartels, H. Clemens, S. Kremmer, F.P. Schimansky, R. Gerling, Microstructure and texture formation during near conventional forging of an intermetallic Ti-45Al-5Nb alloy, Advanced Engineering Materials. 11 (2009) 976–981.

[146] Y.B. Chun, S.L. Semiatin, S.K. Hwang, Monte Carlo modeling of microstructure evolution during the static recrystallization of cold-rolled, commercial-purity titanium, Acta Materialia. 54 (2006) 3673–3689.

[147] F. Wagner, N. Bozzolo, O. Van Landuyt, T. Grosdidier, Evolution of recrystallisation texture and microstructure in low alloyed titanium sheets, Acta Materialia. 50 (2002) 1245–1259.

[148] N. Bozzolo, N. Dewobroto, T. Grosdidier, F. Wagner, Texture evolution during grain

growth in recrystallized commercially pure titanium, Materials Science and Engineering: A. 397 (2005) 346–355.

[149] S. Müller, K. Mueller, W. Reimers, Modifications of the Extrusion Process of Magnesium Alloys for Improved Mechanical Properties, Key Engineering Materials. 367 (2008) 9–16.

[150] M.T. Pérez-Prado, O.A. Ruano, Texture evolution during annealing of magnesium AZ31 alloy, Scripta Materialia. 46 (2002) 149–155.

[151] M.G. Jiang, C. Xu, H. Yan, G.H. Fan, T. Nakata, C.S. Lao, R.S. Chen, S. Kamado, E.H. Han, B.H. Lu, Unveiling the formation of basal texture variations based on twinning and dynamic recrystallization in AZ31 magnesium alloy during extrusion, Acta Materialia. 157 (2018) 53–71.

[152] F. Gerspach, N. Bozzolo, F. Wagner, About texture stability during primary recrystallization of cold-rolled low alloyed zirconium, Scripta Materialia. 60 (2009) 203–206.

[153] K.Y. Zhu, D. Chaubet, B. Bacroix, F. Brisset, A study of recovery and primary recrystallization mechanisms in a Zr-2Hf alloy, Acta Materialia. 53 (2005) 5131–5140.

[154] N. Dewobroto, N. Bozzolo, P. Barberis, F. Wagner, On the mechanisms governing the texture and microstructure evolution during static recrystallization and grain growth of low alloyed zirconium sheets (Zr702), Zeitschrift Fuer Metallkunde/Materials Research and Advanced Techniques. 97 (2006) 826–833.

[155] R.K. McGeary, B. Lustman, Preferred Orientation in Zirconium, Journal of Metals. 3 (1951) 994–1002.

[156] A.N. Behera, A. Chaudhuri, R. Kapoor, J.K. Chakravartty, S. Suwas, High temperature deformation behavior of Nb-1wt.%Zr alloy, Materials and Design. 92 (2016) 750–759.

[157] J.G. Wang, T.G. Nieh, Creep of a beta phase-containing TiAl alloy, Intermetallics. 8 (2000) 737–748.

[158] J. Shen, Y. Sun, Y. Ning, H. Yu, Z. Yao, L. Hu, Superplasticity induced by the competitive DRX between BCC beta and HCP alpha in Ti-4Al-3V-2Mo-2Fe alloy, Materials Characterization. 153 (2019) 304–317.

[159] S. Balachandran, S. Kumar, D. Banerjee, On recrystallization of the α and β phases in titanium alloys, Acta Materialia. 131 (2017) 423–434.

[160] S. Roy, S. Suwas, Deformation mechanisms during superplastic testing of Ti-6Al-4V-0.1B alloy, Materials Science and Engineering A. 574 (2013) 205–217.

[161] S.R. Dey, A. Hazotte, E. Bouzy, Crystallography and phase transformation mechanisms in TiAl-based alloys - A synthesis, Intermetallics. 17 (2009) 1052–1064.

[162] L. Germain, N. Gey, R. Mercier, P. Blaineau, M. Humbert, An advanced approach to reconstructing parent orientation maps in the case of approximate orientation relations: Application to steels, Acta Materialia. 60 (2012) 4551–4562.

[163] E. Schwaighofer, H. Clemens, S. Mayer, J. Lindemann, J. Klose, W. Smarsly, V. Güther, Microstructural design and mechanical properties of a cast and heat-treated intermetallic multi-phase γ-TiAl based alloy, Intermetallics. 44 (2014) 128–140.

[164] J.J. Fundenberger, A. Morawiec, E. Bouzy, J.S. Lecomte, Polycrystal orientation maps from TEM, Ultramicroscopy. 96 (2003) 127–137.

[165] B. Beausir, J.-J. Fundenberger, Analysis Tools for Electron and X-ray diffraction, ATEX - software, www.atex-software.eu, Université de Lorraine - Metz, (2017).

[166] Y.B. Chun, M. Battaini, C.H.J. Davies, S.K. Hwang, Distribution characteristics of in-grain Misorientation axes in cold-rolled commercially pure titanium and their correlation with active slip modes, Metallurgical and Materials Transactions A. 41 (2010) 3473–3487.

[167] Y.B. Chun, C.H.J. Davies, Investigation of prism <a> slip in warm-rolled AZ31 alloy, Metallurgical and Materials Transactions A. 42 (2011) 4113–4125.

[168] J.P. Hadorn, K. Hantzsche, S. Yi, J.A.N. Bohlen, D. Letzig, J.A. Wollmershauser, S.R.

Agnew, Role of solute in the texture modification during hot deformation of Mg-rare earth alloys, Metallurgical and Materials Transactions A. 43 (2012) 1347–1362.

[169] M. Yamasaki, K. Hagihara, S.I. Inoue, J.P. Hadorn, Y. Kawamura, Crystallographic classification of kink bands in an extruded Mg-Zn-Y alloy using intragranular misorientation axis analysis, Acta Materialia. 61 (2013) 2065–2076.

[170] R. Maddin, N.K. Chen, Geometrical aspects of the plastic deformation of metal single crystals, Progress in Metal Physics. 5 (1954) 53–95.

[171] S.L.S. S. Mironov, M. Murzinova, S. Zherebtsov, G.A. Salishchev, S. Mironov, M. Murzinova, S. Zherebtsov, G.A. Salishchev, S.L. Semiatin, Microstructure evolution during warm working of Ti–6Al–4V with a colony-α microstructure, Acta Materialia. 57 (2009) 2470–2481.

[172] C. Randau, U. Garbe, H.G. Brokmeier, StressTextureCalculator: A software tool to extract texture, strain and microstructure information from area-detector measurements, Journal of Applied Crystallography. 44 (2011) 641–646.

[173] H.J. Bunge, C. Esling, J. Muller, The role of the inversion centre in texture analysis, Journal of Applied Crystallography. 13 (1980) 544–554.

[174] H.J. Bunge, C. Esling, J. Muller, The influence of crystal and sample symmetries on the orientation distribution function of the crystallites in polycrystalline materials, Acta Crystallographica Section A. 37 (1981) 889–899.

[175] O. Engler, V. Randle, Introduction to texture analysis: Macrotexture, Microtexture, and Orientation Mapping, 2010.

[176] H.J. Bunge, Texture Analysis in Materials Science, 1982.

[177] A.G. Khachaturyan, Theory of structural transformations in solids, 2013.

[178] J.K. Mackenzie, Second paper on statistics associated with the random disorientation of cubes, Biometrika. 45 (1958) 229–240.

[179] H.W. Son, J.W. Lee, S.K. Hyun, Mechanism of grain boundary serration during hot

deformation of AZ31 alloy: Role of grain boundary dislocations and grain boundary sliding, International Journal of Plasticity. 125 (2020) 118–132.

[180] P.R. Rios, F. Siciliano, H.R.Z. Sandim, R.L. Plaut, A.F. Padilha, Nucleation and growth during recrystallization, Materials Research. 8 (2005) 225–238.

[181] T. Jun, Z. Zhang, G. Sernicola, F.P.E. Dunne, T.B. Britton, Local strain rate sensitivity of single a phase within a dual-phase Ti alloy, Acta Materialia. 107 (2016) 298–309.

[182] J. Wang, Y. Chen, Z. Chen, J. Llorca, X. Zeng, Deformation mechanisms of Mg-Ca-Zn alloys studied by means of micropillar compression tests, Acta Materialia. 217 (2021) 117151.

[183] J.B. Hess, C.S. Barrett, Structure and nature of kink bands in zinc, JOM. 1 (1949) 599–606.

[184] E.Orowan, A type of plastic deformation new in metals, Nature. 149 (1942) 643–644.

[185] T. Matsumoto, M. Yamasaki, K. Hagihara, Y. Kawamura, Configuration of dislocations in low-angle kink boundaries formed in a single crystalline long-period stacking ordered Mg-Zn-Y alloy, Acta Materialia. 151 (2018) 112–124.

[186] S.E. Ion, F.J. Humphreys, S.H. White, Dynamic recrystallisation and the development of microstructure during the high temperature deformation of magnesium, Acta Metallurgica. 30 (1982) 1909–1919.

[187] K. Hagihara, T. Mayama, M. Honnami, M. Yamasaki, H. Izuno, T. Okamoto, T. Ohashi, T. Nakano, Y. Kawamura, Orientation dependence of the deformation kink band formation behavior in Zn single crystal, International Journal of Plasticity. 77 (2016) 174–191.

[188] T.J. Nizolek, M.R. Begley, R.J. McCabe, J.T. Avallone, N.A. Mara, I.J. Beyerlein, T.M. Pollock, Strain fields induced by kink band propagation in Cu-Nb nanolaminate composites, Acta Materialia. 133 (2017) 303–315.

[189] R. Matsumoto, M. Uranagase, N. Miyazaki, Molecular dynamics analyses of

deformation behavior of long-period- stacking-ordered structures, Materials Transactions. 54 (2013) 686–692.

[190] K. Hagihara, T. Okamoto, M. Yamasaki, Y. Kawamura, T. Nakano, Electron backscatter diffraction pattern analysis of the deformation band formed in the Mg-based long-period stacking ordered phase, Scripta Materialia. 117 (2016) 32–36.

[191] U.F. Kocks, C.N. Tomé, H.R. Wenk, Texture And Anisotropy: Preferred Orientations in Polycrystals and their Effect on Materials Properties, 1998.

[192] G. Yang, H. Kou, J. Yang, J. Li, H. Fu, Microstructure control of Ti-45Al-8.5Nb-(W, B, Y) alloy during the solidification process, Acta Materialia. 112 (2016) 121–131.

[193] M. Shahzad, L. Wagner, Influence of extrusion parameters on microstructure and texture developments, and their effects on mechanical properties of the magnesium alloy AZ80, Materials Science and Engineering A. 506 (2009) 141–147.

[194] Z. Yu, C. Xu, J. Meng, K. Liu, J. Fu, S. Kamado, Effects of extrusion ratio and temperature on the mechanical properties and microstructure of as-extruded Mg-Gd-Y-(Nd/Zn)-Zr alloys, Materials Science and Engineering A. 762 (2019) 138080.

[195] D. Zhang, Q. Yang, K. Guan, B. Li, N. Wang, P. Qin, B. Jiang, C. Sun, X. Qin, Z. Tian, Z. Cao, J. Meng, A high-strength low-rare-earth-alloyed magnesium alloy via traditional hot-extrusion, Journal of Alloys and Compounds. 810 (2019) 151967.

[196] G. Huang, Y. Han, X. Guo, D. Qiu, L. Wang, W. Lu, D. Zhang, Effects of extrusion ratio on microstructural evolution and mechanical behavior of in situ synthesized Ti-6Al-4V composites, Materials Science and Engineering A. 688 (2017) 155–163.

[197] N. Allain-Bonasso, F. Wagner, S. Berbenni, D.P. Field, A study of the heterogeneity of plastic deformation in IF steel by EBSD, Materials Science and Engineering A. 548 (2012) 56–63.

[198] P. Peng, J. She, A. Tang, J. Zhang, S. Zhou, X. Xiong, F. Pan, Novel continuous forging extrusion in a one-step extrusion process for bulk ultrafine magnesium alloy,

Materials Science and Engineering A. 764 (2019) 138144.

[199] F. Qiang, E. Bouzy, H. Kou, Y. Zhang, Grain fragmentation associated continuous dynamic recrystallization ( CDRX ) of hexagonal structure during uniaxial isothermal compression : High-temperature α phase in TiAl alloys, Intermetallics. 129 (2021) 107028.

[200] R. Kainuma, Y. Fujita, H. Mitsui, I. Ohnuma, K. Ishida, Phase equilibria among α (hcp), β (bcc) and γ (L10) phases in Ti-Al base ternary alloys, Intermetallics. 8 (2000) 855–867.

[201] S. Zherebtsov, G. Salishchev, W. Łojkowski, Strengthening of a Ti-6Al-4V titanium alloy by means of hydrostatic extrusion and other methods, Materials Science and Engineering A. 515 (2009) 43–48.

# Publication List

## I: Publications in International Journals

[1]. **Fengming Qiang**, Hongchao Kou, Yudong Zhang, Mengyu Jia, Nana Chen, Jishan Li, Emmanuel Bouzy. Thermally-induced α → β phase transformation interweaving with abnormal α grain growth in hot extruded TNM alloy [J]. Journal of Materials Research and Technology, 2021, 15:2036-2044.

[2]. **Fengming Qiang**, Emmanuel Bouzy, Hongchao Kou, Yudong Zhang, Lingling Wang, Jishan Li. Grain fragmentation associated continuous dynamic recrystallization (CDRX) of hexagonal structure during uniaxial isothermal compression: High-temperature α phase in TiAl alloys [J]. Intermetallics, 2021, 129: 107028.

[3]. **Fengming Qiang**, Hongchao Kou, Lingling Wang, Jishan Li. $\beta_0$ precipitation in $\alpha_2$ lamellae of the β-solidifying multiple-phase γ-TiAl alloy [J]. Materials Characterization, 2020, 167:110474.

[4]. **Fengming Qiang**, Hongchao Kou, Bin Tang, Lin Song, Jishan Li. Effect of cooling rate on microstructure evolution of Ti-45Al-8.5Nb-0.2W-0.2B-0.02Y alloy during multi-step heat treatment [J]. Materials Characterization, 2018, 145: 210-217.

[5]. **Fengming Qiang**, Hongchao Kou, Guang Yang, Bin Tang, Jishan Li. Multi-step heat treatment design for nano-scale lamellar structures of a cast Ti-45Al-8.5Nb-(W, B, Y) alloy [J]. Intermetallics, 2016, 79: 35-40.

[6]. Liang Cheng, **Fengming Qiang**, Jinshan Li, Emmanuel Bouzy. Quantitative evaluation of the lamellar kinking&rotation on the flow softening of γ-TiAl-based alloys at elevated temperatures [J]. Materials Letter, 2021: 129458.

[7]. Yonghao Yu, Hongchao Kou, **Fengming Qiang**, Lingling Wang, Yuqing Li, Ruifeng Zhao, Jishan Li. The $\alpha_2$ precipitation from equiaxed γ phase in as-cast Ti-44Al-4Nb-2Cr-0.1B alloy [J]. Materials Letter, 2021, 284: 128978.

## II: Contributions to International Conferences

[1]. **Fengming Qiang**, Hongchao Kou, Emmanuel Bouzy, Yudong Zhang, Jinshan Li. Texture evolution and deformation behavior of α-phase in a β-solidified γ-TiAl based alloy during high-temperature extrusion. *"EUROMAT 2019"*, September 1-5, 2019, Stockholm, Sweden. **Oral Presentation**.

[2]. **Fengming Qiang**, Hongchao Kou, Emmanuel Bouzy, Yudong Zhang, Jinshan Li. Microstructure evolution of α phase in TNM intermetallic during high-temperature uniaxial compression. *"The 14th World Conference on Titanium"*, June 10-14, 2019, Nantes, France. **Oral presentation**.

[3]. **Fengming Qiang,** Hongchao Kou, Jinshan Li. Effect of cooling rate on microstructure evolution of Ti-45Al-8.5Nb-0.2W-0.2B-0.02Y alloy during multi-step heat treatment. *"EUROMAT 2017"*, September 17-22, 2017, Thessaloniki, Greece. **Oral Presentation**.